Functional Wet/Underwater Adhesives Enabled by Hydrogen-Bonding Interaction-Driven Coacervation

by

Qiongyao Peng

A thesis submitted in partial fulfillment of the requirements for the degree of

Doctor of Philosophy

in

Chemical Engineering

Department of Chemical and Materials Engineering
University of Alberta

Abstract

Robust instant and repeatable underwater adhesion is a great challenge for the development of adhesives as water is a notorious destroyer to prevent the intimate contact of adhesives and substrates by forming hydration layers on surfaces. Long-lasting and strong underwater adhesion of sessile organisms has inspired substantial research attraction in biomimetic underwater adhesives, whose formation involves a critical biological process named coacervation. Coacervation is a liquid-liquid phase separation phenomenon where a material-rich dense coacervate phase and a co-existing immiscible dilute supernatant simultaneously generated from a homogeneous aqueous solution consisting of one (simple coacervation) or two different types of (complex coacervation) macromolecules (e.g., proteins, polymers, and colloids). Current coacervation-derived wet/underwater adhesives usually suffer from complex polymer synthesis, delicate formation conditions, weak mechanical properties, and low yields. Additionally, increasing demands of advanced and smart materials impels the fabrication of wet/underwater adhesives with multifunctionalities, which is rarely achieved. In this thesis, a review of recent advances in coacervation and underlying noncovalent intermolecular interactions is presented first, followed by three original studies regarding the development of multifunctional wet/underwater adhesives based on hydrogen-bonding interaction-driven coacervates.

Wet adhesives have been recognized as attractive candidates of tissue glues and wound dressings. In the first project, an instant paintable antimicrobial hemostatic agent was developed based on hydrogen-bonding interaction-enabled coacervates. The fabrication of the coacervate was achieved via one-step mixing of silicotungstic acid (SiW) and poly(ethylene glycol) (PEG) aqueous solutions, which is extremely facile and could be scaled up. Phase behaviors, rheological properties, and associated intermolecular interaction of the coacervates were investigated. This

work demonstrates that coacervation can occur in salt-free environments via non-electrostatic interactions, providing a new platform for engineering multifunctional coacervate materials as tissue glues, wound dressings, and membrane-free cell systems.

Instant underwater adhesives have gained special interest as paintable electrodes in the development of next-generation aqueous batteries. In the second project, coacervation-driven instant paintable underwater adhesives with tunable optical and electrochromic properties were prepared. The formation of the adhesives was induced through the facile one-step mixing of SiW and poly(ethylene glycol)-block-poly(propylene glycol)-block-poly(ethylene glycol) (P123) micelles aqueous solutions, which was driven by hydrogen-bonding and hydrophobic interactions. The as-prepared adhesive possesses instant and excellent underwater adhesion (up to 479.6 kPa on poly(methyl methacrylate)) and can be readily painted underwater on diverse substrates, showing resistance to water flush as well as repeatable stretching and bending of the substrates. The adhesive also exhibited outstanding stability in aqueous solutions of high salinity up to 3 M for at least 1200 h. The introduction of P123 endows the adhesives with thermo-responsive optical property, while the innate reduction-related color switch of SiW offers the electrochromic property. The functional adhesives hold great promise in bioengineering applications and for the fabrication of novel flexible electronics such as smart aqueous batteries and low-power electrochromic windows.

In the third project, novel instant and repeatable underwater adhesives with anticancer and antibacterial properties were fabricated via the one-step mixing of tannic acid (TA) and poly(ethylene glycol)-block-poly(propylene glycol)-block-poly(ethylene glycol) (F68) micelles aqueous solutions. This coacervation phenomenon was also driven by hydrogen-bonding and hydrophobic interactions. Meanwhile, the coacervates could be facilely painted on different

substrates, exhibiting robust and instant underwater adhesion (with adhesion strength up to 1.1 MPa on porcine skin) and excellent repeatability (at least 1000 cycles). Due to the biological activities of TA, the underwater adhesive displayed innate anticancer and antibacterial properties against different types of cancer cells and bacteria, showing great potential for diverse biomedical applications, such as injectable drug carriers, tissue glues and wound dressings.

Three novel functional wet/underwater adhesives have been developed in this work, which are based on coacervation driven by hydrogen-bonding interaction. This work expands the applicability of hydrogen-bonding interaction to different multifunctional materials such as antibacterial hemostatic agent and paintable electrodes, providing new insights and approaches to the development of advanced functional materials based on hydrogen-bonding interaction for diverse biomedical and engineering applications.

Preface

This thesis is an original work conducted by Qiongyao Peng under the supervision from Dr. Hongbo Zeng.

Chapter 1 of this thesis is a review manuscript named "Recent Advances in Coacervation and Underlying Non-covalent Intermolecular Interactions", which is originally written by Qiongyao Peng and has never been published before.

Chapter 2 of this thesis has been published as Qiongyao Peng, Jingsi Chen, Zicheng Zeng, Tao Wang, Li Xiang, Xuwen Peng, Jifang Liu, Hongbo Zeng, "Adhesive Coacervates Driven by Hydrogen-Bonding Interaction", *Small*. 2020, 16, 2004132. I was responsible for experimental design, data collection and analysis, as well as the manuscript composition. Dr. Jingsi Chen was involved in experimental design and manuscript revision. Zicheng Zi and Dr. Jifang Liu were involved in the hemostatic and antibacterial experiments. Dr. Li Xiang was involved in the SFA experiment of measuring effective cohesion energy. Tao Wang and Xuwen Peng contributed to the manuscript revision. Dr. Hongbo Zeng was the corresponding author and was involved in the experimental design as well as manuscript composition and revision.

Chapter 3 of this thesis has been published as Qiongyao Peng, Jingsi Chen, Tao Wang, Lu Gong, Xuwen Peng, Meng Wu, Yuhao Ma, Feiyi Wu, Diling Yang, Hao Zhang, Hongbo Zeng, "Coacervation-driven instant paintable underwater adhesives with tunable optical and electrochromic properties", *Journal of Materials Chemistry A*, https://doi.org/10.1039/D1TA01658J. The manuscript was written through contributions of all the authors. The more specific contributions of the authors are as follows. Conceptualization (Q. Peng, H. Zeng), investigation (Q. Peng), writing – original draft (Q. Peng), methodology,

validation and writing – review & editing (Q. Peng, J. Chen, T. Wang, L. Gong, X. Peng, M. Wu, Y. Ma, F. Wu, D. Yang, H. Zhang, H. Zeng), resources, funding acquisition and supervision (H. Zeng).

Chapter 4 of this thesis is a paper manuscript named “Coacervate-based Instant and Repeatable Underwater Adhesive with Anticancer and Antibacterial Applications”, which is originally written by Qiongyao Peng and has never been published before.

Chapter 5 of this thesis is the conclusions and future work.

Dedicated to

Dream and my family

Acknowledgements

My foremost gratitude goes to Dr. Hongbo Zeng, who provides me the great opportunity to study in University of Alberta and guided me into the fantastic world of coacervation. I really appreciate his elaborate guidance through my graduate study, and his immense knowledge, thoughtful insights and passion for science encourage me to pursue my future career in this field. The insightful discussions with Dr. Zeng always lead me into deep thinking, which would be beneficial for my entire life.

Secondly, I would like to thank all my group members, both past and present, for their support, advice, and friendship. Especially thanks to Dr. Jingsi Chen, Dr. Bin Yan and Dr. Lin Li, who helped me with polymer synthesis and various analytical techniques as well as encouraged me when I felt depressed.

Financial support from Alberta Innovates is also appreciated.

Last but not least, I would like to thank my family, for their continuous support and love during my study overseas. Although I spend more than six years to finish my PhD program, I always feel thankful because I finally conquer those confronted difficulties and I gave birth to two kids during the period. In the later life, I will always stick to lifelong learning and unremitting efforts.

Table of Contents

List of Tables

List of Figures

Abbreviations and Symbols

SFA	surface forces apparatus
SLS	static light scattering
SANS	small-angle neutron scattering
ELP	elastin-like polypeptides
DLS	dynamic light scattering
OM	optical microscope
DSC	differential scanning calorimetry
UVS	UV-vis spectrometer
EFM	epifluorescence microscope
AFM	atomic force microscopy
CD	circular dichroism
FS	fluorescence spectroscopy
ICP-OES	inductively coupled plasma-optical emission spectrometry
Mfp	mussel foot protein
QCM-D	quartz crystal microbalance dissipation
XPS	X-ray photoelectron spectroscopy
CM	confocal microscope

DIC	differential interference contrast
FM	fluorescence microscopy
DgHBPs	D. gigas histidine-rich beak proteins
MD	molecular dynamics
ITC	isothermal titration calorimetry
MeTro	methacryloyl-substituted tropoelastin
FRAP	fluorescence recovery after photobleaching
HSQC	heteronuclear single quantum coherence
EDS	energy-dispersive X-ray spectroscopy
PEO-b-PCL	poly(ethylene oxide)-block-poly(caprolactone)
LPEM	liquid-phase transmission electron microscopy
SCF	self-consistent mean field
BPLE	bipyridinium-functionalized poly-lipoic ester
HPLC	high-performance liquid chromatography
CLSM	confocal laser scanning microscopy
XANES	X-ray near edge adsorption fine structure spectroscopy
FESEM	field emission scanning electron microscopy

PAA	poly(α,β)-DL-aspartic acid sodium salt
Rmfp-1	recombinant mussel foot protein-1
MADQUAT	poly(2-(trimethylamino)ethyl methacrylate)
UCST	upper critical solution temperature
PSPM	poly(3-sulfopropyl methacrylate)
HA	hyaluronic acid
SMFS	single-molecule force spectroscopy
PEG	poly(ethylene glycol)
SiW	silicotungstic acid
PEI	poly(ethyleneimine)
PGlu	poly(D,L-glutamic acid)
PDADMAC	poly(diallyldimethylammonium chloride)
SDS	sodium dodecyl sulfate
PSS	poly(styrenesulfonate)
PDADMA	poly(diallyldimethylammonium)
PSBMA	poly(sulfobetaine methacrylamide)
NMR	nuclear magnetic resonance

hADAS	human adipose derived adult stem
NIPAAm	N-isopropylacrylamide
HIPAAm	hydroxyisopropylacrylamide
N-WASP	neural Wiskott-Aldrich syndrome protein
NCK	non-catalytic region of tyrosine kinase adaptor protein
PRM	proline-rich motif
CMC	sodium carboxymethyl cellulose
DEAE-dextran	diethylaminoethyldextran chloride
PAH	poly(allylamine hydrochloride)
CM-dextran	carboxymethyldextran
Q-Dex	glycidyl trimethylammonium chloride functionalized dextran
DTAB	dodecyl trimethyl ammonium bromide
ATP	adenosine triphosphate
βCD-DPA	cyclodextrin-modified dipicolinic acids
PAM	polyacrylamide
DMAPAA	N, N-dimethylaminopropyl acrylamide
MAPTAC	[3-(methacryloylamino)propyl]trimethylammonium chloride

W_{12}	$Li_6H_2W_{12}O_{34}$
PVA	poly(vinyl alcohol)
PAs	peptide amphiphiles
HFIP	hexafluoroisopropanol
ACP	atmospheric cold plasma
$C_{12\text{-}6\text{-}12}$	hexamethylene-1,6-bis(dodecyldimethylammonium bromide)
H_2Bzglu	N-benzoylglutamic acid
SfNAPs	sequence-defined functionalized nucleic acid polymers
NPM1	Nucleophosmin
HLM	leucine-rich motifs
PEGME	poly (ethylene glycol) methyl ether
PEGdME	poly (ethylene glycol) dimethyl ether
DPBS	Dulbecco's phosphate-buffered saline
CFU	colony forming unit
DMF	dimethylformamide
PTFE	polytetrafluoroethylene
PC	polycarbonate

PVC	polyvinyl chloride
hBRCs	human red blood cells
E. coli	*Escherichia coli*
DOPA	3, 4-dihydroxyphenylalanine
P123	poly(ethylene glycol)$_{19}$-*b*-poly(propylene glycol)$_{69}$-*b*-poly(ethylene glycol)$_{19}$
PMMA	poly(methyl methacrylate)
F68	(poly(ethylene glycol)$_{77}$-*b*-poly(propylene glycol)$_{29}$-*b*-poly(ethylene glycol)$_{77}$
ITO	indium tin oxide
cryo-TEM	cryogenic transmission electron microscopy
CNTs	carbon nanotubes
UPy	2-ureido-4[1H]-pyrimidinone
TA	tannic acid
LB	Luria-Bertani
DMSO	dimethyl sulfoxide
A549	human lung epithelial cancer cell line
Huh7	human hepatoma cell line

S. aureus	*Staphylococcus aureus*
W_{eff}	effective cohesion energy
η	viscosity
ΔP	Laplace pressure difference
γ	interfacial energy of the coacervate phase
r_1	the radius of the outer meniscus
r_2	the radius of the neck of the coacervate bridge
S	an area between the spherical surface and the flat surface where the Laplace pressure acts
R	the geometric mean of the radii of the two cylindrically curved surfaces for SFA or the radius of the colloidal probe for AFM
F	the part of the adhesion force contributed by the Laplace pressure
θ	the contact angle of the coacervate on the flat surface
$F_{pull\text{-}off}$	the experimentally measured force needed to pull off the coacervate-bridged surfaces
$F_{adhesion}$ or F_{ad}	the capillary adhesion force originating from the coacervate meniscus
W_{ad}	the capillary adhesion energy originating from the coacervate meniscus
G'	storage modulus

G''	loss modulus

CHAPTER 1 Recent Advances in Coacervation and Underlying Non-covalent Intermolecular Interactions

1.1 Introduction

Coacervation is a liquid-liquid phase separation phenomenon where a material-rich dense coacervate phase and a co-existing immiscible dilute supernatant simultaneously generated from a homogeneous aqueous solution consisting of one (simple coacervation) or two different types of (complex coacervation) macromolecules (e.g., proteins, polymers, and colloids). It is usually driven by specific triggers such as temperature and salt, or actuated by electrostatic interaction, hydrophobic interaction, hydrogen-bonding interaction, cation-π interaction, etc.[1-5] It was considered as "the origin of life", because the material-rich coacervate phase highly resembles protoplasm[6], precellular systems[7] and membraneless organelles[8] in biological systems. Meanwhile, coacervate phase has been demonstrated to possess protective function against UV light on the primitive earth as concentrating nutritious matters within its phase can prevent them from decomposition by irradiation.[9] Coacervation is also proposed to play a crucial role in fabricating extracellular matrix such as elastin of skin, lung and blood vessels, via coacervation of tropoelastin followed by crosslinking.[10] Moreover, formation of biological tissues with gradient material properties like squid beak took advantage of low interfacial energy and shear thinning property of coacervate phase to impregnate through chitin networks where the coacervate was dehydrated and crosslinked with varying degrees.[11, 12] Protein Tau was demonstrated to undergo coacervation through interacting negatively charged molecules with positively charged domains, promoting formation of amyloid related to Alzheimer diseases.[13] In the past two decades, coacervation was discovered as a critical process in the secretion and delivery of wet/underwater adhesives of sessile organisms, which inspires extensive biomimetic researches to achieve

wet/underwater adhesion.[14-17] As coacervation unveils a lot of secrets of biology in nature and their underlying intermolecular interactions, it provides paradigms and directions for design of new materials as well as practical applications. Owing to the ability of concentrating materials, coacervation has been extensively applied in microencapsulation in food and cosmetic industry[18, 19], purification of biomaterials[20], gene/drug delivery[21-23] and wastewater treatment[24] via rational manipulation of intermolecular interactions. The low interfacial energy of the coacervate phase enables it to be easily spread on surfaces and interfaces, exhibiting promising potential applications in surface/interface modification[25-27], coating[28], endovascular embolics[29], etc. Coacervation has drawn intensive research attraction and the applications of coacervates are illustrated in **Figure 1.1**.

Figure 1.1. Schematic illustration of various applications of coacervates.

Started with the first introduction of "coacervation" by Kruyt and Bungenberg de Jong in 1929[30], related publications have experienced a growth spurt as illustrated in **Figure 1.2** which displays the number of publications within every ten years since 1930 by searching "coacervation" and "liquid-liquid phase separation" on google scholar. Several review articles with various focuses in this field have been published. Especially, the journal of Advances in Colloid and Interface Science has ever organized three special issue symposiums on Complex Coacervation in 2011, 2015 and 2017, respectively, covering major developments in the field.[31, 32] Development of theoretical analysis of coacervation has been reviewed from initial Voorn-Overbeek model which only combined the Flory-Huggins theory of polymer mixing and the Debye-Hückel theory of simple electrolytes, to modern approaches which take polyion size, heterogeneity, chain stiffness, charge density, etc. into account.[33-36] Physical properties such as low interfacial energy and linear viscoelasticity of complex coacervates were summarized from perspective of molecular and structural basis.[37, 38] In terms of constructing intracellular structures and extracellular matrix in biology, both intrinsically disordered proteins and tropoelastin seized great attraction for their critical intermediate process of coacervation to achieve final biological roles, coacervation mechanism of which inspired considerable smart materials.[39-42] The character coacervation played in sessile organisms' underwater adhesion was unveiled, which promoted advancement of bioinspired underwater adhesives.[17, 43, 44] Compartmentalization and microencapsulation of coacervation enabled its wide applications in food and cosmetic industry as well as drug delivery, among which protein and polysaccharide coacervation system got substantial attention.[5, 45-47] As charge status of proteins which contained various amino acids were complex, oppositely charged polyelectrolytes with known charge distributions were extensively studied.[48, 49] Besides, surfactants with different molecular weights could also take part in coacervation, exhibiting great potential as carrier and reactor systems thanks to their ability of self-assembly enabled by

amphiphilic counterparts.[50-55] Many other coacervation-related reviews were also reported from various emphases such as low energy fabrication methods of coacervates[56], and phase separation from different aspects of biology (mitosis[57], cell physiology and disease[2], cellular biochemistry[58]). From viewpoint of rational design of coacervation system, macromolecular assemblies were reviewed from different parameters such as macromolecular structure, mixing ratio, ionic strength, pH, and temperature, etc.[59] The contribution of cation-π interactions to underwater adhesion was elucidated through investigating intermolecular interactions via a surface forces apparatus (SFA).[44] However, systematic introduction of simple and complex coacervation systems from perspective of intermolecular interactions including hydrophobic interactions, electrostatic interactions, hydrogen-bonding interactions, cation-π interactions, multivalent interactions, etc. is rare while which would provide significant guidance and directions for design strategies of new materials, reactor systems, biological structures, and so on.

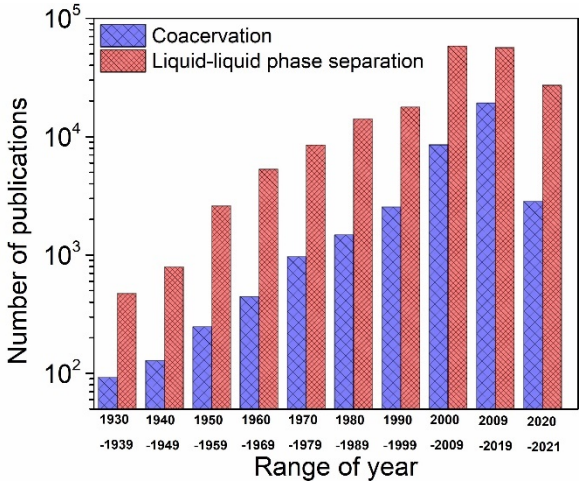

Figure 1.2. Number of publications by searching "coacervation" and "Liquid-liquid phase separation" on google scholar within every ten years since 1930 (The latest data of 2020-2021 was ended on Jan12, 2021).

In this review, we first introduce basic experimental techniques of studying coacervation phenomena, focusing on those that can be applied for exploring intermolecular interactions. Then simple coacervation and complex coacervation are discussed based on the various intermolecular interactions involved. The remaining challenges and future research perspectives of coacervation are also discussed, aiming to bring new insights into the development of coacervation-inspired materials, engineering technologies, and biological models.

1.2. Basic experimental techniques

Various instruments and experimental techniques have been developed to investigate liquid-liquid phase separation phenomena of coacervation systems and reveal the related underlying intermolecular interactions. **Table 1.1** summarizes the component, intermolecular interactions, basic experimental techniques, and corresponding applications of some typical examples of simple coacervation reported in past two decades.

Table 1.1. Component, driving forces, experimental techniques, applications of some typical simple coacervation.

Component	Intermolecular interaction	Experimental techniques	Applications	Ref
Cationic surfactants with an erucyl tail	van der Waals forces or entropic attraction	Rheometer, Static Light Scattering (SLS), Small-Angle Neutron Scattering (SANS)		[60]
Non-ionic surfactant Triton X-100	Hydrophobic interaction	Spectrophotometer	Remove toxic dyes such as congo red or eosin from wastewater.	[61, 62]
Elastin-like polypeptides (ELP)	Hydrophobic interaction	Turbidity	Encapsulation of stem cells.	[63]
Poly(N-isopropylacrylamide-co-2-hydroxyisopropylacrylamide)	Hydrophobic interaction	NMR, Dynamic Light Scattering (DLS), Optical Microscope (OM), Differential Scanning Calorimetry (DSC), UV-vis spectrometer (UVS)	Separation and purification of model solutes.	[64]
Recombinant ELP	Hydrophobic interaction	UVS, Epifluorescence microscope (EFM)	Study the complex architecture of elastic fiber.	[65, 66]
Anionic surfactants	Salting-out effect	Rheometer, Microscope	Hand Dishwashing Liquids.	[67-69]
Polyethylene glycol	Salting-out effect	Phase diagram	Understand phase behavior.	[70]
Recombinant ELP	Hydrophobic interaction	Atomic force microscopy (AFM)	Study nucleation and growth mechanisms of fibril- and amyloid-forming proteins.	[71]

ELP	Hydrophobic interaction and crosslinking among lysing residues	Circular dichroism (CD) spectroscopy, UV spectrophotometer	Effect of minor gene mutation of ELP on elastin-concerned cardiovascular disease.	[72]
Hydrophobic drug such as ritonavir	Hydrophobic interaction	UV-vis spectrometer, DLS, Fluorescence Spectroscopy (FS)	Hydrophobic drug delivery.	[73]
Human tropoelastin	Hydrophobic interaction	CD, Surface Plasmon Resonance (SPR), UVS, EFM	Effect of elastin binding protein and FKBP65 on self-assembly of tropoelastin.	[74]
ELP	Hydrophobic interaction	UVS, UV-vis spectrophotometer, DLS	Curcumin-carrier to treat neuroinflammation.	[21]
Polyethylene glycol	Salting-out effect	OM, FS, Inductively coupled plasma-optical emission spectrometry (ICP-OES)	Coacervate-based membrane-free protocell concentrating cell lysate enhanced transcription rates of mRNA.	[75]
ELP and tropoelastin	Hydrophobic interaction	OM, AFM, FS	Stimulus-responsive ELP nanoparticles for biomedical drug delivery.	[76]
Mfp (mussel foot protein)-3S, a zwitterionic protein	Electrostatic interaction and hydrophobic interaction	Zeta potential, UVS, Inverted light microscopy, FS, Surface Forces Apparatus (SFA), Quartz crystal microbalance dissipation (QCM-D)	Potential dental or orthopaedic adhesive applications.	[77]
Catecholic zwitterionic surfactant inspired by mfp-5	Electrostatic interaction and hydrophobic interaction	OM, Cryo-TEM, SFA, AFM, QCM-D, X-ray Photoelectron Spectroscopy (XPS)	Coatings or adhesive primers for diverse surfaces.	[78]
ELP	Hydrophobic interaction	Turbidity, DSC	For rational design of ELP	[79]
Caenorhabditis elegans protein LAF-1, a DDX3 RNA helicase found in P granules	Electrostatic interaction	Confocal microscope (CM), Single molecule fluorescence resonance energy transfer, EFM	Liquid phase organelles with tunable properties.	[80]
The evolutionarily conserved low-complexity protein, spindle regulatory protein BuGZ	Hydrophobic interaction	OM, Differential interference contrast (DIC), Fluorescence microscopy (FM), UVS, Turbidity	Study structural properties and functions of the spindle matrix in different organisms.	[81]
The disordered tails of Ddx4, a primary constituent of nuage or germ granules	Multivalency	OM, Confocal fluorescence microscopy, Differential interference contrast (DIC)	Generate environmentally responsive membraneless organelles.	[82]
Highly modular D. gigas histidine-rich beak proteins (DgHBPs)	Hydrophobic interaction	OM, CD, Rheometer, UVS, Fluorescence microscopy	Provide novel molecular-scale strategies for designing functional gradient materials.	[11]
Linear and dendritic (branched) Elastin-like peptides (ELP) based on the GLPGL pentamer repeat unit.	Hydrophobic interaction	Quartz capillary, UVS, CD	Be useful for the design of complex ELP-based thermo-responsive materials.	[83]
A series of elastin-derived peptide $(Phe\text{-}Pro\text{-}Gly\text{-}Val\text{-}Gly)_5$ dimers	Hydrophobic interaction	Spectral photometer, Turbidity, Molecular Dynamics (MD) simulation, CD	Develop various biomedical products, skin substitutes, synthetic vascular grafts, and drug delivery systems.	[84]
Histidine-rich beak proteins (HBP-1 and -2)	Hydrophobic interaction	OM, DLS, UVS, Rheometer, Isothermal titration calorimetry (ITC), CD, SAXS	Bio-inspired composite materials, smart hydrogels, adhesives, and biomedical implants.	[85]

A modified recombinant protein, methacryloyl-substituted tropoelastin (MeTro)	Hydrophobic interaction		MeTro sealant with superior adhesion and mechanical properties fit desired surgical applications.	[86]
Recombinant ELP	Hydrophobic interaction	CD, EFM, NMR, Pulsed Field Gradient Diffusion, Solid-State MAS NMR	Direct observation of structure and dynamics of simple coacervation of ELP.	[87]
Recombinant ELP	Hydrophobic interaction	DLS, SLS, FM, Confocal microscopy	Predict and program IDP (intrinsically disordered proteins)-rich assemblies.	[88]
The budding yeast translation termination factor Sup35, an archetypal prion-domain-containing protein.	Electrostatic interaction	FM, OM, Fluorescence recovery after photobleaching (FRAP) experiments, CM, Cryo-TEM, Optical tweezer	Phase separation is a stimuli-responsiveness of prion protein as conserved environmental stress sensors.	[89]
Recombinant protein inspired by spider silk protein	Protein concentration-dependent or phosphate-dependent	OM, Cryo-TEM, FRAP experiments	Demonstrate a correlation between protein architecture and coacervation phenomena.	[90]
The intrinsically disordered, arginine/glycine-rich RGG domain from the P granule protein LAF-1	Multivalency	Turbidity, OM, UVS, FM, FRAP experiments	Generates dynamic membraneless organelles with programmable phase behavior and composition.	[8]
Dimeric elastin-like peptides analogue (H-C$(WPGVG)_3$-$NH_2)_2$	Hydrophobic interaction	Turbidity, Spectral photometer, Fluorescence spectrometer, DLS, OM, MD simulation, CD	Elucidate the coacervation mechanism of short-length ELP dimer.	[91]
Histidine-rich squid beak proteins	Hydrogen-bonding interaction and π-π interaction	Heteronuclear single quantum coherence (HSQC) spectrum, OM, SAXS, NMR, DLS, OM	Bioinspired protocells and stimuli-responsive drug delivery system.	[92]
ELP	Hydrophobic interaction	SEM, Energy-Dispersive X-ray Spectroscopy (EDS), XPS, FTIR, XRD, NMR	Shed light on medial calcification on extracellular matrix of arteries.	[93, 94]
Poly(ethylene oxide)-block-poly(caprolactone) (PEO-b-PCL) or similar nonionic block copolymers	Hydrophobic interaction	Liquid-phase transmission electron microscopy (LPEM), Self-consistent mean field (SCF) theory, OM	Reveal the role of phase separation in the vesicle formation process.	[95, 96]
A water-insoluble polymer bipyridinium-functionalized poly-lipoic ester (BPLE)	Hydrophobic interaction and π-π interaction	OM, High-performance liquid chromatography (HPLC), UVS, DLS	Remove organic pollutants from water.	[24]
Plant protein soy glycinin	Hydrophobic interaction and screened electrostatic interaction	OM, Turbidity, Confocal laser scanning microscopy (CLSM), polarization microscopy, FRAP	Design novel functional materials from plant protein.	[97]
Imine-based covalent trimeric surfactants with different hydrophobic chain length	Hydrophobic interaction	NMR, Turbidity, Cryo-TEM, CLSM, OM	Innovative pesticide formula.	[98]
Polyampholytic polypeptides containing both positive and negative charges along the backbone	Electrostatic interaction	Transfer matrix theory, Turbidity, OM, FTIR	Design bioinspired materials via engineering sequence of polypeptides.	[99]
Recombinant spider silk protein	Salting-out effect	Confocal scanning microscopy, Turbidity, OM, SEM, Electron tomogram, FM, CD, NMR, FRAP, DLS, FTIR	Shed light on assembly of protein-based biomaterials and potential application in coatings, adhesives, etc.	[100]

Recombinant intrinsically disordered RGG domain from the protein LAF-1	Multivalency	Absorbance Spectrum, Inverted microscope, Image analysis with MATLAB	Provide novel strategies for inducing protein phase separation using light.	[101]
Solubilized elastin extracted from bovine ligament with a naturally derived cross-linker, genipin	Hydrophobic interaction	UVS, X-ray near edge adsorption fine structure spectroscopy (XANES)	Study mineralization or calcification of elastin.	[102]
Gelatin	Driven by ethanol as a poor solvent	Field emission scanning electron microscopy (FESEM), TEM, DLS, FTIR, Turbidity, UVS	Construct gelatin-based materials using coacervation method.	[103]

1.2.1 Optical microscope, turbidity and dynamic light scattering

According to **Table 1.1**, various instruments and experimental techniques have been harnessed to investigate coacervation phenomena, among which optical microscope is one of the most frequently used ones because it is an easy, fast, and convenient way of detecting liquid-liquid phase separation. Generation and coalescence of coacervate droplets are typical characteristics of coacervation phenomenon, which can be facilely observed under optical microscope. As show in **Figure 1.3A**, HRV3C protease can liberate solubility-enhancing tag maltose-binding protein (MBP) from the recombinant sequence of MBP-RGG-RGG so that the two tandem RGG domains can undergo self-coacervation to form coacervate droplets driven by multivalency.[8] High-end optical microscopes such as confocal laser scanning microscopy (CLSM), confocal scanning microscopy, confocal fluorescence microscopy, fluorescence microscopy (FM), can provide more detailed information of coacervation like partitioning of different components. For instance, the assembly (**Figure 1.3B**, upper graphs) and dissociation (**Figure 1.3B**, lower graphs) of Ca^{2+}/polyaspartate-rich coacervate phase in a mineralizing microreactor system based on vesicle-coated multiphase droplets was monitored under a confocal microscope, where the coacervate formation required the co-existence of both polyaspartate and Ca^{2+} while the dissociation of the coacervate could be induced through the loss of Ca^{2+}.[104] Herein, rhodamine-labeled lipid vesicles showed red fluorescence; green fluorescence represents negatively charged Alexa 488-labeled

poly(α,β)-DL-aspartic acid sodium salt (PAA), which formed green coacervate phase upon interacting with Ca^{2+} via electrostatic interaction and then was expelled from the coacervate phase to be homogeneously distributed within lipid vesicles by losing Ca^{2+} from competition with CO_3^{2-}; Alexa 647-labeled dextran exhibited blue fluorescence. Through observing the appearance of coacervation phenomena by varying different influencing parameters using an optical microscope, phase diagrams can be obtained to provide a general information of formation conditions of coacervates. As illustrated in **Figure 1.3C**, the phase diagram of the complex coacervation between recombinant mussel foot protein-1 (Rmfp-1) and poly(2-(trimethylamino)ethyl methacrylate) (MADQUAT) can be obtained by mixing the aqueous solutions of the two components based on either weight percentages or molar concentrations, resulting in the formation of either aqueous solution or coacervate.[105] In short, optical microscopes can provide qualitative information about if coacervation can occur where phase diagrams can be drawn by integrating batches of coacervation results.

Turbidity is another widely adopted parameter to indicate the formation of coacervate droplets, which is generally implemented by UV-vis spectrophotometry at a specific wavelength. Generally, turbidity is defined as $T/T_0 \times 100\%$ or in the form of relative turbidity as $-\ln(T/T_0)$ where T and T_0 are light transmittance with and without sample, respectively.[106] For example, temperature-responsive turbidity of single RGG domain, tandem RGG-RGG domains and triplet RGG-RGG-RGG domains in physiological buffer (150 mM NaCl, pH 7.5) were studied with UV-vis spectrophotometry at 600 nm.[8] All the three recombinant polypeptides displayed upper critical solution temperature (UCST) phase behavior, where they turned to be turbid upon cooling to their specific temperatures by giving rise to considerable coacervate droplets while they were transparent at elevated temperatures (**Figure 1.3D**). At the same time, turbidity measurements can

provide optimal condition of coacervation with highest yield of coacervate droplets. Take recombinant D. gigas histidine-rich beak proteins (DgHBPs) as an example, its simple coacervation exhibited highest turbidity at pH of 8 with 0.5 M ionic strength, where the coacervation condition was similar to seawater (**Figure 1.3E**).[11] However, although turbidity can produce quantitative comparison about yield of coacervate droplets, it can't provide information reflecting size of coacervate droplets. As for this, dynamic light scattering (DLS) technology can make its contribution by calculating out average size of coacervate droplets based on measured size distribution.[107] As plotted in **Figure 1.3F**, self-coacervation of recombinant spider silk protein experienced nucleation, growth and stationary phases along with time by analyzing mean size of coacervate droplets.[100] Meanwhile, pH- and temperature-dependent coacervation phenomena can also be studied via DLS technique by comparing size of coacervate droplets.[91, 92] It is noted that the formation of precipitate could lead to variation of turbidity.[107] Therefore, both "macro" liquid-liquid phase separation, where the formed coacervate phase is visible to naked eyes, and "micro" liquid-liquid phase separation with the generated coacervate droplets only visible using an optical microscope should be characterized when applying turbidity measurements.

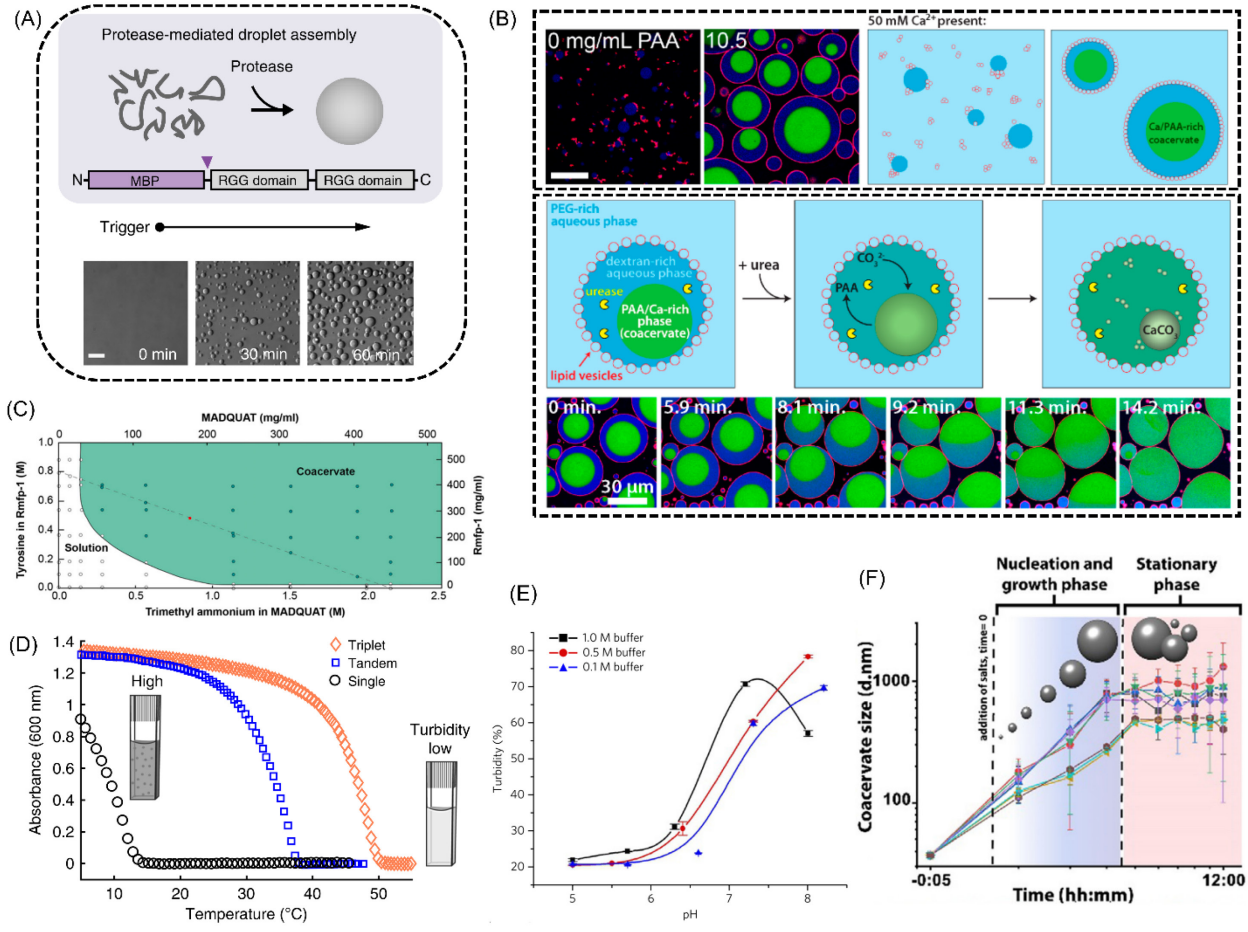

Figure 1.3. Optical microscope, turbidity and dynamic light scattering in the study of liquid-liquid phase separation of the coacervation phenomena. (A) Observation of self-coacervation of tandem RGG (RGG is a sequence from the P granule protein LAF-1) domains triggered by liberating soluble MBP protein with optical microscope.[8] (B) Assembly (upper graphs) and dissociation (lower graphs) of Ca^{2+}/polyaspartate-rich coacervate phase in a mineralizing microreactor system.[104] (C) Phase diagram of coacervation between Rmfp-1 and MADQUAT.[105] (D) Temperature-responsive coacervation phenomena of single RGG domain, tandem RGG-RGG domains and triplet RGG-RGG-RGG domains.[8] (E) Turbidity of simple coacervation of a recombinant D. gigas histidine-rich beak proteins (DgHBPs) at different pH and ionic strength.[11] (F) Size of recombinant spider silk protein coacervate droplets along with time.[100]

1.2.2 Atomic force microscopy (AFM) and Surface forces apparatus (SFA)

Atomic force microscopy (AFM) and surface forces apparatus (SFA) have been widely used to measure physical forces, such as van der Waals force, electrostatic interaction, hydrophobic interaction, cation-π interaction, of molecules or two surfaces of the same material or different materials (polymer, protein, bubble, particle, colloidal, etc.) in vapors or complex fluids.[100, 108-111] These techniques can also be applied to provide useful information on physical properties such as interfacial tension/interfacial energy and viscosity of coacervate phases as well as intermolecular interactions within coacervate phases.[105, 106, 112-117]

1.2.2.1 Interfacial energy

When two immiscible liquids are in contact, the free energy change of expanding their interfacial area by unit area is known as their interfacial energy or interfacial tension γ.[118] Generally, coacervate phase displays low interfacial energy and can easily spread on various substrates to achieve wet adhesion or penetrate through soft scaffolds to constructing tissues with gradient properties.[11, 105, 117] In order to determine the exact interfacial energy between a coacervate phase and a dilute phase, the adhesion force between a spherical and a flat surface bridged by coacervate phase can be measured via either AFM or SFA (**Figure 1.4**).[106, 112, 113, 115, 118] In detail, there are two contributions to the capillary force: the Laplace pressure difference across the interface to hold the surfaces together and the interfacial tension which is trying to minimize the interfacial area. The first part can be expressed by the Young-Laplace equation as follows:

$$\Delta P = \gamma \left(\frac{1}{r_1} + \frac{1}{r_2}\right) \quad (1)$$

where ΔP is the Laplace pressure difference, γ is the interfacial energy of the coacervate phase, r_1 is the radius of the outer meniscus, r_2 is the radius of the neck of the coacervate bridge. Here, the Laplace pressure acts on an area of S between the spherical surface and the flat surface where S can be calculated as below:

$$S = \pi x^2 = \pi\lfloor R^2 - (R-d)^2 \rfloor = \pi(2Rd - d^2) \quad (2)$$

As $r_2 >> r_1$ and $R >> d$ (R is the geometric mean of the radii of the two cylindrically curved surfaces for SFA or R is the radius of the colloidal probe for AFM), ΔP and S can be simplified as γ/r_1 and $2\pi Rd$, respectively. Hence, the part of the adhesion force contributed by the Laplace pressure is:

$$F = -\Delta P \cdot S = -2\pi Rd\gamma/r_1 \quad (3)$$

When φ is small, $d+D=2r_1cos\theta$ (θ is the contact angle of the coacervate on the flat surface, which usually refers to mica surface), and equation (3) can be expressed as follows:

$$F(D) = -2\pi Rd\gamma\frac{2cos\theta}{d+D} = -\frac{4\pi R\gamma cos\theta}{1+D/d} \quad (4)$$

The second part of the adhesion force is attributed to the resolved normal surface tension around the circumference, which is $2\pi x\gamma sin\theta$. Combining the two parts, the experimentally measured force needed to pull off the coacervate-bridged surfaces ($F_{pull\text{-}off}$) as well as the capillary adhesion force originating from the coacervate meniscus ($F_{adhesion}$) can be denoted as below:

$$F_{pull-off} = -F_{adhesion} = \frac{4\pi R\gamma cos\theta}{1+\frac{D}{d}} - 2\pi x\gamma sin\theta \quad (5)$$

Here, θ is assumed to be zero consider the fact that the wetting behavior of coacervate phase on mica is a strongly favorable hydrophilic interaction. Therefore, the maximum value is

achieved when the distance between the spherical surface and the flat surface is zero, and pull-off force as well as the capillary adhesion force can be further simplified as:

$$F_{pull-off}(D=0) = -F_{adhesion}(D=0) = 4\pi R\gamma \quad (6)$$

So, the interfacial energy of the coacervate phase can be calculated as:

$$\gamma = F_{pull-off}/4\pi R \quad (7)$$

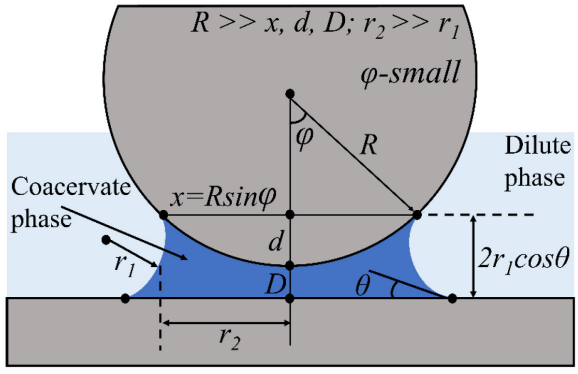

Figure 1.4. Schematic diagram of a coacervate capillary bridge between a spherical surface and a flat surface for capillary adhesion force measurement.

Interfacial energies of various coacervate phases have been measured via AFM or SFA. Interfacial energy of a complex coacervate formed between positively charged polymer poly(trimethylaminoethyl methacrylate) (MADQUAT) and negatively charged polymer poly(3-sulfopropyl methacrylate) (PSPM) was determined to be 100 μN m^{-1} by colloidal probe AFM technique (**Figure 1.5A**).[113] Recombinant mussel foot protein fp-151 and hyaluronic acid (HA) with weight percentage ratio of 8:2 in phosphate buffer can generate complex coacervate, whose interfacial energy was anion-dependent following the Hofmeister ordering according to force

measurements via AFM (**Figure 1.5B**). Corresponding interfacial energies were measured as 0.236, 0.256, and 0.287 mN m^{-1} in 250 mM NaHCOO, NaCl, and $NaNO_3$ solutions, respectively.[114] Meanwhile, complex coacervate between another cationic recombinant mussel adhesive protein fp-151-RGD and HA with weight percentage ratio of 3:1 in sodium acetate buffer had interfacial energy less than 1 mJ m^{-2} based on SFA force measurements.[106] Similar interfacial energy of less than 1 mJ m^{-2} was also detected for coacervation between oppositely charged poly(L-lysine hydrochloride) and poly(L-glutamic acid sodium salt) making use of SFA.[115] Like-charged polyelectrolytes poly(2-(trimethylamino)ethyl methacrylate) (MADQUAT) and recombinant mussel foot protein-1 (Rmfp-1) coacervated with each other to be a coacervate phase possessing interfacial energy of about 0.57 mJ m^{-2} figured out by SFA measurements (**Figure 1.5C**).[105] Inspired by coacervation between like-charged polyelectrolytes driven by short-range cation-π interaction, the single cationic recombinant mussel foot protein, Rmfp-1, was employed to study coacervation behavior under analogous seawater condition, whose coacervate had interfacial energy ranging from 0.2 to 0.8 mJ m^{-2} determined by SFA (**Figure 1.5D**).[117] Although both AFM and SFA can carry out force measurements to determine interfacial energy, there are some differences deserving to be paid attention to. For example, for force measurements via AFM (**Figure 1.5A and B**), the adhesion forces used to calculate interfacial energy were linearly extrapolated to zero separation based on batches of force-distance curves while SFA force measurements just use the maximum pull-off forces as received (**Figure 1.5C and D**). Besides, it is worth noting that scan rate of AFM tips and velocity of pull-off force might have effects on the final capillary adhesion force as coacervates are usually viscoelastic soft matters.[38]

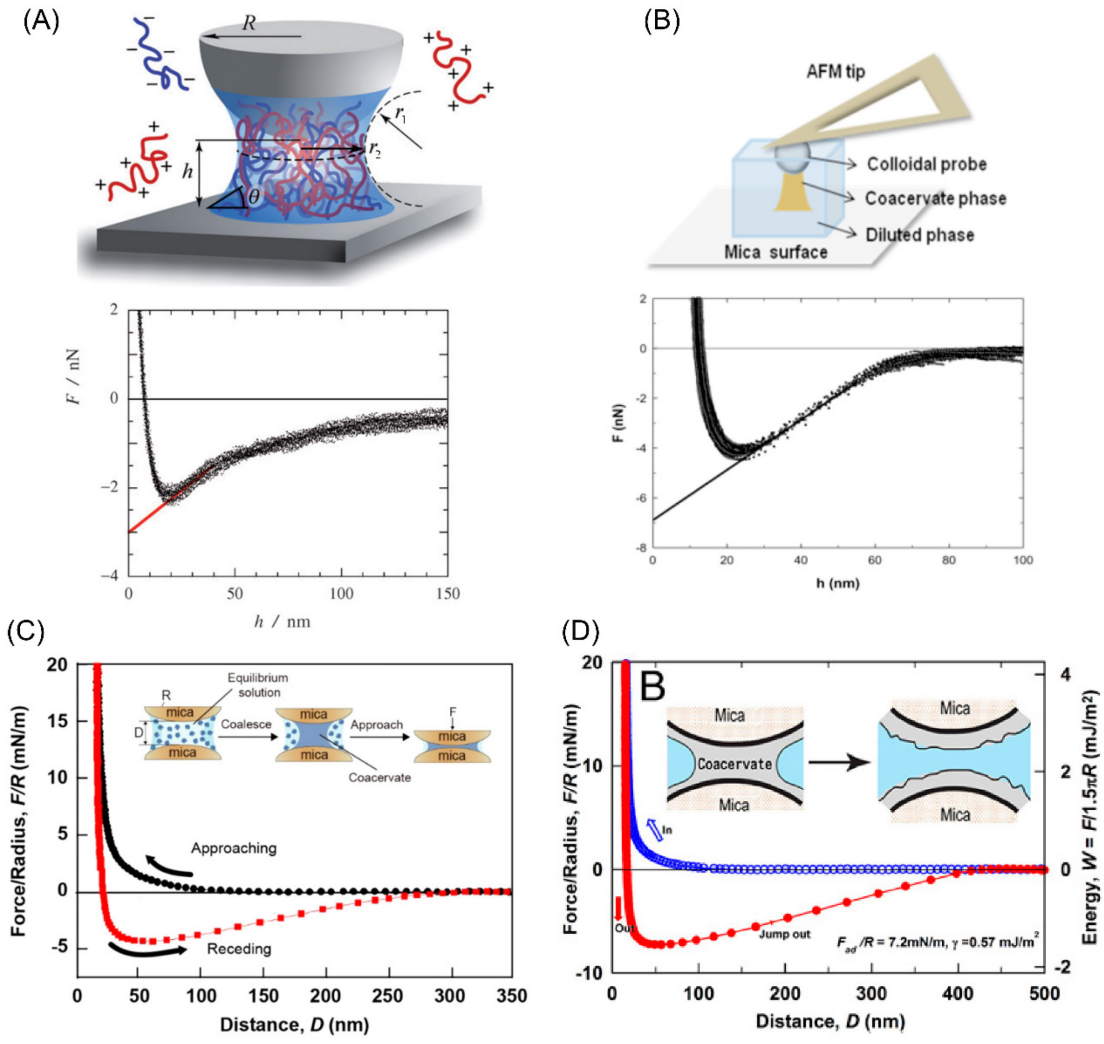

Figure 1.5. Typical experiment setup using AFM or SFA and the corresponding force-distance profiles for the determination of interfacial energies of different coacervate phases. (A) Schematic diagram of a capillary bridge formed by MADQUAT-PSPM complex coacervate and corresponding AFM force-distance profile of capillary force measurements.[113] (B) Schematic diagram of a capillary bridge formed by fp-151-HA complex coacervate and corresponding AFM force-distance profile of capillary force measurements.[114] (C) SFA force-distance curves of capillary force measurements for capillary bridge formed by MADQUAT-Rmfp-1 complex coacervate.[105] (D) SFA force-distance curves of capillary force measurements for capillary bridge formed by self-coacervated Rmfp-1.[117]

1.2.2.2 Intermolecular interactions

Intermolecular interactions have been extensively studied for various materials and engineering systems.[119] Molecules are constructed by atoms with strong covalent bonds while supramolecular compounds are connected by molecules with intermolecular interactions.[120] Coacervates are supramolecular compounds which are usually held together by weak, non-covalent interactions such as electrostatic interaction, hydrophobic interaction, hydrogen-bonding interaction, and cation-π interaction, thereby generally exhibiting reversibility, directionality and tunability. The underlying intermolecular interactions serve as driving force for coacervation phenomena, and understanding these interaction mechanisms facilitates the design and fabrication of novel materials and engineering technologies as well as sheds light on various biological and chemical processes. As an example, cation-π interaction, investigated via direct force measurements using SFA technique, was introduced.

As more than 20 mussel adhesive proteins have been deciphered as cationic and polyphenolic proteins, traditional electrostatic interaction would not act as the main driving force to initiate coacervation.[121, 122] Considering DOPA's instability in oxidative seawater environment despite it can be involved in π-π interaction and hydrogen-bonding interaction, recombinant DOPA-deficient mussel foot protein Rmfp-1 $((AKPSYPPTYK)_{12})$ and corresponding decapeptide $((AKPSYPPTYK)_1)$ were employed to probe possible contrition of cation-π interaction to cross-linking mechanism of sessile organism's underwater proteinous adhesives via SFA.[116] It turned out that strong cation-π interaction was detected between Rmfp-1-coated surfaces and between decapeptide-coated surfaces although there was repulsive electrostatic interaction between positively charged lysine residues. However, Rmfp-1-related coacervation was not reported until recently. The intermolecular interaction between recombinant mussel foot protein Rmfp-1 and

poly(2-(trimethylamino)ethyl methacrylate) (MADQUAT) was measured using an SFA.[105] Strong short-range cation-π interaction between Rmfp-1 and MADQUAT overcame repulsive electrostatic interaction between positively charged trimethylammonium groups, generating coacervate owning thinner polyelectrolyte framework with homogeneously distributed pores (**Figure 1.6A**); while the conventional electrostatic interaction-driven hyaluronic acid-Rmfp-1 coacervate possessing thicker polyelectrolyte framework with heterogeneous pores (**Figure 1.6B**). Typical force-distance profiles plotted in **Figure 1.6C** demonstrated strong adhesion of $F_{ad}/R \sim -22.4$ mN m^{-1} ($W_{ad} \sim 4.8$ mJ m^{-2}) during the separation of the Rmfp-1 and MADQUAT surfaces. Moreover, single Rmfp-1 can form coacervate originating from cation-π interaction triggered by seawater-level salt.[117] When the two Rmfp-1-functionalized mica surfaces were immersed in 100 mM acetic acid the same condition as that of **Figure 1.6C**, the measured adhesion was $F_{ad}/R \sim -15.5$ mN m^{-1} ($W_{ad} \sim 3.3$ mJ m^{-2}) (**Figure 1.6D**), which was ~ 31% less than that between mica surfaces modified by Rmfp-1 and MADQUAT. The higher adhesion between Rmfp-1 and MADQUAT surfaces indicated that cation-π interaction between aromatic tyrosine and positive trimethylammonium groups were stronger than that between aromatic tyrosine and positive lysine residues. It was noted that for single Rmfp-1 in 100 mM acetic acid without NaCl only complexes was formed (**Figure 1.6D, E**, weak cation-π interaction), whereas addition of salt at seawater level led to coacervate formation (**Figure 1.6D, F**, strong cation-π interaction) owing to suppression of repulsive electrostatic interaction. Direct force measurements via SFA provides valuable information regarding the intermolecular interaction mechanisms involved in coacervation phenomena. AFM-based single-molecule force spectroscopy (AFM-SMFS) has also been employed for characterizing the intermolecular interactions.[123]

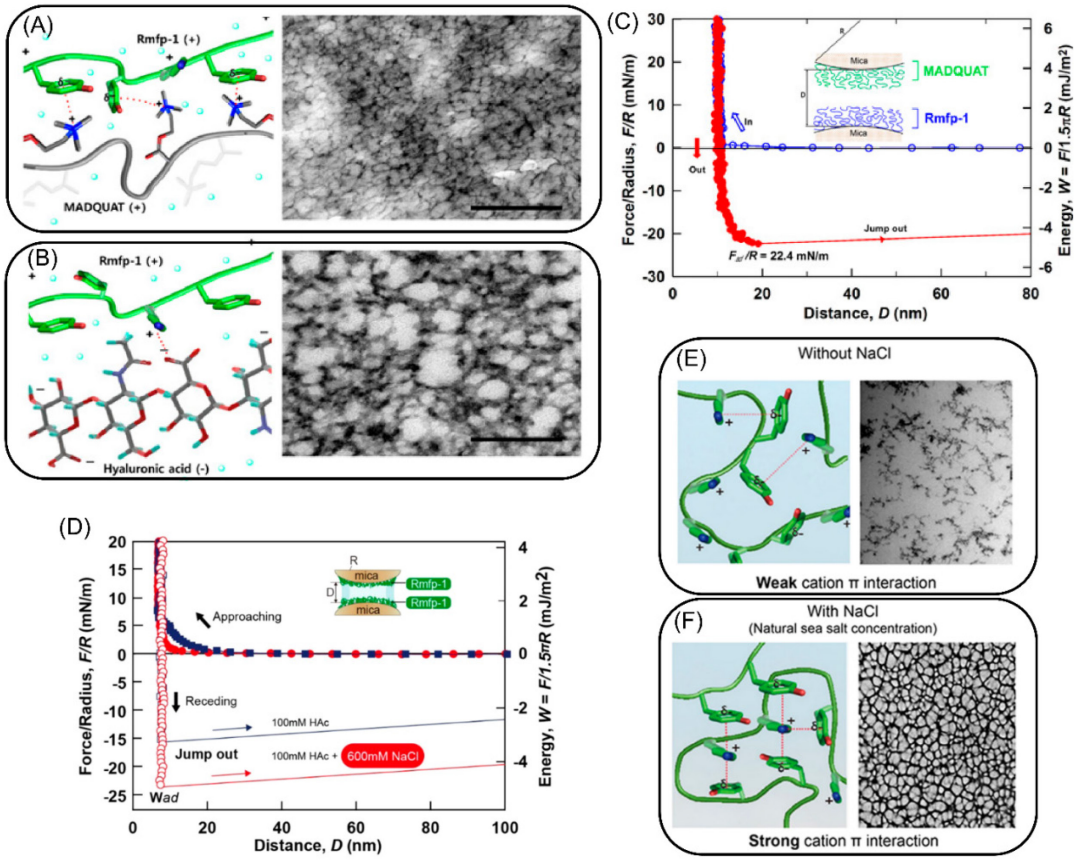

Figure 1.6. Characterization of intermolecular interactions involved in coacervation phenomena via direct force measurements. (A-C) Intermolecular interaction between Rmfp-1 and MADQUAT (C) as well as corresponding schematic diagram and cryo-TEM image of the coacervate (A); Schematic diagram of intermolecular interaction between Rmfp-1 and hyaluronic acid as well as corresponding cryo-TEM image was displayed as a comparison (B).[105] (D-F) Intermolecular interaction between Rmfp-1-coated mica surfaces without NaCl and with 600 mM NaCl (D) as well as corresponding schematic diagrams and cryo-TEM images of the formed complexes (E) or coacervate (F).[117]

1.2.3 Rheometer

As coacervation phenomenon refers to liquid-liquid phase separation where a concentrated dense coacervate phase is generated, the dynamic mechanical properties of the coacervates are generally detected by a rheometer through measurements of viscosity and frequency sweep, which can be correlated to the phase behavior of coacervation.[38] Such characterizations can unveil intermolecular interactions within coacervate phases and are significant for tailoring mechanical properties of coacervates required by practical applications.

The viscosity of coacervates can not only demonstrate the phase behavior of coacervation but also suggest that the newly formed coacervate phase is a shear-rate-independent Newtonian fluid or a shear thinning fluid. For example, aqueous solutions of poly(ethylene glycol) (molecular weight of 20000 g mol^{-1}, PEG20000, 30 mM) and silicotungstic acid (SiW, 300 mM) had very low viscosities of 0.42 Pa·s and ~ 10^{-3} Pa·s while their coacervate exhibited viscosity of 126.6 Pa·s (sharply increased by more than 300 times compared with that of PEG20000) (**Figure 1.7A**), indicating strong intermolecular interactions between SiW clusters and PEG chains.[124] As the viscosity of PEG20000-SiW coacervate was shear-rate-independent (**Figure 1.7A**), it was regarded as Newtonian fluid, whose intermolecular interactions were considered insensitive to shear rate. Coacervate generated from poly(ethyleneimine) (PEI) and poly(D,L-glutamic acid) (PGlu) was also Newtonian fluid, and its viscosity varied with different molar ratios of PEI to PGlu with shear rate ranging from 1-1000 s^{-1}.[125] Sodium polyphosphate can form coacervate with addition of small divalent metallic cations, corresponding coacervates also were Newtonian fluid at low shear rates in the range of 0.001-10 s^{-1}.[126] Viscosity of complex coacervate from poly(diallyldimethylammonium chloride) (PDADMAC) and mixed micelles of anionic surfactant sodium dodecyl sulfate (SDS) and nonionic surfactant Triton X-100 was temperature-dependent,

which behaved like Newtonian fluid at low temperature below 18 ℃ but displayed shear thinning at higher temperature.[127] Here, it was proposed that shear and temperature could cooperatively induce coiled polyelectrolyte/micelle complexes to be extended chains decorated with micelle beads, which created more efficient intermolecular interactions between these extended chains to form coacervate droplets.[127] Shear thinning is an advantageous property for coacervate phase to be delivered through confined tunnels of tissue scaffolds. As shown in **Figure 1.7B**, recDgHBPs-1 can undergo self-coacervation to form shear thinning coacervate with viscosity drastically decreased from 300 Pa·s to less than 10 Pa·s with shear rate ranging from 0.1 s^{-1} to 0.3 s^{-1}. Whereas its corresponding solution had much lower viscosity and no obvious shear thinning was detected, demonstrating that stronger intermolecular interactions within concentrated coacervate phase.[11] Besides, viscosity of coacervates can be tuned by varying composition ratios and concentrations, addition of salts, etc.[29, 128, 129] Take coacervate originated from cationic poly(salmine sulfate) and negatively charged phytic acid as an example, addition of NaCl up to 1.2 M enabled the coacervate to be an injectable coacervate fluid. According to **Figure 1.7C**, viscosity of poly(salmine sulfate)-phytic acid coacervate (Tantalum metal powder was added for X-ray contrast) fell from 39.7 Pa·s to 1.1 Pa·s with concentration of NaCl increased from 150 mM to 1.2 M. Thanks to the low viscosity, the coacervate can be accurately injected to targeted position such as the fine branching blood vessels of the entire renal arterial vasculature of a mouse, where the coacervate would be turned into nonflowing solid morphology triggered by the physiological ionic strength to block blood supply, showing great potential as endovascular embolics (for example, to starve tumors or to reduce blood loss during surgical resection via intra-arterial embolization).[29]

Frequency sweep can provide dynamic storage modulus G’ and loss modulus G’’ of materials through analyzing their in-phase and out-of-phase responses within specific range of

angular frequency.[38] It is naturally to regard coacervate as a liquid with loss modulus G'' higher than storage modulus G', considering coacervate is born from liquid-liquid phase separation. However, the truth is that coacervate has been reported possessing either liquid-like property or gel-like property, or even both.[11, 85, 125, 126, 129-131] For instance, coacervate derived from coacervation between strong polyelectrolytes poly(styrenesulfonate) (PSS) and poly(diallyldimethylammonium) (PDADMA) exhibited liquid-like property whose loss modulus G'' was always bigger than storage modulus G' with addition of KBr ranging from 1.0 M to 1.6 M (**Figure 1.7D**).[129] Coacervates driven from self-coacervation of recombinant D. gigas histidine-rich beak proteins usually had gel-like property whose loss modulus G'' was less than storage modulus G' within tested frequencies.[11, 85] Net neutral zwitterionic polymer poly(sulfobetaine methacrylamide) (PSBMA) and inorganic anionic polyoxometalate polytungstate ($Li_6H_2W_{12}O_{34}$) can generate coacervate displaying liquid-gel transition at certain angular frequency (**Figure 1.7E**).[131] Meantime, this coacervate can be strengthened by salt in the form of that both dynamic modulus G' and G'' were enhanced by increasement of salt concentration (**Figure 1.7E**), which was in stark contrast with that in **Figure 1.7D**. It was interpreted that polytungstate clusters was not only involved in coacervation but also was serving as crosslinkers to give rise to stable and strong intermolecular interactions.

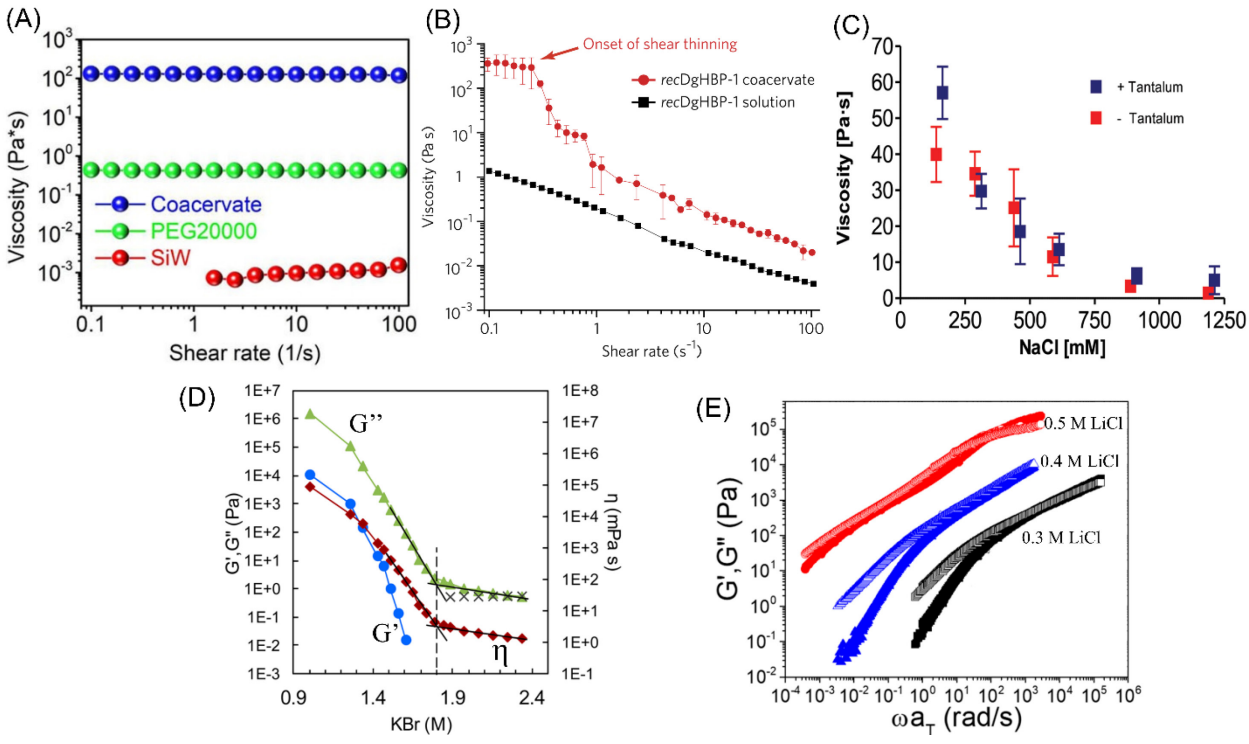

Figure 1.7. Rheological properties of various coacervates. (A) Viscosity of 30 mM PEG20000 and 300 mM SiW as well as their coacervate.[124] (B) Viscosity of recDgHBP-1 coacervate and recDgHBP-1 solution with shear rate ranging from 0.1-100 s^{-1}.[11] (C) Effect of NaCl on viscosity of salmine sulfate-phytic acid coacervate with and without Tantalum powder (for X-ray contrast).[29] (D) Effect of KBr on storage modulus G', loss modulus G'', and viscosity η of PSS-PDADMA coacervate.[129] (E) Liquid-gel transition of PSBMA- polytungstate coacervate as well as its unique salt-hardening behavior.[131]

1.2.4 Other techniques

Many other techniques also have been employed to unveil the intermolecular interactions relevant to coacervation process in a synergistic way from aspects of formation, structure, and properties according to Table. 1.1. For example, results of isothermal titration calorimetry (ITC)

can indicate whether the coacervation process is an endothermic process or an exothermic process.[85, 132] It was reported that coacervate formation of histidine-rich beak proteins was endothermic, arising from entropic contribution mostly owing to that water molecules changed from a semi-ordered state in solution to a liquid state in coacervate phase.[85] Molecular dynamics simulation has also been employed to imitate coacervation process through analyzing conformation behaviors such as primary structures and secondary structures of research objects based on intermolecular interactions, which can be furthered verified by measurements of circular dichroism (CD).[84, 91] Fourier transform infrared spectroscopy (FTIR), nuclear magnetic resonance (NMR), and differential scanning calorimetry usually focus on characterizing intermolecular interactions like hydrogen-bonding interaction and electrostatic interaction as well as molecular conformation.[64, 99, 100, 133, 134] Fluorescence spectroscopy can be used to investigate molecular conformation of coacervates.[73, 76] Small angle X-ray scattering (SAXS) is generally served as tool of probing multiscale assembly of materials for coacervation.[85, 92, 135] Scanning electron microscopy and transmission electron microscopy are tools of studying network structures, which are supplementary ways to Cryo-TEM due to their dry testing environment being unable to reflect real structure of liquid coacervate phases.[93, 94, 103, 135] Apart from AFM, SFA and rheometer for measuring mechanical properties of coacervates, tensile test machine has been adopted to test macroscopic adhesion strength of coacervates through lap-shear test or axial adhesion test.[124, 134] Rational combination of various experimental techniques can yield a comprehensive understanding of coacervation from formation mechanisms to resulted structures and properties, so as to better direct design of novel materials and engineering technologies.

1.3. Intermolecular interactions of simple coacervation

Simple coacervation usually refers to liquid-liquid phase separation associated with one kind of polymer, protein, or macromolecule, which is generally triggered by temperature, pH, salt, etc.,[51] where much effort has been dedicated to revealing the underlying intermolecular interaction mechanisms. Simple coacervation is usually initiated and driven by non-covalent intermolecular interactions such as hydrophobic interaction, electrostatic interaction, cation-π interaction, hydrogen-bonding interaction, and multivalency since no newly formed covalent bonds could be detected. Understanding the roles of specific molecule groups or types of intermolecular interactions involved in coacervation will lay a foundation for designing novel coacervate-based materials and engineering technologies.

1.3.1 Hydrophobic interaction

The hydrophobic interaction is mainly responsible for the aggregation of nonpolar species in aqueous media, as the amount of solvating water molecules needed to create a cavity to surround two lipophilic particles at a time is less than that required to build two cavities to separately accommodate the two lipophilic particles.[136] Tropoelastin is one of the mostly studied bio-inspired proteins owing to its significant role in constructing biological tissues, including elastin of skin, lung, and blood vessels.[10, 137] It has been reported that coacervation is a critical process in the transition of tropoelastin to elastin and usually driven by hydrophobic interactions between hydrophobic moieties of tropoelastin triggered by the increase of temperature. As illustrated in **Figure 1.8A**, schematic sequence blocks of mature human tropoelastin exhibit an alternating domain structure where hydrophobic domain occupied more than 50 %.[10, 76] Hydrophobic domains are abundant in proline (P, hydrophobic), valine (V, hydrophobic) and glycine (G,

hydrophilic for solubility in aqueous media) residues which usually display certain patterns like VPG and PGVG (**Figure 1.8A**). KP-type (lysine residues usually separated by proline residues) and KA-type (lysine residues generally spaced by alanine residues) crosslinking domains are important for tropoelastin coacervate droplets turning into fibrous elastic networks through crosslinking of lysine residues. D. gigas histidine-rich beak proteins (DgHBPs) has also got considerable research attractions attributed to its crucial role in generating biological structures with gradient mechanical properties by taking advantage of low interfacial energy and shear thinning property of coacervate to penetrate through porous biological scaffolds.[11, 12, 85] There are three different D. gigas histidine-rich beak proteins deciphered with variable modular domains as drawn in **Figure 1.8B**. It was demonstrated that the modular domain of GHGXY pentapeptide, where X is usually valine or leucine, sharing high resemblance with proline- and valine-rich tropoelastin because they both possess a good deal of methyl groups and aromatic rings. Combining sequence constitutions of tropoelastin and D. gigas histidine-rich beak proteins, proline, valine, alanine, and glycine residues were the mostly used building blocks of recombinant proteins which were able to undergo coacervation for various applications.

A recombinant elastin-like polypeptides (ELP) with pentapeptide repeat (Valine-Proline-Glycine-Xaa-Glycine) as shown in **Figure 1.8C** was designed and expressed in *E. coli* bacteria, which can self-coacervate at 35 ℃ to encapsulate human adipose derived adult stem (hADAS) cells for chondrocytic differentiation.[63] Another ELP comprised of exons 20, 21, 23 and 24 of mature human tropoelastin as listed in **Figure 1.8D** exhibited reversible coacervation at transition temperature of ~ 41 ℃. A similar and longer ELP with additional exons 21, 23 and 24 can coacervate at lower temperature of ~ 28 ℃. They were employed to study the nucleation and growth of elastin-like peptide fibril multilayers via AFM tapping mode in fluid under variable

temperatures.[71] Traditionally, more than 40 repeats of VPGVG were needed to initiate the coacervation of ELP, and Takeru Nose et al. synthesizd three kinds of $(Phe\text{-}Pro\text{-}Gly\text{-}Val\text{-}Gly)_5$ dimers (e.g., $H\text{-}(Phe\text{-}Pro\text{-}Gly\text{-}Val\text{-}Gly)_5\text{-}NH\text{-}CH(CONH_2)\text{-}CH_2\text{-}S\text{-}S\text{-}CH_2\text{-}CH(CONH_2)\text{-}NH\text{-}(Phe\text{-}Pro\text{-}Gly\text{-}Val\text{-}Gly)_5\text{-}H$) with shorter sequences that could also go through coacervation. These dimers can experience temperature-dependent reversible coacervation at lower concentrations and temperatures, showing great potential as model peptides for the study of elastin structure and the design of novel temperature-responsive biomaterials.[84] Furthermore, a much shorter elastin-derived dimer $(H\text{-}C(WPGVG)_3\text{-}NH_2)_2$ was reported to undergo coacervation with a much lower protein concentration than corresponding monomeric form by introducing more hydrophobic tryptophan (W) residues.[91] All the above-mentioned recombinant ELP were linear polypeptides. Ronit Bitton and coworkers designed both linear and dendritic ELPs based on GLPGL pentamer repeat to investigate effect of branching on coacervation. The results indicated that higher temperature was required to impel the coacervation of dendritic ELP while the dendritic structure had less influence on the microscopic secondary structure transition of coacervation.[83] Except for recombination of sequences, modify tropoelastin with functional groups can also endow it with various abilities. A methacryloyl-substituted tropoelastin can be crosslinked by UV light within 3 minutes to be a sealant with low toxicity and controlled degradation.[86] Besides, multiple bio-mimetic strategies (tropoelastin-inspired coacervation process and mussel-inspired interfacial adhesion) aided by photo-controllable crosslinking mechanism enabled the synthesis of a polyester (**Figure 1.8E**) which can serve as a robust instant (setting less than 300 s) underwater adhesive.[138]

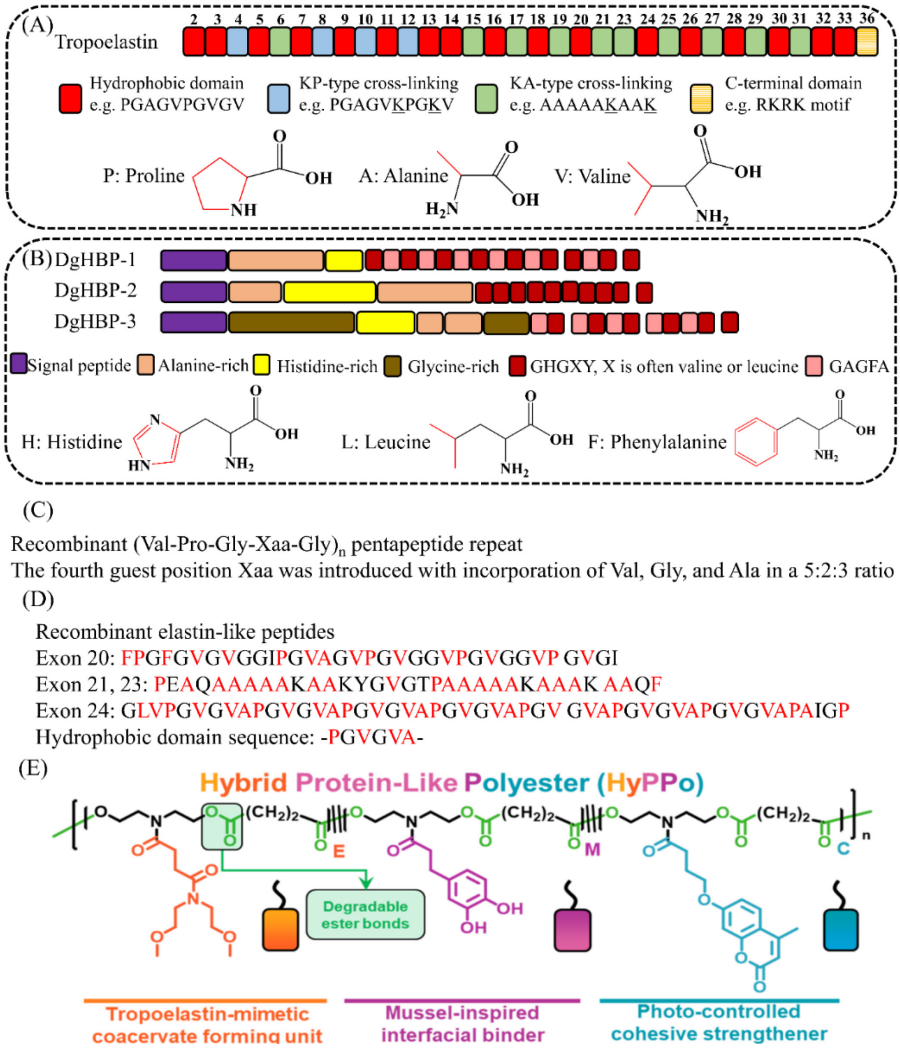

Figure 1.8. Deciphered sequences of mature human tropoelastin and D. gigas histidine-rich beak proteins, sequences of some recombinant EPL and a bio-inspired polyester underwater adhesive, all of which can undergo simple coacervation driven by hydrophobic interaction. (A) Schematic domain structure of mature human tropoelastin and molecular structures of some major hydrophobic residues. (B) Schematic domain structure of D. gigas histidine-rich beak proteins and molecular structures of some major hydrophobic residues. (C) and (D) Sequences of two examples of recombinant EPL. (E) A bio-inspired polyester instant underwater adhesive with tropoelastin-inspired coacervation process, mussel-inspired interfacial adhesion and photo-controlled crosslinking mechanism.[138]

Some synthesized polymers and surfactants containing hydrophobic moieties such as methyl groups, aromatic rings, alkane chains, etc. can also assemble into coiled polymers or conjugated surfactants by hydrophobic interaction and turn into coacervate phases. A series of thermo-responsive polymers poly(*N*-isopropylacrylamide-*co*-2-hydroxyisopropylacrylamide) (poly(NIPAAm-*co*-HIPAAm)) as shown in **Figure 1.9A** were synthesized with different contents of hydrophilic comonomer HIPAAm. Their coacervation was triggered by being incubated above 50 ℃ for 30 minutes where hydrogen-bonding interactions among water molecules were weakened by heat and then water molecules were dissociated from polymer chains to induce hydrophobic interactions among methyl groups. Relatively low content of HIPAAm or increasing NaCl concentration would enhance the extent of dehydration of the copolymer, making liquid-liquid phase separation much easier.[64] Non-ionic block polymer poly(ethylene oxide)-*block*-poly(caprolactone) (PEO-b-PCL) (**Figure 1.9B**) was employed to study its self-assembly behavior with solvent switching from pure acetone/dioxane (good solvent) to gradual water-rich (selective solvent). Herein, water content was a key parameter to balance hydrophobicity of PCL and hydrophilicity of PEO to form coacervate phase, where a solution was formed without the presence of water and high water content would trigger the self-assembly of micelles or vesicles due to the increased high amphiphilicity of the polymer.[95, 96] Triton X-100 is also a non-ionic polymer (**Figure 1.9C**) which can self-assemble to micelles at room temperature, whereas high temperature above its clouding point temperature would render it to undergo liquid-liquid phase separation through enhancing the inter-micellar attractive force or reducing the interaction between water and hydrophilic shell of assembled micelles. Toxic dyes such as congo red and eosin can be firstly encapsulated into hydrophobic cores of Triton X-100 micelles and then be concentrated into coacervate phase, which can be applied to wastewater treatment.[61, 62] Apart from non-ionic amphiphilic polymer-based coacervation system, coacervation also occurs within

oligomeric ionic amphiphilic surfactants. Temperature and salt can synergistically induce phase separation of cationic surfactants with an erucyl tail (**Figure 1.9D**) via hydrophobic interaction-impelled self-assembly and the association of micelles was triggered by temperature followed with the screening of repulsive electrostatic interaction between positively charged micelles activated by the addition of salt.[60] Based on the similar coacervation mechanism with cationic surfactants, anionic surfactants such as sodium alkylbenzene sulfonate (**Figure 1.9E**) were employed to produce coacervate-based concentrated hand dishwashing liquids.[67-69] Oligomeric surfactants with multiple amphiphilic moieties were reported possessing a robust ability of self-assembly as well as bearing active sites to promote generation of coacervate phases.[139, 140] A series of imine-based covalent trimeric surfactants were synthesized to fabricate a novel coacervate-based pesticide carrier through stimulating self-coacervation of these surfactants driven by hydrophobic interaction via facilely adjusting concentration. Low interfacial energy of coacervate incorporated with entangled microstructures enabled the pesticide-encapsulated surfactant coacervate droplets stably deposited on hydrophobic surfaces of plant leaves followed by controlled release lasting 3 months via degradation of imine bonds initiated by ubiquitous CO_2 in air.[98]

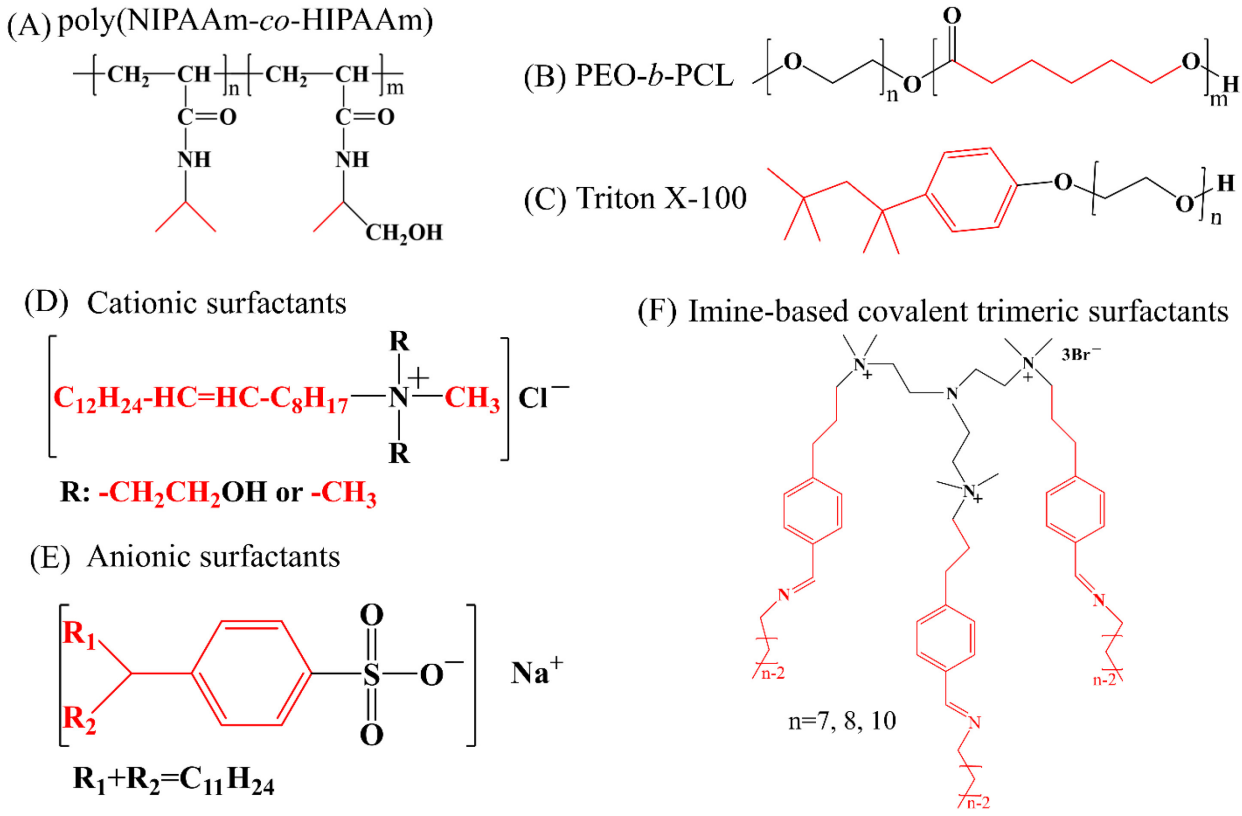

Figure 1.9. Molecular structures of some synthesized polymers and surfactants which can undergo coacervation under specific conditions. (A) Synthesized thermo-responsive copolymers poly(NIPAAm-co-HIPAAm). (B) Synthesized block polymer PEO-b-PCL. (C) Trion X-100. (D) Cationic surfactants bearing an erucyl tail with cis unsaturation at the 13-carbon position, erucyl bis(hydroxyethyl)methylammonium chloride (R: $-CH_2CH_2OH$) and erucyl trimethylammonium chloride (R: $-CH_3$). (E) Sodium alkylbenzene sulfonate. (F) Imine-based covalent trimeric surfactants with different hydrophobic chain length.

Additionally, non-ionic polymer poly(ethylene glycol), with molecular formula of $H(OCH_2CH_2)_nOH$, was demonstrated experiencing coacervation with addition of kosmotropic ions such as Na^+ and K^+, which usually had negative Gibbs free energy of hydration and resulted

in ordered water lattice around these ions. This phenomenon also could be interpreted from hydrophobic interaction: as water molecules were involved in forming ordered water lattice around kosmotropic ions, free water molecules around methylene groups would relatively decrease which in turn would drive association of hydrophobic methylene groups.[70, 75] Recombinant spider silk protein was reported with similar coacervation phenomenon using kosmotropic salts, where the hydrophobic poly-alanine stretches in the load bearing repetitive region were proposed as the major sequences undergoing liquid-liquid phase separation.[100] Moreover, when hydrophobic drugs including ritonavir, efavirenz, loratadine, ketoconazole, indomethacin, felodipine, clotrimazole, clozapine of high concentrations were separately dissolved in small amount of organic solvent, they can coacervate out to be a new liquid phase by addition of appropriate amount of water. The hydrophobic drug-rich coacervate phases were supposed to be driven by hydrophobic interactions among hydrophobic drug molecules.[73]

1.3.2 Electrostatic interaction

Simple coacervation driven by electrostatic interaction was less frequently reported compared with that actuated by hydrophobic interaction according to Table. 1.1, but these material systems still provide a paradigm of mimicking coacervation with one single component. As an RNA helicase found in P granules (a kind of membrane-less organelles, which is implicated in germ cell lineage maintenance in *C. elegans*), LAF-1 protein was demonstrated being able to go through liquid-liquid phase separation to be P granule-like droplets in vitro, which was associated with the liquid-like behaviors such as wetting, dripping, and relaxation to spherical structures upon fusion and shearing in the regulation of gene expression. Sequences of the LAF-1 protein with full length (FL) or truncated sequences without C terminus (ΔC), or without N terminus RGG

(ΔRGG), or just with RGG (Fig. 1.10A upper left) were separately employed to study coacervation phenomena, and the results suggested that only single domain of RGG would be sufficient to undergo coacervation process. RGG domain is intrinsically-ordered and rich in positively charged arginine (**Figure 1.10A** upper right) as well as negatively charged aspartic acid (D) and glutamic acid (E), together with the fact that LAF-1 protein experienced coacervation only if concentration of NaCl was decreased to a specific value (excessive salt would screen electrostatic interaction), both of which demonstrate that electrostatic interaction was proposed as the main driving force for coacervation.[80] Inspired by intrinsically-disordered proteins which carries both positive and negative charges and are able to generate coacervate phase predominantly impelled by electrostatic interaction, a series of polyampholytic polypeptides with alternating positively charged lysine blocks and negatively charged glutamate blocks were synthesized to study influence of sequence variation on coacervation phenomenon.[99] A schematic interacting polypeptides structure of corresponding coacervate phase was depicted in **Figure 1.10B**, where oppositely charged sites interacted with each other basically between polypeptides chains or adsorbed oppositely charged ions dispersed in solution. Varying the number of adjacent like-charges, it was found that at least 8-12 identical charges were needed for each block of the polyampholytes to undergo coacervation and more alternating blocks resulted in higher yield of coacervate phase. Herein, salt concentration and pH had significant effects on tuning the strength of electrostatic interaction and influencing the coacervate formation.

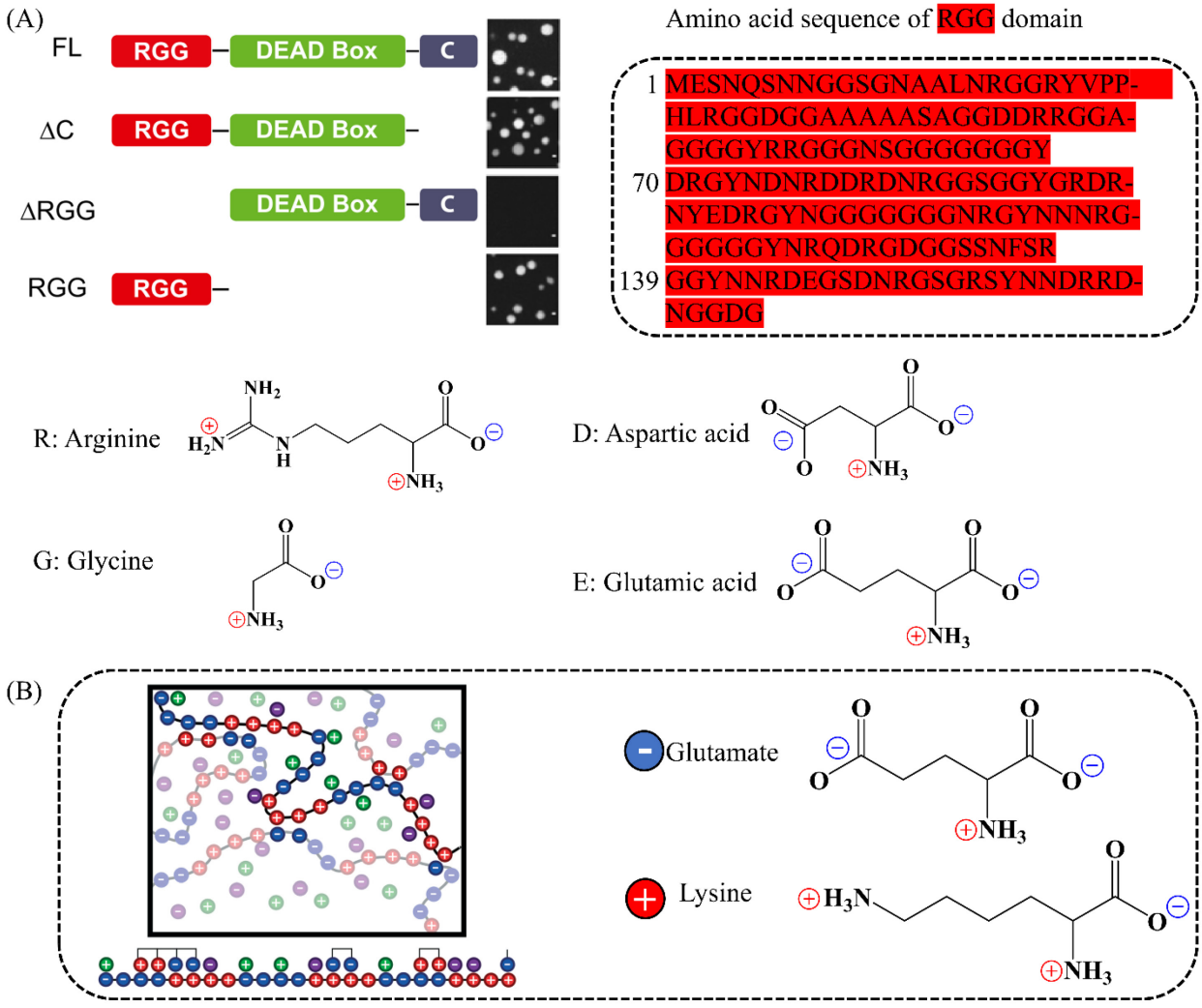

Figure 1.10. Two examples of simple coacervation driven by electrostatic interaction. (A) Upper left: Full length (FL) sequence of the Caenorhabditis elegans protein LAF-1 and three corresponding truncated sequences as well as their phase behavior under optical microscope.[80] Upper right: Amino acid sequence of the N terminus RGG domain.[80] Lower: Molecular structures of arginine, glycine, aspartic acid, and glutamic acid. (B) Left: Schematic intermolecular interactions between synthesized lysine-glutamate polyampholytes with surrounding salt ions.[99] Right: Molecular structure of building blocks of lysine-glutamate polyampholytes.

1.3.3 Hybrid intermolecular interactions

Generally, single polymer, polypeptide, protein, or oligomer usually possesses multiple moieties such as hydrophobic methyl groups, alkane chains or aromatic rings, positively charged amine or trimethylammonium groups, and negatively charged carboxyl, phosphate, or sulfate groups. Although some specific intermolecular interaction was considered to play a predominant role in the formation of simple coacervation, more often the process was attributed to the synergy of two or more intermolecular interactions.

Mfp-3S is a zwitterionic protein rich in hydrophobic aromatic rings (**Figure 1.11A**), which is found in mussels' plaque for wet adhesion on various substrates and plays a significant role as both adhesive primer and cured sealant.[77] Coacervate droplets were detected by directly dissolving Mfp-3S in 10 mM acetic acid buffer with pH of 3. The coacervation behavior of Mfp-3S was highly dependent on pH and ionic strength. Coacervate droplets were well dispersed in acid buffer aqueous media with low concentration of monovalent salt ascribing to the long-range electric double-layer repulsion between net positively charged groups. Further elevating both pH and ionic strength under a certain critical value resulted in net charge zwitterionic state of the protein together with screened long-range electric double-layer repulsion and increased short-range coulombic attraction, where coacervate droplets underwent coalescence to be a bulk coacervate phase. But excessive ionic strength would lead to formation of precipitates. Therefore, the authors proposed that electrostatic interaction made a significant contribution to coacervation. Besides, the coacervation behavior of Mfp-3S was thermo-responsive and the turbidity of coacervate droplets-dispersed solution decreased with increasing temperature, which was in stark contrast with hydrophobic interaction-driven coacervation behavior of elastin-like polypeptides. It was hypothesized that the positive contribution of thermo-induced hydrophobic interaction was

compensated by the negative effect of thermo-weakened electrostatic interaction.[77, 141] Inspired by the coacervation nature of Mfp-3 and dopa-endowed strong adhesion of Mfp-5, Israelachvili and Waite et al. designed a catecholic zwitterionic surfactants with reduced complexity as shown in **Figure 1.11B**, which can associate into coacervate adhesive driven by the cooperation of electrostatic interaction and hydrophobic interaction.[78] As an animal-derived protein, histidine-rich squid beak proteins (HBPs) were considered to undergo self-coacervation triggered by thermo-induced hydrophobic interaction, and the underlying molecular interactions were investigated.[92] By focusing on the phase separation-responsible GHGXY (X is usually alanine or leucine) motif, a series of recombinant sequences as listed in the table of **Figure 1.11C** were synthesized and their phase separation behaviors were examined. By comparing the phase behaviors of sequences with various number of pentapeptides, at least four pentapeptides were necessary for coacervation. GY-25-V1 containing three hydrophobic GAGFA motifs would evolve into a dense hydrogel while GY-25-V2 and GY-20 just exhibited as dispersed coacervate microdroplets. GY-23 combining the very best of GY-25-V1 and GY-25-V2, was able to firstly generate coacervate microdroplets and then coalesce into macro coacervate phase. Further substitute single amino acid within GY-23 revealed more information associated with intermolecular interaction. For example, altering the two tyrosine with alanine, respectively, could lead to the disappearance of liquid-liquid phase separation, demonstrating the two tyrosine amino acids were indispensable for driving coacervation. Furthermore, the position of positively charged histidine was also critical for the coacervation process, which cannot be replaced by lysine, indicating that the histidine not only served as positively charged residues. NMR spectroscopy demonstrated that hydrogen-bonding interaction between the hydroxyl group of tyrosine and the deprotonated amine group of histidine served as a guidance for successive π-π interaction between hydrophobic aromatic rings of tyrosine and histidine residues to initiate coacervation. Therefore,

hydrogen-bonding interaction, π-π interaction and hydrophobic interaction worked synergistically to induce the liquid-liquid phase separation of recombinant histidine-rich beak proteins, shedding light on the design of pH-responsive bio-inspired protocells and smart drug-delivery systems.[92]

Although animal protein-inspired coacervation has attracted substantial attention, plant protein-based (e.g. soy glycinin, fava bean legumin, pea protein) self-coacervation were also reported.[97, 142, 143] Soy glycinin is a hexamer, every subunit of which has an acidic polypeptides and a basic polypeptides domains connected with disulfide bond (**Figure 1.11D**).[97] The acidic domain is rich in aspartate and glutamate residues while the basic domain bears a lot of hydrophobic leucine residues.[144] At pH above 7, the acid domain was negatively charged and majorly arranged facing outside of the hexamers while the hydrophobic basic domain was mainly wrapped within the hexamers, where the hexamers were homogeneously dispersed in the aqueous media owing to repulsive electrostatic interaction (**Figure 1.11D**). Appropriate concentration of NaCl salt can screen the repulsive electrostatic interaction and simultaneously enable weak hydrophobic interaction among basic domain-exposed hexamers, promoting the generation of coacervate droplets. Hence, the self-coacervation of soy glycinin was regarded as the result of cooperation between screened electrostatic interaction and hydrophobic interaction, which provides useful information on understanding the accumulation and dissociation of protein condensates in plant seed cells.

Simple coacervation of a single cationic recombinant mussel foot protein, rmfp-1[117] or synthesized poly(trimethylammonium-phenoxyethyl) polymers[145] driven by strong short-range cation-π interaction were classified into this section, considering screened repulsive electrostatic interaction among positively charged groups were required and involved.

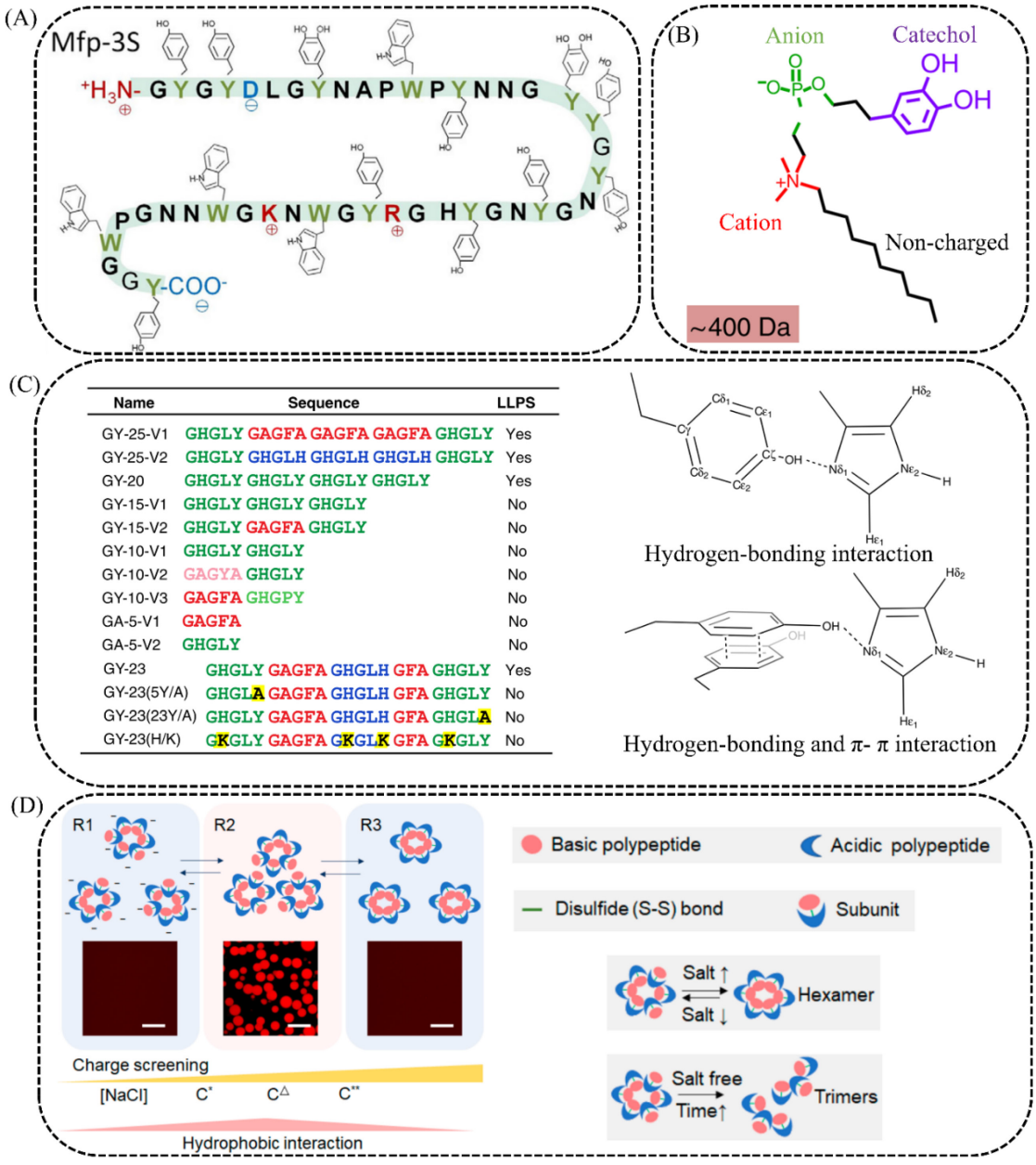

Figure 1.11. Some simple coacervation examples driven by hybrid intermolecular interactions, emphasizing on molecular structures. (A) Amino acid sequence of Mfp-3S, which is a zwitterionic protein rich in hydrophobic aromatic rings.[77] (B) Molecular structure of a catecholic zwitterionic surfactants with reduced complexity inspired by mussel foot proteins.[78] (C) Recombinant histidine-rich beak proteins and associated intermolecular interactions responsible for coacervation.[92] (D) Coacervation mechanism of soy glycinin.[97]

In biological/biomedical fields, "multivalency" generally refers to multiple ligand-receptor interactions between interfaces or molecules, where the synergistic binding strength between these recognition sites are usually greater than the sum of corresponding monovalent interactions.[146] "Multivalency" is the synergy of multiple intermolecular interactions, which could be considered as the consequence of evolution, aiming at achieving robust binding affinity by integrating the existing non-covalent interactions rather than trying to develop more complicated stronger interactions.[147] Multivalency has been proposed as the driving force for liquid-liquid phase separation of a lot of biomolecular condensates between different molecules (**Figure 1.12A**) or between different modular domains of the identical molecules (**Figure 1.12B, C**), where the latter ones belong to the range of simple coacervation.[58, 82, 148, 149] For example, the intrinsically disordered domains of DDX4 proteins can associate by multivalency to undergo liquid-liquid phase separation, leading to the formation of environment-responsive membraneless organelles. In this work, the multivalency was considered as patterned electrostatic interaction coupled with cation-π interaction from local domains between aromatic and basic residues of proteins (**Figure 1.12B**).[82] Low-complexity domains of hnRNPA2 protein are featured with highly skewed distribution of amino acids. The polypeptides backbones of hnRNPA2 proteins can interact with each other through these orderly curled β-strands (multivalent interactions) (**Figure 1.12C**) to form coacervate droplets, which showed potential application for studying information transfer from gene to protein.[149]

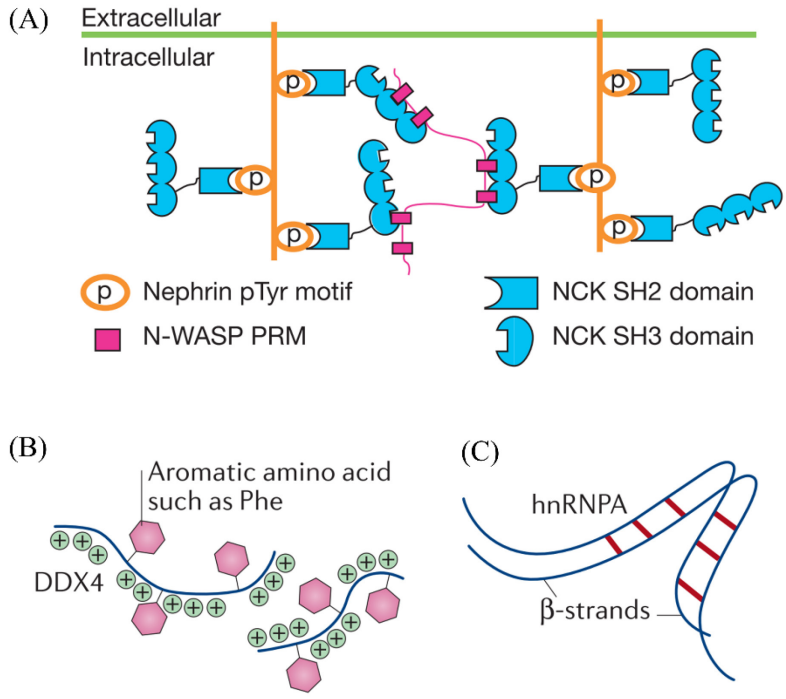

Figure 1.12. Multivalency-driven coacervation. (A) Multivalency-driven coacervation between actin-regulatory protein neural Wiskott-Aldrich syndrome protein (N-WASP) and non-catalytic region of tyrosine kinase adaptor protein (NCK). The transmembrane protein nephrin contains three tyrosine phosphorylation (pTyr) sites, which can bind the SH2 domain of NCK. Each NCK has three SH3 domains, which can bind the six proline-rich motif (PRM) ligands of N-WASP. N-WASP-NCK coacervation is highly related with nucleation of actin.[148] (B) Multivalency-driven coacervation between intrinsically disordered domains of DDX4 proteins through patterned cation-π interactions between aromatic and basic residues.[58, 82] (C) Multivalency-driven coacervation between polypeptides backbones of hnRNPA2 protein via interaction between orderly curled β-strands.[58, 149]

1.4. Intermolecular interactions of complex coacervation

Complex coacervation is a liquid-liquid phase separation phenomenon usually occurred upon the mixing of two different aqueous media, which was enabled by non-covalent intermolecular interactions between the two components. It has been extensively and intensively studied owing to the multiple choices of the two components, where the two components can be combinations of non-ionic/charged polymers, polyelectrolytes (positively charged, negatively charged or zwitterionic), proteins, small molecules, inorganic clusters, etc. Intermolecular interactions between each pair of participants could be electrostatic interaction, hydrogen-bonding interaction, cation-π interaction, multivalency, or could be synergy of two or more of them. Probing intermolecular interactions associated with complex coacervation can direct the design of novel coacervation system as well as improve the properties of the existing ones.

1.4.1 Electrostatic interaction

As most natural polymers, proteins, inorganic clusters, etc. usually bear charges that may contribute to the coacervation processes, **Table 1.2** summarizes the most common employed positively charged and negatively charged moieties of coacervation partners, aiming at rational design of coacervation systems by reasonably functionalizing natural polymers, directly synthesizing polyelectrolytes with expected charged groups, properly choosing charged proteins, organic/inorganic small molecules, and so on.

Table 1.2. Complex coacervation systems driven by electrostatic interaction and corresponding oppositely charged components as well as applications.

	Positively charged components (occasionally zwitterionic)	Negatively charged components	Applications	Refs
Natural polymers	Gelatin, chitosan, agar	Sodium carboxymethyl cellulose (CMC), gum Arabic, hyaluronic acid, sodium alginate, chia mucilage, carboxymethyl tara gum, zedo gum, cress seed gum, Persian gum, κ-carrageenan	Nano-/Micro-encapsulation, electronic ink	150-169
Natural/functionalized natural polymer and protein	Whey protein isolate, ovalbumin, Spirulina platensis protein, potato protein isolate, pea whey protein, Scallop male gonad hydrolysates, chitosan, collagen hydrolysate, oak protein isolate, Tau protein, diethylaminoethyldextran chloride (DEAE-dextran), dextran-graft poly[ethyl 3-(N,N-dimethylamino) acrylate], dextran-graft-poly(2-diethylaminoethyl methacrylate), mfp-1, mfp-151	κ-carrageenan, gum Arabic, sodium alginate, pectin, heparin, double-stranded DNA, RNA, sugar beet pectin, quince seed mucilage, siRNA, hyaluronic acid	Nano-/Micro-encapsulation, emulsion stabilizer, protein purification, gene delivery	13, 23, 26, 170-190
Polyelectrolytes/natural or functionalized polymer/protein and inorganic clusters/polymer/salt	Gelatin, green fluorescent protein +36GFP, zein, poly(2-acrylamido-2-methyl-1-propanesulfonic acid (AMPS)-*co*-[3-(methacryloylamino)propyl]trimethylammonium chloride (MAPTAC)), poly(allylamine hydrochloride) (PAH), Ca^{2+}, protamine, low molecular weight polyaluminium complex, poly(sulfobetaine methacrylamide) (PSBMA)	Sodium hexametaphosphate $Na_6[(PO_3)_6]$, polyphosphate, laponite, lithium metatungstate $Li_6H_2W_{12}O_{40}$, phosphomolybdic acid $H_3PMo_{12}O_{40}$, polyaspartic acid, tripolyphosphate, sucrose octasulfate, $K_5[BW_{12}O_{40}]$, $K_7[PW_{11}O_{39}]$, $K_{28}Li_5H_7[P_8W_{48}O_{184}]$,	Microencapsulation, drug delivery, surface modification, coating	25, 104, 131, 191-198
Polyelectrolytes and natural polymer/functionalized natural polymer/protein	ε-poly-L-lysine, polylysine, ammonium/guanidinium-PEO-ammonium/guanidinium triblock copolymers, poly(ethylene argininylaspartate diglyceride) (PEAD), poly(diallyl dimethylammonium chloride) (PDADMAC), mfp-1, mfp-151, lysozyme, cystine peptide	Hyaluronic acid, carboxymethyldextran (CM-dextran), heparin, sodium alginate, short single strands of DNA, poly(aspartic acid), poly(4-styrenesulfonic acid, sodium salt) (PSS), siRNA	Biomolecular condensation, drug delivery, gene delivery	189, 199-208
Polyelectrolytes	Polylysine, poly(diallyl dimethylammonium chloride) (PDADMAC), poly(allylamine hydrochloride) (PAH), glycidyl trimethylammonium chloride functionalized dextran (Q-Dex), poly(N,N-dimethylaminopropyl acrylamide)-*g*-poly(N-isopropylacrylamide) (PDMAPAA-*g*-PNIPAM), poly(lysine-*co*-glycine), JR-400, poly (ethylenimine) (PEI), Ac-(Lys-Ser)6-Lys-OH, poly-L-histidine, guanidinium-functionalized PEO triblock polymer, poly(L-ornithine hydrobromide), polyamine, poly(trimethylaminoethyl methacrylate) (MADQUAT)	Polyglutamate, poly(3-sulfopropyl methacrylate) (PSPMA), poly(acrylic acid) (PAA), Poly(acrylic acid)-*g*-poly(N-isopropylacrylamide) (PAA-*g*-PNIPAM), potassium cocoyl glutamate, potassium cocoyl glycinate, poly(4-styrenesulfonic acid, sodium salt) (PSS), poly(aspartic acid), sulfonate-functionalized PEO triblock polymer, polyphosphodopa, poly(3-sulfopropyl methacrylate) (PSPMA)	Transportation and storage of vaccines, hierarchical subcellular condensation, underwater adhesive	16, 113, 125, 128, 129, 132, 141, 209-227

Polyelectrolytes/protein/polymer and small organic molecules	Polylysine, poly(diallyl dimethylammonium chloride) (PDADMAC), poly(N-methyl-2-vinylpyridinium iodide)-b-poly(ethyleneoxide) ($P2MVP_{128}$-*b*-PEO_{477}), protamine, salmine sulfate, dodecyl trimethylammonium bromide, cetylpyridinium, hexamethylene-1,6-bis(dodecyldimethylammonium bromide), dodecyl trimethyl ammonium bromide (DTAB)	Adenosine triphosphate (ATP), cyclodextrin-modified dipicolinic acids (βCD-DPA), citrate, phytic acid, sodium oligoarene sulfonates, sodium dodecyl sulfate, poly(4-styrenesulfonic acid, sodium salt) (PSS), polyacrylamide (PAM), gum Arabic	Enzymatic reactions, Microencapsulation	7, 29, 195, 201, 228-238
Proteins	Lactotransferrin, lactoferrin, lysozyme	β-lactoglobulin, β-casein, κ-casein	Stabilization of emulsion	239-243
Protein and small molecules	Spermine, a peptide sequence RRASLRRASL	RNA, polyuridylic acid RNA	Biomolecular condensation	244, 245
Amino acids and inorganic clusters	Arginine, Histidine	$K_8[\alpha\text{-}SiW_{11}O_{39}]$, $H_4SiW_{12}O_{40}$	Anticorrosive coatings, wet and functional adhesive	134, 246
Inorganic components	Ca^{2+}	Polyphosphate	Drug delivery	104, 247

According to the complex coacervation systems and the associated oppositely charged components summarized in **Table 1.2**, molecular structures of some frequently studied negatively charged components and corresponding positively charged counterparts were drawn in **Figure 1.13** and **Figure 1.14**, respectively. Based on Table 1.2, natural polymers such as gelatin, chitosan, agar, gum Arabic (**Figure 1.13A**), sodium carboxymethyl cellulose, hyaluronic acid (**Figure 1.13B**), sodium alginate (**Figure 1.13C**), κ-carrageenan (**Figure 1.13M**), etc. have been widely and intensively investigated in the field of micro-/nano-encapsulation technologies via complex coacervation for food and cosmetic industries, owing to their excellent biocompatibility and inexpensive cost. Functionalization of natural polymers and synthesis of polyelectrolytes have been broadly employed by researchers to acquire materials with desired properties, via introducing specific charged groups to achieve complex coacervation through electrostatic interaction. Proteins can also be involved in complex coacervation systems as they usually carry on net positive/negative charges despite existence of oppositely charged domains. Inspired by protein's capability of initiating coacervation, small amino acid molecules have also been demonstrated to

participate in complex coacervation with polyoxometalates clusters. Additionally, organic and inorganic small molecules have also been reported in complex coacervation systems.

Positively charged amino acids including arginine (**Figure 1.14A**), lysine (**Figure 1.14B**), and histidine (**Figure 1.14C**) have been harnessed as basic units of synthesized polymers, among which polylysine was the most popular one. It was usually employed to study protocell models and membrane-free microenvironments as well as related enzymatic catalysis reactions, where its oppositely charged partners were generally hyaluronic acid (**Figure 1.13B**),[199] sodium alginate (**Figure 1.13C**),[203] single strands of DNA (**Figure 1.13H**),[206] oligo- or polyribonucleotides,[233] adenosine triphosphate (ATP, **Figure 1.13I**),[7, 201, 233] carboxymethyldextran.[201, 205] Encapsulation and efficient delivery of proteins as therapeutic agents through coacervation with polyglutamic acid was also studied, owing to pH-responsive release of the proteins, biocompatibility of the coacervate system, and intact preservation of the secondary structure of the proteins.[222] Arginine and histidine could directly form coacervate phases via coacervation with polyoxometalates $K_8[\alpha\text{-}SiW_{11}O_{39}]$[246] and $H_4SiW_{12}O_{40}$,[134] serving as sprayable anticorrosive coatings and functional wet adhesives, respectively. Besides, the guanidinium group of arginine was adopted to functionalized polymers as it can provide stronger electrostatic interaction than ammonium group with the same negatively charged polymers.[200, 224] However, ammonium groups have still been the most frequently exploited positively charged moieties (**Figure 1.14D-I**) not only for naturally-born spermine/protamine/salmine,[29, 244, 248] but also for functionalizing natural polymers or synthesizing polyelectrolytes. For example, dextran was modified to diethylaminoethyldextran chloride (DEAE-dextran), dextran-graft poly[ethyl 3-(N,N-dimethylamino) acrylate], or dextran-graft-poly(2-diethylaminoethyl methacrylate), serving as the positive part of complex coacervation.[23, 26] Moreover, dextran could also be functionalized to carboxymethyl dextran, being

the negative part of complex coacervation.[205] Other amine-bearing positively charged polyelectrolytes such as poly(allylamine hydrochloride) (PAH, **Figure 1.14D**),[25, 221, 225, 226] poly(L-ornithine hydrobromide) (**Figure 1.14F**),[132] poly(ethylene argininylaspartate diglyceride) (PEAD, **Figure 1.14G**)[202] and branched polyethylenimine,[125, 128, 218] have also be widely used for complex coacervation. Moreover, considering amine groups tend to be oxidized as well as being sensitive to pH, quaternary ammonium groups have been popular substituents of them[249, 250], where typical examples including N, N-dimethylaminopropyl acrylamide (DMAPAA, **Figure 1.14J**),[211] poly(2-(trimethylamine)ethyl methacrylate) (MADQUAT, **Figure 1.14K**),[105, 113] dodecyl trimethyl ammonium bromide (DTAB, **Figure 1.14L**),[238] poly(diallyldimethylammonium chloride) (PDADMAC, **Figure 1.14M**),[129, 204, 215, 216, 219, 228, 231, 232, 235] and [3-(methacryloylamino)propyl]trimethylammonium chloride (MAPTAC, **Figure 1.14N**).

In contrast, there is a large variety of negatively charged components, such as deprotonated carboxyl group -COO^-, phosphate group -PO_4^-, and sulfate group -SO_3^-. According to Table 1.2, natural polymers gum Arabic (**Figure 1.13A**), hyaluronic acid (**Figure 1.13B**),[106, 164, 189, 190, 199] sodium alginate (**Figure 1.13C**), etc. usually serve as negative components of complex coacervation nano-/micro-encapsulation system owing to their negatively charged carboxyl groups and superior biocompatibility. Amino acids aspartic acid and glutamic acid motivated synthesis of polyglutamate (**Figure 1.13D**)[125, 212, 217] and polyasprtic acid (**Figure 1.13E**).[189, 223] Fruit-derived citrate (**Figure 1.13F**) could form coacervate with cationic protamine.[195] As an easily available by-product of gasline industry, acrylic acid was usually polymerized to be poly(acrylic acid) (**Figure 1.13G**), being a frequently used negatively charged component of complex coacervation.[141, 216, 221, 225, 226] Additionally, natural biological DNA (**Figure 1.13H**),[23, 26]

adenosine triphosphate (ATP, **Figure 1.13I**),[7, 201, 228, 232] and RNA,[23, 244] have been extensively studied in the field of biomolecular liquid condensates owing to their in vivo-borne nature and negative phosphate groups. Inspired by these biological molecules, inorganic polyphosphate (**Figure 1.13J**) was employed as an excellent substituent due to homogeneously distributed negative phosphate groups.[49, 192, 195, 247] Furthermore, plant-derived phytic acid (**Figure 1.13K**) was demonstrated to form coacervate with salmine sulfate.[29] Finally, mammals-originated heparin (**Figure 1.13L**)[13, 182, 202] and plant-derived κ-carrageenan (**Figure 1.13M**)[165, 170, 176] as well as corresponding inspired synthesized polyelectrolytes poly(3-sulfopropyl methacrylate) (PSPMA, **Figure 1.13N**)[210] and poly(4-styrenesulfonic acid) (PSS, **Figure 1.13O**)[129, 215, 219, 236] also made their contribution to complex coacervation system owing to their negative sulfate groups.

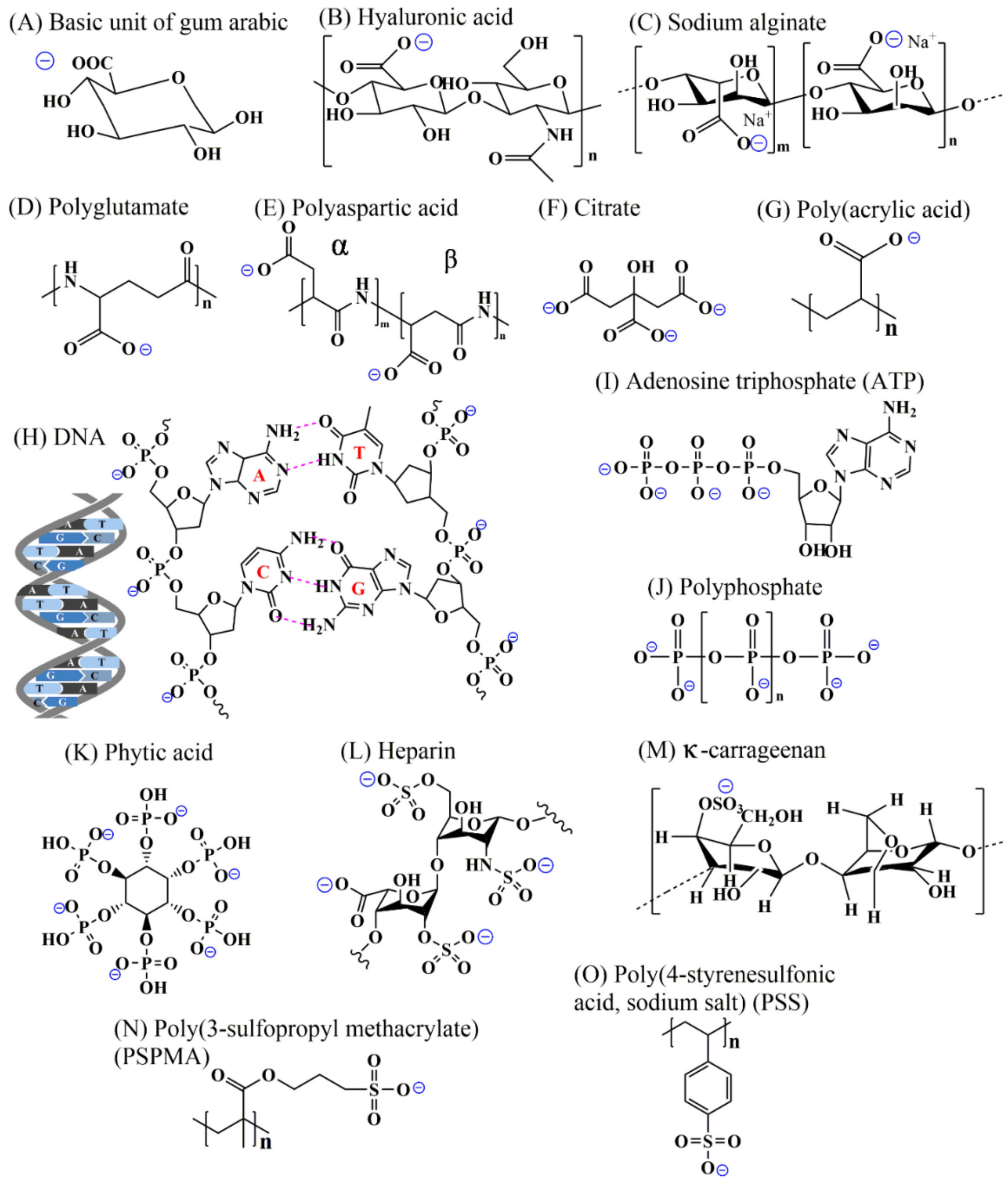

Figure 1.13. Common negatively charged monomers, small molecules, and polyelectrolytes involved in electrostatic interaction-driven complex coacervation. (A) Basic unit of gum Arabic. (B) Hyaluronic acid. (C) Sodium alginate. (D) Polyglutamate. (E) Polyaspartic acid. (F) Citrate. (G) Poly(acrylic acid). (H) Schematic diagram of double helix structure of DNA and a basic unit of it. (I) Adenosine triphosphate (ATP). (J) Polyphosphate. (K) Phytic acid. (L) Heparin. (M) κ-carrageenan. (N) Poly(3-sulfopropyl methacrylate) (PSPMA). (O) Poly(4-styrenesulfonic acid, sodium salt) (PSS).

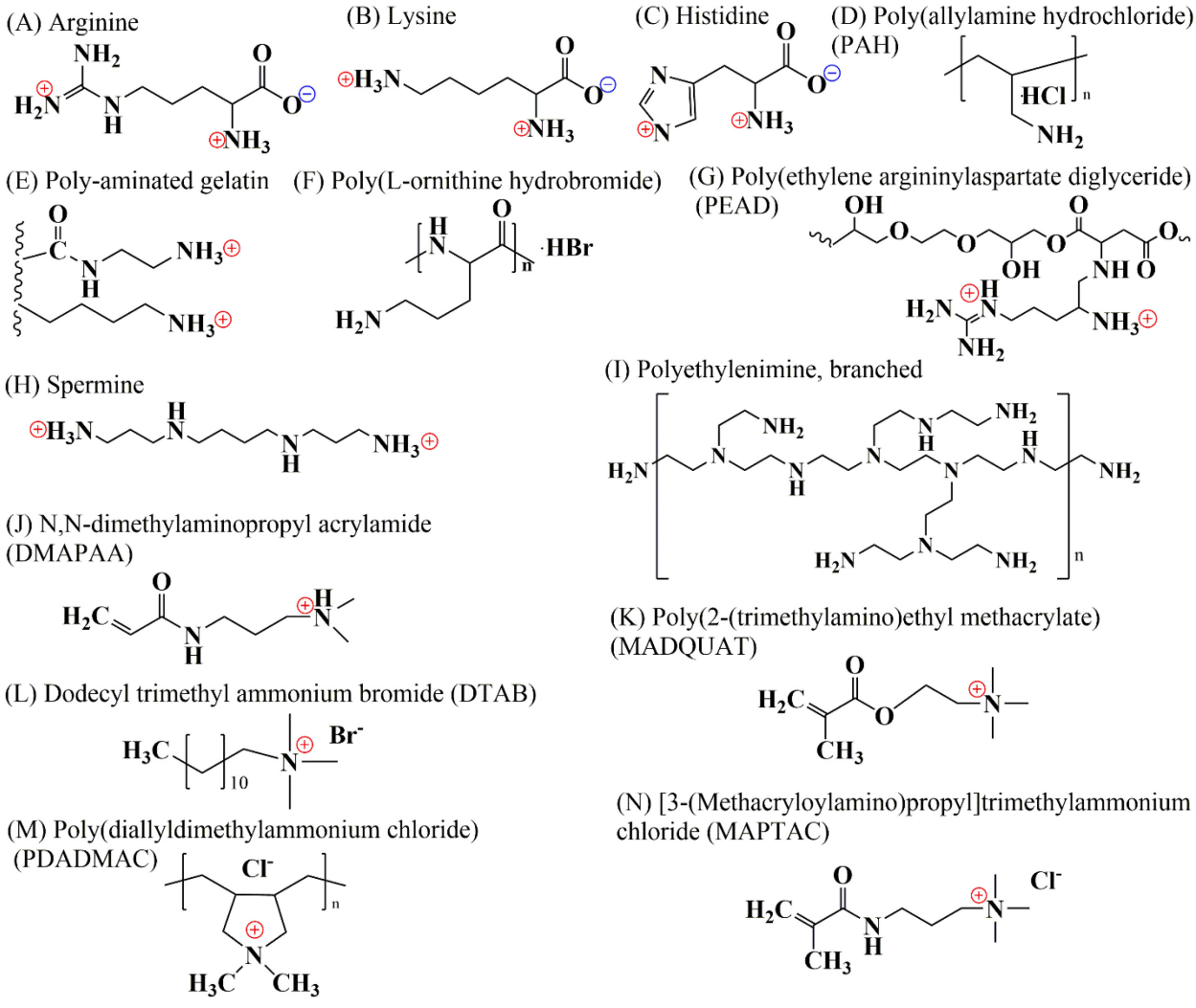

Figure 1.14. Common positively charged monomers, small molecules, and polyelectrolytes involved in electrostatic interaction-driven complex coacervation. (A-C) Amino acids arginine, lysine, and histidine. (D) Poly(allylamine hydrochloride) (PAH). (E) Poly-aminated gelatin. (F) Poly(L-ornithine hydrobromide). (G) Poly(ethylene argininylaspartate diglyceride) (PEAD). (H) Spermine. (I) Polyethylenimine, branched. (J) N, N-dimethylaminopropyl acrylamide (DMAPAA). (K) Poly(2-(trimethylamine)ethyl methacrylate) (MADQUAT). (L) Dodecyl trimethyl ammonium bromide (DTAB). (M) Poly(diallyldimethylammonium chloride) (PDADMAC). (N) [3-(methacryloylamino)propyl]trimethylammonium chloride (MAPTAC).

It is worth noting that electrostatic interaction-driven complex coacervations are usually affected by pH, mixing ratio, ionic strength, temperature, etc. owing to deprotonation and protonation of charged groups, homogeneous and heterogeneous distribution of charges, charge density and so on. For example, polylysine and carboxymethyldextran (CM-dextran) or adenosine triphosphate (ATP) could undergo reversible pH-responsive coacervation when pH was switched between 9 and 11. As pK_a of polylysine was 10.5, amine groups were protonated at pH of 9 to be able to electrostatically interact with negatively charged component while they were deprotonated at pH of 11, incapacitating the process of coacervation (**Figure 1.15A**).[201] Despite the verification of appropriate pH of coacervation, mixing ratio of the two oppositely charged components also plays an important role as it is highly related with the yield of coacervate phase. Some of the generated coacervate phases exhibited as stable dispersed coacervate droplets within a specific timescale while sometimes coacervate droplets rapidly coalesce with each other to form a bulk coacervate phase, where the yield of coacervate phase under the two situations could be measured via turbidity[106, 251] and weight/volume ratio of the bulk coacervate phase[124, 252], respectively. Polypeptides usually share identical backbones whereas vary with different side chains, which seized considerable research attraction. Mixing ratio of poly(L-lysine) to poly(L-glutamic acid) significantly affect final yield of coacervate according to measurement of turbidity, achieving the maximum with 1:1 stoichiometric ratio (**Figure 1.15B**). Meantime, the effect of mixing ratio became more crucial with the increase of total polypeptide concentration (**Figure 1.15B**).[253] Ionic strength also plays a significant role in coacervation process because it can directly influent electrostatic interaction. Strong polyelectrolytes like poly(styrenesulfonate) (PSS) and poly(diallyldimethylammonium) (PDADMA) are inert to pH but their complexes are susceptible to salts. With concentration of KBr ranging from 0 to 1.88 M, PSS-PDADMA complexes successively experienced solid, coacervate and solution states due to gradually screened attractive

electrostatic interaction (**Figure 1.15C**).[129] Usually, electrostatic interaction-driven coacervation would be weaken by addition of salt, however, coacervate originated from coacervation between net neutral zwitterionic poly(sulfobetaine methacrylamide) (PSBMA) and inorganic polytungstate $Li_6H_2W_{12}O_{34}$ (W_{12}) was strengthened by increasing concentration of LiCl from 0.3 M to 0.5M.[131] At the same time, effect of temperature on the coacervation behaviors of PSS-PDADMA and PSBMA-W_{12} were different. For PSS-PDADMA coacervation system, increasing temperature led to more concentrated coacervate phase and more dilute supernatant phase, while PSBMA-W_{12} coacervation system evolved into solution by heating (**Figure 1.15D**).[129, 131] For coacervation system comprising biopolymers, the effect of temperature is more complex due to possible existence of thermo-responsive hydrophobic groups and/or hydrogen-bonding interaction associated moieties.[254] Therefore, the formation of electrostatic interaction-driven complex coacervation not only depends on the reasonable choice of oppositely charged components but also requires desirable surrounding environments.

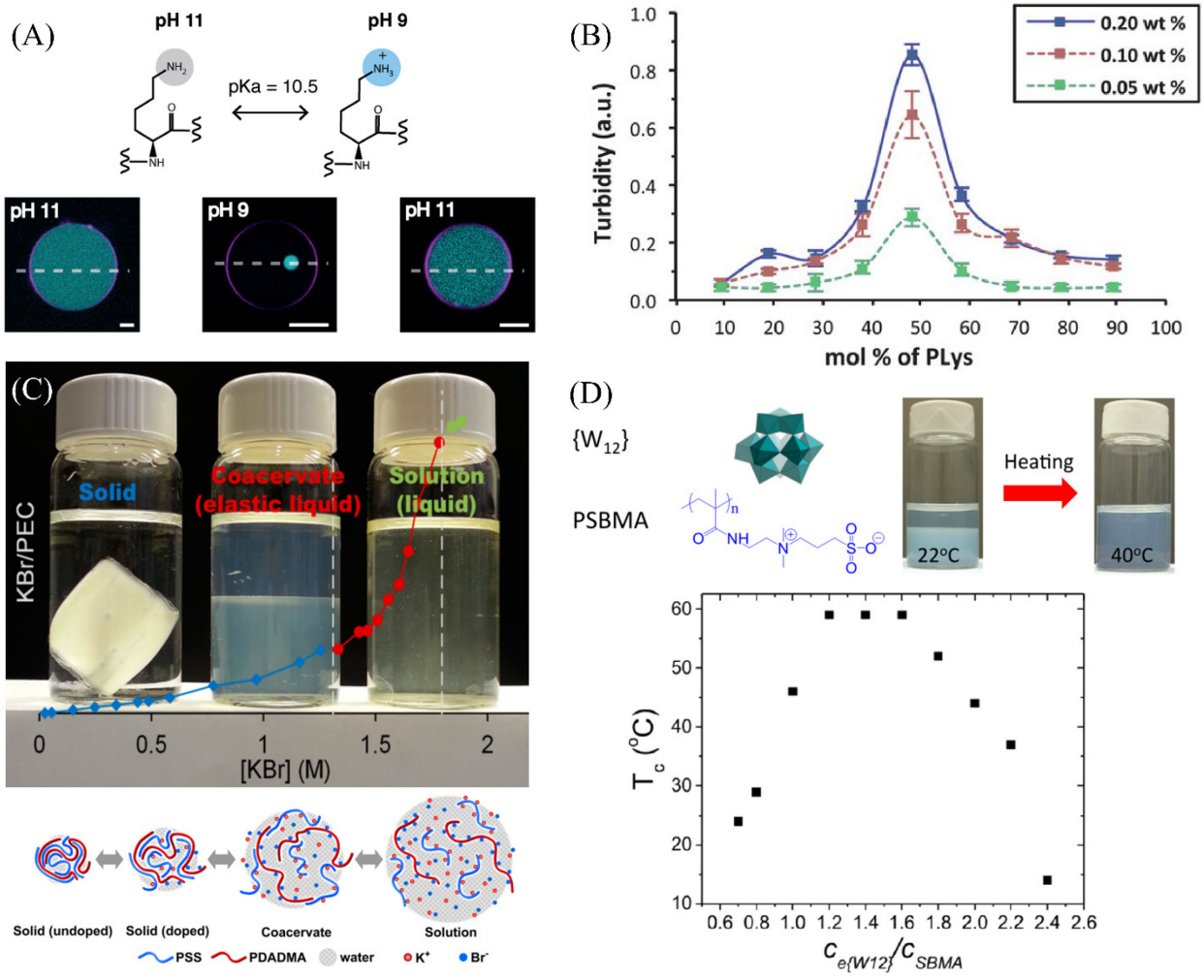

Figure 1.15. Effects of pH, mixing ratio, ionic strength, and temperature on complex coacervation. (A) pH-responsive coacervation between polylysine and carboxymethyldextran (CM-dextran) or adenosine triphosphate (ATP).[201] (B) Effect of mixing ratio of poly(L-lysine) to poly(L-glutamic acid) on yield of coacervate phase through measuring turbidity, where total concentration of polypeptides also exerted influence.[253] (C) Effect of KBr on phase behaviors of PSS-PDADMA complexes.[129] (D) Effect of temperature on coacervation between PSBMA and inorganic polytungstate $Li_6H_2W_{12}O_{34}$ (W_{12}). Coacervate phase disappeared when heated to 40 °C, and this phase transition temperature varied with mixing ratio of W_{12} to PSBMA.[131]

1.4.2 Hydrogen-bonding interaction

Hydrogen bonding is a type of noncovalent inter/intra-molecular attraction between an electronegative atom and a hydrogen atom bonded to another electronegative atom, such as nitrogen, oxygen, or fluorine.[120] Hydrogen-bonding interaction is one of the most important noncovalent intermolecular interactions in living organisms, such as the abundant hydrogen bonding-connected water and DNA molecules.[255] As coacervate-based biomolecular condensates are commonly found in biological systems, researchers tried to figure out if coacervation could be driven by hydrogen-bonding interaction. Lee and coworkers reported a medical adhesive generated from liquid-liquid phase separation between tannic acid and poly(ethylene glycol) (PEG) aqueous solutions enabled by hydrogen-bonding interaction between hydroxyl groups in tannic acid and etheric oxygens in poly(ethylene glycol) (**Figure 1.16A**). This medical adhesive was demonstrated as an effective hemostatic material and a biodegradable patch for detecting gastroesophageal reflux disease in vivo.[133] They also developed an underwater adhesive with instant underwater adhesion strength of about 80 kPa originating from coacervation between tannic acid and poly(vinyl alcohol) (PVA) aqueous solutions, where the driving force was hydrogen-bonding interaction between hydroxyl groups of PVA and oxygen atoms of oxidized catechol groups of tannic acid (**Figure 1.16B**).[256] Zeng et al. found that silicotungstic acid (SiW, $H_4SiW_{12}O_{40}$) and PEG could form adhesive coacervate through hydrogen-bonding interaction between terminal and bridging oxygens of SiW and etheric oxygens of PEG bridged by hydrated protons. The acquired adhesive coacervate was demonstrated as an effective hemostatic agent with innate antimicrobial property (**Figure 1.16C**).[124] Comparing with electrostatic interactions-enabled coacervation, where the addition of salt is critical to tune strength of electrostatic interaction, coacervation actuated by hydrogen-bonding interaction could occur with or without

the presence of salt. Their mechanical properties are mainly affected by molecular weight, concentration and mixing ratio of the two participants.

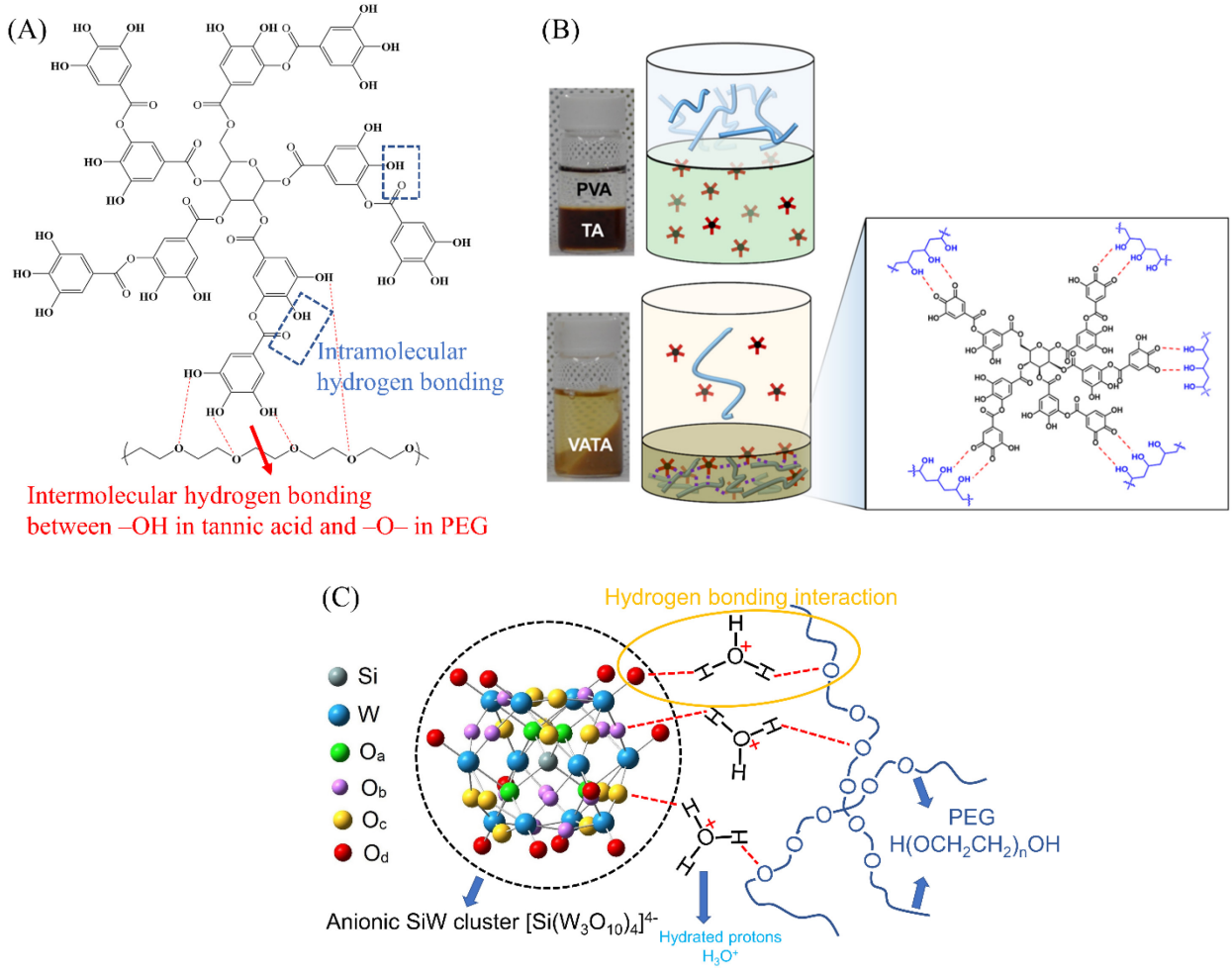

Figure 1.16. Hydrogen-bonding interaction-driven complex coacervation. (A) A medical adhesive originated from liquid-liquid phase separation between tannic acid and PEG.[133] (B) An underwater adhesive driven by hydrogen-bonding interaction between tannic acid and PVA.[256] (C) A wet adhesive with innate antibacterial property enabled by hydrogen-bonding interaction-driven coacervation between SiW and PEG.[124]

1.4.3 Hybrid intermolecular interactions

Cooperativity of two or more intermolecular interactions usually endows complex coacervates with desired functionalities or more opportunities for exploring biological phenomena, where the synergy between electrostatic interaction and hydrophobic interaction has been widely investigated. Elastin-like polypeptides (ELP) has been widely employed by researchers owing to its facilely controlled reversible phase transition. Coacervation between negatively charged ELP and positively charged peptide amphiphiles (PAs) enabled a multifunctional membrane with manipulable assembly and disassembly, adhesive and self-healing capabilities, as well as spatiotemporal-controlled structures, where the temperature-responsive hydrophobicity of ELP enhanced the final tubular structures of the membrane.[135] Globular proteins (mCherry or enhanced green fluorescent protein, eGFP) modified with a glutamic acid-rich leucine zipper (globule-Z_E) (negatively charged) and an arginine-rich leucine zipper linked with an elastin-like polypeptide (Z_R-ELP) (positively charged) were mixed to generate complexes in aqueous solution, which subsequently turned into coacervate droplets upon heating while further heating induced the formation of vesicles (**Figure 1.17A**). This transition was proposed to be triggered by the tunable hydrophobicity of ELP with controlled heating, where the generation of vesicles with expected size showing great potential for drug delivery, microreactors, and protocell models.[257] Hydrophobic polyampholyte elastin and strong negatively charged DNA were harnessed to study coacervation, which was driven by the weakened electrostatic interaction by the addition of NaCl. The authors therefore claimed that the ubiquitous coacervation between DNA and proteins was mainly induced by very weak electrostatic interactions.[258] Although hexafluoroisopropanol (HFIP) was water-miscible, it could promote cationic surfactant dodecyltrimethylammonium hydroxide to self-assembled into positively charged micelles with hydrophobic core, followed by coacervating with negatively charged lauric acid. Owing to the convenient and high-efficient

phase separation, this technique was applied to detect trace fluoroquinolones in milk.[259] Oppositely charged components encapsulated within liposomes could be stimulated to undergo coacervation by transmembrane proton flux (**Figure 1.17B**, upper part). Here, the charge-dense coacervate droplets can be employed to interact with inner surface of charged lipids (**Figure 1.17B**, lower left). When the negatively charged RNA was functionalized with hydrophobic cholesterol and mixed with positively charge spermine, nucleation of coacervate droplets would be induced on the hydrophobic inner vesicle surface (**Figure 1.17B**, lower right). Manipulation of charge distribution and hydrophobicity of coacervation components in controlled coacervation systems exhibited great potential for fabricating synthetic cells.[260]

Collaboration between electrostatic interaction and hydrogen-bonding interaction also seized much attraction. For instance, atmospheric cold plasma (ACP) was demonstrated to be capable of enhancing hydrogen bonding and electrostatic interactions between zein and chitosan through unfolding polypeptide chain of zein while maintaining the primary structure to be intact, resulting in high encapsulation efficiency and excellent dispersion stability.[261] Electrostatically interacted ionic polypeptides could either generate coacervate phase or solid precipitate, Perry et al. proposed this might have correlation with the chirality of their monomers, which could form hydrogen-bonding interaction-driven secondary structures such as coiled structure or α-/β-sheets structure. They found that at least one kind of racemic polypeptides was required to form fluid coacervate owing to the disruption of backbone hydrogen-bonding networks while two chiral polypeptides form compact, fibrillar solids with α-/β-sheets structure.[262] Besides, Wang and colleagues introduced a cost-efficient strategy of producing substantial coacervate via taking advantage of electrostatic interaction, hydrogen-bonding interaction, and hydrophobic interaction between cationic gemini surfactant hexamethylene-1,6-bis(dodecyldimethylammonium bromide)

($C_{12\text{-}6\text{-}12}$) and pH-sensitive N-benzoylglutamic acid (H_2Bzglu). The double hydrophobic chains of the gemini surfactant propelled the formation of hydrophobic cores, exposing the positively charged shells. Deprotonated acid $HBzglu^-$ interacted with each other via hydrogen-bonding interaction between -COOH groups and then inserted into positively charged gemini surfactants shells to form coacervate phase (**Figure 1.17C**).

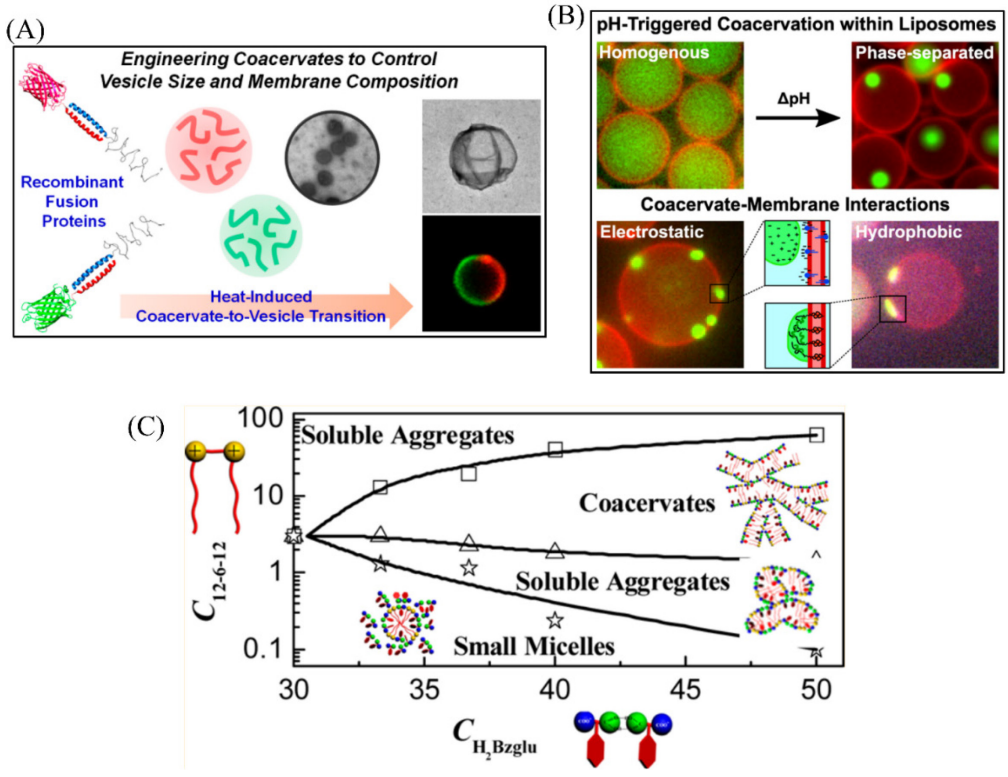

Figure 1.17. Complex coacervation systems involving hybrid intermolecular interactions. (A) Globular protein mCherry (red coiled structure) and eGFP (green coiled structure) were modified with a glutamic acid-rich leucine zipper Z_E (red ribbon structure), respectively. ELP (curled black strings) was functionalized with an arginine-rich basic leucine zipper Z_R (blue ribbon structure). Globule-Z_E and Z_R-ELP interacted with each other via electrostatic interaction between oppositely charged Z_E and Z_R zippers. Corresponding complexes were induced to be coacervate droplets by heating and further to be vesicles via continuous heating.[257] (B) A transmembrane proton flux

could regulate the pH of enclosed environment of liposomes to be appropriate for complex coacervation between oppositely charged polylysine and adenosine triphosphate (ATP) (upper part of the diagram). Charge-dense coacervate droplets could interact with charged lipids of inner surface of liposomes (lower left part of the diagram). Spermine and cholesterol-tagged RNA started the nucleation of their coacervate droplets on the hydrophobic inner surface of liposomes and their coacervate droplets could spread on the surface (lower right part of the diagram).[260] (C) Varying ratios of cationic gemini surfactant $C_{12\text{-}6\text{-}12}$ to H_2Bzglu, corresponding products could be small micelles, soluble aggregates, or coacervates, depending on synergy among electrostatic interaction, hydrophobic interaction and hydrogen-bonding interaction.[263]

Similar to simple coacervation, multivalency (multiple intermolecular interactions of the same kind) also serves as driving force for the formation of complex coacervate-based biomolecular condensates between molecules, where multiple ligand-receptor interactions occur. For example, two orthogonal sequence-defined functionalized nucleic acid polymers (SfNAPs) with complementary side chains can undergo liquid-liquid phase separation when being mixed and shaken under 37 °C (**Figure 1.18A**), while the solutions of corresponding monomers could not give rise to coacervation due to absence of multivalency.[264] Nucleophosmin (NPM1) can assemble into pentamers (N130) which bears two highly conserved acidic tracts A1 and A2 (**Figure 1.18B**). Titration of rpL5 peptides into N130 would induce liquid-liquid phase separation upon reaching a critical concentration, through multivalency between positively charged arginine-rich linear motifs R1 of rpL5 and acidic residues within the A1 binding groove as well as disordered A2 tract of N130.[265] Complex coacervation comprising three components was also reported. In order to unveil the molecular structures required for the formation of P-bodies through

rapid phase transition, Sprangers and coworkers try to reconstruct the liquid-liquid phase separation process with mRNA degradation factors, where they found that the mRNA decapping enzyme Schizosaccharomyces pombe Dcp2, its prime activator Dcp1, and the scaffolding proteins Edc3 and Pdc1 were sufficient to carry on a coacervation process (**Figure 1.18C**). Here, both Dcp2 and Pdc1 could undergo coacervation with Edc3, respectively, through multivalency between their short helical leucine-rich motifs (HLM) and the LSm domain of Edc3.[266] Generally, multivalency-driven coacervation is studied associating with biological proteins and peptides as they usually possess multiple modular domains, which is still challenging for synthesized polymers.[58, 145]

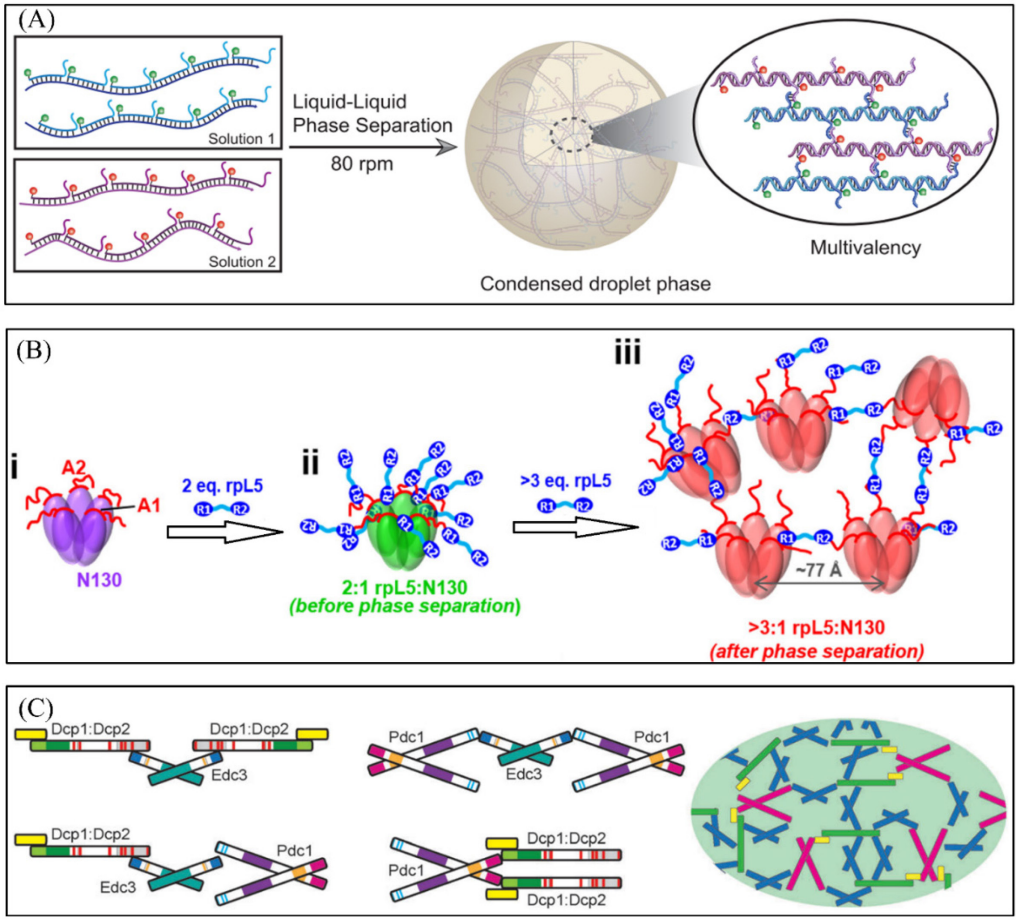

Figure 1.18. Coacervate-based biomolecular condensates driven by multivalency. (A) Multivalency-driven coacervation between two orthogonal sequence-defined functionalized nucleic acid polymers (SfNAPs) with complementary side chains.[264] (B) Multivalency-driven coacervation between nucleophosmin (NPM1) assembled pentamers (N130) and rpL5 peptides.[265] (C) Multivalency-driven coacervation among mRNA decapping enzyme Schizosaccharomyces pombe Dcp2, its prime activator Dcp1, and the scaffolding proteins Edc3 and Pdc1.[266]

1.5. Summary and Perspectives

During the past two decades, coacervation have attracted substantial research interest and holds great promise in various fields such as intracellular biomolecular condensates, extracellular matrices, synthesis cells, Alzheimer disease treatment, gene/drug delivery, gradient materials, wet/underwater adhesives, surface modification, protein purification, nano-/micro-encapsulation, wastewater treatment, stabilization of emulsions, etc. This chapter focuses on summarizing underlying non-covalent intermolecular interactions of both simple coacervation and complex coacervation systems. Non-covalent intermolecular interactions including hydrophobic interaction, electrostatic interaction, hydrogen-bonding interaction, cation-π interaction, and multivalency as well as associated constituents with detailed molecular structures have been elucidated, which can serve as instructive materials for the design and fabrication of new coacervation system. Due to the combination of diverse intermolecular interactions and specific molecular structures novel coacervation systems can be developed with a considerable choice of synthesizing polymers or functionalizing existing natural polymers and proteins.

Despite much progress achieved, there are still some challenging issues. First, although coacervate protocells can mimic some functions of biological cells such as membrane-mediated compartmentalization, chemical enrichment, internalized structuration, and catalytic generation of oxygen, there is a long way toward real accomplishment of artificial cell.[228, 233] Second, three-phase complex coacervate droplets have been acquired by combining two pairs of coacervation system which shared the same positively charged component, but biomimetic gradient materials that can serve as substituent of biological tissues have not been achieved.[210] Third, Alzheimer disease-related Tau protein with positively charged microtubule-binding domain was discovered to form coacervate droplets via interacting with negatively charged molecules, promoting the

generation of amyloid.[13] However, to treat Alzheimer disease which is still troubling about 30 million people all over the world requires the prevention of amyloid formation, which has not been realized.[267] Fourth, biomimetic coacervate-based wet/underwater adhesive reported are not robust enough compared with the high efficiency and strength of sessile organisms, indicating that instant, repeatable and strong coacervate-based wet/underwater adhesive are demanding.[268]

1.6 Objectives of the Thesis

The development of adhesives that can achieve instant, repeatable, and robust adhesion to various substrates at wet/underwater environments is challenging as water is a notorious destroyer to prevent the intimate contact between adhesives and substrates by forming hydration layers on surfaces and interfaces. Further endowing wet/underwater adhesives with functionalities to satisfy increasing demands of advanced and smart materials is another difficulty. Coacervation has been discovered to play a critical role in the formation of sessile organism's long-lasting underwater adhesives and has inspired extensive research interests in fabricating bio-inspired underwater adhesives, with great potential applications in tissue glues, wound dressings, water-based devices, underwater transfer/repair, underwater soft robots, etc. Conventional coacervations are usually driven by electrostatic interaction and generally suffer from complex polymer synthesis, sensitivities to formation conditions, weak mechanical properties and low yields.

The overall goal of this thesis is to develop functional wet/underwater adhesives based on hydrogen-bonding interaction-driven coacervation with facile fabrication methods towards engineering and biomedical applications. The detailed objectives are listed below.

(1) Develop wet adhesives from hydrogen-bonded coacervates as antibacterial hemostatic agents, which can be easily prepared and scaled up through a one-step mixing method.

(2) Fabricate instant underwater adhesives from hydrogen-bonded coacervates, which integrates thermo-tunable optical property and electrochromism to be promising candidates for paintable cathode of portable aqueous batteries as well as energy-saving windows.

(3) Design instant and repeatable underwater adhesives from hydrogen-bonded coacervates that combine robust underwater adhesion with anticancer and antibacterial properties for potential application in drug delivery, tissue glue and wound dressing.

1.7 Thesis Outline

Chapter 1 gives a literature review of recent advances in coacervation and underlying noncovalent intermolecular interactions where basic experimental techniques of studying coacervation are introduced and primary noncovalent intermolecular interactions for driving simple and complex coacervation are elucidated. The objectives of this work are also listed.

Chapter 2 reports a facile one-step mixing method for the fabrication of an adhesive coacervate with hemostatic and antibacterial properties. Phase behavior and mechanism of intermolecular interactions of the coacervation phenomena between SiW and PEG have been investigated. The excellent wet adhesive property of the SiW-PEG coacervate suggests its great potential applications as strong tissue adhesives and in hemostasis, and its hemostatic ability was investigated using a mouse liver bleeding model. The innate antibacterial property of the coacervate was also demonstrated, which was endowed by SiW, a typical representative of the next-generation metallodrugs polyoxometalates.

Chapter 3 introduces an instant underwater adhesive derived from coacervation via one-step mixing of SiW and P123 aqueous solutions driven by hydrogen-bonding interaction, where hydrophobic interaction among PPG cores of P123 micelles serves as a second crosslinking to reinforce the network. Phase behavior, mechanism of intermolecular interactions, and rheological properties of SiW-P123 coacervates have been interrogated. Besides, the coacervate exhibits excellent instant underwater adhesive properties, being able to bind various substrates underwater, resist repeatable stretching and bending of the substrates, and keep stable in high salinity aqueous solutions. The coacervate shows thermo-tunable optical properties and electrochromic properties owing to thermo-responsiveness of P123 micelles and reduction-associated color change of SiW, respectively.

Chapter 4 presents an instant and repeatable underwater adhesive with innate anticancer and antibacterial properties. The underwater adhesives can be prepared by coacervation through one-step mixing of TA and F68 aqueous solutions, where the driving force is hydrogen-bonding interaction while hydrophobic interaction among PPG cores of F68 micelles serves as a second crosslinking to strengthen the network. Phase behavior, mechanism of intermolecular interactions, and rheological properties of TA-F68 coacervates have been studied. The as-prepared coacervate shows robust instant underwater adhesion on diverse substrates and possesses repeatable underwater adhesion which can be further enhanced by mechanical training. The innate anticancer and antibacterial properties of the coacervates are conferred by TA, a well-known polyphenol.

Chapter 5 summarizes the major conclusions and contributions of this work, with suggestions for future research work.

References

1. Sing, C. E.; Perry, S. L. Recent progress in the science of complex coacervation. *Soft Matter* **2020,** *16*, 2885-2914.

2. Shin, Y.; Brangwynne, C. P. Liquid phase condensation in cell physiology and disease. *Science* **2017,** *357*, eaaf4382.

3. Holehouse, A. S., Pappu, R. V. Protein polymers: Encoding phase transitions. *Nat. Mater.* **2015,** *14*, 1083-1084.

4. Hyman, A. A.; Weber, C. A.; Julicher, F. Liquid-liquid phase separation in biology. *Annu. Rev. Cell Dev. Biol.* **2014,** *30*, 39-58.

5. Keating, C. D. Aqueous phase separation as a possible route to compartmentalization of biological molecules. *Acc. Chem. Res.* **2012,** *45*, 2114-2124.

6. de Jong, H. G. B. Die Koazervation und ihre Bedeutung für die Biologie. *Protoplasm* **1932,** *15*, 110-173.

7. Koga, S.; Williams, D. S.; Perriman, A. W.; Mann, S. Peptide-nucleotide microdroplets as a step towards a membrane-free protocell model. *Nat. Chem.* **2011,** *3*, 720-724.

8. Schuster, B. S.; Reed, E. H.; Parthasarathy, R.; Jahnke, C. N.; Caldwell, R. M.; Bermudez, J. G.; Ramage, H.; Good, M. C.; Hammer, D. A. Controllable protein phase separation and modular recruitment to form responsive membraneless organelles. *Nat. Commun.* **2018,** *9*, 2985.

9. Okihana, H.; Ponnamperuma, C. A protective function of the coacervates against UV light on the primitive Earth. *Nature* **1982,** *299*, 347–349.

10. Yeo, G. C.; Keeley, F. W.; Weiss, A. S. Coacervation of tropoelastin. *Adv. Colloid Interface Sci.* **2011,** *167*, 94-103.

11. Tan, Y.; Hoon, S.; Guerette, P. A.; Wei, W.; Ghadban, A.; Hao, C.; Miserez, A.; Waite, J. H. Infiltration of chitin by protein coacervates defines the squid beak mechanical gradient. *Nat. Chem. Biol.* **2015,** *11*, 488-495.

12. Miserez, A.; Schneberk, T.; Sun, C.; Zok, F. W.; Waite, J. H. The transition from stiff to compliant materials in squid beaks. *Science* **2008,** *319*, 1816-1819.

13. Ambadipudi, S.; Biernat, J.; Riedel, D.; Mandelkow, E.; Zweckstetter, M. Liquid-liquid phase separation of the microtubule-binding repeats of the Alzheimer-related protein Tau. *Nat. Commun.* **2017,** *8*, 275.

14. Stewart, R. J.; Weaver, J. C.; Morse, D. E.; Waite, J. H. The tube cement of Phragmatopoma californica: a solid foam. *J. Exp. Biol.* **2004,** *207*, 4727-4734.

15. Zhao, H.; Sun, C.; Stewart, R. J.; Waite, J. H. Cement proteins of the tube-building polychaete Phragmatopoma californica. *J Biol Chem* **2005,** *280*, 42938-42944.

16. Stewart, R. J.; Wang, C. S.; Shao, H. Complex coacervates as a foundation for synthetic underwater adhesives. *Adv. Colloid Interface Sci.* **2011,** *167*, 85-93.

17. Hofman, A. H.; van Hees, I. A.; Yang, J.; Kamperman, M. Bioinspired underwater adhesives by using the supramolecular toolbox. *Adv. Mater.* **2018,** *30*, 1704640.

18. Muhoza, B.; Xia, S.; Wang, X.; Zhang, X.; Li, Y.; Zhang, S. Microencapsulation of essential oils by complex coacervation method: preparation, thermal stability, release properties and applications. *Crit. Rev. Food Sci. Nutr.* **2020**, 1-20.

19. Llamas, S.; Guzman, E.; Ortega, F.; Baghdadli, N.; Cazeneuve, C.; Rubio, R. G.; Luengo, G. S. Adsorption of polyelectrolytes and polyelectrolytes-surfactant mixtures at surfaces: a physico-chemical approach to a cosmetic challenge. *Adv. Colloid Interface Sci.* **2015,** *222*, 461-487.

20. Xu, Y.; Mazzawi, M.; Chen, K.; Sun, L.; Dubin, P. L. Protein purification by polyelectrolyte coacervation: influence of protein charge anisotropy on selectivity. *Biomacromolecules* **2011,** *12*, 1512-1522.

21. Sinclair, S. M.; Bhattacharyya, J.; McDaniel, J. R.; Gooden, D. M.; Gopalaswamy, R.; Chilkoti, A.; Setton, L. A. A genetically engineered thermally responsive sustained release curcumin depot to treat neuroinflammation. *J. Controlled Release* **2013,** *171*, 38-47.

22. McDaniel, J. R.; Callahan, D. J.; Chilkoti, A. Drug delivery to solid tumors by elastin-like polypeptides. *Adv. Drug Deliv. Rev.* **2010,** *62*, 1456-1467.

23. Chenglong, W.; Shuhan, X.; Jiayi, Y.; Wencai, G.; Guoxiong, X.; Hongjing, D. Dextran-based coacervate nanodroplets as potential gene carriers for efficient cancer therapy. *Carbohydr. Polym.* **2020,** *231*, 115687.

24. Zhang, Z.; Liu, Q.; Sun, Z.; Phillips, B. K.; Wang, Z.; Al-Hashimi, M.; Fang, L.; Olson, M. A. Poly-lipoic ester-based coacervates for the efficient removal of organic pollutants from water and increased point-of-use versatility. *Chem. Mater.* **2019,** *31*, 4405-4417.

25. Chilivery, R.; Begum, G.; Chaitanya, V.; Rana, R. K. Tunable surface wrinkling by a bio-inspired polyamine anion coacervation process that mediates the assembly of polyoxometalate nanoclusters. *Angew. Chem. Int. Ed.* **2020,** *59*, 8160-8165.

26. Liu, J.; Tian, L.; Qiao, Y.; Zhou, S.; Patil, A.; Wang, K.; Li, M.; Mann, S. Hydrogel-immobilized coacervate droplets as modular micro-reactor assemblies. *Angew. Chem. Int. Ed.* **2020,** *59*, 6853-6859.

27. Lv, K.; Perriman, A. W.; Mann, S. Photocatalytic multiphase micro-droplet reactors based on complex coacervation. *Chem. Commun.* **2015,** *51*, 8600-8602.

28. Jehle, F.; Macias-Sanchez, E.; Fratzl, P.; Bertinetti, L.; Harrington, M. J. Hierarchically-structured metalloprotein composite coatings biofabricated from co-existing condensed liquid phases. *Nat. Commun.* **2020,** *11*, 862.

29. Jones, J. P.; Sima, M.; O'Hara, R. G.; Stewart, R. J. Water-borne endovascular embolics inspired by the undersea adhesive of marine sandcastle worms. *Adv. Healthcare Mater.* **2016,** *5*, 795-801.

30. Tjaden Modderman, R. S.; Holleman, L. W. J. Coacervation. *Nature* **1932,** *129*, 654.

31. Dubin, P.; Perry, S.; Xu, Y. Foreword. *Adv Colloid Interface Sci* **2017,** *239*, 1.

32. Dubin, P. L.; Kayitmazer, A. B.; Huang, Q. Polyelectrolyte-macroion coacervation. Foreword. *Adv Colloid Interface Sci* **2011,** *167*, 1.

33. Veis, A. A review of the early development of the thermodynamics of the complex coacervation phase separation. *Adv. Colloid Interface Sci.* **2011,** *167*, 2-11.

34. Kayitmazer, A. B. Thermodynamics of complex coacervation. *Adv. Colloid Interface Sci.* **2017,** *239*, 169-177.

35. Sing, C. E. Development of the modern theory of polymeric complex coacervation. *Adv. Colloid Interface Sci.* **2017,** *239*, 2-16.

36. Xiao, J.; Li, Y.; Huang, Q. Application of Monte Carlo simulation in addressing key issues of complex coacervation formed by polyelectrolytes and oppositely charged colloids. *Adv. Colloid Interface Sci.* **2017,** *239*, 31-45.

37. Jho, Y.; Yoo, H. Y.; Lin, Y.; Han, S.; Hwang, D. S. Molecular and structural basis of low interfacial energy of complex coacervates in water. *Adv. Colloid Interface Sci.* **2017,** *239*, 61-73.

38. Liu, Y.; Winter, H. H.; Perry, S. L. Linear viscoelasticity of complex coacervates. *Adv. Colloid Interface Sci.* **2017,** *239*, 46-60.

39. Uversky, V. N. Protein intrinsic disorder-based liquid-liquid phase transitions in biological systems: Complex coacervates and membrane-less organelles. *Adv Colloid Interface Sci* **2017,** *239*, 97-114.

40. Muiznieks, L. D.; Keeley, F. W. Biomechanical Design of Elastic Protein Biomaterials: A Balance of Protein Structure and Conformational Disorder. *ACS Biomater. Sci. Eng.* **2016,** *3*, 661-679.

41. Wise, S. G.; Yeo, G. C.; Hiob, M. A.; Rnjak-Kovacina, J.; Kaplan, D. L.; Ng, M. K.; Weiss, A. S. Tropoelastin: a versatile, bioactive assembly module. *Acta Biomater.* **2014,** *10*, 1532-1541.

42. Mithieux, S. M.; Wise, S. G.; Weiss, A. S. Tropoelastin-a multifaceted naturally smart material. *Adv. Drug Deliv. Rev.* **2013,** *65*, 421-428.

43. Stewart, R. J.; Wang, C. S.; Song, I. T.; Jones, J. P. The role of coacervation and phase transitions in the sandcastle worm adhesive system. *Adv. Colloid Interface Sci.* **2017,** *239*, 88-96.

44. Park, S.; Kim, S.; Jho, Y.; Hwang, D. S. Cation-pi interactions and their contribution to mussel underwater adhesion studied using a surface forces apparatus: A Mini-Review. *Langmuir* **2019,** *35*, 16002-16012.

45. Schmitt, C.; Turgeon, S. L. Protein/polysaccharide complexes and coacervates in food systems. *Adv. Colloid Interface Sci.* **2011,** *167*, 63-70.

46. Blocher, W. C.; Perry, S. L. Complex coacervate-based materials for biomedicine. *Wiley Interdiscip. Rev. Nanomed. Nanobiotechnol.* **2017,** *9*, 1442.

47. Devi, N.; Sarmah, M.; Khatun, B.; Maji, T. K. Encapsulation of active ingredients in polysaccharide-protein complex coacervates. *Adv. Colloid Interface Sci.* **2017,** *239*, 136-145.

48. Kizilay, E.; Kayitmazer, A. B.; Dubin, P. L. Complexation and coacervation of polyelectrolytes with oppositely charged colloids. *Adv. Colloid Interface Sci.* **2011,** *167*, 24-37.

49. Cini, N.; Ball, V. Polyphosphates as inorganic polyelectrolytes interacting with oppositely charged ions, polymers and deposited on surfaces: fundamentals and applications. *Adv. Colloid Interface Sci.* **2014,** *209*, 84-97.

50. Berret, J. F. Controlling electrostatic co-assembly using ion-containing copolymers: from surfactants to nanoparticles. *Adv. Colloid Interface Sci.* **2011,** *167*, 38-48.

51. Wang, M.; Wang, Y. Development of surfactant coacervation in aqueous solution. *Soft Matter* **2014,** *10*, 7909-7919.

52. Guzman, E.; Llamas, S.; Maestro, A.; Fernandez-Pena, L.; Akanno, A.; Miller, R.; Ortega, F.; Rubio, R. G. Polymer-surfactant systems in bulk and at fluid interfaces. *Adv. Colloid Interface Sci.* **2016,** *233*, 38-64.

53. Miyake, M. Recent progress of the characterization of oppositely charged polymer/surfactant complex in dilution deposition system. *Adv. Colloid Interface Sci.* **2017,** *239*, 146-157.

54. Zhao, W.; Wang, Y. Coacervation with surfactants: From single-chain surfactants to gemini surfactants. *Adv. Colloid Interface Sci.* **2017,** *239*, 199-212.

55. Voets, I. K.; de Keizer, A.; Cohen Stuart, M. A. Complex coacervate core micelles. *Adv. Colloid Interface Sci.* **2009,** *147-148*, 300-318.

56. Myakonkaya, O.; Eastoe, J. Low energy methods of phase separation in colloidal dispersions and microemulsions. *Adv. Colloid Interface Sci.* **2009,** *149*, 39-46.

57. Tiwary, A. K.; Zheng, Y. Protein phase separation in mitosis. *Curr. Opin. Cell Biol.* **2019,** *60*, 92-98.

58. Banani, S. F.; Lee, H. O.; Hyman, A. A.; Rosen, M. K. Biomolecular condensates: organizers of cellular biochemistry. *Nat. Rev. Mol. Cell Biol.* **2017,** *18*, 285-298.

59. Zhou, L.; Shi, H.; Li, Z.; He, C. Recent advances in complex coacervation design from macromolecular assemblies and emerging applications. *Macromol. Rapid Commun.* **2020,** *41*, 2000149.

60. Raghavan, S. R.; Edlund, H.; Kaler, E. W. Cloud-point phenomena in wormlike micellar systems containing cationic surfactant and salt. *Langmuir* **2002,** *18*, 1056–1064.

61. Purkait, M. K.; Vijay, S. S.; DasGupta, S.; De, S. Separation of congo red by surfactant mediated cloud point extraction. *Dyes Pigm.* **2004,** *63*, 151-159.

62. Purkait, M. K.; Banerjee, S.; Mewara, S.; DasGupta, S.; De, S. Cloud point extraction of toxic eosin dye using Triton X-100 as nonionic surfactant. *Water Res.* **2005,** *39*, 3885-3890.

63. Betre, H.; Ong, S. R.; Guilak, F.; Chilkoti, A.; Fermor, B.; Setton, L. A. Chondrocytic differentiation of human adipose-derived adult stem cells in elastin-like polypeptide. *Biomaterials* **2006,** *27*, 91-99.

64. Maeda, T.; Takenouchi, M.; Yamamoto, K.; Aoyagi, T. Analysis of the formation mechanism for thermoresponsive-type coacervate with functional copolymers consisting of N-Isopropylacrylamide and 2-Hydroxyisopropylacrylamide. *Biomacromolecules* **2006,** *7*, 2230-2236.

65. Cirulis, J. T.; Bellingham, C. M.; Davis, E. C.; Hubmacher, D.; Reinhardt, D. P.; Mecham, R. P.; Keeley, F. W. Fibrillins, fibulins, and matrix-associated glycoprotein modulate the kinetics and morphology of in vitro self-assembly of a recombinant elastin-like polypeptide. *Biochemistry* **2008,** *47*, 12601–12613.

66. Cirulis, J. T.; Keeley, F. W. Kinetics and morphology of self-assembly of an elastin-like polypeptide based on the alternating domain arrangement of human tropoelastin. *Biochemistry* **2010,** *49*, 5726-5733.

67. Wasilewski, T. Coacervates as a modern delivery system of hand dishwashing liquids. *J. Surfactants Deterg.* **2010,** *13*, 513-520.

68. Wasilewski, T.; Bujak, T. Effect of the type of nonionic surfactant on the manufacture and properties of hand dishwashing liquids in the coacervate form. *Ind. Eng. Chem. Res.* **2014,** *53*, 13356-13361.

69. Seweryn, A.; Wasilewski, T.; Bujak, T. Effect of salt on the manufacturing and properties of hand dishwashing liquids in the coacervate form. *Ind. Eng. Chem. Res.* **2016,** *55*, 1134-1141.

70. Ferreira, L. A.; Teixeira, J. A. Salt effect on the aqueous two-phase system PEG 8000-sodium sulfate. *J. Chem. Eng. Data* **2011,** *56*, 133-137.

71. Yang, G.; Wong, M. K.; Lin, L. E.; Yip, C. M. Nucleation and growth of elastin-like peptide fibril multilayers: an in situ atomic force microscopy study. *Nanotechnology* **2011,** *22*, 494018.

72. He, D.; Miao, M.; Sitarz, E. E.; Muiznieks, L. D.; Reichheld, S.; Stahl, R. J.; Keeley, F. W.; Parkinson, J. Polymorphisms in the human tropoelastin gene modify in vitro self-assembly and mechanical properties of elastin-like polypeptides. *PLoS One* **2012,** *7*, e46130.

73. Ilevbare, G. A.; Taylor, L. S. Liquid-liquid phase separation in highly supersaturated aqueous solutions of poorly water-soluble drugs: Implications for solubility enhancing formulations. *Cryst. Growth Des.* **2013,** *13*, 1497-1509.

74. Miao, M.; Reichheld, S. E.; Muiznieks, L. D.; Huang, Y.; Keeley, F. W. Elastin binding protein and FKBP65 modulate in vitro self-assembly of human tropoelastin. *Biochemistry* **2013,** *52*, 7731-7741.

75. Sokolova, E.; Spruijt, E.; Hansen, M. M.; Dubuc, E.; Groen, J.; Chokkalingam, V.; Piruska, A.; Heus, H. A.; Huck, W. T. Enhanced transcription rates in membrane-free protocells formed by coacervation of cell lysate. *Proc. Natl. Acad. Sci. U.S.A.* **2013,** *110*, 11692-11697.

76. Muiznieks, L. D.; Cirulis, J. T.; van der Horst, A.; Reinhardt, D. P.; Wuite, G. J.; Pomes, R.; Keeley, F. W. Modulated growth, stability and interactions of liquid-like coacervate assemblies of elastin. *Matrix Biol.* **2014,** *36*, 39-50.

77. Wei, W.; Tan, Y.; Martinez Rodriguez, N. R.; Yu, J.; Israelachvili, J. N.; Waite, J. H. A mussel-derived one component adhesive coacervate. *Acta Biomater.* **2014,** *10*, 1663-1670.

78. Ahn, B. K.; Das, S.; Linstadt, R.; Kaufman, Y.; Martinez-Rodriguez, N. R.; Mirshafian, R.; Kesselman, E.; Talmon, Y.; Lipshutz, B. H.; Israelachvili, J. N.; Waite, J. H. High-performance mussel-inspired adhesives of reduced complexity. *Nat. Commun.* **2015,** *6*, 8663.

79. Dandurand, J.; Samouillan, V.; Lacabanne, C.; Pepe, A.; Bochicchio, B. Water structure and elastin-like peptide aggregation. *J. Therm. Anal. Calorim.* **2015,** *120*, 419-426.

80. Elbaum-Garfinkle, S.; Kim, Y.; Szczepaniak, K.; Chen, C. C.; Eckmann, C. R.; Myong, S.; Brangwynne, C. P. The disordered P granule protein LAF-1 drives phase separation into droplets with tunable viscosity and dynamics. *Proc. Natl. Acad. Sci. U.S.A.* **2015,** *112*, 7189-7194.

81. Jiang, H.; Wang, S.; Huang, Y.; He, X.; Cui, H.; Zhu, X.; Zheng, Y. Phase transition of spindle-associated protein regulate spindle apparatus assembly. *Cell* **2015,** *163*, 108-122.

82. Nott, T. J.; Petsalaki, E.; Farber, P.; Jervis, D.; Fussner, E.; Plochowietz, A.; Craggs, T. D.; Bazett-Jones, D. P.; Pawson, T.; Forman-Kay, J. D.; Baldwin, A. J. Phase transition of a disordered nuage protein generates environmentally responsive membraneless organelles. *Mol. Cell* **2015,** *57*, 936-947.

83. Navon, Y.; Zhou, M.; Matson, J. B.; Bitton, R. Dendritic Elastin-like Peptides: The effect of branching on thermoresponsiveness. *Biomacromolecules* **2016,** *17*, 262-270.

84. Suyama, K.; Taniguchi, S.; Tatsubo, D.; Maeda, I.; Nose, T. Dimerization effects on coacervation property of an elastin-derived synthetic peptide $(FPGVG)_5$. *J. Pept. Sci.* **2016,** *22*, 236-243.

85. Cai, H.; Gabryelczyk, B.; Manimekalai, M. S. S.; Gruber, G.; Salentinig, S.; Miserez, A. Self-coacervation of modular squid beak proteins-a comparative study. *Soft Matter* **2017,** *13*, 7740-7752.

86. Annabi, N.; Zhang, Y.; Assmann, A.; Sani, E. S.; Cheng, G.; Lassaletta, A. D.; Vegh, A.; Dehghani, B.; Ruiz-Esparza, G. U.; Wang, X.; Gangadharan, S.; Weiss, A. S.; Khademhosseini, A. Engineering a highly elastic human protein-based sealant for surgical applications. *Sci. Transl. Med.* **2017,** *9*, eaai7466.

87. Reichheld, S. E.; Muiznieks, L. D.; Keeley, F. W.; Sharpe, S. Direct observation of structure and dynamics during phase separation of an elastomeric protein. *Proc. Natl. Acad. Sci. U.S.A.* **2017,** *114*, E4408-E4415.

88. Simon, J. R.; Carroll, N. J.; Rubinstein, M.; Chilkoti, A.; Lopez, G. P. Programming molecular self-assembly of intrinsically disordered proteins containing sequences of low complexity. *Nat. Chem.* **2017,** *9*, 509-515.

89. Franzmann, T. M.; Jahnel, M.; Pozniakovsky, A.; Mahamid, J.; Holehouse, A. S.; Nuske, E.; Richter, D.; Baumeister, W.; Grill, S. W.; Pappu, R. V.; Hyman, A. A.; Alberti, S. Phase separation of a yeast prion protein promotes cellular fitness. *Science* **2018,** *359*, eaao5654.

90. Mohammadi, P.; Aranko, A. S.; Lemetti, L.; Cenev, Z.; Zhou, Q.; Virtanen, S.; Landowski, C. P.; Penttila, M.; Fischer, W. J.; Wagermaier, W.; Linder, M. B. Phase transitions as intermediate steps in the formation of molecularly engineered protein fibers. *Commun. Biol.* **2018,** *1*, 86.

91.Tatsubo, D.; Suyama, K.; Miyazaki, M.; Maeda, I.; Nose, T. Stepwise mechanism of temperature-dependent coacervation of the elastin-like peptide analogue dimer, (C(WPGVG)3)2. *Biochemistry* **2018,** *57*, 1582-1590.

92. Gabryelczyk, B.; Cai, H.; Shi, X.; Sun, Y.; Swinkels, P. J. M.; Salentinig, S.; Pervushin, K.; Miserez, A. Hydrogen bond guidance and aromatic stacking drive liquid-liquid phase separation of intrinsically disordered histidine-rich peptides. *Nat. Commun.* **2019,** *10*, 5465.

93. Gourgas, O.; Cole, G. B.; Muiznieks, L. D.; Sharpe, S.; Cerruti, M. Effect of the ionic concentration of simulated body fluid on the minerals formed on cross-linked elastin-like polypeptide membranes. *Langmuir* **2019,** *35*, 15364-15375.

94. Gourgas, O.; Muiznieks, L. D.; Bello, D. G.; Nanci, A.; Sharpe, S.; Cerruti, M. Cross-linked elastin-like polypeptide membranes as a model for medial arterial calcification. *Biomacromolecules* **2019,** *20*, 2625-2636.

95. Ianiro, A.; Wu, H.; van Rijt, M. M. J.; Vena, M. P.; Keizer, A. D. A.; Esteves, A. C. C.; Tuinier, R.; Friedrich, H.; Sommerdijk, N.; Patterson, J. P. Liquid-liquid phase separation during amphiphilic self-assembly. *Nat. Chem.* **2019,** *11*, 320-328.

96. Rizvi, A.; Patel, U.; Ianiro, A.; Hurst, P. J.; Merham, J. G.; Patterson, J. P. Nonionic block copolymer coacervates. *Macromolecules* **2020,** *53*, 6078-6086.

97. Chen, N.; Zhao, Z.; Wang, Y.; Dimova, R. Resolving the mechanisms of soy glycinin self-coacervation and hollow-condensate formation. *ACS Macro Lett.* **2020,** *9*, 1844-1852.

98. Liu, B.; Fan, Y.; Li, H.; Zhao, W.; Luo, S.; Wang, H.; Guan, B.; Li, Q.; Yue, J.; Dong, Z.; Wang, Y.; Jiang, L. Control the entire journey of pesticide application on superhydrophobic plant surface by dynamic covalent trimeric surfactant coacervation. *Adv. Funct. Mater.* **2020,** *31*, 2006606.

99. Madinya, J. J.; Chang, L.-W.; Perry, S. L.; Sing, C. E. Sequence-dependent self-coacervation in high charge-density polyampholytes. *Mol. Syst. Des. Eng.* **2020,** *5*, 632-644.

100. Mohammadi, P.; Jonkergouw, C.; Beaune, G.; Engelhardt, P.; Kamada, A.; Timonen, J. V. I.; Knowles, T. P. J.; Penttila, M.; Linder, M. B. Controllable coacervation of recombinantly produced spider silk protein using kosmotropic salts. *J. Colloid Interface Sci.* **2020,** *560*, 149-160.

101. Reed, E. H.; Schuster, B. S.; Good, M. C.; Hammer, D. A. SPLIT: stable protein coacervation using a light induced transition. *ACS Synth. Biol.* **2020,** *9*, 500-507.

102. Zhang, P.; Gourgas, O.; Lainé, A.; Murshed, M.; Mantovani, D.; Cerruti, M. Coacervation conditions and cross-linking determines availability of carbonyl groups on elastin and its calcification. *Cryst. Growth Des.* **2020,** *20*, 7170-7179.

103. Pei, Y.; Zheng, Y.; Li, Z.; Liu, J.; Zheng, X.; Tang, K.; Kaplan, D. L. Ethanol-induced coacervation in aqueous gelatin solution for constructing nanospheres and networks: Morphology, dynamics and thermal sensitivity. *J. Colloid Interface Sci.* **2021,** *582*, 610-618.

104. Rowland, A. T.; Cacace, D. N.; Pulati, N.; Gulley, M. L.; Keating, C. D. Bioinspired mineralizing microenvironments generated by liquid-liquid phase coexistence. *Chem. Mater.* **2019,** *31*, 10243-10255.

105. Kim, S.; Huang, J.; Lee, Y.; Dutta, S.; Yoo, H. Y.; Jung, Y. M.; Jho, Y.; Zeng, H.; Hwang, D. S. Complexation and coacervation of like-charged polyelectrolytes inspired by mussels. *Proc. Natl. Acad. Sci. U.S.A.* **2016,** *113*, E847-E853.

106. Hwang, D. S.; Zeng, H.; Srivastava, A.; Krogstad, D. V.; Tirrell, M.; Israelachvili, J. N.; Waite, J. H. Viscosity and interfacial properties in a mussel-inspired adhesive coacervate. *Soft Matter* **2010,** *6*, 3232-3236.

107. Zheng, J.; Tang, C. H.; Sun, W. Heteroprotein complex coacervation: Focus on experimental strategies to investigate structure formation as a function of intrinsic and external physicochemical parameters for food applications. *Adv. Colloid Interface Sci.* **2020,** *284*, 102268.

108. Ducker, W. A.; Senden, T. J.; Pashley, R. M. Measurement of forces in liquids using a force microscope. *Langmuir* **1992,** *8*, 1831-1836.

109. Ducker, W. A.; Senden, T. J.; Pashley, R. M. Direct measurement of colloidal forces using an atomic force microscope. *Nature* **1991,** 353, 239–241.

110. Butt, H. J.; Cappella, B.; Kappl, M. Force measurements with the atomic force microscope: Technique, interpretation and applications. *Surf. Sci. Rep.* **2005,** *59*, 1-152.

111. Lu, Q.; Oh, D. X.; Lee, Y.; Jho, Y.; Hwang, D. S.; Zeng, H. Nanomechanics of cation-pi interactions in aqueous solution. *Angew. Chem. Int. Ed.* **2013,** *52*, 3944-3948.

112. Sprakel, J.; Besseling, N. A.; Leermakers, F. A.; Cohen Stuart, M. A. Equilibrium capillary forces with atomic force microscopy. *Phys. Rev. Lett.* **2007,** *99*, 104504.

113. Spruijt, E.; Sprakel, J.; Cohen Stuart, M. A.; van der Gucht, J. Interfacial tension between a complex coacervate phase and its coexisting aqueous phase. *Soft Matter* **2010,** *6*, 172-178.

114. Lim, S.; Moon, D.; Kim, H. J.; Seo, J. H.; Kang, I. S.; Cha, H. J. Interfacial tension of complex coacervated mussel adhesive protein according to the Hofmeister series. *Langmuir* **2014,** *30*, 1108-1115.

115. Priftis, D.; Farina, R.; Tirrell, M. Interfacial energy of polypeptide complex coacervates measured via capillary adhesion. *Langmuir* **2012,** *28*, 8721-8729.

116. Kim, S.; Faghihnejad, A.; Lee, Y.; Jho, Y.; Zeng, H.; Hwang, D. S. Cation-pi interaction in DOPA-deficient mussel adhesive protein mfp-1. *J. Mater. Chem. B* **2015,** *3*, 738-743.

117. Kim, S.; Yoo, H. Y.; Huang, J.; Lee, Y.; Park, S.; Park, Y.; Jin, S.; Jung, Y. M.; Zeng, H. Hwang, D. S.; Jho, Y. Salt triggers the simple coacervation of an underwater adhesive when cations meet aromatic pi electrons in seawater. *ACS Nano* **2017,** *11*, 6764-6772.

118. Israelachvili, J. N. Intermolecular and surface forces. **2011**.

119. Desiraju, G. R. Chemistry beyond the molecule. *Nature* **2001,** *412*, 397–400.

120. Yang, L.; Tan, X.; Wang, Z.; Zhang, X. Supramolecular polymers: Historical development, preparation, characterization, and functions. *Chem. Rev.* **2015,** *115*, 7196-239.

121. Lee, B. P.; Messersmith, P. B.; Israelachvili, J. N.; Waite, J. H. Mussel-inspired adhesives and coatings. *Annu. Rev. Mater. Res.* **2011,** *41*, 99-132.

122. Waite, J. H.; Andersen, N. H.; Jewhurst, S.; Sun, C. Mussel adhesion: Finding the tricks worth mimicking. *J. Adhes.* **2005,** *81*, 297-317.

123. Hinterdorfer, P.; Dufrene, Y. F. Detection and localization of single molecular recognition events using atomic force microscopy. *Nat. Methods* **2006,** *3*, 347-355.

124. Peng, Q.; Chen, J.; Zeng, Z.; Wang, T.; Xiang, L.; Peng, X.; Liu, J.; Zeng, H. Adhesive coacervates driven by hydrogen-bonding interaction. *Small* **2020,** 16, 2004132.

125. Priftis, D.; Megley, K.; Laugel, N.; Tirrell, M. Complex coacervation of poly(ethylene-imine)/polypeptide aqueous solutions: thermodynamic and rheological characterization. *J. Colloid. Interface. Sci.* **2013,** *398*, 39-50.

126. Momeni, A.; Filiaggi, M. J. Rheology of polyphosphate coacervates. *J. Rheol.* **2016,** *60*, 25-34.

127. Liberatore, M. W.; Wyatt, N. B.; Henry, M.; Dubin, P. L.; Foun, E. Shear-induced phase separation in polyelectrolyte/mixed micelle coacervates. *Langmuir* **2009,** *25*, 13376-13383.

128. Xu, M.; Lewis, J. A. Phase behavior and rheological properties of polyamine-rich complexes for direct-write assembly. *Langmuir* **2007,** *23*, 12752–12759.

129. Wang, Q.; Schlenoff, J. B. The polyelectrolyte complex/coacervate continuum. *Macromolecules* **2014,** *47*, 3108-3116.

130. Spruijt, E.; Cohen Stuart, M. A.; van der Gucht, J. Linear viscoelasticity of polyelectrolyte complex coacervates. *Macromolecules* **2013,** *46*, 1633-1641.

131. Jing, B.; Xu, D.; Wang, X.; Zhu, Y. Multiresponsive, critical gel behaviors of polyzwitterion-polyoxometalate coacervate complexes. *Macromolecules* **2018,** *51*, 9405-9411.

132. Priftis, D.; Laugel, N.; Tirrell, M. Thermodynamic characterization of polypeptide complex coacervation. *Langmuir* **2012,** *28*, 15947-15957.

133. Kim, K.; Shin, M.; Koh, M.-Y.; Ryu, J. H.; Lee, M. S.; Hong, S.; Lee, H. TAPE: A medical adhesive inspired by a ubiquitous compound in plants. *Adv. Funct. Mater.* **2015,** *25*, 2402-2410.

134. Xu, J.; Li, X.; Li, J.; Li, X.; Li, B.; Wang, Y.; Wu, L.; Li, W. Wet and functional adhesives from one-step aqueous self-assembly of natural amino acids and polyoxometalates. *Angew. Chem. Int. Ed.* **2017,** *56*, 8731-8735.

135. Inostroza-Brito, K. E.; Collin, E.; Siton-Mendelson, O.; Smith, K. H.; Monge-Marcet, A.; Ferreira, D. S.; Rodriguez, R. P.; Alonso, M.; Rodriguez-Cabello, J. C.; Reis, R. L.; Sagues, F.; Botto, L.; Bitton, R.; Azevedo, H. S.; Mata, A. Co-assembly, spatiotemporal control and morphogenesis of a hybrid protein-peptide system. *Nat. Chem.* **2015,** *7*, 897-904.

136. Biedermann, F.; Schneider, H. J. Experimental binding energies in supramolecular complexes. *Chem. Rev.* **2016,** *116*, 5216-5300.

137. Ozsvar, J.; Mithieux, S. M.; Wang, R.; Weiss, A. S. Elastin-based biomaterials and mesenchymal stem cells. *Biomater. Sci.* **2015,** *3*, 800-809.

138. Narayanan, A.; Menefee, J. R.; Liu, Q.; Dhinojwala, A.; Joy, A. Lower critical solution temperature-driven self-coacervation of nonionic polyester underwater adhesives. *ACS Nano* **2020,** *14*, 8359-8367.

139. Fan, Y.; Wang, Y. Self-assembly and functions of star-shaped oligomeric surfactants. *Langmuir* **2018,** *34*, 11220-11241.

140. Danino, D.; Talmon, Y.; Levy, H.; Beinert, G.; Zana, R. Branched threadlike micelles in an aqueous solution of a trimeric surfactant. *Science* **1995,** *269*, 1420-1421.

141. Chollakup, R.; Smitthipong, W.; Eisenbach, C. D.; Tirrell, M. Phase behavior and coacervation of aqueous poly(acrylic acid)-poly(allylamine) solutions. *Macromolecules* **2010,** *43*, 2518-2528.

142. Cochereau, R.; Nicolai, T.; Chassenieux, C.; Silva, J. V. C. Mechanism of the spontaneous formation of plant protein microcapsules in aqueous solution. *Colloids Surf., A* **2019,** *562*, 213-219.

143. Zhao, H.; Zhou, X.; Wang, J.; Ma, X.; Guo, M.; Liu, D. Heat-induced hollow microcapsule formation using fava bean legumin. *Food Hydrocolloids* **2021,** *112*, 106207.

144. Yuan, D.; Yang, X.; Tang, C.; Zheng, Z.; Wei, M.; Ahmad, I.; Yin, S. Physicochemical and functional properties of acidic and basic polypeptides of soy glycinin. *Food Res. Int.* **2009,** *42*, 700-706.

145. Fan, H.; Wang, J.; Tao, Z.; Huang, J.; Rao, P.; Kurokawa, T.; Gong, J. P. Adjacent cationic-aromatic sequences yield strong electrostatic adhesion of hydrogels in seawater. *Nat. Commun.* **2019,** *10*, 5127.

146. Fasting, C.; Schalley, C. A.; Weber, M.; Seitz, O.; Hecht, S.; Koksch, B.; Dernedde, J.; Graf, C.; Knapp, E. W.; Haag, R. Multivalency as a chemical organization and action principle. *Angew. Chem. Int. Ed.* **2012,** *51*, 10472-98.

147. Badjic, J. D.; Nelson, A.; Cantrill, S. J.; Turnbull, W. B.; Stoddart, J. F. Multivalency and cooperativity in supramolecular chemistry. *Acc. Chem. Res.* **2005,** *38*, 723-732.

148. Li, P.; Banjade, S.; Cheng, H. C.; Kim, S.; Chen, B.; Guo, L.; Llaguno, M.; Hollingsworth, J. V.; King, D. S.; Banani, S. F.; Russo, P. S.; Jiang, Q. X.; Nixon, B. T.; Rosen, M. K. Phase transitions in the assembly of multivalent signalling proteins. *Nature* **2012,** *483*, 336-340.

149. Xiang, S.; Kato, M.; Wu, L. C.; Lin, Y.; Ding, M.; Zhang, Y.; Yu, Y.; McKnight, S. L. The LC Domain of hnRNPA2 adopts similar conformations in hydrogel polymers, liquid-like droplets, and nuclei. *Cell* **2015,** *163*, 829-839.

150. Zhang, J.; Jia, G.; Wanbin, Z.; Minghao, J.; Wei, Y.; Hao, J.; Liu, X.; Gan, Z.; Sun, A. Nanoencapsulation of zeaxanthin extracted from Lycium barbarum L. by complex coacervation with gelatin and CMC. *Food Hydrocolloids* **2021,** *112*, 106280.

151. Ferreira, S.; Nicoletti, V. R. Microencapsulation of ginger oil by complex coacervation using atomization: Effects of polymer ratio and wall material concentration. *J. Food Eng.* **2021,** *291*, 110214.

152. Vecchies, F.; Sacco, P.; Marsich, E.; Cinelli, G.; Lopez, F.; Donati, I. Binary solutions of hyaluronan and lactose-modified chitosan: The influence of experimental variables in assembling complex coacervates. *Polymers* **2020,** *12*, 897.

153. Tang, Y.; Scher, H. B.; Jeoh, T. Industrially scalable complex coacervation process to microencapsulate food ingredients. *Innovative Food Sci. Emerg. Technol.* **2020,** *59*, 102257.

154. Santos, M. B.; de Carvalho, C. W. P.; Garcia-Rojas, E. E. Microencapsulation of vitamin D3 by complex coacervation using carboxymethyl tara gum (Caesalpinia spinosa) and gelatin A. *Food Chem.* **2021**, *343*, 128529.

155. Kanha, N.; Surawang, S.; Pitchakarn, P.; Laokuldilok, T. Microencapsulation of copigmented anthocyanins using double emulsion followed by complex coacervation: Preparation, characterization and stability. *LWT Food Sci. Technol.* **2020,** *133*, 110154.

156. Hernández-Nava, R.; López-Malo, A.; Palou, E.; Ramírez-Corona, N.; Jiménez-Munguía, M. T. Encapsulation of oregano essential oil (Origanum vulgare) by complex coacervation between gelatin and chia mucilage and its properties after spray drying. *Food Hydrocolloids* **2020,** *109*, 106077.

157. Hernandez-Fernandez, M. A.; Garcia-Pinilla, S.; Ocampo-Salinas, O. I.; Gutierrez-Lopez, G. F.; Hernandez-Sanchez, H.; Cornejo-Mazon, M.; Perea-Flores, M. J.; Davila-Ortiz, G. Microencapsulation of vanilla oleoresin (V. planifolia Andrews) by complex coacervation and spray drying: Physicochemical and microstructural characterization. *Foods* **2020,** *9*, 1375.

158. Heckert Bastos, L. P.; Vicente, J.; Corrêa dos Santos, C. H.; Geraldo de Carvalho, M.; Garcia-Rojas, E. E. Encapsulation of black pepper (Piper nigrum L.) essential oil with gelatin and sodium alginate by complex coacervation. *Food Hydrocolloids* **2020,** *102*, 105605.

159. Gharanjig, H.; Gharanjig, K.; Hosseinnezhad, M.; Jafari, S. M. Development and optimization of complex coacervates based on zedo gum, cress seed gum and gelatin. *Int. J. Biol. Macromol.* **2020,** *148*, 31-40.

160. Furlani, F.; Donati, I.; Marsich, E.; Sacco, P. Characterization of chitosan/hyaluronan complex coacervates assembled by varying polymers weight ratio and chitosan physical-chemical composition. *Colloids Interfaces* **2020,** *4*, 12.

161. Ferreira, S.; Nicoletti, V. R. Complex coacervation assisted by a two-fluid nozzle for microencapsulation of ginger oil: Effect of atomization parameters. *Food Res. Int.* **2020,** *138* (Pt B), 109828.

162. Emamverdian, P.; Moghaddas Kia, E.; Ghanbarzadeh, B.; Ghasempour, Z. Characterization and optimization of complex coacervation between soluble fraction of Persian gum and gelatin. *Colloids Surf., A* **2020,** *607*, 125436.

163. Dai, H. H.; Li, X. D.; Wei, A. C.; Wang, X. D.; Wang, D. Y. Characterization and oxidative stability of cold-pressed sesame oil microcapsules prepared by complex coacervation. *J. Oleo Sci.* **2020,** *69*, 685-692.

164. Vecchione, D.; Grimaldi, A. M.; Forte, E.; Bevilacqua, P.; Netti, P. A.; Torino, E. Hybrid core-shell (HyCoS) nanoparticles produced by complex coacervation for multimodal applications. *Sci Rep* **2017,** *7*, 45121.

165. Cao, Y.; Fang, Y.; Nishinari, K.; Phillips, G. O. Effects of conformational ordering on protein/polyelectrolyte electrostatic complexation: ionic binding and chain stiffening. *Sci. Rep.* **2016,** *6*, 23739.

166. Kayitmazer, A. B.; Koksal, A. F.; Kilic Iyilik, E. Complex coacervation of hyaluronic acid and chitosan: effects of pH, ionic strength, charge density, chain length and the charge ratio. *Soft Matter* **2015,** *11*, 8605-8612.

167. Boral, S.; Bohidar, H. B. Effect of ionic strength on surface-selective patch binding-induced phase separation and coacervation in similarly charged gelatin-agar molecular systems. *J. Phys. Chem. B* **2010,** *114*, 12027–12035.

168. Song, J. K.; Kang, H. C.; Kim, K. S.; Chin, I.-J. Microcapsules by complex coacervation for electronic ink. *Molecular Crystals and Liquid Crystals* **2007,** *464*, 263-269.

169. Nakagawa, K.; Iwamoto, S.; Nakajima, M.; Shono, A.; Satoh, K. Microchannel emulsification using gelatin and surfactant-free coacervate microencapsulation. *J. Colloid Interface Sci.* **2004,** *278*, 198-205.

170. Vargas, S. A.; Delgado-Macuil, R. J.; Ruiz-Espinosa, H.; Rojas-Lopez, M.; Amador-Espejo, G. G. High-intensity ultrasound pretreatment influence on whey protein isolate and its use on complex coacervation with kappa carrageenan: Evaluation of selected functional properties. *Ultrason. Sonochem.* **2021,** *70*, 105340.

171. Gheonea, I.; Aprodu, I.; Cîrciumaru, A.; Râpeanu, G.; Bahrim, G. E.; Stănciuc, N. Microencapsulation of lycopene from tomatoes peels by complex coacervation and freeze-drying:

Evidences on phytochemical profile, stability and food applications. *J. Food Eng.* **2021,** *288*, 110166.

172. Zhang, Z.-K.; Xiao, J.-X.; Huang, G.-Q. Pickering emulsions stabilized by ovalbumin-sodium alginate coacervates. *Colloids Surf., A* **2020,** *595*, 124712.

173. Yücetepe, A.; Yavuz-Düzgün, M.; Şensu, E.; Bildik, F.; Demircan, E.; Özçelik, B. The impact of pH and biopolymer ratio on the complex coacervation of Spirulina platensis protein concentrate with chitosan. *Journal of Food Science and Technology* **2020**. https://doi.org/10.1007/s13197-020-04636-7

174. Yavuz-Düzgün, M.; Zeeb, B.; Dreher, J.; Özçelik, B.; Weiss, J. The impact of esterification degree and source of pectins on complex coacervation as a tool to mask the bitterness of potato protein isolates. *Food Biophysics* **2020,** *15*, 376-385.

175. Yang, S.; Li, X.; Hua, Y.; Chen, Y.; Kong, X.; Zhang, C. Selective complex coacervation of pea whey proteins with chitosan to purify main 2S albumins. *J. Agric. Food Chem.* **2020,** *68*, 1698-1706.

176. Yan, J. N.; Nie, B.; Jiang, X. Y.; Han, J. R.; Du, Y. N.; Wu, H. T. Complex coacervation of scallop (Patinopecten yessoensis) male gonad hydrolysates and kappa-carrageenan: Effect of NaCl and KCl. *Food Res. Int.* **2020,** *137*, 109659.

177. Tavares, L.; Souza, H. K. S.; Gonçalves, M. P.; Rocha, C. M. R. Physicochemical and microstructural properties of composite edible film obtained by complex coacervation between chitosan and whey protein isolate. *Food Hydrocolloids* **2021,** *113*, 106471.

178. Tavares, L.; Noreña, C. P. Z. Encapsulation of ginger essential oil using complex coacervation method: Coacervate formation, rheological property, and physicochemical characterization. *Food Bioprocess Technol.* **2020,** *13*, 1405-1420.

179. Sarkar, R.; Dutta, A.; Patra, A.; Saha, S. Bio-inspired biopolymeric coacervation for entrapment and targeted release of anthocyanin. *Cellulose* **2021,** *28*, 377–388.

180. Ocak, B. Gum arabic and collagen hydrolysate extracted from hide fleshing wastes as novel wall materials for microencapsulation of Origanum onites L. essential oil through complex coacervation. *Environ. Sci. Pollut. Res. Int.* **2020,** *27*, 42727-42737.

181. Naderi, B.; Keramat, J.; Nasirpour, A.; Aminifar, M. Complex coacervation between oak protein isolate and gum Arabic: optimization & functional characterization. *Int. J. Food Prop.* **2020,** *23*, 1854-1873.

182. Lin, Y.; Fichou, Y.; Zeng, Z.; Hu, N. Y.; Han, S. Electrostatically driven complex coacervation and amyloid aggregation of Tau are independent processes with overlapping conditions. *ACS Chem. Neurosci.* **2020,** *11*, 615-627.

183. Lan, Y.; Ohm, J.-B.; Chen, B.; Rao, J. Microencapsulation of hemp seed oil by pea protein isolate−sugar beet pectin complex coacervation: Influence of coacervation pH and wall/core ratio. *Food Hydrocolloids* **2020,** *113*, 106423.

184. Lan, Y.; Ohm, J. B.; Chen, B.; Rao, J. Phase behavior and complex coacervation of concentrated pea protein isolate-beet pectin solution. *Food Chem.* **2020,** *307*, 125536.

185. Ghadermazi, R.; Khosrowshahi Asl, A.; Tamjidi, F. Complexation and coacervation of whey protein isolate with quince seed mucilage. *J. Dispersion Sci. Technol.* **2020**, 1822862.

186. Costa, A. M. M.; Moretti, L. K.; Simões, G.; Silva, K. A.; Calado, V.; Tonon, R. V.; Torres, A. G. Microencapsulation of pomegranate (Punica granatum L.) seed oil by complex coacervation: Development of a potential functional ingredient for food application. *LWT Food Sci. Technol.* **2020,** *131*, 109519.

187. Huang, K. Y.; Yoo, H. Y.; Jho, Y.; Han, S.; Hwang, D. S. Bicontinuous fluid structure with low cohesive energy: Molecular basis for exceptionally low interfacial tension of complex coacervate fluids. *ACS Nano* **2016,** *10*, 5051-5062.

188. Niu, F.; Dong, Y.; Shen, F.; Wang, J.; Liu, Y.; Su, Y.; Xu, R.; Wang, J.; Yang, Y. Phase separation behavior and structural analysis of ovalbumin–gum arabic complex coacervation. *Food Hydrocolloids* **2015,** *43*, 1-7.

189. Ortony, J. H.; Hwang, D. S.; Franck, J. M.; Waite, J. H.; Han, S. Asymmetric collapse in biomimetic complex coacervates revealed by local polymer and water dynamics. *Biomacromolecules* **2013,** *14*, 1395-1402.

190. Hwang, D. S.; Waite, J. H.; Tirrell, M. Promotion of osteoblast proliferation on complex coacervation-based hyaluronic acid-recombinant mussel adhesive protein coatings on titanium. *Biomaterials* **2010,** *31*, 1080-1084.

191. Xia, Q.; Akanbi, T. O.; Wang, B.; Li, R.; Liu, S.; Barrow, C. J. Investigation of enhanced oxidation stability of microencapsulated enzymatically produced tuna oil concentrates using complex coacervation. *Food Funct.* **2020,** *11*, 10748-10757.

192. Wang, X.; Shi, C.; Mo, J.; Xu, Y.; Wei, W.; Zhao, J. An inorganic biopolymer polyphosphate controls positively charged protein phase transitions. *Angew. Chem. Int. Ed.* **2020,** *59*, 2679-2683.

193. Tiwari, P.; Bharti, I.; Bohidar, H. B.; Quadir, S.; Joshi, M. C.; Arfin, N. Complex coacervation and overcharging during interaction between hydrophobic zein and hydrophilic laponite in aqueous ethanol solution. *ACS Omega* **2020,** *5*, 33064–33074.

194. Ferreira, M.; Jing, B.; Lorenzana, A.; Zhu, Y. Effect of polyampholyte net charge on complex coacervation between polyampholytes and inorganic polyoxometalate giant anions. *Soft Matter* **2020,** *16*, 10280-10289.

195. Kim, H.; Jeon, B. J.; Kim, S.; Jho, Y.; Hwang, D. S. Upper critical solution temperature (UCST) behavior of coacervate of cationic protamine and multivalent anions. *Polymers* **2019,** *11*, 691.

196. Lee, Y.; Deelman, T. E.; Chen, K.; Lin, D. S. Y.; Tavakkoli, A.; Karp, J. M. Therapeutic luminal coating of the intestine. *Nat. Mater.* **2018,** *17*, 834-842.

197. Baroudi, I.; Simonnet-Jégat, C.; Roch-Marchal, C.; Leclerc-Laronze, N.; Livage, C.; Martineau, C.; Gervais, C.; Cadot, E.; Carn, F.; Fayolle, B.; Steunou, N. Supramolecular assembly of gelatin and inorganic polyanions: Fine-tuning the mechanical properties of nanocomposites by varying their composition and microstructure. *Chem.Mater.* **2015,** *27*, 1452-1464.

198. Pawar, N.; Bohidar, H. B. Anisotropic domain growth and complex coacervation in nanoclay-polyelectrolyte solutions. *Adv. Colloid Interface Sci.* **2011,** *167*, 12-23.

199. Park, S.; Barnes, R.; Lin, Y.; Jeon, B.-j.; Najafi, S.; Delaney, K. T.; Fredrickson, G. H.; Shea, J.-E.; Hwang, D. S.; Han, S. Dehydration entropy drives liquid-liquid phase separation by molecular crowding. *Commun. Chem.* **2020,** *3*, 83.

200. Mabesoone, M. F. J.; Gopez, J. D.; Paulus, I. E.; Klinger, D. Tunable biohybrid hydrogels from coacervation of hyaluronic acid and PEO-based block copolymers. *Journal of Polymer Science* **2020,** *58*, 1276-1287.

201. Love, C.; Steinkuhler, J.; Gonzales, D. T.; Yandrapalli, N.; Robinson, T.; Dimova, R.; Tang, T. D. Reversible pH-responsive coacervate formation in lipid vesicles activates dormant enzymatic reactions. *Angew. Chem. Int. Ed.* **2020,** *59*, 5950-5957.

202. Hwang, M. P.; Fecek, R. J.; Qin, T.; Storkus, W. J.; Wang, Y. Single injection of IL-12 coacervate as an effective therapy against B16-F10 melanoma in mice. *J. Controlled Release* **2020,** *318*, 270-278.

203. Huang, X.; Tian, L.; Wang, Z.; Zhang, J.; Chan, Y. S.; Cheng, S. H.; Yao, X. Bioinspired robust all-aqueous droplet via diffusion-controlled interfacial coacervation. *Adv. Funct. Mater.* **2020,** *30*, 2004166.

204. Dos Santos de Macedo, B.; de Almeida, T.; da Costa Cruz, R.; Netto, A. D. P.; da Silva, L.; Berret, J. F.; Vitorazi, L. Effect of pH on the complex coacervation and on the formation of layers of sodium alginate and PDADMAC. *Langmuir* **2020,** *36*, 2510-2523.

205. Drobot, B.; Iglesias-Artola, J. M.; Le Vay, K.; Mayr, V.; Kar, M.; Kreysing, M.; Mutschler, H.; Tang, T. D. Compartmentalised RNA catalysis in membrane-free coacervate protocells. *Nat. Commun.* **2018,** *9*, 3643.

206. Yin, Y.; Niu, L.; Zhu, X.; Zhao, M.; Zhang, Z.; Mann, S.; Liang, D. Non-equilibrium behaviour in coacervate-based protocells under electric-field-induced excitation. *Nat. Commun.* **2016,** *7*, 10658.

207. Cousin, F.; Gummel, J.; Combet, S.; Boue, F. The model Lysozyme-PSSNa system for electrostatic complexation: Similarities and differences with complex coacervation. *Adv. Colloid Interface Sci.* **2011,** *167*, 71-84.

208. Choi, S. W.; Lee, S. H.; Mok, H.; Park, T. G. Multifunctional siRNA delivery system: polyelectrolyte complex micelles of six-arm PEG conjugate of siRNA and cell penetrating peptide with crosslinked fusogenic peptide. *Biotechnol. Prog.* **2010,** *26*, 57-63.

209. Mi, X.; Blocher McTigue, W. C.; Joshi, P. U.; Bunker, M. K.; Heldt, C. L.; Perry, S. L. Thermostabilization of viruses via complex coacervation. *Biomater. Sci.* **2020,** *8*, 7082-7092.

210. Lu, T.; Spruijt, E. Multiphase complex coacervate droplets. *J. Am. Chem. Soc.* **2020,** *142*, 2905-2914.

211. Dompe, M.; Cedano-Serrano, F. J.; Vahdati, M.; Hourdet, D.; van der Gucht, J.; Kamperman, M.; Kodger, T. E. Hybrid complex coacervate. *Polymers* **2020,** *12*, 320.

212. Blocher McTigue, W. C.; Voke, E.; Chang, L. W.; Perry, S. L. The benefit of poor mixing: kinetics of coacervation. *Phys. Chem. Chem. Phys.* **2020,** *22*, 20643-20657.

213. Aramaki, K.; Shiozaki, Y.; Kosono, S.; Ikeda, N. Coacervation in cationic polyelectrolyte solutions with anionic amino acid surfactants. *J. Oleo Sci.* **2020,** *69*, 1411-1416.

214. Dompe, M.; Cedano-Serrano, F. J.; Vahdati, M.; Sidoli, U.; Heckert, O.; Synytska, A.; Hourdet, D.; Creton, C.; van der Gucht, J.; Kodger, T.; Kamperman, M. Tuning the interactions in multiresponsive complex coacervate-based underwater adhesives. *Int. J. Mol. Sci.* **2019,** *21*, 100.

215. Meng, X.; Perry, S. L.; Schiffman, J. D. Complex coacervation: Chemically stable fibers electrospun from aqueous polyelectrolyte solutions. *ACS Macro Lett.* **2017,** *6*, 505-511.

216. Liu, X.; Chapel, J. P.; Schatz, C. Structure, thermodynamic and kinetic signatures of a synthetic polyelectrolyte coacervating system. *Adv. Colloid Interface Sci.* **2017,** *239*, 178-186.

217. Chang, L. W.; Lytle, T. K.; Radhakrishna, M.; Madinya, J. J.; Velez, J.; Sing, C. E.; Perry, S. L. Sequence and entropy-based control of complex coacervates. *Nat. Commun.* **2017,** *8*, 1273.

218. Sun, Y.; Peng, C.; Wang, X.; Wang, R.; Chen, Y.; Zhang, D.; Ferreira, J. Phase behavior of polyelectrolyte complexes and rheological behavior of alumina suspensions for direct ink writing. *J. Am. Ceram. Soc.* **2016,** *99*, 1902-1910.

219. Fu, J.; Schlenoff, J. B. Driving forces for oppositely charged polyion association in aqueous solutions: Enthalpic, entropic, but not electrostatic. *J. Am. Chem. Soc.* **2016,** *138*, 980-990.

220. Semenov, S. N.; Wong, A. S.; van der Made, R. M.; Postma, S. G.; Groen, J.; van Roekel, H. W.; de Greef, T. F.; Huck, W. T. Rational design of functional and tunable oscillating enzymatic networks. *Nat. Chem.* **2015,** *7*, 160-165.

221. Perry, S.; Li, Y.; Priftis, D.; Leon, L.; Tirrell, M. The effect of salt on the complex coacervation of vinyl polyelectrolytes. *Polymers* **2014,** *6*, 1756-1772.

222. Black, K. A.; Priftis, D.; Perry, S. L.; Yip, J.; Byun, W. Y.; Tirrell, M. Protein encapsulation via polypeptide complex coacervation. *ACS Macro Lett.* **2014,** *3*, 1088-1091.

223. Tan, Y.; Yildiz, U. H.; Wei, W.; Waite, J. H.; Miserez, A. Layer-by-layer polyelectrolyte deposition: a mechanism for forming biocomposite materials. *Biomacromolecules* **2013,** *14*, 1715-1726.

224. Krogstad, D. V.; Lynd, N. A.; Choi, S.-H.; Spruell, J. M.; Hawker, C. J.; Kramer, E. J.; Tirrell, M. V. Effects of polymer and salt concentration on the structure and properties of triblock copolymer coacervate hydrogels. *Macromolecules* **2013,** *46*, 1512-1518.

225. Chollakup, R.; Beck, J. B.; Dirnberger, K.; Tirrell, M.; Eisenbach, C. D. Polyelectrolyte molecular weight and salt effects on the phase behavior and coacervation of aqueous solutions of poly(acrylic acid) sodium salt and poly(allylamine) hydrochloride. *Macromolecules* **2013,** *46*, 2376-2390.

226. Gratson, G. M.; Lewis, J. A. Phase behavior and rheological properties of polyelectrolyte inks for direct-write assembly. *Langmuir* **2005,** *21*, 457–464.

227. van der Burgh, S.; de Keizer, A.; Stuart, M. A. C. Complex coacervation core micelles. colloidal stability and aggregation mechanism. *Langmuir* **2004,** *20*, 1073-1084.

228. Gobbo, P.; Tian, L.; Pavan Kumar, B.; Turvey, S.; Cattelan, M.; Patil, A. J.; Carraro, M.; Bonchio, M.; Mann, S. Catalytic processing in ruthenium-based polyoxometalate coacervate protocells. *Nat. Commun.* **2020,** *11*, 41.

229. Facciotti, C.; Saggiomo, V.; Bunschoten, A.; Hove, J. B.; Rood, M. T. M.; Leeuwen, F. W. B.; Velders, A. H. Assembly, disassembly and reassembly of complex coacervate core micelles with redox-responsive supramolecular cross-linkers. *ChemSystemsChem* **2020,** *2*, e1900032.

230. Facciotti, C.; Saggiomo, V.; Bunschoten, A.; Fokkink, R.; Hove, J. B. T.; Wang, J.; Velders, A. H. Cyclodextrin-based complex coacervate core micelles with tuneable supramolecular host-guest, metal-to-ligand and charge interactions. *Soft Matter* **2018,** *14*, 9542-9549.

231. Qiao, Y.; Li, M.; Booth, R.; Mann, S. Predatory behaviour in synthetic protocell communities. *Nat. Chem.* **2017,** *9*, 110-119.

232. Tian, L.; Martin, N.; Bassindale, P. G.; Patil, A. J.; Li, M.; Barnes, A.; Drinkwater, B. W.; Mann, S. Spontaneous assembly of chemically encoded two-dimensional coacervate droplet arrays by acoustic wave patterning. *Nat. Commun.* **2016,** *7*, 13068.

233. Dora Tang, T. Y.; Che Hak, C.; Thompson, A. J.; Kuimova, M. K.; Williams, D. S.; Perriman, A. W.; Mann, S. Fatty acid membrane assembly on coacervate microdroplets as a step towards a hybrid protocell model. *Nat. Chem.* **2014,** *6*, 527-533.

234. Jiang, L. X.; Huang, J. B.; Bahramian, A.; Li, P. X.; Thomas, R. K.; Penfold, J. Surface behavior, aggregation and phase separation of aqueous mixtures of dodecyl trimethylammonium bromide and sodium oligoarene sulfonates: the transition to polyelectrolyte/surfactant behavior. *Langmuir* **2012,** *28*, 327-338.

235. Kizilay, E.; Maccarrone, S.; Foun, E.; Dinsmore, A. D.; Dubin, P. L. Cluster formation in polyelectrolyte-micelle complex coacervation. *J. Phys. Chem. B* **2011,** *115*, 7256-7263.

236. Kogej, K. Association and structure formation in oppositely charged polyelectrolyte-surfactant mixtures. *Adv. Colloid Interface Sci.* **2010,** *158*, 68-83.

237. Deng, M.; Cao, M.; Wang, Y. Coacervation of cationic gemini surfactant with weakly charged anionic polyacrylamide *J. Phys. Chem. B* **2009,** *113*, 9436-9440.

238. Bhattacharyya, A.; Argillier, J. Microencapsulation by complex coacervation : Effect of cationic surfactants. *J. Surface Sci. Technol.* **2005,** *21*, 161-168.

239. Anema, S. G.; de Kruif, C. G. Complex coacervates of lactotransferrin and beta-lactoglobulin. *J. Colloid Interface Sci.* **2014,** *430*, 214-220.

240. Yan, Y.; Kizilay, E.; Seeman, D.; Flanagan, S.; Dubin, P. L.; Bovetto, L.; Donato, L.; Schmitt, C. Heteroprotein complex coacervation: bovine beta-lactoglobulin and lactoferrin. *Langmuir* **2013,** *29*, 15614-15623.

241. de Kruif, C. G.; Pedersen, J.; Huppertz, T.; Anema, S. G. Coacervates of lactotransferrin and beta- or kappa-casein: structure determined using SAXS. *Langmuir* **2013,** *29*, 10483-10490.

242. Anema, S. G.; de Kruif, C. G. Coacervates of lysozyme and beta-casein. *J. Colloid Interface Sci.* **2013,** *398*, 255-261.

243. Anema, S. G.; de Kruif, C. G. Co-acervates of lactoferrin and caseins. *Soft Matter* **2012,** *8*, 4471-4478.

244. Spoelstra, W. K.; van der Sluis, E. O.; Dogterom, M.; Reese, L. Nonspherical coacervate shapes in an enzyme-driven active system. *Langmuir* **2020,** *36*, 1956–1964.

245. Aumiller Jr, W. M.; Keating, C. D. Phosphorylation-mediated RNA/peptide complex coacervation as a model for intracellular liquid organelles. *Nat. Chem.* **2016,** *8*, 129-137.

246. Liu, X.; Xie, X.; Du, Z.; Li, B.; Wu, L.; Li, W. Aqueous self-assembly of arginine and K8SiW11O39: fine-tuning the formation of a coacervate intended for sprayable anticorrosive coatings. *Soft Matter* **2019,** *15*, 9178-9186.

247. Muller, W. E. G.; Tolba, E.; Wang, S.; Neufurth, M.; Lieberwirth, I.; Ackermann, M.; Schroder, H. C.; Wang, X. Nanoparticle-directed and ionically forced polyphosphate coacervation: a versatile and reversible core-shell system for drug delivery. *Sci. Rep.* **2020,** *10*, 17147.

248. Prather, L. J.; Weerasekare, G. M.; Sima, M.; Quinn, C.; Stewart, R. J. Aqueous liquid-liquid phase separation of natural and synthetic polyguanidiniums. *Polymers* **2019,** *11*, 649.

249. Hoang, J.; Park, C. S.; Lee, H. J.; Marquez, M. D.; Zenasni, O.; Gunaratne, P. H.; Lee, T. R. Quaternary ammonium-terminated films formed from mixed bidentate adsorbates provide a high-capacity platform for oligonucleotide delivery. *ACS Appl. Mater. Interfaces* **2018,** *10*, 40890-40900.

250. Lee, S.; Lin, W.; Kuo, C.; Karakachian, M.; Lin, Y.; Yu, B.; Shyue, J. Photooxidation of amine-terminated self-assembled monolayers on gold. *J. Phys. Chem. C* **2010,** *114*, 10512-10519.

251. Lim, S.; Choi, Y. S.; Kang, D. G.; Song, Y. H.; Cha, H. J. The adhesive properties of coacervated recombinant hybrid mussel adhesive proteins. *Biomaterials* **2010,** *31*, 3715-3722.

252. Shao, H.; Stewart, R. J. Biomimetic underwater adhesives with environmentally triggered setting mechanisms. *Adv. Mater.* **2010,** *22*, 729-733.

253. Priftis, D.; Tirrell, M. Phase behaviour and complex coacervation of aqueous polypeptide solutions. *Soft Matter* **2012,** *8*, 9396-9405.

254. Pathak, J.; Priyadarshini, E.; Rawat, K.; Bohidar, H. B. Complex coacervation in charge complementary biopolymers: Electrostatic versus surface patch binding. *Adv. Colloid Interface Sci.* **2017,** *250*, 40-53.

255. Chen, J.; Wu, M.; Gong, L.; Zhang, J.; Yan, B.; Liu, J.; Zhang, H.; Thundat, T.; Zeng, H. Mechanistic understanding and nanomechanics of multiple hydrogen-bonding interactions in aqueous environment. *J. Phys. Chem. C* **2019,** *123*, 4540-4548.

256. Lee, D.; Hwang, H.; Kim, J. S.; Park, J.; Youn, D.; Kim, D.; Hahn, J.; Seo, M.; Lee, H. VATA: A poly(vinyl alcohol)- and tannic acid-based nontoxic underwater adhesive. *ACS Appl. Mater. Interfaces* **2020,** *12*, 20933-20941.

257. Jang, Y.; Hsieh, M. C.; Dautel, D.; Guo, S.; Grover, M. A.; Champion, J. A. Understanding the coacervate-to-vesicle transition of globular fusion proteins to engineer protein vesicle size and membrane heterogeneity. *Biomacromolecules* **2019,** *20*, 3494-3503.

258. Kaushik, P.; Pandey, P. K.; Aswal, V. K.; Bohidar, H. B. Ubiquity of complex coacervation of DNA and proteins in aqueous solution. *Soft Matter* **2020,** *16*, 9525-9533.

259. Xu, J.; Li, X.; Li, C.; Chen, J.; Xiao, Y. Hexafluoroisopropanol-induced salt-free catanionic surfactant coacervate extraction method for determination of fluoroquinolones in milk samples. *Food Chem.* **2018,** *242*, 122-130.

260. Last, M. G. F.; Deshpande, S.; Dekker, C. pH-Controlled coacervate-membrane interactions within liposomes. *ACS Nano* **2020,** *14*, 4487-4498.

261. Chen, G.; Dong, S.; Chen, Y.; Gao, Y.; Zhang, Z.; Li, S.; Chen, Y. Complex coacervation of zein-chitosan via atmospheric cold plasma treatment: Improvement of encapsulation efficiency and dispersion stability. *Food Hydrocolloids* **2020,** *107*, 105943.

262. Perry, S. L.; Leon, L.; Hoffmann, K. Q.; Kade, M. J.; Priftis, D.; Black, K. A.; Wong, D.; Klein, R. A.; Pierce, C. F.; Margossian, K. O.; Whitmer, J. K.; Qin, J.; de Pablo, J. J.; Tirrell, M. Chirality-selected phase behaviour in ionic polypeptide complexes. *Nat. Commun.* **2015,** *6*, 6052.

263. Wang, M.; Fan, Y.; Han, Y.; Nie, Z.; Wang, Y. Coacervation of cationic gemini surfactant with N-benzoylglutamic acid in aqueous solution. *Langmuir* **2013,** *29*, 14839-47.

264. Deng, J.; Walther, A. Programmable ATP-fueled DNA coacervates by transient liquid-liquid phase separation. *Chem* **2020,** *6*, 3329-3343.

265. Mitrea, D. M.; Cika, J. A.; Guy, C. S.; Ban, D.; Banerjee, P. R.; Stanley, C. B.; Nourse, A.; Deniz, A. A.; Kriwacki, R. W. Nucleophosmin integrates within the nucleolus via multi-modal interactions with proteins displaying R-rich linear motifs and rRNA. *Elife* **2016,** *5*, e13571.

266. Fromm, S. A.; Kamenz, J.; Noldeke, E. R.; Neu, A.; Zocher, G.; Sprangers, R. In vitro reconstitution of a cellular phase-transition process that involves the mRNA decapping machinery. *Angew. Chem. Int. Ed.* **2014,** *53*, 7354-7359.

267. Saez-Atienzar, S.; Masliah, E. Cellular senescence and Alzheimer disease: the egg and the chicken scenario. *Nat. Rev. Neurosci.* **2020,** *21*, 433-444.

268. Fan, H.; Wang, J.; Gong, J. P. Barnacle cement proteins-inspired tough hydrogels with robust, long-lasting, and repeatable underwater adhesion. *Adv. Funct. Mater.* **2020,** *2009334*.

CHAPTER 2 Adhesive Coacervates Driven by Hydrogen-Bonding Interaction

2.1 Introduction

Coacervate is the concentrated polymer-rich liquid phase that originates from the spontaneous liquid-liquid phase separation of a colloidal system, which has been considered as "the origin of life" for its high resemblance with protoplasm,[1] precellular systems,[2] and membrane-free organelles.[3] Coacervation also plays a critical role in constructing biological tissues (e.g., forming extracellular matrices via assembling elastin with tropoelastin)[4] and developing gradient properties in materials (e.g., squid beak possessing 200 times stiffness gradient),[5] with important applications in various industrial, biological, and medical fields.[6] Coacervates are extensively employed by sessile organisms such as sandcastle worm and mussel to realize strong adhesion under turbulent seawater,[7] which inspires potential applications of coacervates as implanted biomaterials like tissue glues, wound dressings, and drug carriers.

Conventional complex coacervation is mainly driven by electrostatic interactions between oppositely charged polyelectrolytes, usually being affected by various factors such as pH, ionic strength, mixing ratio, concentration, and molecular weight.[8] Underwater proteinaceous adhesive secreted by sandcastle worm is a typical example of complex coacervation, however, its formation requires certain stoichiometry of amine sidechain, phosphate sidechain and Ca^{2+}/Mg^{2+}.[9] Replacing anionic polyelectrolytes with multivalent anions such as phytic acid,[10] pyrophosphate and tripolyphosphate[11] enabled the coacervation system to be salt-responsive, but pH adjustment was still needed. The employment of strong polyelectrolytes like poly(styrenesulfonate) and poly(diallyldimethylammonium) could lead to pH-independent coacervation systems, but high concentration salt (1.3-1.8 M) such as KBr was required.[12] Recently, coacervation phenomena were reported between like-charged polyelectrolytes or within a single cationic recombinant

mussel foot protein, mainly driven by short-range cation-π interactions.[8e,13] But this coacervation mechanism still shows a strong reliance on salt and the coacervates can easily spread on substrates which require further solidification process to achieve strong adhesion.[14] A recently reported research demonstrated an underwater adhesive developed from nonionic polyester, where its self-coacervation was driven by temperature change in wide ranges of pH (3-12) and ionic strength (0-1 M NaCl); while it is noted that complex polymer synthesis and UV-triggered curing mechanism were needed.[15] Therefore, it is highly desirable to develop new coacervates whose formation is not dependent on salt and exhibit innate adhesive performance. As a prevalent interaction in living organisms, hydrogen bonding has been exploited as a primary molecular interaction mechanism for the preparation of biomimetic materials.[16] Recent research has revealed that hydrogen bonding plays a remarkable role in initiating underwater self-healing of hydrogels[17] and can contribute to the formation of polymer complexes with macroscopic liquid-liquid phase separation behaviors.[18] As hydrogen-bonding interaction can arise from various building blocks in salt-free environments, it holds great potential to direct the coacervation process of nonionic polymers and lead to adhesive coacervates with universal stability.

The intrinsic underwater adhesiveness of the adhesive coacervates is a double-edged sword for practical applications, which is likely to result in inflammation, delay tissue healing and block the release of drugs due to the microorganism accumulation.[19] Therefore, much effort has been devoted to the development of adhesive coacervates with innate antimicrobial properties and on-demand bioactivities.[20] Polyoxometalates, as a class of inorganic transition metal oxides clusters, exhibit negatively charged surfaces with specific and adjustable topological structures and sizes. Due to the multiple interactions of polyoxometalates with various polymers, small molecules, and surfactants, these complexes have emerged as the next-generation metallodrugs

with anticancer, antitumor, and antibacterial properties.[21] Negatively charged polyoxometalates can form coacervates with positively charged natural amino acids or zwitterionic polyelectrolytes.[22] Nevertheless, all previously reported coacervate systems require charged organic components or a high concentration of salts, which significantly impairs the applicability of the coacervates in physiological conditions as well as their bioactive activities.

In this work, we report the formation of a series of novel adhesive coacervates solely based on non-electrostatic interactions, by one-step mixing of aqueous solutions of silicotungstic acid (SiW, $H_4[Si(W_3O_{10})_4]$), a representative polyoxometalate, and nonionic polyethylene glycol (PEG), in the absence of any salts. Unlike conventional coacervation processes based on electrostatic or cation-π interactions, here the formation of the coacervates was driven by hydrogen-bonding interactions, which could be readily obtained and scaled up in salt-free environments, expanding coacervation to nonionic systems. The coacervates could be painted rather than spread on diverse organic and inorganic substrates, to which they displayed strong wet adhesion due to the multiple non-covalent interactions. The excellent hemostatic and antimicrobial properties of the SiW-PEG coacervates were demonstrated, which provides a promising paradigm for the development of bioactive tissue adhesives with easy manipulation and flexible modification for various biomedical applications.

2.2 Experimental Section

2.2.1 Materials

Silicotungstic acid (SiW), molecular weight of 2878.17 g mol^{-1} (anhydrous basis), was purchased from Millipore Sigma Canada Co. Poly (ethylene glycol) (PEG) BioUltra 2000, poly

(ethylene glycol) BioUltra 4000, and poly (ethylene glycol) BioUltra, 20000 were all purchased from Sigma Life Science. Poly (ethylene glycol) methyl ether (PEGME), average molecular weight of 2000 g mol^{-1} and poly (ethylene glycol) dimethyl ether (PEGdME), average molecular weight of 2000 g mol^{-1} were both purchased from Aldrich Chemistry.

2.2.2 Cohesion Energy of SiW-PEG Adhesive Coacervate

Adhesive SiW-PEG coacervate was directly injected into the confined and water-filled space between two orthogonal cylindrical silica disks (radius of 2 cm) in the sample chamber of a surface forces apparatus (SFA), both of which were glued with back silver-coated mica sheets (1-5 μm). The surface separation was monitored in real time using an optical technique called multiple beam interferometry by employing fringes of equal chromatic order. The interaction force was determined based on the Hook's law. The adhesion force was measured at least three times at two different interaction position of a pair of mica surfaces, and at least two independently prepared mica pairs were used under each condition for confirmation of repeatability.

2.2.3 Adhesive Properties of Coacervate

Lap shear tests and uniaxial tensile tests of the adhesive coacervate were implemented on a SHIMADZU AGS-X tensile machine. In lap shear tests, 100 μL of coacervate was injected on the adherent region (1 cm × 1 cm) of one of a pair of substrates and was evenly distributed between the two plates for 5 mins. In tensile tests, the adherent area was a circle with a diameter of 6 mm, and 10 μL sample was applied first. Then the glued samples were mounted on the machine and the tests were performed at a velocity of 10 mm min^{-1}. For cyclic tensile tests, a compressive force

of 10 N lasted for 60 s to adhere the porcine skins during each attachment, and the upper limit of the displacement of detachment was set to be 4 mm without rest time. To examine the wet adhesion, 10 μL Milli Q water was added onto the lower porcine skin after each separation to maintain the wet status of the coacervate. The creep test was conducted on adhered porcine skins by maintaining the tensile stress at 40 kPa for 10 h. The deformation of the adhered porcine skins was recorded.

2.2.4 Hemostatic Ability of Coacervate

Mouse liver bleeding model was used to investigate the in vivo hemostatic ability of the SiW-PEG coacervate. 25 Kunming female mice (Female Kunming mouse, 4-6 weeks old, 25-30 g, were obtained from the Laboratory Animal Service Center of Guangdong Province.) were anesthetized by intraperitoneal injection of tiletamine. A 2.5 cm horizontal wound was created by a scalpel on each mouse to expose the liver. The wounds on livers were made by stabbing with an 18-gauge needle, and the masses of bleeding were recorded within 2 mins by weighting the filter papers which were replaced every 30 s. For the experimental group, the wounds were treated with 100 μl coacervate, while no treatment was applied to the control group. All animal procedures were performed in accordance with the guidelines approved by the Animal Experimentation Ethics Committee of Guangzhou Medical University.

2.2.5 Hemolysis Analysis of Coacervate

8 ml fresh human blood sample (provided by the Fifth Affiliated Hospital of Guangzhou Medical University from healthy volunteers approved by Ethics Committee of Guangzhou

Medical University) was transferred into a conical flask with glass beads, mildly stirred for 10 min to remove fibrous protein. Human red blood cells (hRBCs) were separated from the mixture by adding 8 ml sterile Dulbecco's phosphate-buffered saline (DPBS) to 4 ml fibrous protein-free human blood and then centrifuging at 3000 rpm for 5 min at 4 °C. The hRBCs solution was washed with DPBS at least five times until the supernatant was colorless and transparent. hRBCs suspension of 0.25% (v/v) for hemolysis experiment was prepared by introducing 30 μl hRBCs solution into 12 ml DPBS of 0.9 wt%. 50 μl coacervate sample was added to each well of a 96-well plate, standing for 1 h under UV light to sterilize and enable a flat surface of the coacervate. Subsequently, 80 μl hRBCs suspension was added onto the coacervate as the experimental group, into 50 μl DPBS as a negative control, and into 50 μl 0.4% Triton-X as a positive control, respectively. After this, another 170 μl DPBS was dropped into each well, resulting in an hRBCs suspension of 0.08% (v/v). The 96-well plate was shaken at 50 rpm for 1 h at 4 °C. After incubation, 200 μl of each hRBCs suspension was transferred into an Eppendorf tube to centrifuge at 14000 rpm for 10 min at 4 °C, removing the undamaged cells. The light absorbance at 415 nm of the remaining solutions was measured to figure out the amount of hemoglobin released from hRBCs due to membrane fracture. Haemolysis of pure hRBCs suspension was defined as 0, while that of hRBCs suspension mixed with 0.4% Triton-X was considered as 100%. Images of hRBCs after treatments were obtained with an optical microscope.

2.2.6 Antimicrobial Properties of Coacervate

70 μL coacervate was injected to wells of a 96-well plate, and then incubate for 10 mins at 37 °C to acquire flat surfaces. The bacteria concentration of the original E. coli CFT073 stock solution was determined to be 3.75×10^{9} CFU mL^{-1} based on agar plating and colony counting.

Then 100 μl of this bacteria suspension was transferred onto the surface of the coacervate. For other bacterial concentrations, 90 μl bacteria-free LB broth was introduced to each well. Afterward, sequential 10-time dilution of bacteria suspensions was obtained by adding 10 μL of the previous diluted bacteria suspension to the next 90 μl bacteria-free LB broth in the adjacent well. For the control group, bacteria suspensions were introduced to coacervate-free wells. For experimental and control groups of each bacteria concentration, two sets of 96-well plates were used in each plate, four samples were prepared. The final values of colony forming unit (CFU) were divided by the surface area (0.0032 dm^2) to convert from CFU ml^{-1} to CFU dm^{-2}.

2.2.7 Antimicrobial Properties of SiW-treated LB Broth

E. coli strain was incubated in LB broth at 37 °C for 24 h to prepare E. coli suspension. Next, 100 μl E. coli suspension was added into a centrifuge tube containing 2.5 ml LB broth and 400 μl 3×10^{-4} mol ml^{-1} SiW aqueous solution. As a control, 100 μL E. coli suspension was added into another centrifuge tube that only contained LB broth. Then the two centrifuge tubes were incubated at 37 °C for 24 h with a mild shake. Nutrient agar media was made by adding 25 g LB (10 g tryptone, 5 g yeast extract, 10 g NaCl) and 15 g agar into 1000 ml deionized water, autoclaving at 121 °C for 30 min. Subsequently, every 15 ml of the nutrient mixture was poured into a sterilized glass petri dish at 70 °C to prepare LB solid plate for bacteria incubation and colony counting. After agar plate cooled and solidified, 100 μl of SiW-treated E. coli suspension and non-treated E. coli suspension as well as their corresponding diluted solutions were applied on the entire surface of an agar plate, respectively. The agar plates were incubated at 37 °C for 24 h for calculation E. coli colony forming units.

2.2.8 Determination of Yield of Coacervate

Firstly, the weight of each vial was measured denoted as W_{vial}. Then SiW and PEG aqueous solutions were added into vials in sequence. Thereafter, the total weight of SiW solution, PEG solution and the vial was measured. After vigorously mixing SiW and PEG aqueous solutions and the following liquid-liquid phase separation, the SiW-PEG coacervate phase was obtained. Subsequently, the supernatant was discarded, and the weight of the coacervate-containing vial was measured. The yield of coacervate was calculated by the following equation.

$$Yield\ of\ coacervate = \frac{W_{vial+coacervate} - W_{vial}}{W_{vial+SiW+PEG} - W_{vial}} \times 100\%$$

2.3 Results and Discussion

2.3.1 Preparation of coacervate

The SiW-PEG coacervate was facilely prepared by directly mixing a 300 mM SiW aqueous solution with a 30 mM PEG20000 (molecular weight of 20 kDa) aqueous solution (**Figure 2.1A**) at a volume ratio of 3:2. A highly viscous water-immiscible substance immediately formed via vigorously stirring (**Figure 2.1B**). Coacervate droplets with sizes in the range of several to tens of micrometers were dispersed in the aqueous solution (**Figure 2.1D**). The droplets could hardly move, attributed to the confined geometry and high viscosity of the liquid phase. When the molecular weight of PEG decreased from 20 kDa to 2 kDa, coalescence phenomenon was detected, where the small coacervate droplets could move and got coalesced into larger ones. The cryogenic transmission electron microscopy (cryo-TEM) image of the SiW-PEG coacervate exhibited a continuous sponge-like network structure (**Figure 2.1E**), indicating stable and strong

physical interactions between the SiW clusters and PEG chains (**Figure 2.1F**). After aging for 2 hours, the system underwent complete phase separation, leading to a translucent dense coacervate phase at the bottom and a top layer of dilute aqueous solution (**Figure 2.1C**). Rheological measurements of the coacervate (**Figure 2.S1**) indicated its liquid-like property (loss modulus G'' higher than storage modulus G'). The water contents of the coacervates prepared with different ratios of SiW to PEG were determined to be between 15.8% and 21.8% (**Figure 2.S2**), revealing the coacervates were rich in SiW and PEG. Due to the simple fabrication process, the mass production of coacervate can be readily achieved and stored at room temperature for future usage.

The SiW-PEG coacervate could act as an adhesive to strongly bind various materials including glass, metal, stone, and wood to a plastic substrate both in air and underwater. It was also capable of seamlessly repairing the cuts on a porcine skin, which showed load-bearing property (**Figure 2.S3**). Although the mechanical properties and adhesiveness of the coacervate were undermined with the loss of trapped water, these characteristics could be immediately recovered by adding water to the dried material, indicating the facile storage/transport and reusability of the adhesive (**Figure 2.1G-J**). Unlike the conventional coacervates that easily spread over a surface, the as-prepared new coacervate could not only be injected and painted on substrates through a needle (**Figure 2.1K**) but also maintain its integrity and the designed shapes underwater even with vigorous shaking, suggesting its great potential as tissue adhesives. Moreover, the adhesive SiW-PEG coacervate was stable when immersed in NaCl aqueous solutions ranging from 50 mM to 1 M (**Figure 2.S4**), suggesting its applications in salt environments.

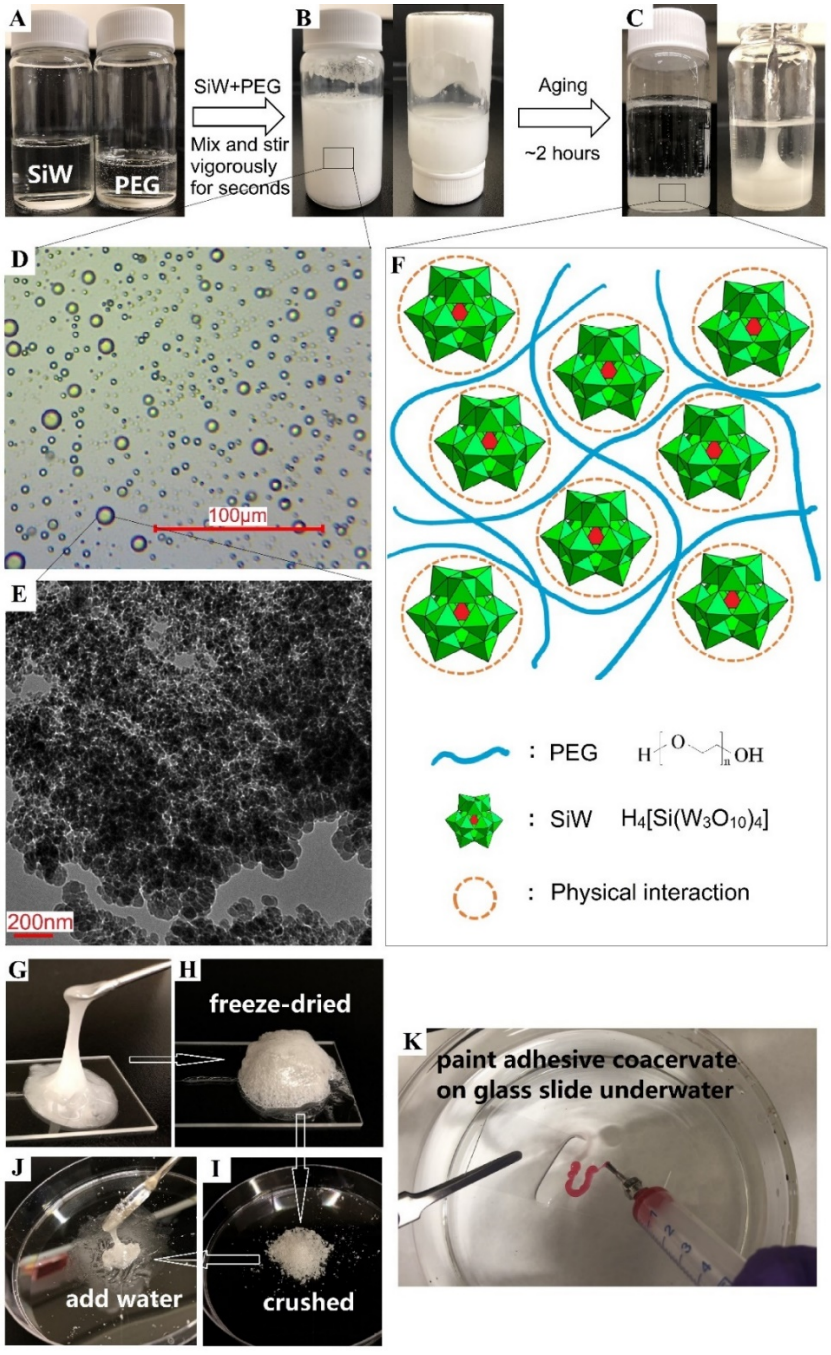

Figure 2.1. Formation of SiW-PEG coacervate. (A) Pictures of 300 mM SiW aqueous solution (left) and 30 mM PEG20000 aqueous solution (right). (B) The mixture of SiW and PEG aqueous solutions after stirring. (C) Complete separation of coacervate phase (lower dense phase) and supernatant (upper phase). (D) Microscopic image of the dispersed coacervate droplets. (E) Cryo-TEM image of the coacervate phase. (F) Schematic molecular interactions of SiW-PEG

coacervate. (G) Picture of viscous and adhesive SiW-PEG coacervate after preparation. (H, I) Pictures of freeze-dried and crushed SiW-PEG coacervate. (J) Picture of reformed viscous and adhesive coacervate with the addition of water. (K) SiW-PEG coacervate dyed with methyl orange is injected and painted into a "U" shape on a glass slide underwater.

2.3.2 Phase Behavior and Intermolecular Interactions of Coacervation

Phase behaviors between PEG20000 (30 mM) and SiW (300 mM) aqueous solutions were investigated as shown in **Figure 2.2A**. When the volume ratio of SiW to PEG ranged from 5:5 to 9:1, coacervation phenomenon could be observed with the highest yield of coacervate under the ratio of 6:4, where the yield was determined by the weight ratio of the as-prepared coacervate to the total of SiW and PEG solutions after mixing (the adhesive coacervates studied in this work were prepared at this ratio if not specifically mentioned). The mixtures of other ratios only appeared as transparent solutions. Compared to the low viscosity of PEG20000 solution (0.42 Pa·s), the viscosity of the SiW-PEG20000 coacervate drastically increased by more than 300 times to 126.6 Pa·s, indicating strong intermolecular interactions between SiW clusters and PEG chains (**Figure 2.2B**). In aqueous solution, SiW is considered as a strong acid which can be fully dissociated, exhibiting a Keggin structure with negative surface charges surrounded by hydrated protons, and its anionic Keggin cluster structure is a well-known proton acceptor.[21c, 23] Although PEG does not carry any charges, its end-functional hydroxyl groups -OH can serve as both proton donors and acceptors and its etheric oxygen atoms -O- can act as proton acceptors. To verify the contribution of the end-functional groups, the coacervation behaviors between SiW (300 mM) aqueous solution and solutions containing different types of PEG (300 mM, PEG2000 with hydroxyl groups at both ends, PEGME2000 with hydroxyl group and methyl group at each end

respectively, and PEGdME2000 with methyl groups at both ends) were characterized (**Figure 2.2C**). To minimize the effect of the large size of the PEG chain, PEG polymers with molecular weight of 2kDa were used instead of PEG20000 employed for adhesive coacervate. All PEG solutions displayed similar phase behaviors after one-step mixing with SiW aqueous solutions (**Figure 2.2C** and **Figure 2.S5**) and the viscosities of the prepared coacervates were close to each other (**Figure 2.2D**), demonstrating the coacervation process was mainly driven by interactions between SiW and etheric oxygen atoms of PEG rather than the end groups. When the concentrations of PEG2000, PEGME2000, and PEGdME2000 aqueous solutions were decreased to 30 mM, coacervates still could be generated yet with very low yields (**Figure 2.S6**). By changing the molecular weight of PEG from 20 kDa to 2 kDa at a fixed polymer concentration (600 mg ml^{-1}, 37.5 wt%), the viscosity of the coacervates was drastically reduced by more than 30 times (**Figure 2.2B, D**). The entanglement concentrations (C_e)[24] of PEG20000 and PEG2000 aqueous solutions were determined to be 17.5 wt% and 35.0 wt%, respectively (**Figure 2.S7**). Although both of the polymers were entangled in solutions, the percentage of the entanglements of PEG20000 should be much higher than that of PEG2000. Therefore, the entanglements within and between polymer chains played a crucial role in the intermolecular interactions of coacervates. To investigate the role of hydrated protons, LiOH was employed to gradually neutralize the H_3O^+ in SiW solution. As presented in **Figure 2.2E**, when the molar ratio of LiOH to H_3O^+ of SiW increased from 0 to 0.25, 0.5, 0.75, the weight ratio of the obtained coacervate decreased from 46.0% to 44.4%, 23.1%, and finally 0%, respectively, suggesting that hydrated protons were indispensable for the formation of coacervate in SiW-PEG system. The stability of the formed coacervated was also investigated (**Figure 2.S8**). After preparation, the supernatant was measured to be pH of 1.38. With the increase of the pH of the supernatant by adding LiOH, the coacervate was gradually dissolved into the solution and totally disappeared at pH 4.30. It indicated that the

coacervation could only occur below pH 4.30. However, by mixing PEG20000 aqueous solutions with HCl or H_2SO_4 (with 1.2 M H^+), no coacervate could be detected (**Figure 2.2F**). Therefore, the coacervation process was most likely originated from the hydrogen bonding between oxygens of SiW and etheric oxygens of PEG bridged by hydrated protons.[25]

Fourier transform infrared spectroscopy (FTIR) spectra of the freeze-dried coacervate demonstrated that the Keggin structure of SiW was well maintained, with typical stretching vibration bands of W=O_d, Si-O_a, W-O_b-W (edge shared), W-O_c-W (corner shared) shifted from 1015, 977, 908, 742 cm^{-1} to 1009, 966, 911, 769 cm^{-1}, respectively (**Figure 2.2G, H**). As for PEG, C-O-C stretching occupied the largest shift of 19 cm^{-1} from 1093 cm^{-1} to 1074 cm^{-1} before and after coacervation. As SiW is usually regarded a strong acid with fully ionized protons,[23] it was proposed that the primary driving force for coacervation was the hydrogen-bonding interactions W=O···H_3O^+···O between oxygens (both terminal O_d atoms (predominant)[26] and bridging oxygens O_b and O_c) of SiW and etheric oxygens of PEG bridged by hydrated protons (**Figure 2.2I**). However, it is possible that a certain amount of OH groups still exist on the acid, which can play a minor role on the formation of coacervate by interaction with PEG. To investigate and tune the hydrogen-bonding interaction within the coacervates, different polar organic solvents including dimethylformamide (DMF), acetonitrile and ethanol were introduced as additives[25a, 27] to the PEG aqueous solutions before mixing with SiW. As DMF and acetonitrile can only act as hydrogen bond acceptors, they tended to compete with etheric oxygens of PEG to form hydrogen bonds with SiW. Coacervates could still form when the volume fraction of the organic solvents was below 50%, while no coacervate generated when the fraction increased to 90% (**Figure 2.S9**). Differently, ethanol can simultaneously serve as both hydrogen bonding acceptor and hydrogen bonding donor. The addition of ethanol could accelerate the coacervation process as well as

increase the final yield of the coacervates, which was likely attributed to the enhanced interaction of PEG and SiW in the presence of ethanol (**Figure 2.S10**).[25]

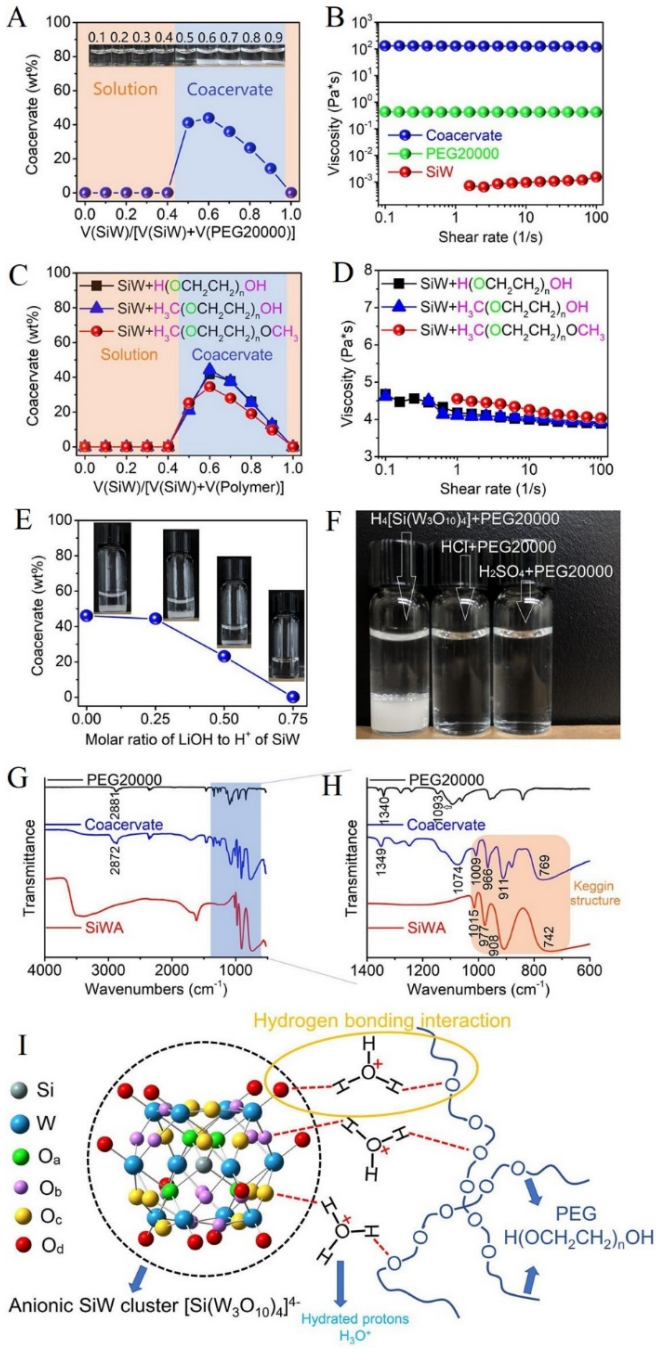

Figure 2.2. Phase behaviors between SiW and PEG aqueous solutions. (A) Phase behavior between 300 mM SiW aqueous solution and 30 mM PEG20000 aqueous solution. (B) Viscosities of 300 mM SiW aqueous solution, 30 mM PEG20000 aqueous solution, and the corresponding

coacervate. (C) Phase behaviors between 300 mM SiW aqueous solution and 300 mM PEG2000, PEGME2000, PEGdME2000 polymer solutions. (D) Viscosities of SiW-PEG2000, SiW-PEGME2000, and SiW-PEGdME2000 coacervates. (E) Gradual neutralization of hydrated protons in the coacervation system of 300 mM SiW and 30 mM PEG20000 using LiOH. (F) Phase behaviors between 30 mM PEG20000 aqueous solution and 300 mM SiW aqueous solution, 1.2 M HCl aqueous solution, 0.6 M H_2SO_4 aqueous solution, respectively. (G, H) FTIR spectra of SiW, PEG20000 and the corresponding freeze-dried coacervate. (I) Schematic illustration of the proposed interaction mechanism between SiW and PEG for the coacervate formation.

2.3.3 Cohesion Energy and Adhesive Properties of Coacervate

The cohesion energy of the SiW-PEG coacervate were characterized by a surface forces apparatus (SFA) with the configuration shown in **Figure 2.3A**.[28] In a typical SFA measurement, a dense SiW-PEG20000 coacervate was first deposited on the lower mica surface covered with water and then it was confined between two opposing mica surfaces forming a coacervate meniscus bridge. A pull-off force F_{ad} (also denoted as adhesion) was measured during the following separation. Strong pull-off forces were detected with a maximum of 249.9 mN m^{-1} after a contact time of 60 minutes, which was more than 30 times higher than that of the like-charged complex coacervate (7.2 mN m^{-1}) driven by cation-π interactions.[8e] The time-dependent enhancement of adhesion was most likely attributed to the rearrangement of PEG chains which balanced the interactions within the coacervate and at the interface of coacervate/substrate.[29] Simultaneously, water pockets at the coacervate/substrate interface and coacervate/coacervate interface might be removed by compression or through the reconfiguration of PEG polymer chains, creating a larger contact area and leading to a stronger adhesion.[30] It is noted that during separation,

the coacervate meniscus was broken, while the coacervate strongly adhered to mica surfaces, which was attributed to the strong hydrogen-bonding interaction between SiW clusters and oxygen atoms on mica. Thus, the effective cohesion energy W_{eff} can be estimated as ~13.2 to 39.8 mJ m^{-2} at a contact of 1 to 6 min according to $W_{eff} = F_{ad}/2\pi R$, where R is the radius of curvature of the cylindrical silica disk.[28a] Compared to conventional coacervates based on electrostatic interaction of oppositely charged polyelectrolytes, the relatively high effective cohesion energy of the SiW-PEG coacervate enables them to be directly paintable and adhere to various substrates rather than spontaneous spreading.

The adhesive properties of the SiW-PEG coacervate on different substrates were examined and are illustrated in **Figure 2.3B**, showing the highest adhesion to stainless steel (74.2 kPa) and copper (56 kPa), contributed by the synergetic effect of hydrogen bonding and coordination interactions.[22a] The measured adhesion of the coacervate on PTFE (polytetrafluoroethylene), PC (polycarbonate), PVC (polyvinyl chloride) and glass substrates were determined to be 15.7, 23.8, 29.1, and 57.6 kPa, respectively, which was mainly ascribed to hydrogen-bonding interaction between SiW and electronegative F, O, Cl. To investigate the adhesiveness of the coacervate on biological tissues, it was painted between two pieces of porcine skins with a tensile setup shown in **Figure 2.3C** and the adhesive strength was acquired to be 76.4 kPa. The strong adhesion was most likely originated from hydrogen-bonding interaction (SiW and -OH, $-NH_2$ groups on porcine skin) and electrostatic interaction (negatively charged SiW and $-NH_2$ on porcine skin).[31] Moreover, the coacervate bonding between two pieces of porcine skins can resist tensile stress of 40 kPa for 10 hours without separation, indicating its excellent flow resistance when applied as tissue adhesives (**Figure 2.S11**).[32] It should be noted that the coacervate could exhibit repeatable adhesion on porcine skin and its performances were characterized both in air and with the presence of water (**Figure 2.3D**). In the absence of water, the average adhesion strength of the SiW-PEG

coacervate was 60.4 kPa. The gradual water evaporation impaired hydrogen-bonding interactions between coacervate and porcine skin. While in the presence of water (i.e., a 10 μL water droplet was added after each detachment), adhesive coacervate possessed an average adhesion strength of 98.2 kPa, improved by 62.6 % with respect to that in air, which was attributed to the increased mobility of PEG and hydrated protons.

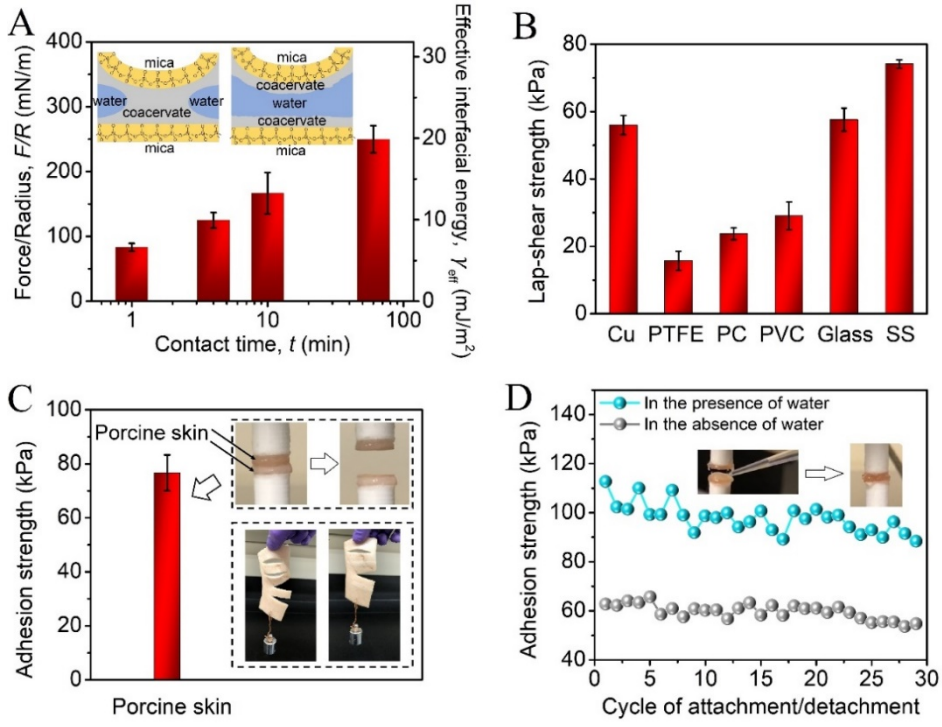

Figure 2.3. Adhesive properties of SiW-PEG coacervate. (A) Adhesion force and corresponding effective cohesive energy of coacervate under different contact time. Insets: the typical SFA setup. (B) Lap-shear strength of the coacervate binding to different substrates (PTFE, PC, PVC, SS). (C) Adhesive strength of coacervate between porcine skins. (Inset: uniaxial tensile test setup and the demonstration of the coacervate used as tissue adhesive). (D) Adhesion strength of SiW-PEG coacervate in the presence of water and in the absence of water during cyclic attachment/detachment tests.

2.3.4 Hemostatic Ability and Hemolysis of Coacervate

The excellent wet adhesive property of the SiW-PEG coacervate suggests its great potential applications as strong tissue adhesives and in hemostasis, and thus its hemostatic ability was investigated using a mouse liver bleeding model.[18c, 33] When the mouse liver was stabbed with a needle, only after 30 s, the average blood loss reached 141 (± 16.5) mg without any treatment, while the amount of bleeding with the application of SiW-PEG coacervate significantly decreased to 32.4 (± 28.7) mg, which was reduced by 77% (**Figure 2.4A**). In the following 90 s, the mass of bleeding of the control group was gradually increased to 177.7 mg; while no further bleeding was detected for the coacervate-treated mice after 60 s (**Figure 2.4B-D**). The hemostatic performance of the developed coacervate was better than that of the commercialized and reported adhesives,[18c] demonstrating the high efficiency of the SiW-PEG coacervate as a local hemostatic agent for wound care, especially for wounds on vulnerable organs. **Figure 2.4E-H** show the hemolytic results of the adhesive coacervate, using the amount of hemoglobin released from human red blood cells (hBRCs) to indicate the hemolytic activity.[34] The hemolysis of fresh hRBCs suspension (**Figure 2.4G**) was defined as 0, while that of Triton-X-treated hRBCs suspension (**Figure 2.4H**) was considered to be 100%. Interestingly, when the hRBCs suspension contacted with adhesive coacervate, the absorbance of the released hemoglobin was even lower than that of the fresh hRBCs suspension (**Figure 2.4E**), which was likely due to hydrogen bonding interactions between SiW clusters and cell membranes of hRBCs (e.g., containing phosphate groups). Such attractive interaction could bridge and induce slight aggregation of hRBCs (**Figure 2.4F**) which might to some extent reduce natural fracture of hRBCs. Such low hemolysis activity

of the as-prepared adhesive coacervate satisfies the requirements for practical medical applications (relative absorbance of hemoglobin ≤ 5% in protocol ASTM-F756).

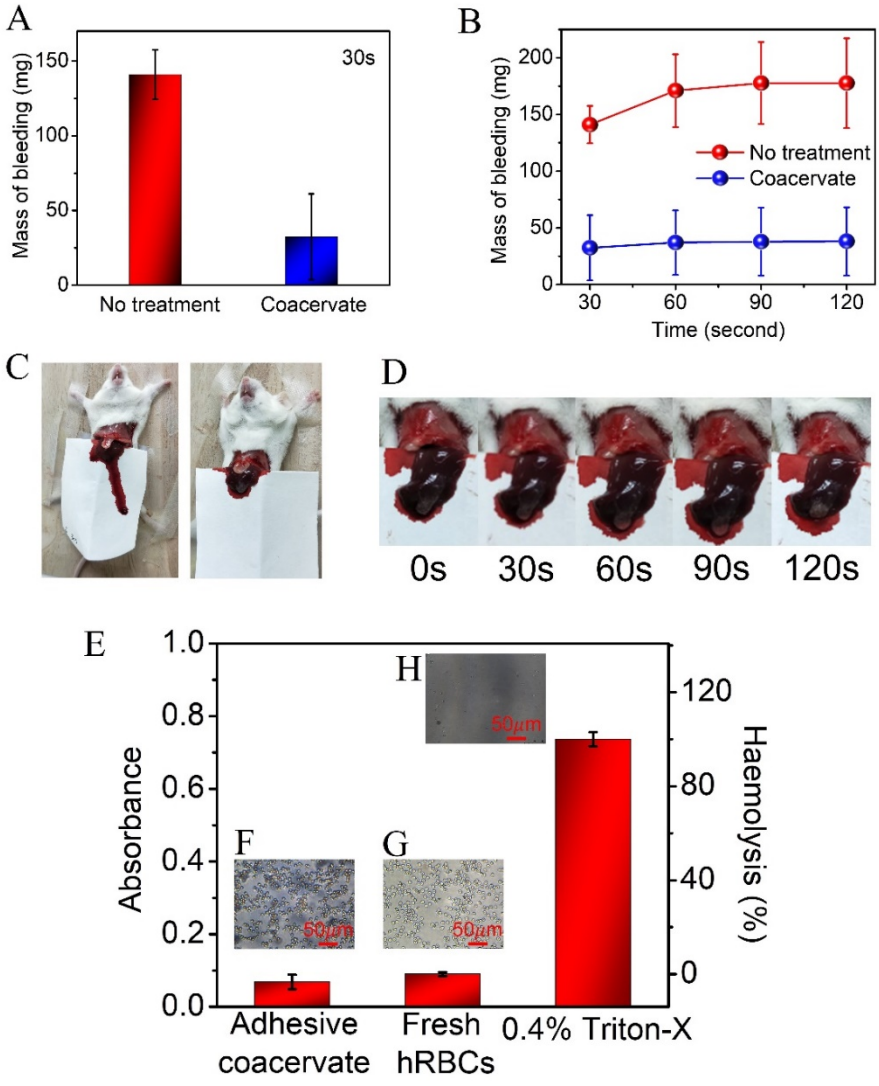

Figure 2.4. Hemostatic ability and hemolysis of SiW-PEG coacervate. (A) Mass of bleeding of mouse livers with or without the treatment of coacervate after 30 s. (B) Mass of bleeding of the mouse livers with or without the treatment of coacervate within 120 s. (C) The bleeding of mouse liver with or without the application of SiW-PEG coacervate after 120 s. (D) The bleeding of the mouse liver treated with SiW-PEG coacervate within 120 s. (E) Absorbance of hemoglobin in hRBCs suspensions (fresh, treated with SiW-PEG coacervate, and treated with 0.4% Triton-X,

respectively) as well as their corresponding hemolysis percentages. (F) Phase-contrast image of hRBCs suspension on coacervate surface. (G) Phase-contrast image of fresh hRBCs suspension. (H) Phase-contrast image of hRBCs in 0.4% Triton-X solution.

2.3.5 Antimicrobial Properties

As microorganisms accumulation on tissue adhesives can generally lead to risks of wound inflammation and infection, hemostatic agents possessing innate antimicrobial properties show overwhelming advantages for practical applications.[20c, 34] Gram-negative *Escherichia coli* (*E. coli*) is one of the top 5 microbials causing surgical infections,[35] especially after liver transportation (top 3),[36] and it was used to evaluate the antimicrobial performance of the developed SiW-PEG coacervate.[20c] As presented in **Figure 2.5A**, the coacervate displayed a 100% reduction of *E. coli* up to 1.17×10^{10} CFU dm^{-2} , and this concentration is about eight orders of magnitude higher than that of an operating theatre in activity.[34] The antimicrobial activity was ascribed to the existence of SiW, as only 1 wt % SiW in a Luria-Bertani broth could efficiently kill *E. coli* with 99.998% reduction in bacterial counts (**Figure 2.5B-D**). The excellent antimicrobial property was most likely due to the electrostatic interactions between polyoxometalates and proteins/enzymes,[37] which would impair cell functions of *E. coli* after absorption.

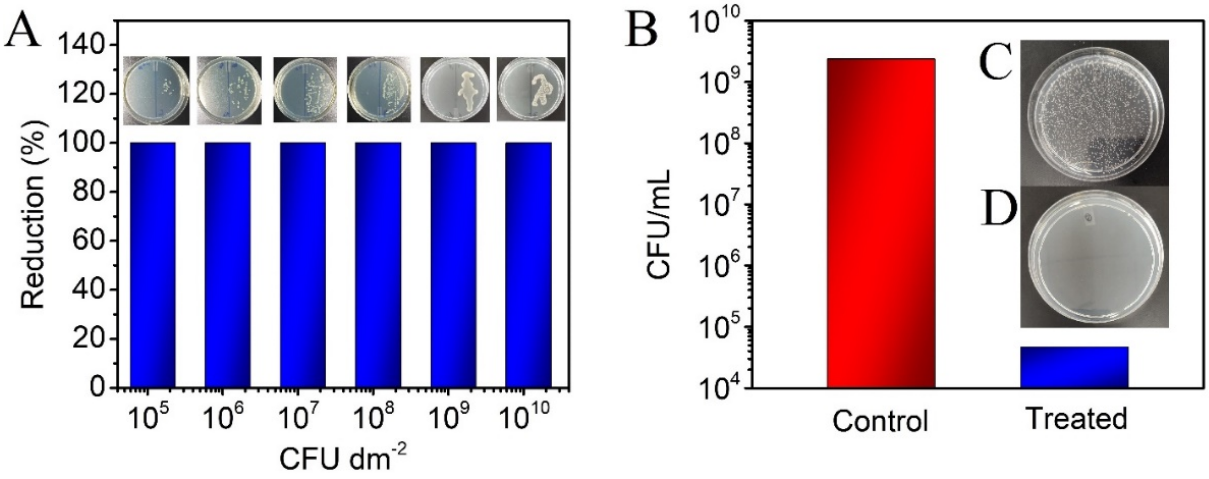

Figure 2.5. Antimicrobial performances of SiW-PEG coacervate and SiW. (A) Surface antimicrobial property of the coacervate with different concentrations of original microbial suspension. Insets: Images of E. coli colonies on agar plates with (left) or without (right) the treatment of the coacervate. (B) CFUs of E. coli in control broth and 1 wt% SiW-containing broth after 24 h incubation. (C) Images of E. coli colonies on an agar plate from a diluted bacterial suspension without treatment. (D) Images of E. coli colonies on an agar plate from a diluted bacterial suspension treated with 1 wt% SiW.

2.4 Conclusions

In this work, we have developed a novel adhesive coacervate solely based on non-electrostatic interactions via one-step mixing of SiW and PEG aqueous solutions, where the coacervation process is mainly driven by intermolecular hydrogen bonding between terminal and bridging oxygens of SiW and etheric oxygens of PEG bridged by hydrated protons. Compared to previously reported electrostatic or cation-π interaction-induced coacervation, our work demonstrates that coacervation can occur in salt-free environments without the presence of polyelectrolytes, expanding coacervates to nonionic systems. This coacervate can be readily

scaled up and painted on various substrates, displaying robust wet adhesion to various substrates. The as-prepared coacervate is demonstrated as an effective hemostatic agent for the treatment of injuries with inherent antimicrobial property, which is beneficial for practical surgical treatments. This novel hydrogen-bonding-driven coacervate holds great potential in biomedical applications, such as biocompatible tissue glues and wound dressings. As SiW is a member of polyoxometalates possessing catalytic properties, the SiW-involved coacervates provide an ideal platform for the study of active membrane-free cell systems that are related to the "origin of life". Modification of PEG with desired functional groups will further expand the applications of the SiW-PEG coacervates in diverse engineering and bioengineering fields.

2.5 Supporting Information

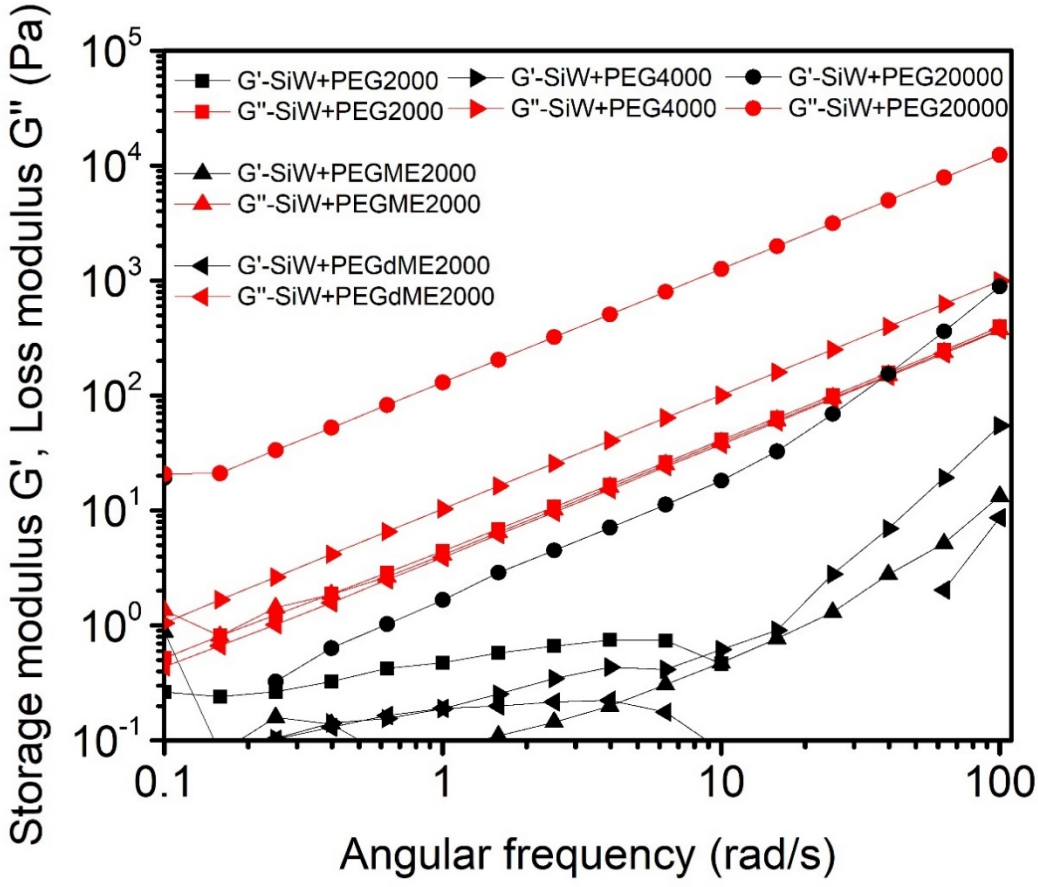

Figure 2.S1. Storage modulus G' and loss modulus G'' of different coacervates formed between 300 mM SiW aqueous solution and aqueous solutions containing different types of PEG (600 mg ml^{-1}, PEG2000, PEGME2000, PEGdME2000, PEG4000, PEG20000).

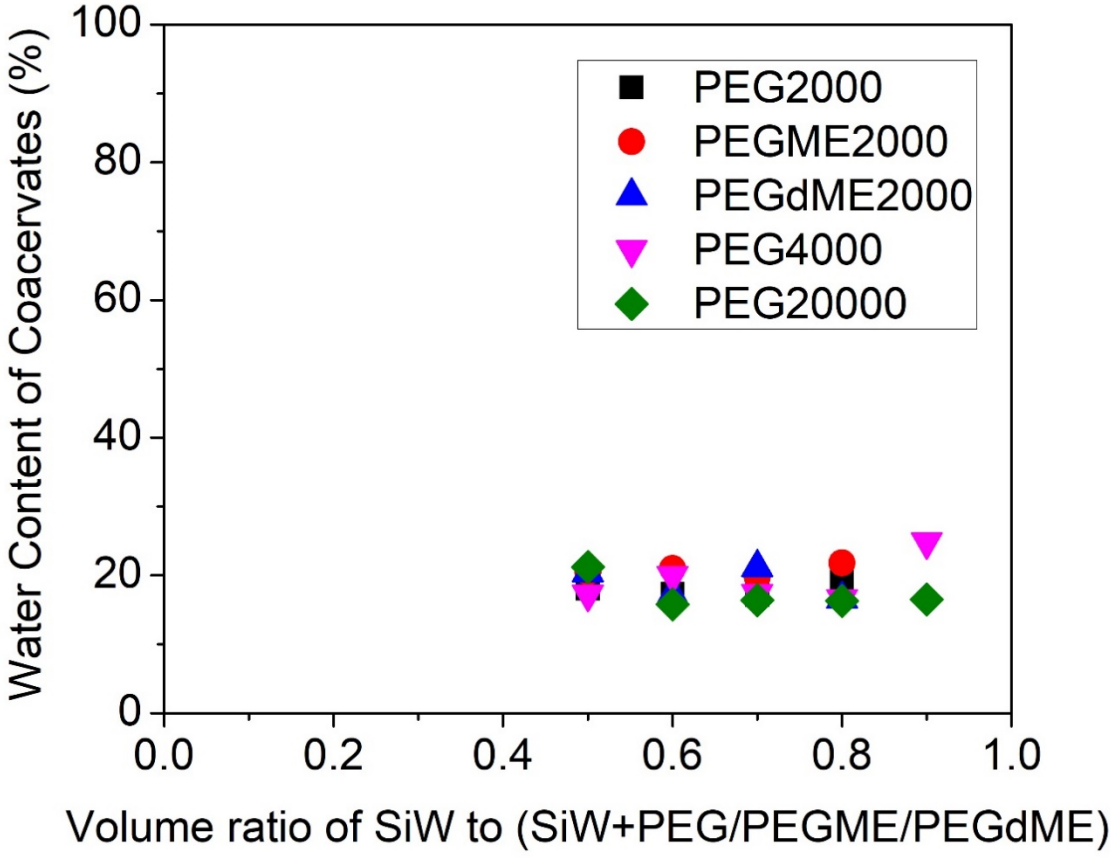

Figure 2.S2. Water content of coacervates. Coacervates were formed by mixing 300 mM SiW aqueous solution with different PEG aqueous solutions (600 mg ml^{-1}, PEG2000, PEGME2000, PEGdME2000, PEG4000, PEG20000).

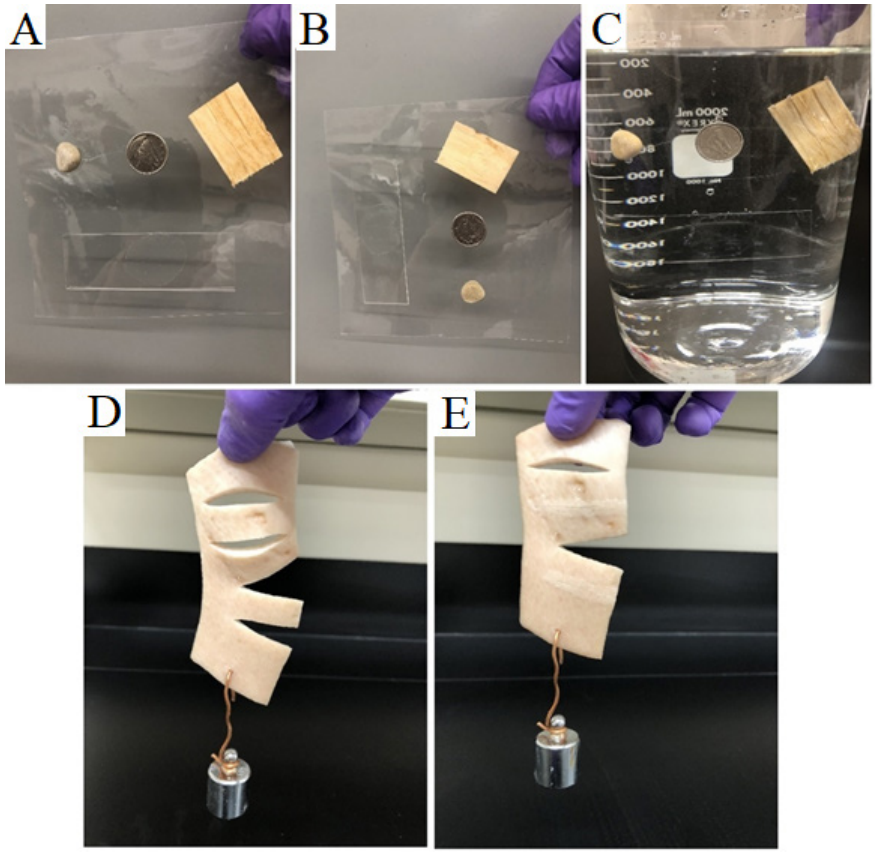

Figure 2.S3. SiW-PEG20000 adhesive coacervate can bind various substrates such as plastic, glass, metal, stone, wood, and porcine skin. (A-C) Stone, coin, wood plate and glass slide are attached to a plastic substrate by the adhesive coacervate (A, front view in the air; B**,** back view in the air; C, front view underwater). (D) Two middle cuts and two side cuts are made on a porcine skin. A 50 g weight can stretch all the four cuts. (E) The lower middle cut and side cut are glued with the adhesive coacervate, showing load-bearing property.

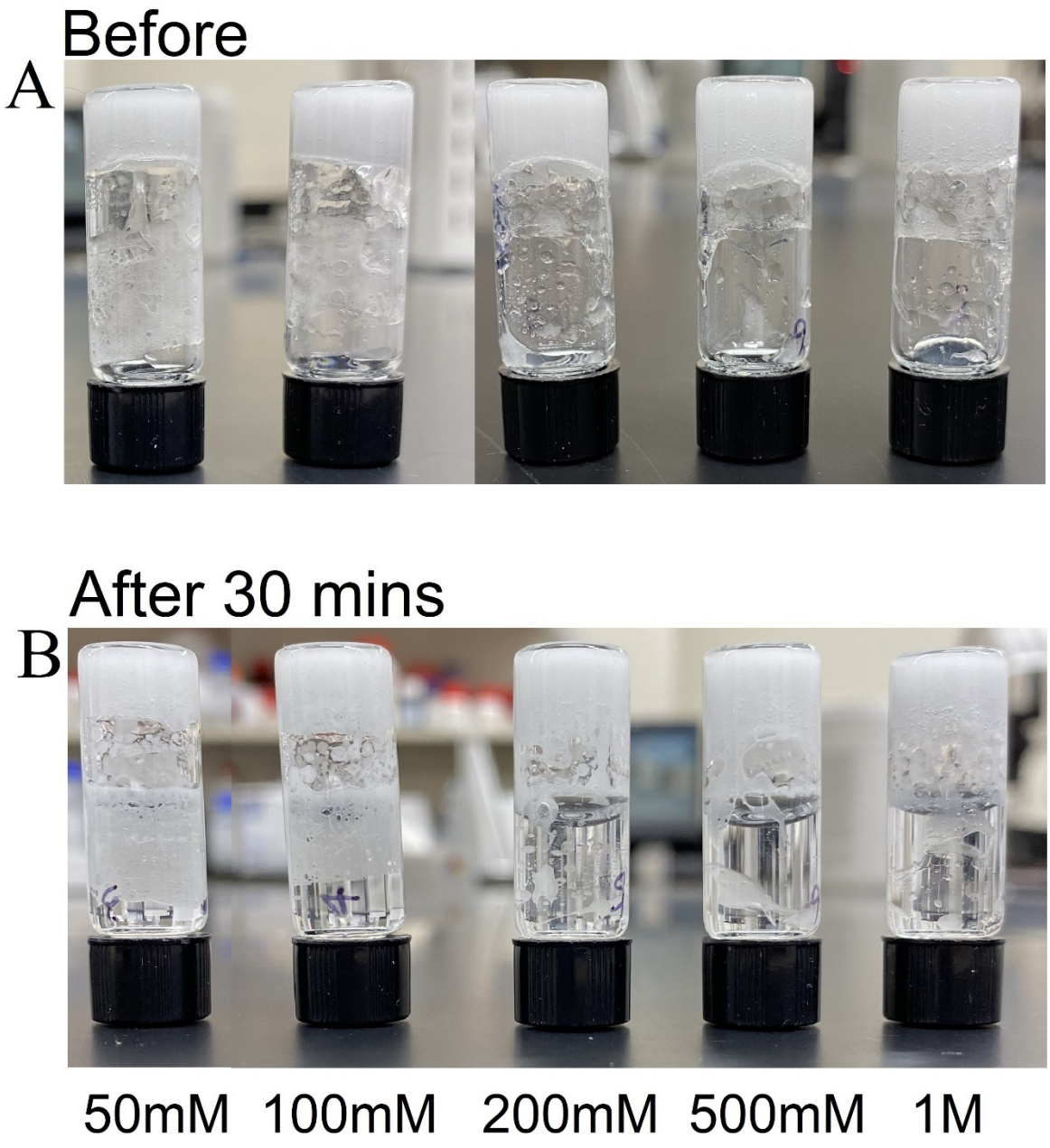

Figure 2.S4. Stability of SiW-PEG coacervate immersed in NaCl aqueous solutions with different concentrations.

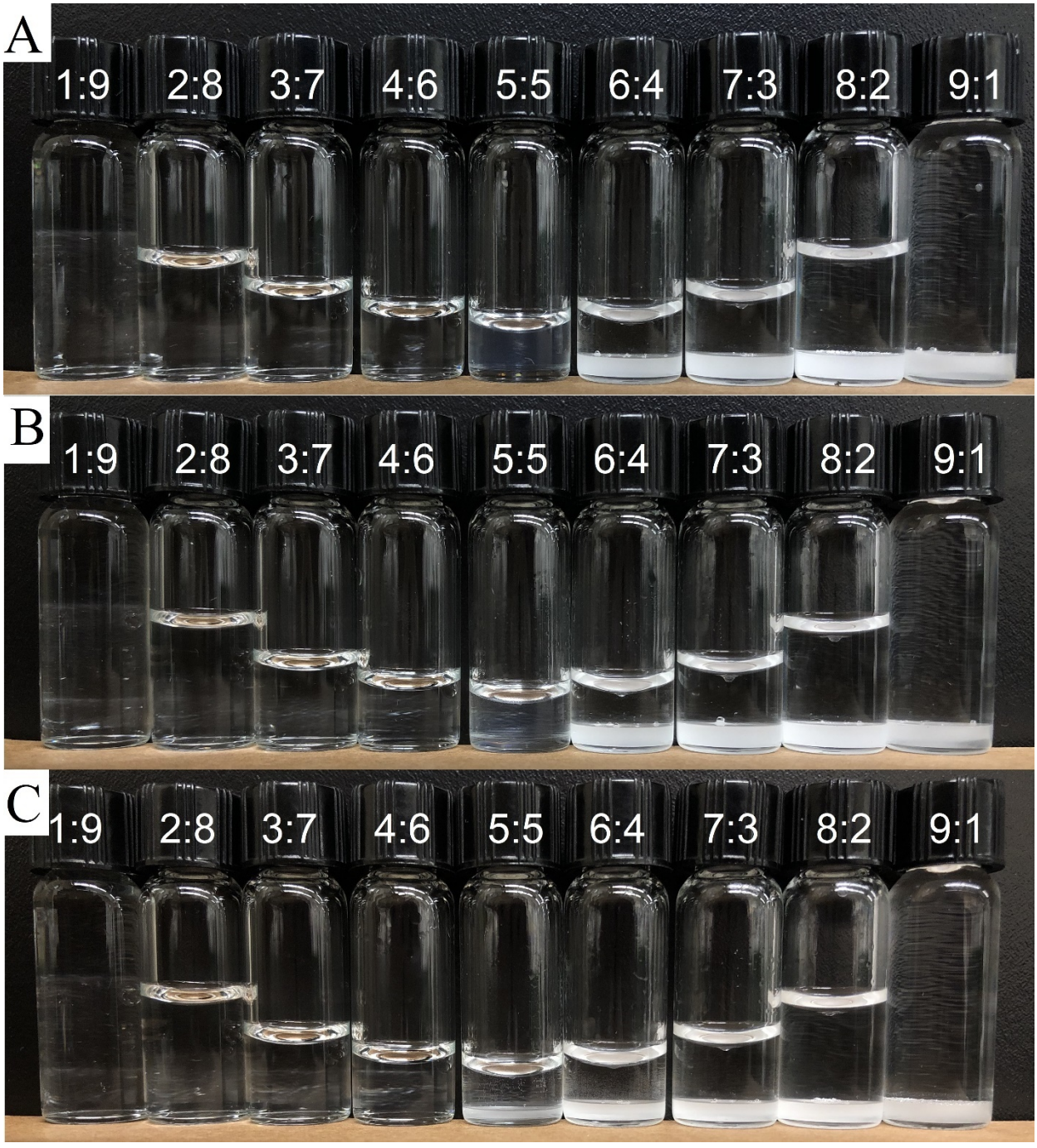

Figure 2.S5. Phase behaviors between 300 mM SiW aqueous solution and 300 mM aqueous solutions of (A) PEG2000, (B) PEGME2000, and (C) PEGdME2000. From left to right, the volume ratio of SiW to polymer solution ranges from 1:9 to 9:1. When the volume ratio of SiW to PEG is higher than 5:5, coacervation phenomenon can be observed.

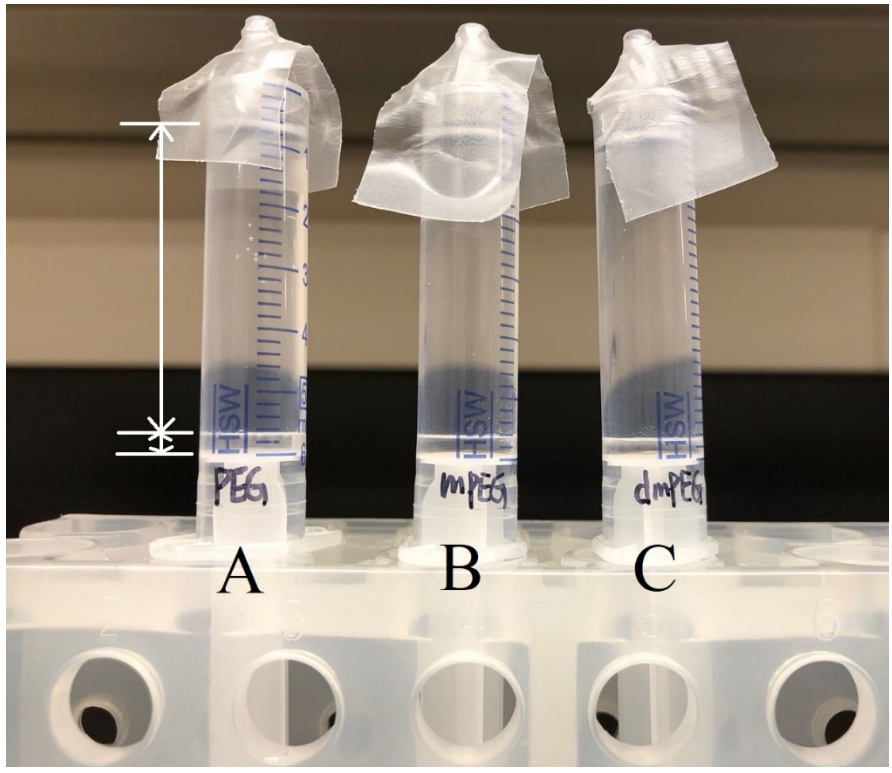

Figure 2.S6. Coacervates formed between 300 mM SiW aqueous solution and 30mM aqueous solutions of (A) PEG2000, (B) PEGME2000, and (C) PEGdME2000. Volumes of SiW solution and polymer solution are 3 ml and 2 ml, respectively. The yields of coacervates are relatively small.

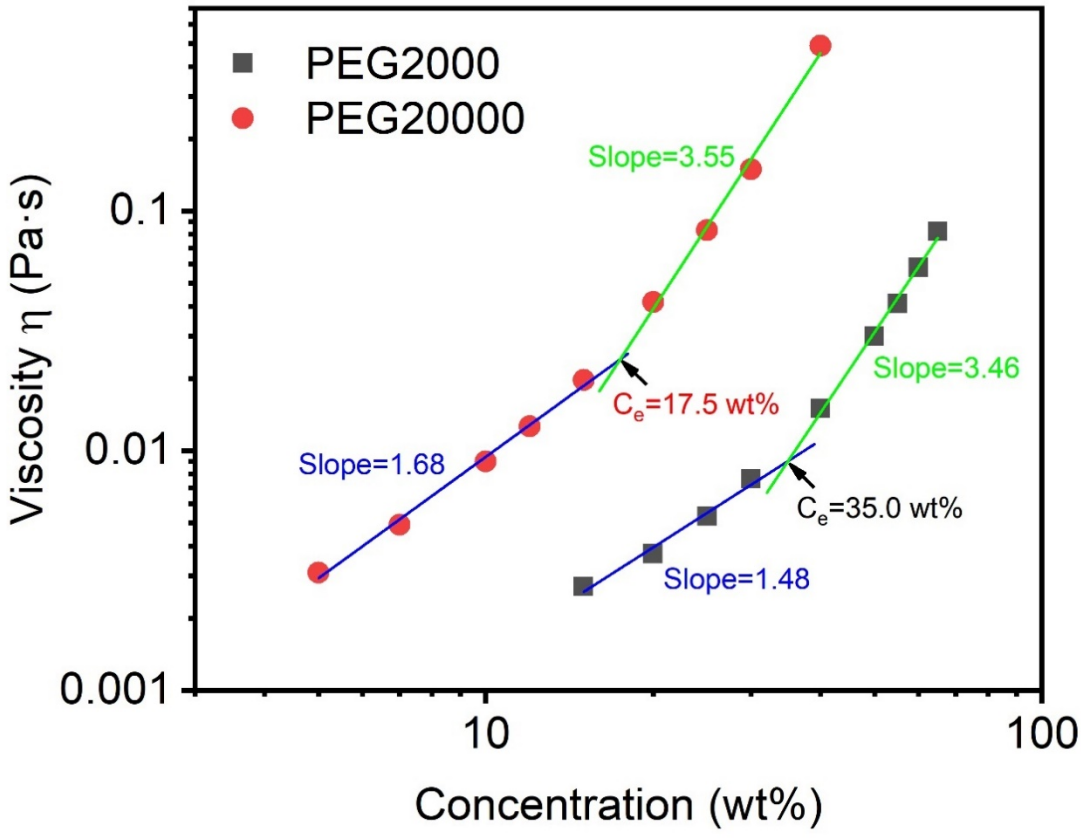

Figure 2.S7. Viscosities of PEG20000 and PEG2000 polymer aqueous solutions under different concentrations.

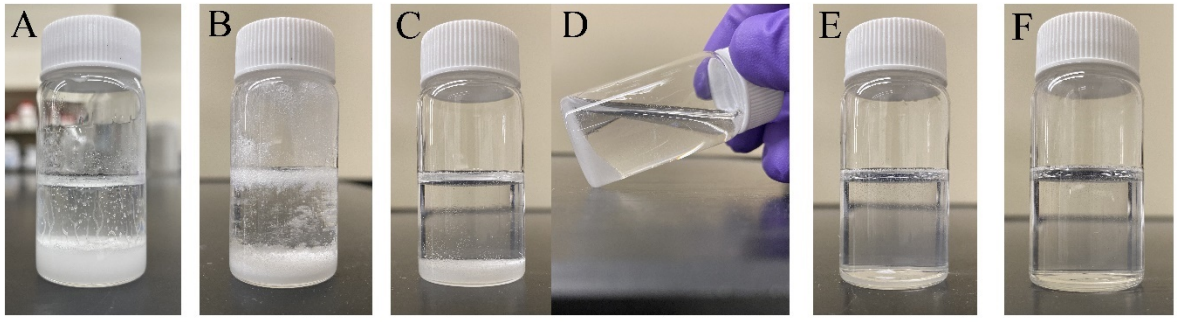

Figure 2.S8. Coacervation phenomenon under varied pH values. (A) The as-prepared coacervate with supernatant of pH 1.38. (B) Coacervate phase under pH of 2.04 adjusted by saturated LiOH aqueous solution. (C-D) Coacervate phase under pH of 2.14 still possessed flow property as a liquid. (E) Only a tiny amount of coacervate remained at the bottom of the vial under pH of 2.25. (F) Coacervate phase totally disappeared when pH increased to 4.30.

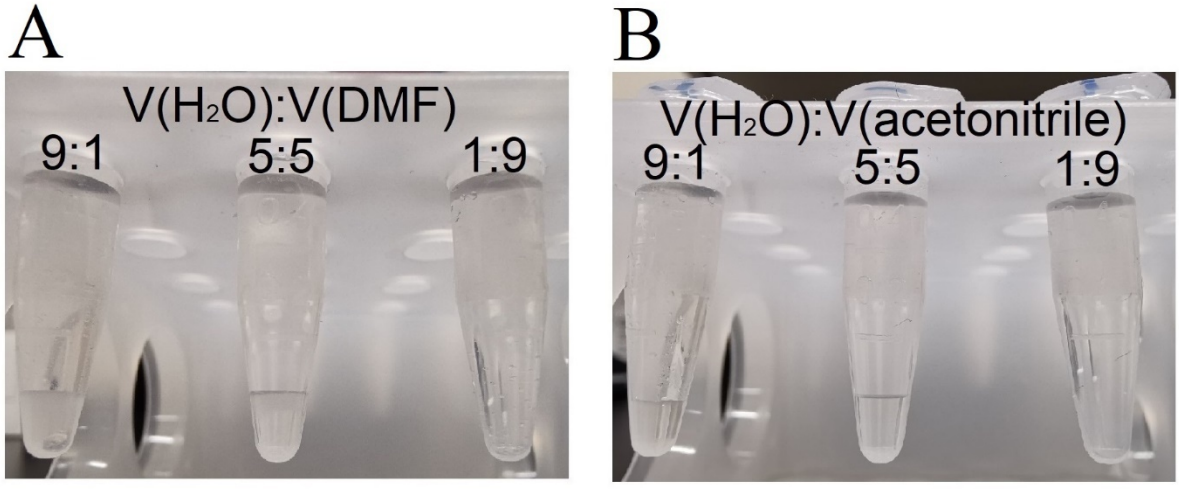

Figure 2.S9. (A**)** 30 mM PEG20000 is dissolved in a mixture of H_2O and dimethylformamide (DMF) (volume ratios of H_2O:DMF are 9:1, 5:5, and 1:9), and then mixed with 300 mM SiW solution at volume ratio of 4:6. (B) 30 mM PEG20000 is dissolved in a mixture of H_2O and acetronitrile (volume ratios of H_2O:acetonitrile are 9:1, 5:5, and 1:9), and then mixed with 300 mM SiW solution at volume ratio of 4:6.

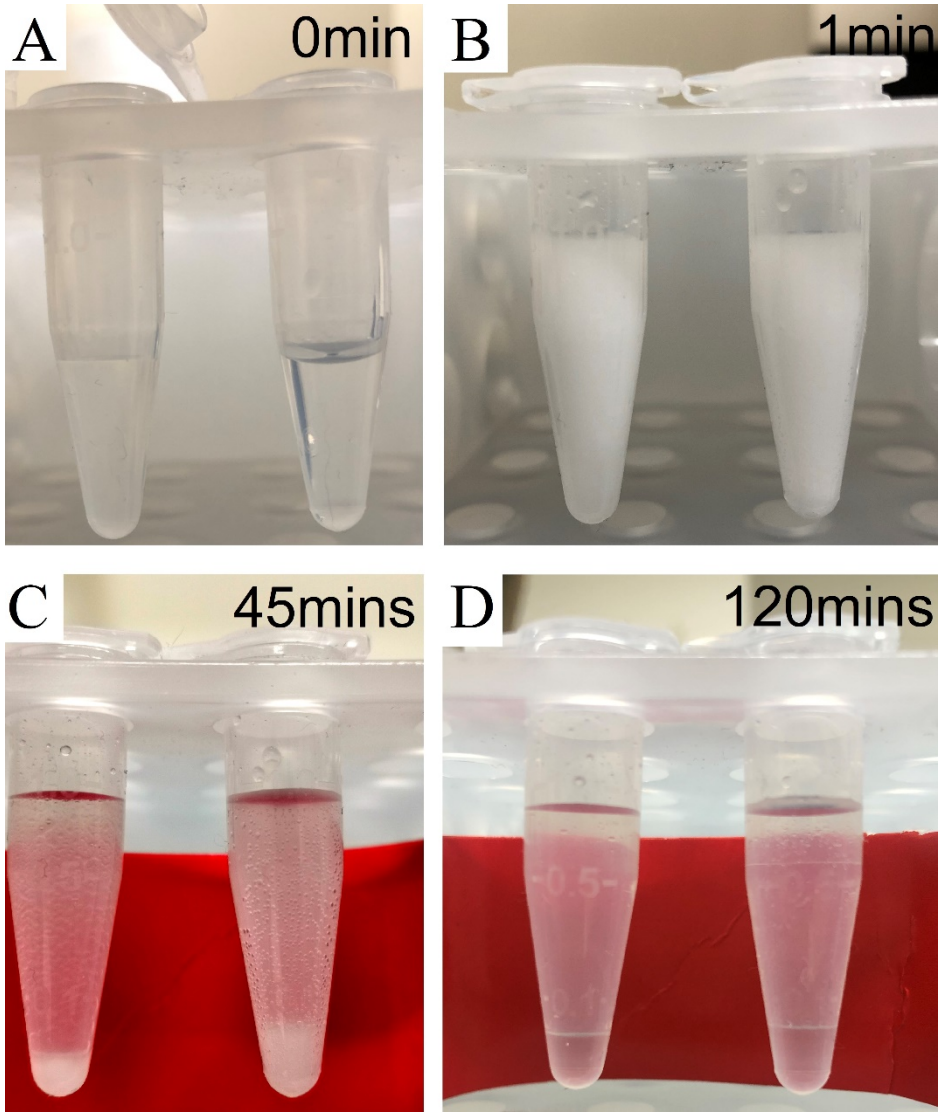

Figure 2.S10. (A**)** 30 mM PEG20000 is dissolved in a mixture of H_2O and ethanol (volume ratios of H_2O:ethanol are 9:1 (left) and 1:9 (right)). (B) With the addition of 300 mM SiW aqueous solution, coacervate droplets are formed immediately. (C) Obvious phase-separation is detected after 45 min. The agglomeration of coacervate droplets in the right solution is faster. (D) Final phase separation showing coacervate phases and their corresponding supernatants. Coacervate yield of the coacervation system is higher with more ethanol added.

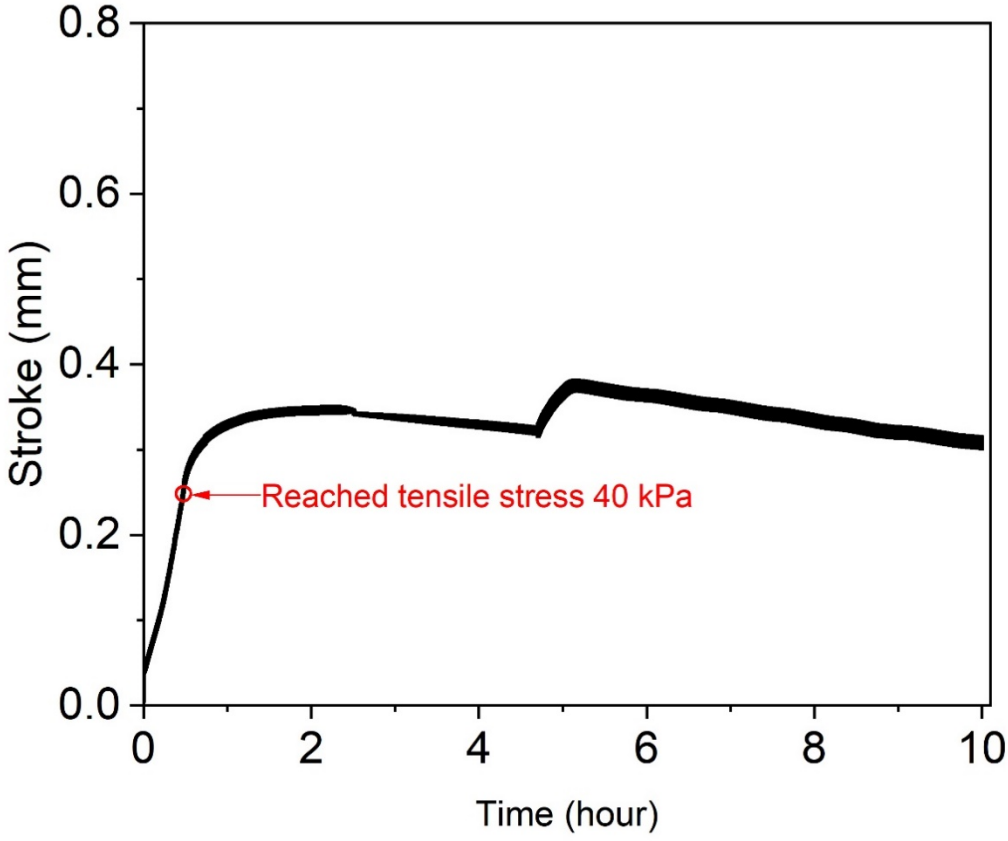

Figure 2.S11. Tensile creep test of coacervate. After 10 h, the two pieces of porcine skins were still attached to each other and no separation occurred. The increase of stroke around 5 h was most likely due to the failure of the adhesive at a certain region. The decrease of stroke in each step was probably caused by the drying of the coacervate and porcine skins.

References

1. a) H. G. Bungenberg de Jong, *Protoplasma* **1932**, *15*, 110; b) R. R. Poudyal, F. P. Cakmak, C. D. Keating, P. C. Bevilacqua, *Biochemistry* **2018**, *57*, 2509.

2. a) H. Okihana, C. Ponnamperuma, *Nature* **1982**, *299*, 347; b) S. Koga, D. S. Williams, A. W. Perriman, S. Mann, *Nat. Chem.* **2011**, *3*, 720.

3. B. S. Schuster, E. H. Reed, R. Parthasarathy, C. N. Jahnke, R. M. Caldwell, J. G. Bermudez, H. Ramage, M. C. Good, D. A. Hammer, *Nat. Commun.* **2018**, *9*, 2985.

4. G. C. Yeo, F. W. Keeley, A. S. Weiss, *Adv. Colloid Interface Sci.* **2011**, *167*, 94.

5. Y. Tan, S. Hoon, P. A. Guerette, W. Wei, A. Ghadban, C. Hao, A. Miserez, J. H. Waite, *Nat. Chem. Biol*. **2015**, *11*, 488.

6. a) K. A. Black, D. Priftis, S. L. Perry, J. Yip, W. Y. Byun, M. Tirrell, *ACS. Macro. Lett.* **2014**, *3*, 1088; b) D. S. Hwang, J. H. Waite, M. Tirrell, *Biomaterials* **2010**, *31*, 1080; c) S. Ambadipudi, J. Biernat, D. Riedel, E. Mandelkow, M. Zweckstetter, *Nat. Commun.* **2017**, *8*, 275.

7. a) H. Zhao, C. Sun, R. J. Stewart, J. H. Waite, *J. Biol. Chem.* **2005**, *280*, 42938; b) J. H. Waite, N. H. Andersen, S. Jewhurst, C. Sun, *J. Adhes.* **2005**, *81*, 297; c) B. P. Lee, P. B. Messersmith, J. N. Israelachvili, J. H. Waite, *Annu. Rev. Mater. Res.* **2011**, *41*, 99.

8. a) S. Basu, G. Bhattacharya, *Science* **1952**, *115,* 544; b) H. B. Bohidar, *J. Surface Sci. Technol.* **2008**, *24*, 105; c) D. Priftis, M. Tirrell, *Soft Matter* **2012**, *8*, 9396; d) J. A. Thomson, P. Schurtenberger, G. M. Thurston, G. B. Benedek, *Proc. Natl. Acad. Sci. USA* **1987**, *84*, 7079; e) S. Kim, J. Huang, Y. Lee, S. Dutta, H. Y. Yoo, Y. M. Jung, Y. Jho, H. Zeng, D. S. Hwang, *Proc. Natl. Acad. Sci. USA* **2016**, *113*, E847; f) M. Dompé, F. J. Cedano-Serrano, O. Heckert, N. van den Heuvel, J. van der Gucht, Y. Tran, D. Hourdet, C. Creton, M. Kamperman, *Adv. Mater.* **2019**, 31, 1808179; g) C. E. Sing, S. L. Perry, *Soft Matter* **2020**, 16, 2885.

9. H. Shao, R. J. Stewart, *Adv. Mater.* **2010**, *22*, 729.

10. J. P. Jones, M. Sima, R. G. O'Hara, R. J. Stewart, *Adv. Healthcare Mater*. **2016**, 5, 795.

11. P. G. Lawrence, Y, Lapitsky, *Langmuir* **2015**, 31, 1564.

12. Q. Wang, J. B. Schlenoff, *Macromolecules* **2014**, 47, 3108.

13. S. Kim, H. Y. Yoo, J. Huang, Y. Lee, S. Park, Y. Park, S. Jin, Y. M. Jung, H. Zeng, D. S. Hwang, Y. Jho, *ACS Nano* **2017**, *11*, 6764.

14. a) H. Shao, G. M. Weerasekare, R. J. Stewart, *J. Biomed. Mater. Res. A.* **2011**, *97*, 46; b) J. Monahan, J. J. Wilker, *Langmuir* **2004***, 20*, 3724.

15. A. Narayanan, J. R. Menefee, Q. Liu, A. Dhinojwala, A. Joy, *ACS Nano* **2020**, 14, 8359.

16. a) J. Chen, Q. Peng, T. Thundat, H. Zeng, *Chem. Mater.* **2019**, *31*, 4553; b) G. A. Williams, R. Ishige, O. R. Cromwell, J. Chung, A. Takahara, Z. Guan, *Adv. Mater.* **2015**, *27*, 3934.

17. a) B. K. Ahn, D. W. Lee, J. N. Israelachvili, J. H. Waite, *Nat. Mater.* **2014**, *13*, 867; b) B. K. Ahn, S. Das, R. Linstadt, Y. Kaufman, N. R. Martinez-Rodriguez, R. Mirshafian, E. Kesselman, Y. Talmon, B. H. Lipshutz, J. N. Israelachvili, J. H. Waite, *Nat. Commun.* **2015**, *6*, 8663.

18. a) M. B. Perrau, I. Iliopoulos, R. Audebert, *Polymer* **1989***, 30*, 2112; b) S. Yang, S. Ma, C. Wang, J. Xu, M. Zhu, *Aust. J. Chem.* **2014**, *67*, 11; c) K. Kim, M. Shin, M. Koh, J. H. Ryu, M. S. Lee, S. Hong, H. Lee, *Adv. Funct. Mater.* **2015**, *25*, 2402.

19. a) L. Li, B. Yan, J. Yang, L. Chen, H. Zeng, *Adv. Mater.* **2015**, *27*, 1294; b) A. Zumbuehl, L. Ferreira, D. Kuhn, A. Astashkina, L. Long, Y. Yeo, T. Iaconis, M. Ghannoum, G. R. Fink, R. Langer, D. S. Kohane, *Proc. Natl. Acad. Sci. USA* **2007***, 104,* 12994.

20. a) R. E. W. Hancock, H. Sahl, *Nat. Biotechnol.* **2006**, *24*, 1551; b) K. Baek, J. Liang, W. T. Lim, H. Zhao, D. H. Kim, H. Kong, *ACS. Appl. Mater. Interfaces* **2015**, *7*, 15359; c) L. Li, B. Yan, J. Yang, W. Huang, L. Chen, H. Zeng, *ACS. Appl. Mater. Interfaces* **2017**, *9*, 9221.

21. a) A. C. Anselmo, S. Mitragotri, *AAPS. J.* **2015**, *17*, 1041; b) A. Bijelic, M. Aureliano, A. Rompel, *Angew. Chem. Int. Ed.* **2019**, *58*, 2980; c) Y. Song, R. Tsunashima, *Chem. Soc. Rev.* **2012**, *41*, 7384.

22. a) J. Xu, X. Li, J. Li, X. Li, B. Li, Y. Wang, L. Wu, W. Li, *Angew. Chem. Int. Ed.* **2017**, *56*, 8731; b) B. Jing, J. Qiu, Y. Zhu, *Soft Matter* **2017**, *13*, 4881.

23. a) I. V. Kozhevnikov, *Chem. Rev*. **1998**, 98, 171; b) I. V. Kozhevnikov, *Russ. Chem. Rev*. **1987**, 56, 811.

24. a) J. Desbrieres, *Biomacromolecules* **2002**, 3, 342; b) J Cho, M. Heuzey, A. Bégin, P. J. Carreau, *J. Food Eng.* **2006**, 74, 500.

25. a) B. Jing, X. Wang, H. Wang, J. Qiu, Y. Shi, H. Gao, Y. Zhu, *J. Phys. Chem. B.* **2017**, *121*, 1723; b) X. Lin, Y. Wang, L. Wu, *Langmuir* **2009**, *25*, 6081.

26. I. V. Kozhevnikov, *Catal. Lett.* **1995**, 34, 213.

27. N. Xue, X. Qiu, V. Aseyev, F. M. Winnik, *Macromolecules* **2017**, *50*, 4446.

28. a) D. S. Hwang, H. Zeng, A. Srivastava, D. V. Krogstad, M. Tirrell, J. N. Israelachvili, J. H. Waite, *Soft Matter* **2010**, *6*, 3232; b) D. Priftis, R. Farina, M. Tirrell, *Langmuir* **2012**, 28, 8721.

29. D. S. Hwang, H. Zeng, Q. Lu, J. Israelachvili, J. H. Waite, *Soft Matter* **2012**, 8, 5640.

30. P. Karnal, P. Roberts, S. Gryska, C. King, C. Barrios, J. Frechette, *ACS Appl. Mater. Interfaces* **2017**, 9, 42344.

31. J. Chen, J. Liu, T. Thundat, H. Zeng, *ACS. Appl. Mater. Interfaces* **2019**, *11*, 18720.

32. a) M. Fujita, A. Takemura, H. Ono, M. Kajiyama, S. Hayashi, H. Mizumachi, *J. Appl. Polym. Sci.* **2000**, 75, 1535; b) H. Kim, H. Mizumachi, *J. Appl. Polym. Sci*. **1995**, 58, 1891.

33. Y. Murakami, M. Yokoyama, H. Nishida, Y. Tomizawa, H. Kurosawa, *Colloids Surf. B: Biointerfaces* **2008**, 65, 186-189.

34. M. C. Giano, Z. Ibrahim, S. H. Medina, K. A. Sarhane, J. M. Christensen, Y. Yamada, G. Brandacher, J. P. Schneider, *Nat. Commun.* **2014**, *5*, 4095.

35. S. Katz, M. Izhar, D. Mirelman, *Ann. Surg.* **1981***, 194,* 35.

36. a) D. L. George, P. M. Arnow, A. S. Fox, A. L. Baker, J. R. Thistlethwaite, J. C. Emond, P. F. Whitington, C. E. Broelsch, *Rev. Infect. Dis.* **1991***, 13,* 387; b) J. J. Wade, N. Rolando, K. Hayllar, J. Philpott-Howard, M. W. Casewell, R. Williams, *Hepatology* **1995***, 21,* 1328.

37. A. Bijelic, M. Aureliano, A. Rompel, *Chem. Commun.* **2018**, *54*, 1153.

CHAPTER 3 Coacervation-Driven Instant Paintable Underwater Adhesives with Tunable Optical and Electrochromic Properties

3.1 Introduction

Underwater adhesion is a great challenge for the development of universal adhesives, as water can hinder the intimate contact between the adhesives and the substrates by forming hydration layers on surfaces and weakening various adhesive bonds.[1, 2] Sessile organisms, such as sandcastle worms and mussels, can survive in turbulent seawater environment and have attracted extensive and intensive research interest for their innate and excellent underwater adhesion on various substrates.[3-7] Coacervation is considered to play a significant role in the secretion process of the underwater adhesives from sessile organisms,[8-10] and it also contributes to the formation of biological tissues such as extracellular matrices[11] and gradient materials like squid beak.[12, 13] Coacervation usually occurs when oppositely charged proteins, polymers and colloids aqueous solutions are mixed, yielding a polyelectrolyte-rich liquid phase named coacervate which coexists with an immiscible polyelectrolyte-sparse supernatant.[14-16] Water-born coacervates generally possess low interfacial energy to easily spread on different substrates, but further environment-triggered curing is required to fulfill the underwater adhesion. Moreover, their fabrication usually suffers from complex synthesis, specific stoichiometry of the components, and the adjustment of ionic strength and pH. Therefore, instant underwater adhesives that can be facilely prepared and delivered are highly desired for practical applications in complex environments (e.g., physiological environment), especially where ideal curing conditions can hardly be achieved.

Various types of intermolecular interactions can induce coacervation, including electrostatic interaction, cation-π interaction, hydrogen-bonding interaction, and hydrophobic interaction. Sandcastle worm secretes two oppositely charged proteins from different glands

interacting with each other via electrostatic interaction to generate coacervate, which is crosslinked by Ca^{2+} and Mg^{2+} ions in the surrounding seawater and oxidized by the pH jump from the acidic glands to the basic seawater to achieve underwater adhesion.[17] Adhesives mimicking sandcastle worm underwater adhesion have been developed, where complicated synthesis and particular environmental triggers such as temperature or pH jump are usually indispensable.[5] Short-range cation-π interaction was found to drive the complex coacervation between like-charged mussel-inspired polyelectrolytes[9] and in a single cationic recombinant mussel foot protein.[10] A high salt concentration (at seawater level of about 0.7 M) was needed for the coacervation of the cationic recombinant mussel foot protein[10] and no macroscopic adhesive property was reported. Hydrogen-bonding interaction has been proved to contribute to the formation of adhesives based on the coacervation between tannic acid/silicotungstic acid and poly(ethylene glycol), which could serve as effective hemostatics.[18, 19] The preparation of such adhesives was very facile, but they were still unable to accomplish robust underwater adhesion. It is expected that the synergy of different intermolecular interactions could endow coacervation systems strong underwater adhesion. A previous study showed that introducing thermo-responsive poly(N-isopropylacrylamide) (PNIPAM) into oppositely charged polyelectrolytes could endow the electrostatic interaction-driven coacervate with thermo-responsiveness, which turned the coacervate to be an underwater adhesive hydrogel upon the increase of temperature, owing to the hydrophobic interaction among methyl groups of PNIPAM.[20] In another study, hydrophobic interaction-actuated tropoelastin-mimetic coacervate was equipped with mussel-inspired 3, 4-dihydroxyphenylalanine (DOPA) groups to gain adhesive property, and UV crosslinking was employed to acquire suitable cohesion.[21] This charge-free coacervate could rapidly achieve underwater adhesion in less than 300 s despite with relatively low adhesion strength of less than 100 kPa.[21] Cooperation of electrostatic and hydrogen-bonding interaction and other interactions

between polyamidoamine-epichlorohydrin and tannic acid produced an instant underwater adhesive with antibacterial property.[22]

Smart and functional underwater adhesives that can simultaneously achieving underwater adhesion and stimuli-responsive functionalities are intriguing and offer great promise for the development of next-generation electronic or biomedical devices. For example, adhesives with electrochemical properties can act as paintable/printable electrodes toward safe, portable and environmental-friendly energy storage devices such as aqueous batteries.[23] Electrochromic devices have been widely studied for their tunable optical properties which have great potential in applications including energy-saving smart windows, visual-comfortable displays, intelligent wearable electronics, eye-friendly rear mirrors and sunglasses, and so on.[24-26] Electrochromic aqueous batteries attracted much research attention due to their charge/discharge-accompanied reversible color switch, showing great potential when used as user/device interfaces.[23, 27, 28] However, achieving suitable flexibility still remains a challenge in the development of electrochromic aqueous batteries, as conventional electrochromic electrodes are usually fabricated by depositing nanostructured electrochromic materials on rigid transparent conductors via high-temperature treatment.[24, 27, 29-32] 3D printing has been demonstrated an efficient and low-cost solution, but up to now, extra elastic polymer binders are required to attach the electrochromic nanomaterials on the conductive substrates, during which toxic organic solvents are usually used.[33] Aqueous-based inks are desirable for 3D printing thanks to their inexpensiveness and environment-friendliness, however, organic solvents were still widely exploited to acquire good wettability.[34] Therefore, water-borne adhesive coacervates with low interfacial tension, liquid-like property and instant adhesiveness are ideal candidates for 3D printing to fabricate flexible devices, such as electrochromic electrodes used in aqueous environment.[23, 35]

In this work, we report the fabrication of a series of novel instant underwater electrochromic adhesives via simple mixing of silicotungstic acid (SiW, $H_4[Si(W_3O_{10})_4]$) and poly(ethylene glycol)$_{19}$-*b*-poly(propylene glycol)$_{69}$-*b*-poly(ethylene glycol)$_{19}$ (PEG-PPG-PEG, P123) aqueous solutions. The coacervation was mainly driven by the hydrogen bonding between SiW clusters and the PEG shells of P123 micelles, where the hydrophobic cores of P123 micelles provided a second crosslinking to reinforce the network. The synergy of the hydrogen bonding and hydrophobic interactions effectively enhanced the mechanical property and the adhesiveness of the coacervates. The as-prepared coacervates could be painted on and bind various substrates underwater with instant and excellent adhesion strength up to 479.6 kPa on poly(methyl methacrylate) (PMMA). Additionally, the thermo-responsive property of P123 micelles endowed the coacervates with tunable optical property in response to temperature. Owing to the well-known reduction reaction-related color change of SiW[36] and the excellent stability of the coacervates in high-salinity aqueous solution, the coacervates exhibited quick and reversible electrochromic responsiveness to both self-powered electrochemical reaction and external voltages, making them promising electrode materials for flexible electronics.

3.2 Experimental Section

3.2.1 Materials

Silicotungstic acid (SiW), Pluronic® P123 (poly(ethylene glycol)$_{19}$-*b*-poly(propylene glycol)$_{69}$-*b*-poly(ethylene glycol)$_{19}$, average M_n ~5,800), Pluronic® F68 (poly(ethylene glycol)$_{77}$-*b*-poly(propylene glycol)$_{29}$-*b*-poly(ethylene glycol)$_{77}$, average M_n ~8,400), indium tin oxide (ITO) coated glass slide (rectangular, surface resistivity 70-100 Ω/sq, slide), poly(ethylene glycol) (BioUltra, for molecular biology, 8000), and LiOH were purchased from Sigma-Aldrich and used

as received. Lithium chloride (LiCl, 98.5%), sodium chloride, potassium chloride, and calcium chloride were purchased from Fisher Scientific and used as received. Poly(methyl methacrylate) (PMMA) round disks with diameter of 18.5 mm, wood and glass round disks with diameter of 25 mm were purchased from Amazon Canada.

3.2.2 Preparation of Coacervates

Silicotungstic acid (SiW) aqueous solutions with weight percentages of 0.1%, 1%, 10%, 20% and 40% were prepared using deionized water. P123/F68 aqueous solutions with weight percentages of 0.1%, 1%, 10%, 15% and 20% were prepared using deionized water. In a typical preparation process of the coacervate, SiW aqueous solution and P123/F68 aqueous solution were directly mixed at the volume ratio of 1:1, followed by vigorously shaking and centrifugation at the speed of 5000 rpm for 10 mins. The coacervate was acquired as the dense bottom phase. Meanwhile, a corresponding phase diagram of coacervation was obtained using SiW and P123 aqueous solutions of various concentrations. The coalescence process of coacervate droplets was observed under a confocal microscope, and the sample was prepared by dropping 5 μL 40 wt% SiW aqueous solution on a glass slide, followed by the addition of 5 μL 10 wt% P123 aqueous solution on the previous drop, which was then covered by a coverslip.

3.2.3 Rheological Properties of Coacervates

The rheological properties of the coacervates were studied via a TA Instruments AR-G2 rheometer using a 20 mm (diameter) 2° cone geometry with a gap of 53 μm. Oscillatory angular frequency sweep ranging from 0.1 rad/s to 100 rad/s at a fixed strain of 2% was carried out at 20 ℃ to characterize the shear moduli of the coacervates. The viscosity of the coacervates was

characterized with shear rate ranging from 0.1/s to 100/s. For SiW and P123 aqueous solutions, their rheological properties were measured in a DIN concentric cylinder with an operating gap of 5917.1 μm, and the test parameters were consistent with those of the coacervates. To investigate the effect of salts on the viscosity of the coacervates, selected salts (i.e., LiCl, NaCl, KCl, and $CaCl_2$) were first added into SiW and P123 aqueous solutions to a desired concentration before mixing the solutions. All the rheological properties were carried out with three independently prepared samples.

3.2.4 Underwater Adhesion Properties of Coacervates

Underwater adhesion properties of the coacervates were characterized on an AGS-X universal tensile testing machine (Shimadzu, Japan) at room temperature. A water container was attached to the compression cylinders to provide an underwater environment. PMMA, wood and glass round disks were glued on the center of the two compression cylinders with super glue, respectively, until totally dried in air. Then the two compression cylinders were mounted onto the tensile testing machine with a 5000 N load cell and immersed underwater. Subsequently, 100 μL coacervate was injected on the lower cylinder and being compressed by the upper cylinder with a force of 30 N or 300 N for 10 s. The adhesion strength was then obtained by lifting the upper cylinder at a constant speed of 100 mm/min. The underwater adhesion tests in different salt solutions (Milli-Q water, 0.1 M LiCl, NaCl, KCl, $CaCl_2$ and 1.0 M LiCl) were carried out between a stainless steel substrate (upper surface) with diameter of 12 mm and a transparent PMMA disk (lower surface) with diameter of 18.5 mm. The coacervate of 50 μL was injected onto the PMMA surface and compressed by the upper surface with a force of 30 N for 10 s. The adhesion strength

was then obtained by lifting the upper cylinder at a constant speed of 5 mm/min. All the instant underwater adhesion strengths were determined based on at least 8 samples.

3.2.5 Thermo-responsive optical properties of coacervates

The thermo-responsive optical properties of the coacervates were evaluated by alternatively immersing the coacervate-painted glass slide in a 60 ℃ water bath and an ice-water bath for several cycles. The temperature-induced variation of transparency was quantified by a microplate reader (Cytation 5, Biotek, USA) at different temperatures in the visible light range (400-800 nm), with samples of 6.5 mm diameter and 1 mm thickness. The thermo-induced optical property of the coacervates was quantified on a UV-vis spectrometer (Evolution 300, Thermo Scientific, CA) with a temperature controller (Isotemp, Fisher Scientific, CA) and a sample with thickness of 10 mm. The repeatable heat-cool cycles were conducted between 40 and 55 ℃. To unveil the mechanism of the transparency change, the size of 0.1 wt% P123 micelles at various temperatures ranging from 10 to 60 ℃ were characterized by dynamic light scattering (DLS) with a Malvern Zetasizer Nano ZSP. The morphology of P123 micelles at 20 ℃ and 60 ℃ was examined using a Dimension Icon atomic force microscope (AFM) system (Bruker, Santa Barbara, CA, USA) operating in the tapping mode in air. The samples were prepared by dropping 10 μL of 0.1 wt% P123 aqueous solution (stored at the desired temperature) on a clean silicon wafer substrate till fully dried in air at the corresponding temperature.

3.2.6 Electrochromic properties of coacervates

The electrochromic properties were characterized by sandwiching the coacervate between two ITO-coated glass slides, where the external voltages applied on the outer surfaces of the

bonded glass slides were provided by an electrochemical workstation (CHI920, CH Instruments, USA) with a Multi-Potential Steps mode. Coacervates before and after electrochromism were freeze-dried and characterized by X-ray photoelectron spectroscopy (XPS) to reveal the binding energies of the oxidized and reduced states of tungsten.

3.3 Results and discussion

3.3.1 Fabrication and intermolecular interactions of the SiW-P123 coacervate

The fabrication process of the SiW-P123 coacervate adhesives was very facile. For example, 10 wt% P123[37] aqueous solution was directly mixed with 40 wt% SiW aqueous solution at a volume ratio of 1:1, leading to a turbid solution after vigorous shaking (**Figure 3.1A**). Coacervate droplets with sizes ranging from several to tens of micrometers were dispersed in the aqueous environment (**Figure 3.1B**), where small coacervate droplets could coalesce into bigger ones. The cryogenic transmission electron microscopy (cryo-TEM) image of the coacervate droplet exhibited a densely packed continuous sponge-like network structure (**Figure 3.1C**), suggesting stable and strong physical interactions between SiW clusters and P123 micelles (**Figure 3.1A**). After centrifugation of 5000 rpm for 10 minutes, the solution could completely separate into a white coacervate phase and a corresponding transparent supernatant, from which mass production of the adhesive coacervate could be readily achieved.

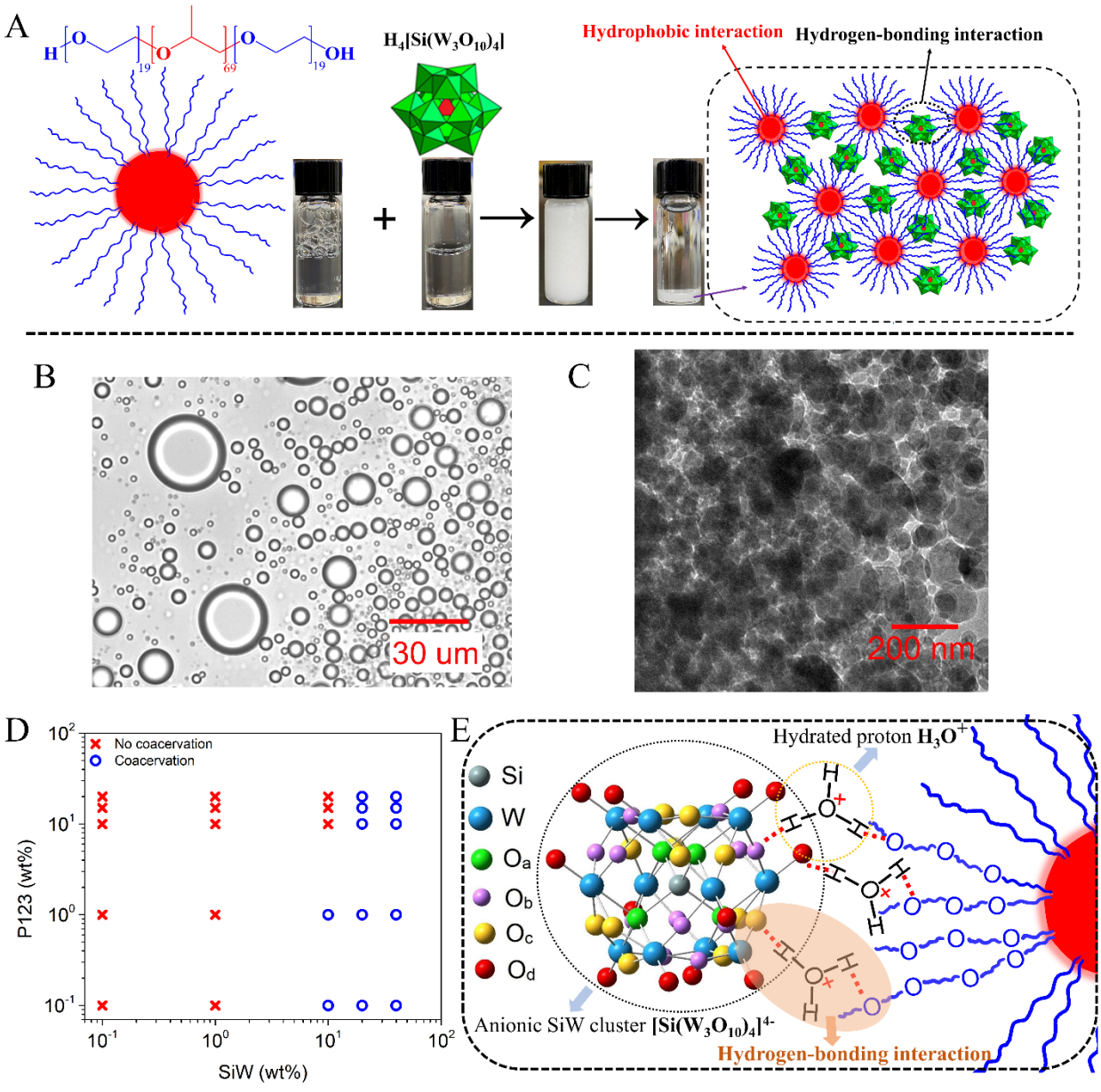

Figure 3.1. Fabrication and intermolecular interaction of the SiW-P123 coacervate. (A) Schematic illustration of the fabrication process of the SiW40-P123-10 coacervate. (B) Distribution of newly formed SiW40-P123-10 coacervate droplets observed under an optical microscope. (C) Cryo-TEM image of the SiW40-P123-10 coacervate. (D) Phase diagram of coacervation between SiW and P123 aqueous solutions. (E) Schematic illustration of the proposed interaction mechanism between SiW and P123 for the coacervate formation.

Different concentrations of SiW and P123 aqueous solutions with a fixed volume ratio 1:1 were employed to yield a series of coacervates, which were denoted as SiWx-P123-y (x and y represent the weight percentage of SiW aqueous solution and P123 aqueous solution, respectively), and their phase behaviors are shown in **Figure 3.1D**. When the concentration of SiW was 0.1 wt% and 1 wt%, no coacervation occurred with P123 solution ranging from 0.1 wt% to 20 wt%, which might be because of the sparse distribution of the small SiW clusters. When the concentration of SiW was increased to 10 wt%, coacervate could be detected only with 0.1 wt% and 1 wt% P123, suggesting that the quantity of SiW clusters was still not sufficient to crosslink concentrated P123 micelles. Further increasing the concentration of SiW to 20 wt% and above, coacervates could be formed with P123 at all the concentrations used (0.1 to 20 wt%). The simple binary phase diagram of the SiW-P123 coacervation system holds great potential to understand and develop platforms with liquid-liquid phase separation. As shown in **Figure 3.S1**, the yields of SiW40-P123-10/15/20 coacervates were relatively high after mixing, among which SiW40-P123-10 exhibited the highest viscosity (**Figure 3.S2**) to resist the flow of the material underwater. Therefore, SiW40-P123-10 was employed for further characterization in this work if not specified.

Our previous study demonstrated that the coacervation between SiW and PEG was most likely originated from the hydrogen bonding between oxygens of SiW and etheric oxygens of PEG bridged by hydrated protons.[19] As P123 micelle contains a hydrophobic PPG core and hydrophilic PEG shell, a similar coacervation mechanism is expected to occur between SiW and PEG shells. According to the FTIR spectra of SiW powder and freeze-dried SiW40-P123-10 coacervate (**Figure 3.S3**), the Keggin structure of SiW was well maintained before and after coacervation, with typical stretching vibration bands of W=O_d, Si-O_a, W-O_b-W (edge shared), W-O_c-W (corner shared) shifted from 1015, 977, 910, 743 cm^{-1} to 1008, 967, 911, 771 cm^{-1}, originating from intermolecular interactions with P123 (**Figure 3.1E** and **Figure 3.S3**).[38] As for

P123, C-O-C shifted from 1103 to 1070 cm^{-1} after coacervation, indicating etheric oxygens were occupied due to intermolecular interactions. Besides, antisymmetric and symmetric stretching of C-H as well as symmetric deformation of $-CH_3$ were observed at 2970, 2870 and 1372 cm^{-1}, respectively, in the coacervate, suggesting the hydrophobic interaction among methyl groups of P123 micelles was maintained after coacervation.[39] SiW is usually regarded as a strong acid with fully ionized protons.[40] According to our previous study, the primary driving force for coacervation was most likely attributed to the hydrogen-bonding interactions ($W{=}O\cdots H_3O^+\cdots O$) between oxygens (both terminal O_d atoms (predominant) and bridging oxygens O_b and O_c)) of SiW and etheric oxygens of PEG bridged by hydrated protons, which was demonstrated not only by FTIR spectra but also by changing end groups of PEG, adjusting the pH of the solutions and modulating the solvents.[19] As both hydrogen-bonding interaction and hydrophobic interaction tend to be affected by temperature,[41, 42] the viscosities of SiW40-P123-10 (driven by hydrogen-bonding interaction and hydrophobic interaction) and SiW40-PEG8000-10 (actuated by hydrogen-bonding interaction, where PEG with molecular weight of 8,000 was used instead of P123) coacervates as well as 10 wt% P123 aqueous solution (assembled by hydrophobic interaction) were characterized with temperature ranging from 20 ℃ to 45 ℃. The results (**Figure 3.S4**) revealed that the viscosities of all the samples decreased with increasing the temperature; while the highest viscosity and the most noticeable decrease were detected for the SiW40-P123-10 coacervate, which was attributed to the weakened hydrogen-bonding interaction between SiW clusters and P123 micelles as well as between the PEG shells of P123.[43] The role of hydrated protons played in the coacervation was also investigated by neutralizing SiW aqueous solution with saturated LiOH aqueous solution. The pH of 40 wt% SiW aqueous solution was measured to be 1.14; however, when it was adjusted to 1.75, the SiW aqueous solution could not form coacervate with 10 wt% P123 (**Figure 3.S5**). The above result demonstrated that the coacervation

of SiW-P123 system was highly dependent on the presence of hydrated protons, and the pH required for the formation of SiW-P123 coacervate was much lower than that of the SiW-PEG coacervate system (pH<4.3) we reported previously.[19] A possible reason was that the chain length of PEG on the shells of P123 was shorter than the previously used linear PEG, therefore, more proton crosslinkers would be required to bind the P123 micelles and SiW clusters. PEG is a well-known nonionic polymer and a hydrogen bonding accepter, while P123 was reported to carry slight negative charges in water (zeta potential of -6.8 mV at pH of 7.4).[44] During the formation of coacervate, concentrated SiW aqueous solution was employed (e.g., 40 wt%), and P123 micelles were dispersed in water with a high concentration of hydrated protons, where the Debye length of the electric double-layer was calculated to be $\kappa^{-1}\sim\sqrt{c}/0.304$ nm~4.2 nm (c is the concentration of electrolytes with unit of mol L^{-1}).[45] Due to the short Debye length, long-range electrostatic interaction between the negatively charged SiW clusters and P123 molecules tends to be significantly suppressed, while electrostatic interaction between the molecules might also play a role in the short range in addition to the strong hydrogen bonding and hydrophobic interaction within the SiW40-P123-10 coacervate. The coacervation of SiW-P123 system was proposed to be mainly driven by hydrogen-bonding interaction between oxygens of SiW and etheric oxygens of P123 shells bridged by hydrated protons, where the hydrophobic interaction, which drove the self-assembly of P123 micellar structures, played a synergetic role in strengthening the coacervate as illustrated in **Figure 3.1A** and **E**.

3.3.2 Rheological properties

Rheological properties including viscosity η, storage modulus G' and loss modulus G'' of the SiW-P123 coacervates were characterized with a rheometer. Compared to the low viscosities

of 40 wt% SiW (~0.00129 Pa·s) and 10 wt% P123 (~0.0057 Pa·s) aqueous solutions, the viscosity of the SiW40-P123-10 coacervate drastically increased to ~193.77 Pa·s, indicating the strong intermolecular interactions between SiW clusters and P123 micelles (**Figure 3.2A**). It is noted that when the concentration of P123 varied from 10 wt% to 20 wt%, the viscosities of the formed coacervates slightly decreased (**Figure 3.2B**) while the volume of the coacervate phase increased by 86.4% (**Figure 3.S6**), which might be due to the slightly weakened intermolecular interaction among P123 micelles and SiW clusters. To illustrate the effect of the hydrophobic cores of polymeric micelles on the coacervates, F68 was also used to form the coacervates, which contained more hydrophilic PEG and less hydrophobic PPG compared to P123. As displayed in **Figure 3.2B**, the viscosities of SiW40-P123-10/15/20 coacervates were much larger than those of SiW40-F68-10/15/20 coacervates, which was mainly attributed to the stronger hydrophobic interactions among the PPG cores of P123 micelles. Moreover, the viscosity of SiW40-PEG8000-10 coacervate was only about 10% of that of SiW40-P123-10 coacervate (**Figure 3.S7**), indicating that stable hydrophobic micelle cores could act as crosslinking points to enhance the mechanical properties of the coacervates.

Traditional coacervates are driven by electrostatic interactions between oppositely charged molecules, where salt plays a crucial role in balancing electrostatic interaction and tuning rheological properties.[14] Generally, above a critical salt concentration, the polyelectrolyte systems are always miscible and coacervation cannot occur due to the screen of electrostatic interaction.[14, 46, 47] In addition, the formation of coacervates based on cation-π interaction require high salt concentration to shield the repulsive electrostatic interaction between likely-charged molecules.[9, 10] In our work, the SiW-P123 coacervation system was triggered by the synergy of hydrogen-bonding interaction and hydrophobic interaction, and the coacervates can form in a salt-free environment. However, their properties can be affected by the addition of salts. As shown in

Figure 2B, C and **Figure 3.S8**, without the addition of salt, the SiW40-P123-20 coacervate exhibited low shear modulus and viscosity. With the addition of LiCl ranging from 0.1 to 1.0 M, the coacervate still maintained its liquid-like property, but the rheological properties were strengthened with increasing the salt concentration (**Figure 3.2C, D**). With 0.1 M LiCl introduced, the viscosity of the coacervate increased from ~166.8 Pa·s to ~209.3 Pa·s (at shear rate of 10 s^{-1}), although their shear moduli were comparable. Further raising the LiCl concentration to 0.5 M and 1.0 M, both shear moduli and viscosity of coacervate were substantially enhanced. The storage modulus, loss modulus (at angular frequency of 10 rad s^{-1}) and viscosity (at shear rate of 10 s^{-1}) of the coacervate were significantly enhanced by 5205%, 1201% and 1145%, respectively, with the addition of 1.0 M LiCl as compared to the case without salt. Therefore, the presence of LiCl up to 1.0 M was still safe for the formation of the SiW-P123 coacervation system. Meanwhile, the effect of different salts including LiCl, NaCl, KCl and $CaCl_2$ on the rheological properties of the coacervate was also studied (**Figure 3.2E, F**). By varying the different types of salts at a fixed concentration 0.1 M, the salt-induced enhancement of shear moduli and viscosity of the coacervate followed the trend: LiCl < NaCl < KCl < $CaCl_2$, where LiCl, NaCl and KCl could salt out PEG from aqueous solution following the Hofmeister series while $CaCl_2$ was capable of interacting with electronegative oxygens of SiW clusters.[48, 49] Therefore, varying the concentration and type of salts provide a feasible way to tune the mechanical properties of the SiW-P123 coacervates over several orders of magnitude for diverse practical applications.

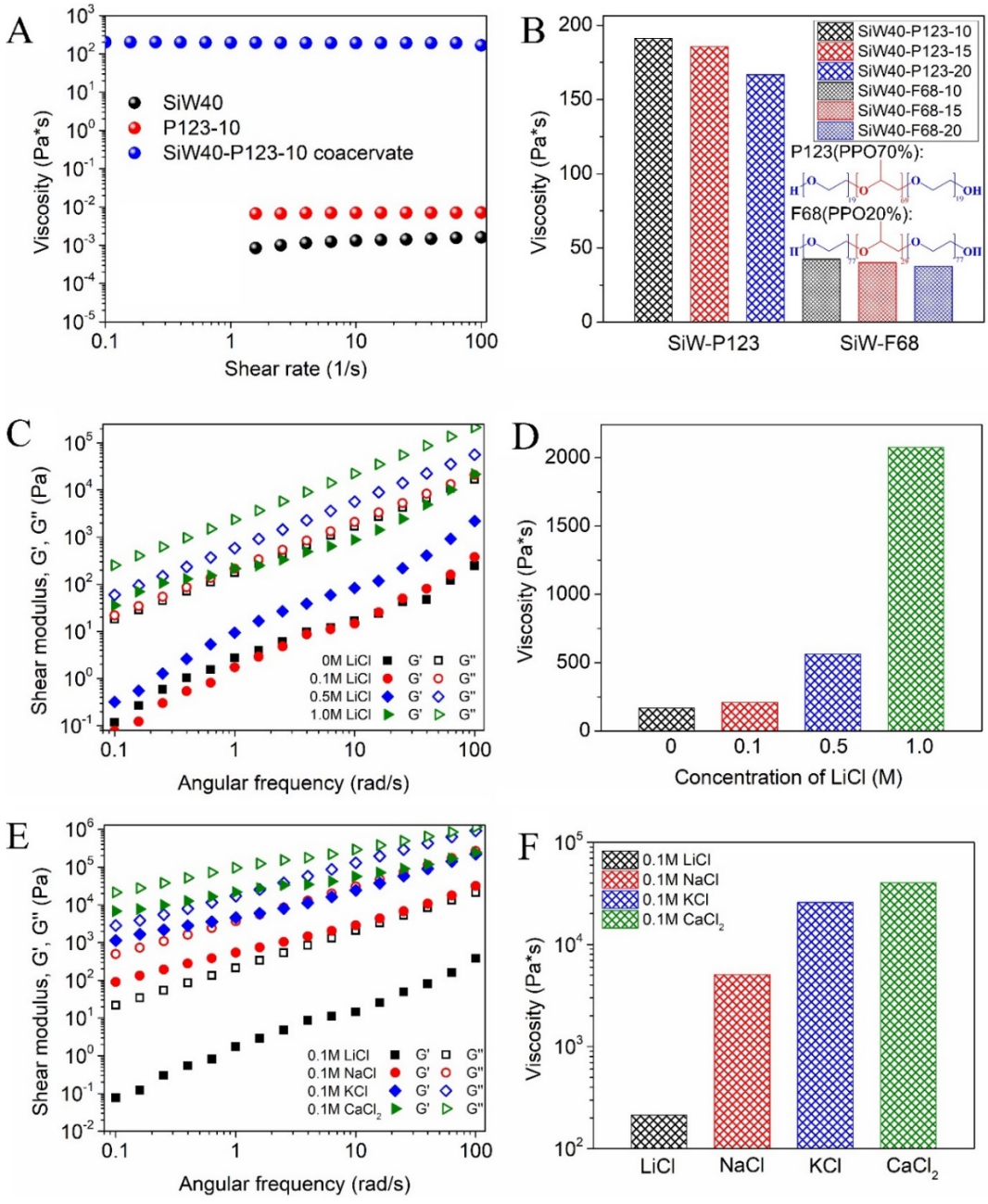

Figure 3.2. Rheological properties of the SiW-P123 coacervates. (A) Viscosities of 40 wt% SiW aqueous solution, 10 wt% P123 aqueous solution, and the corresponding coacervate. (B) Viscosities of SiW40-P123-10/15/20 coacervates and SiW40-F68-10/15/20 coacervates at shear rate of 10 s^{-1}. (C) and (D) Shear moduli and viscosity (at shear rate of 10 s^{-1}) of SiW40-P123-20 coacervate with 0, 0.1, 0.5 and 1.0 M LiCl. (E) Shear moduli and (F) Viscosity (at shear rate of 0.1 s^{-1}) of SiW40-P123-20 coacervate with 0.1 M LiCl, NaCl, KCl and $CaCl_2$.

3.3.3 Underwater adhesive properties

The as-prepared SiW40-P123-10 coacervate could be facilely painted on glass slide underwater with designed shapes and immediately resist the water flush, suggesting its excellent underwater adhesive property (**Figure 3.3A**). Meanwhile, the coacervate could facilely bind different materials such as wood, coin, stone, and glass slide as well as a plastic substrate underwater (**Figure 3.3B**). As shown in **Figure 3.3C**, the coacervate instantly and firmly adhered two weights together underwater and easily support a mass of 100 g. Besides, the coacervate could also instantly bind two porcine skins underwater which could resist repeatable movement and swing (**Figure 3.3D**), holding great potential in the field of biomedical tissue glue. The underwater adhesion of the coacervate on different substrates was quantitatively examined and the results are presented in **Figure. 3.3E**, showing the highest adhesion strength of 479.6 kPa to poly(methyl methacrylate) (PMMA, contact angle of 67.3°). It was most likely attributed to the synergetic effect of hydrogen bonding and hydrophobic interactions, where the electronegative oxygen atoms of -(C=O)-OCH_3 groups served as proton acceptors to form hydrogen bonds and the extensive methyl groups participated in hydrophobic interaction with the coacervate. The instant adhesion strength of the coacervate on the glass substrate (contact angle of 15.1°) was determined to be 297.1 kPa because only hydrogen bonding contributed to the adhesion. The coacervate on the wood surface exhibited a relatively low adhesion of 128.5 kPa, which was possibly due to the existence of micropores and microtubes on the wood surface that adsorbed the coacervate (**Figure 3.S9**), decreasing the effective contact area between the wood surfaces. Additionally, the underwater adhesion of the coacervate was pressure-sensitive as illustrated in **Figure 3.3F**. When two glass substrates bonded by the coacervate was compressed with a force of 300 N for 10 s, the adhesion strength of the coacervate was measured to be 442.4 kPa, which was increased by 48.9% compared to that of the sample under 30 N compression for 10 s. The pressure-sensitivity of the

underwater adhesion might originate from two reasons: first, the rearrangement of P123 polymer chains within the coacervate phase under pressure could affect the molecular interactions within the coacervate and at the interface of coacervate/substrate;[50] second, the water pockets or air bubbles trapped within the coacervate or at the interface of coacervate/substrate tended to be removed by compression or through the reconfiguration of PEG polymer chains, creating a larger contact area and leading to a stronger adhesion.[51, 52] Moreover, as salt is ubiquitous in physiological environment of human,[53] seawater,[5, 10] and aqueous batteries,[23] it is important to study the effect of salts on the underwater adhesion strength of the coacervate. As shown in **Figure 3.3G**, when the salt concentration was fixed at 0.1 M, the adhesion strength of the coacervate increased following the trend of LiCl< NaCl < KCl < $CaCl_2$, which was consistent with the variation of rheological properties (**Figure 3.2F**). The variation of instant underwater adhesion strength of the coacervate in LiCl (0.1 and 1.0 M) aqueous solutions also agreed with the change of rheological properties (**Figure 3.2D**). In Milli-Q water, the coacervate exhibited the highest instant adhesion strength, which might suggest that the addition of saline ions could impair the electrostatic interactions at the coacervate/substrate interfaces.[54] Herein, the underwater instant adhesion strength of the as-prepared coacervate are superior to the previously reported coacervates (<200 kPa for all cases[18] and ~420 kPa for PMMA substrate[22]) and even some adhesive hydrogels (≤180 kPa[55, 56]). A detailed summary of the reported wet/underwater adhesives is presented in **Table 3.S1**, demonstrating the facile fabrication as well as instant and strong underwater adhesion of SiW40P123-10 coacervate, which shows advantages to all the listed adhesives. The instant and robust underwater adhesion of the coacervate enable it a promising adhesive for various applications, especially those in aqueous or wet environments.

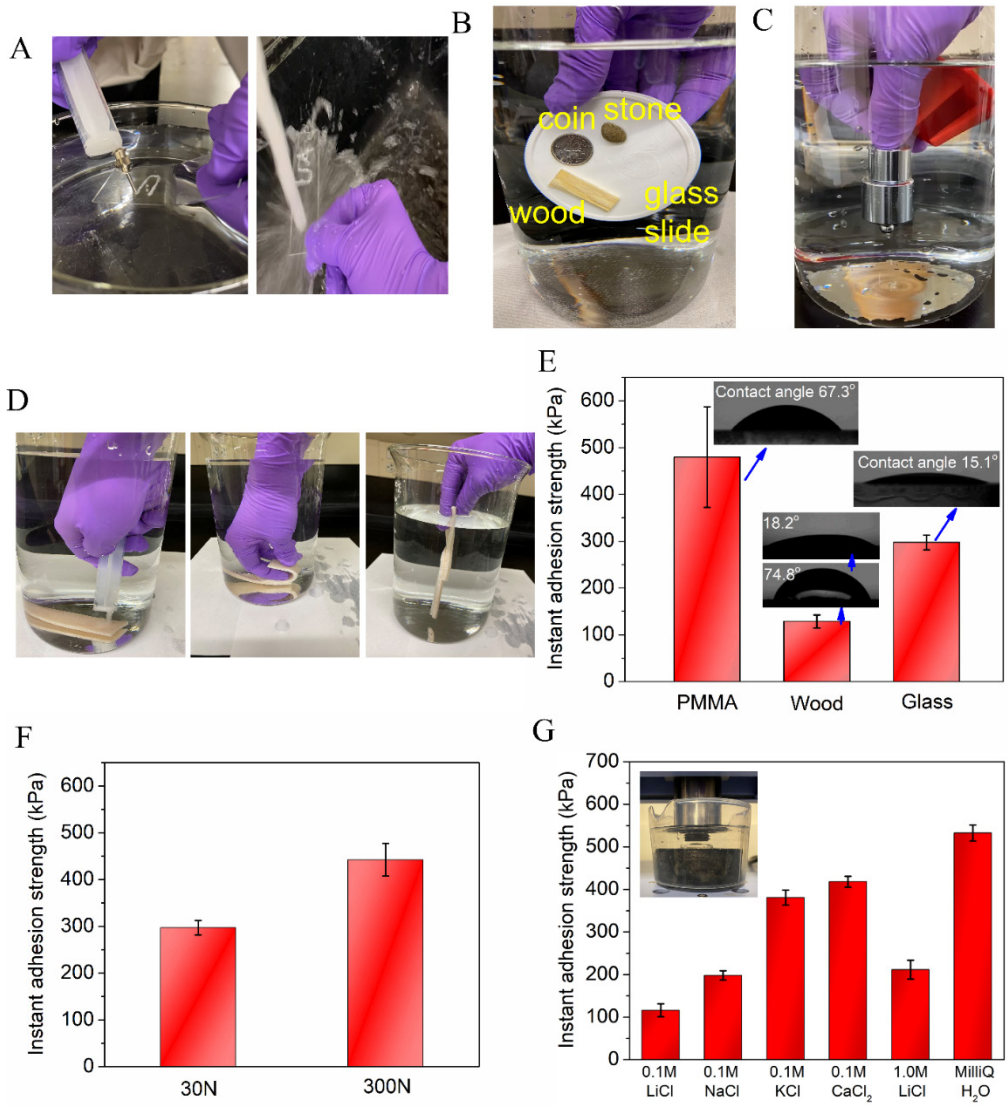

Figure 3.3. Underwater adhesive properties of the SiW40-P123-10 coacervate. (A) The SiW40-P123-10 coacervate was injected and painted on a glass slide underwater (left) and was then immediately flushed by running water which could not noticeably affect the painted patterns (right). (B) The SiW40-P123-10 coacervate can firmly bind various substrates such as wood, coin, stone, glass slide to a plastic substrate underwater. (C) The SiW40-P123-10 coacervate could instantly and firmly adhere two weights together underwater and easily support a mass of 100 g. (D) The SiW40P123-10 coacervate could instantly and firmly adhere two porcine skins together underwater. (E) Instant underwater adhesion strength of the SiW40-P123-10 coacervate on

different substrates including PMMA, wood and glass. The inserted images are contact angles of water on PMMA, wood and glass substrates. (F) Instant underwater adhesion strength of the SiW40-P123-10 coacervate on glass substrate under different compression force of 30 N and 300 N. (G) Effect of salts on the underwater adhesion strength of the SiW40-P123-10 coacervate. The inserted image shows the set-up of test with a stainless steel upper surface and a PMMA lower surface.

3.3.4 Thermo-responsive optical properties

The optical property of the SiW40-P123-10 coacervate could be readily adjusted with temperature, which was white and opaque at 0 ℃ and turned to be transparent when heated to 60 ℃ (**Figure 3.4A**). The transition process was highly reversible and showed a rapid response to temperature change, where the coacervate painted on a glass slide was successively immersed in 60 ℃ water bath and 0 ℃ ice-water bath for several cycles. The variation of transparency was quantitatively determined using an optical microplate reader in the visible light range (400-800 nm). As demonstrated in **Figure 3.4B** and **Figure 3.S10**, the transmittance of the coacervate increased with the increase of temperature, showing an extremely low value at 0 ℃ and reached about 70% at 60 ℃. Meanwhile, transmittance variation of the coacervate under heat-cool cycles between 40 and 55 ℃ is presented in **Figure 3.4C**, showing excellent repeatability of the thermo-tunable optical property of the coacervate. It is noted that as the thickness of the coacervate sample used for the characterization was 10 mm, the transmittance measured at 55 ℃ was lower than that measured with a microplate reader (**Figure 3.4B**, sample thickness of 1 mm). The adjustable optical property of the coacervate was originated from the size change of P123 micelles with temperature, which was characterized by DLS (**Figure 3.4D**). With temperature ranging from 0 ℃

to 60 ℃, P123 micelles presented thermo-sensitive size distribution. At low temperatures (<30 ℃), the micelle size was polydisperse and large aggregates could be detected, while increasing the temperature gradually led to monodisperse micelles. The change of size distribution of micelles was most likely attributed to the enhanced hydrophobic interaction within PPG micelles cores with the increase of temperature, which tended to induce the dissociation of random aggregates and the formation of densely packed micelles.[39] The thermo-responsive size evolution of P123 micelles was also in accordance with AFM topography images as shown in **Figure 3.4E** and **F**. At 20 ℃, the existence of large aggregates could prevent the transmittance of light, while relatively small and homogeneously distributed micelles were observed at 60 ℃, yielding a clear solution. Besides, structural transition of P123 with the increase of temperature could also weaken the intermolecular interaction among the micelles, which was in agreement with the lower shear modulus and viscosity of P123 at the elevated temperature (**Figure 3.S11**).

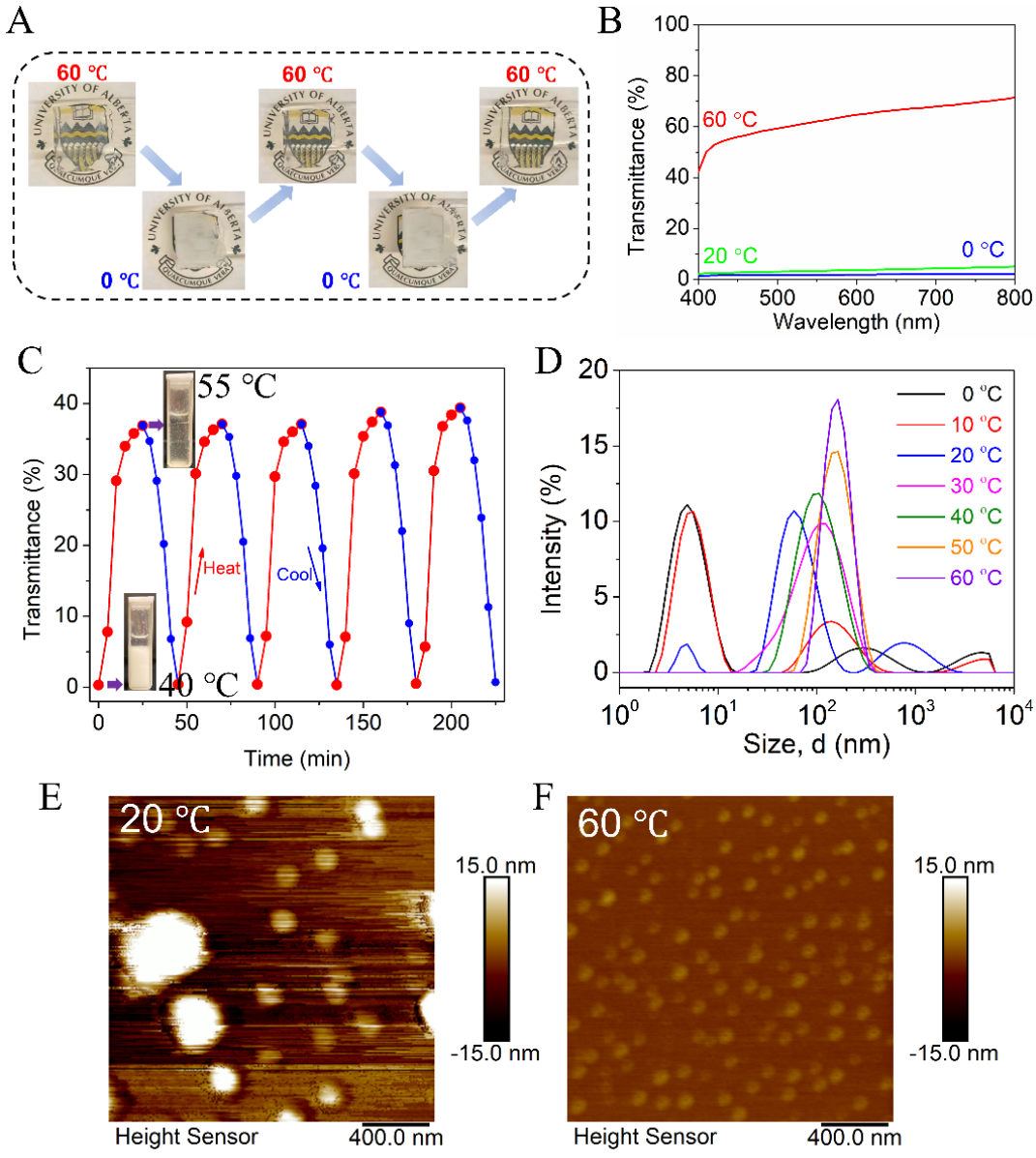

Figure 3.4. Thermo-responsive properties of the SiW40-P123-10 coacervate. (A) Repeatable transparency transition of the SiW40-P123-10 coacervate painted on glass slide which was alternatively immersed in 60 ℃ water bath and ice-water bath. (B) Transmittance variation of the SiW40-P123-10 coacervate at temperatures of 0, 37 and 60 ℃. (C) Transmittance variation of the SiW40-P123-10 coacervate under heat-cool cycles between 40 and 55 ℃. (D) Size distributions of P123 micelles at various temperatures ranging from 0 to 60 ℃. (E) and (F) AFM topography images of P123 micelles deposited on silica surfaces at 20 and 60 ℃.

3.3.5 Electrochromic properties

The SiW40-P123-10 coacervate adhesive could be directly painted on different substrates and display excellent resistance to mechanical deformation such as stretching and bending (the coacervate was dyed with carbon nanotubes (CNTs)). Despite repeatable stretching, bending and vigorously shaking underwater, the coacervate coating can be kept intact, indicating its excellent tolerance to turbulent underwater environment. Besides, the hydrophobic cores of P123 micelles endowed the SiW-P123 coacervation system with capability to load hydrophobic species like CNTs (**Figure 3.S12**), providing great versatility to the platform. The coacervate coating also exhibited exemplary stability in high-salt aqueous solutions (e.g., 3 M LiCl, NaCl or KCl) for at least 1200 h (**Figure 3.5A**). It was observed that the adhesive coacervate changed from opaque to transparent within 5 h, which can be originated from the enhanced hydrophobic interaction within PPG cores and the shrink of PEG shells due to the decrease of free water molecules in the coacervate with the presence of salt.[43, 57]

Combining the facile paintability and excellent stability of the coacervate underwater with the innate redox-driven color-switching behavior of SiW, a self-powered electrochromic device can be built up by connecting a coacervate-painted indium tin oxide (ITO) glass slide with an Al foil through salt bridge and metal wire (**Figure 3.5B**). Associated reduction-oxidation reactions are also illustrated in **Figure 3.5B**. Once the circuit was completed, the coacervate coating instantaneously changed from white to deep blue, and then the blue color could be bleached with the disconnection of the circuit and addition of H_2O_2 (30 wt%) (**Figure 3.5C**). The color-switching property of the coacervate can also be triggered by external voltages. Two ITO-coated glass slides were bonded together with the coacervate and connected to an external voltage provided by an electrochemical workstation (**Figure 3.5D**). When a reduction potential of -0.25 V was applied, the coacervate immediately turned to be deep blue (**Figure 3.5E**), while a subsequent oxidation

potential of +0.8V could bleach the color to light blue (**Figure 3.5F**). The coacervate would turn into translucent by further oxidation of air (**Figure 3.5G**). The electrochromic behavior of the coacervate was ascribed to the reduction of tungsten, which was confirmed by X-ray photoelectron spectroscopy (XPS). As shown in **Figure 3.5H**, the coacervate exhibited two peaks at 38.1 eV and 35.9 eV before electrochemical/electrical reduction, corresponding to the binding energies of W^{6+} $4f_{5/2}$ and W^{6+} $4f_{7/2}$. After reduction (**Figure 3.5I**), the peak at 38.1 eV split into two peaks at 38.2 eV and 36.9 eV, which were assigned to the binding energies of W^{6+} $4f_{5/2}$ and W^{5+} $4f_{5/2}$, respectively. Meanwhile, the peak at 35.9 eV also split into two peaks at 36.1 eV and 34.8 eV, attributed to the binding energies of W^{6+} $4f_{7/2}$ and W^{5+} $4f_{7/2}$. The results are consistent with the reported reducible polyoxometalates, which are named "heteropoly blues" for their innate color-switching property enabled by specific triggers.[23, 38, 58]

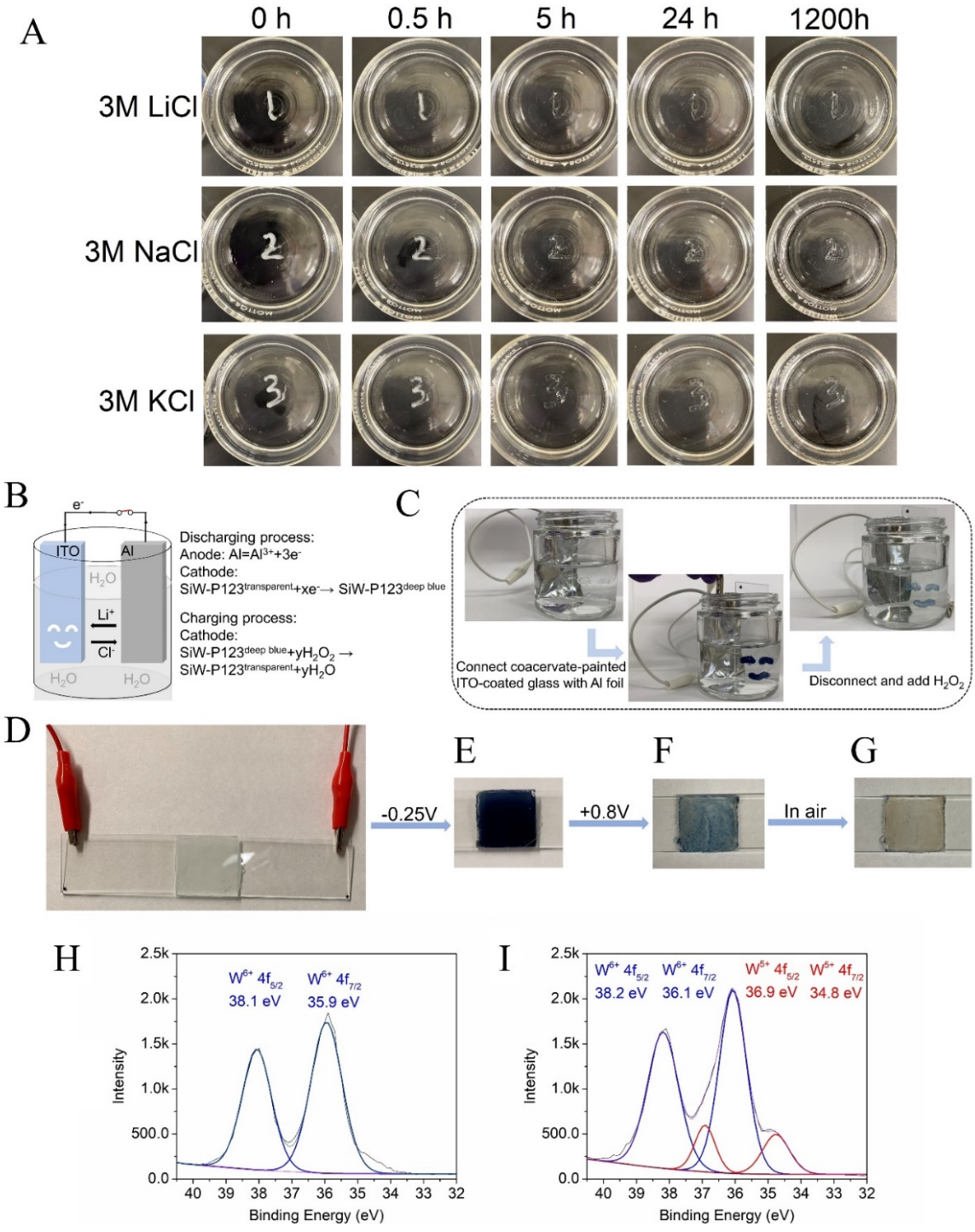

Figure 3.5. Electrochromic properties of the SiW40-P123-10 coacervate. (A) Pictures showing excellent stability of the SiW40-P123-10 coacervate in 3M LiCl, NaCl and KCl solutions. (B) Schematic illustration of the working mechanism for the self-powered electrochromic device with SiW40-P123-10 coacervate painted on an ITO-coated glass slide. (C) The SiW40-P123-10

coacervate painted on the ITO-coated glass slide as a smiling face was turned to deep blue by forming a circuit with an Al foil, which was then bleached to light blue by disconnecting the circuit as well as adding H_2O_2. (D)-(G) The SiW40-P123-10 coacervate sandwiched between two ITO-coated glass slides changed to deep blue by applying a reduction voltage of -0.25 V, followed by bleaching triggered by an oxidation voltage of +0.8 V, which was further bleached to translucent in air. (H) and (I) XPS spectra of the as-prepared coacervate before and after reduction.

3.4 Conclusions

In this work, we have developed a novel instant underwater adhesive with tunable optical and electrochromic properties via a facile one-step mixing of SiW and P123 aqueous solutions, where the formation of the adhesive coacervate was driven by the synergy of hydrogen-bonding interaction and hydrophobic interaction. The coacervation process is mainly actuated by the intermolecular hydrogen bonding between oxygens of SiW and etheric oxygens of P123 micelles bridged by hydrated protons, and the hydrophobic cores of P123 micelles offer an additional crosslinking, significantly enhancing the mechanical properties (e.g., shear moduli, viscosity) of the coacervates. The rheological properties of as-prepared coacervates can be modulated over several orders of magnitude for practical applications by introducing different types and concentrations of salts (e.g., LiCl, NaCl, KCl and $CaCl_2$), and they are able to maintain the integrity in saline aqueous solutions with a concentration up to 3 M for at least 1200 h. Meanwhile, the coacervates show robust and instant underwater adhesion on various substrates with an adhesion strength up to 479.6 kPa on PMMA, which can also resist water flush and repeatable stretching and bending of the substrate. Such wet adhesion performance of the developed SiW-P123 coacervate is superior to that of a lot of previously reported coacervate materials, even some

hydrogels. Moreover, the SiW-P123 coacervate exhibits thermo-responsive optical properties, which was attributed to the configuration change of P123 micelles. The innate reduction-related color switch of SiW endows the coacervate electrochromic properties in response to both chemical oxidation-reduction reactions and external voltages, suggesting great potential of the coacervate in electrochromic devices such as smart batteries. The SiW-P123 coacervation system provides an ideal platform for the development of color-switching underwater adhesives, holding great promise in wearable electronics and energy-saving buildings. It is noted that the SiW can be facilely modified or replaced by other kinds of polyoxometalates[59] and other polymers in the pluronic family[37] can be used to substituent P123, further expanding the versatility and functionality of the SiW-P123 coacervation system.

3.5 Supporting Information

Table 3.S1. Summary of the reported wet/underwater adhesives.

Components of Wet/underwater adhesives	Adhesive type	Fabrication methods	Molecular interactions	Effective time	Adhesive strength (kPa)	Stimuli-responsiveness	Ref.
Silicotungstic acid and P123 micelles	Coacervate	Simple mixing	Hydrogen bonding interactions	Instant or 10 s	479.6, underwater	Thermo-tunable optical property and electrochromism	**This work**
Silicotungstic acid and PEG	Coacervate	Simple mixing	Hydrogen bonding interaction	60 s	98.2, wet	n/a	1
Tannic acid and 4-arm PEG-NH_2	Coacervate	Simple mixing	Hydrogen bonding interaction	60 s	180, wet	n/a	2
Tannic acid and polyamidoamine-epichlorohydrin	Coacervate	Simple mixing	Electrostatic and hydrogen bonding interactions	24 h	458.2, underwater	n/a	3
lignosulfonate and apolyamidoamine-epichlorohydrin	Coacervate	Simple mixing	Electrostatic interaction	Instant	122.3	n/a	4
Tannic acid and poly(vinyl alcohol)	Coacervate	Simple mixing	Hydrogen bonding interaction	30 s	~80, underwater	n/a	5
Silicotungstic acid and histidine	Coacervate	pH adjustment and simple mixing	Electrostatic interaction	4 h	436.7, wet	n/a	6
Nonionic polyester	Coacervate	Complex polymer synthesis	Covalent bond, hydrophobic and hydrogen bonding interactions	20 min	~80, underwater	n/a	7
Poly(allylamine), pyrophosphate/ tripolyphosphate	Coacervate	Simple mixing	Electrostatic interaction	3 h	~440, underwater	pH- and ionic strength-responsiveness	8

Pentaerythritol tetraacrylate, dopamine, PEGDA	Hyperbranched Polymer-based coacervate	Polymer synthesis	Covalent bond and hydrophobic interaction	12 h	390	n/a	9
Cationic and aromatic monomers	Hydrogel	Free-radical polymerization	Covalent bond and cation-π interactions	5 s	~70, underwater	n/a	10
Cationic and aromatic monomers	Hydrogel	Free-radical polymerization	Covalent bond and cation-π interactions	10 s	180, underwater	n/a	11
Tannic acid and silk fibroin	Hydrogel	Simple mixing	Electrostatic and hydrogen bonding interactions	20 min	134.1, wet with water or blood	n/a	12
N-acryloyl 2-glycine and hydroxyapatite	Organic-inorganic Hydrogel	One-pot radical polymerization	Electrostatic and hydrogen bonding interactions	Instant	140, wet	n/a	13
Polyacrylic acid and amorphous calcium carbonate	Organic-inorganic Hydrogel	Mixing and rinsing	Chelation between Ca^{2+} and COO^-	24 h	~250, underwater	n/a	14
Hydrophilic and hydrophobic monomers	Organo-hydrogel	Complex polymer synthesis	Hydrogen bonding and hydrophobic interactions	30 min	13.2, underwater or in organic solvent	n/a	15
$H_6P_2W_{18}O_{62}$ and 3-(2-naphthyl)-l-alanine	Coating	Complex synthesis and 60 ℃ heat treatment	Electrostatic interaction	15 min	14.67, underwater	Electrochromism	16
pDOPA-AD-MEA and pNIPAM-CD	Surface with thermo-responsive coating	Free-radical polymerization and deposition of adhesive coating	Host-guest molecular interaction	Instant	~4, underwater	Thermo-induced underwater adhesion	17
PDMS pillar with p(DMA-co-MEA-coNIPAAm) coating	Structured surface with coating	Micro-structured surface, polymer synthesis, coating	Covalent bond and hydrogen bonding interactions	60 s	~8, underwater	Thermo-responsiveness	18

Poly(dopamine-co-acrylate)	Polymer solution	Complex polymer synthesis	Covalent bond and hydrogen bonding interaction	15 min	~40, wet	n/a	19
P(VGal-*co*-BA)	Polymer solution	Complex polymer synthesis	Covalent bond, hydrophobic and hydrogen bonding interactions	24 h	~200, wet	n/a	20

1. Q. Peng, J. Chen, Z. Zeng, T. Wang, L. Xiang, X. Peng, J. Liu and H. Zeng, *Small,* 2020, **16**, 2004132.
2. K. Kim, M. Shin, M.-Y. Koh, J. H. Ryu, M. S. Lee, S. Hong and H. Lee, *Adv. Funct. Mater.,* 2015, **25**, 2402-2410.
3. Z. Wang, S. Zhang, S. Zhao, H. Kang, Z. Wang, C. Xia, Y. Yu and J. Li, *Chem. Eng. J.,* 2021, **404**, 127069.
4. C. Wei, X. Zhu, H. Peng, J. Chen, F. Zhang and Q. Zhao, *ACS Sustainable Chem. Eng.,* 2019, **7**, 4508-4514.
5. D. Lee, H. Hwang, J. S. Kim, J. Park, D. Youn, D. Kim, J. Hahn, M. Seo and H. Lee, *ACS Appl. Mater. Interfaces,* 2020, **12**, 20933-20941.
6. J. Xu, X. Li, J. Li, X. Li, B. Li, Y. Wang, L. Wu and W. Li, *Angew. Chem. Int. Ed.,* 2017, **56**, 8731-8735.
7. A. Narayanan, J. R. Menefee, Q. Liu, A. Dhinojwala and A. Joy, *ACS Nano,* 2020, **14**, 8359-8367.
8. P. G. Lawrence and Y. Lapitsky, *Langmuir,* 2015, **31**, 1564-1574.
9. C. Cui, C. Fan, Y. Wu, M. Xiao, T. Wu, D. Zhang, X. Chen, B. Liu, Z. Xu, B. Qu and W. Liu, *Adv. Mater.,* 2019, **31**, 1905761.

10. H. Fan, J. Wang, Z. Tao, J. Huang, P. Rao, T. Kurokawa and J. P. Gong, *Nat. Commun.,* 2019, **10**, 5127.

11. H. Fan, J. Wang and J. P.Gong, *Adv. Funct. Mater.,* 2020, **31**, 2009334.

12. S. Bai, X. Zhang, P. Cai, X. Huang, Y. Huang, R. Liu, M. Zhang, J. Song, X. Chen and H. Yang, *Nanoscale Horiz.,* 2019, **4**, 1333-1341.

13. C. Cui,; T. Wu, F. Gao, C. Fan, Z. Xu, H. Wang, B. Liu and W. Liu, *Adv. Funct. Mater.,* 2018, **28**, 1804925.

14. A. Li, Y. Jia, S. Sun, Y. Xu, B. B. Minsky, M. A. C. Stuart, H. Cölfen, R. von Klitzing and X. Guo, *ACS Appl. Mater. Interfaces,* 2018, **10**, 10471-10479.

15. X. Liu, Q. Zhang, L. Duan and G. Gao, *Adv. Funct. Mater.,* 2019, **29**, 1900450.

16. X. Li, Z. Du, Z. Song, B. Li, L. Wu, Q. Liu, H. Zhang and W. Li, *Adv. Funct. Mater.,* 2018, **28**, 1800599.

17. Y. Zhao, Y. Wu, L. Wang, M. Zhang, X. Chen, M. Liu, J. Fan, J. Liu, F. Zhou and Z. Wang, *Nat. Commun.,* 2017, **8**, 2218.

18. Y. Ma, S. Ma, Y. Wu, X. Pei, S. N. Gorb, Z. Wang, W. Liu and F. Zhou, *Adv. Mater.,* 2018, *30*, 1801595.

19. H. Zhang, L. P. Bré, T. Zhao, Y. Zheng, B. Newland and W. Wang, *Biomaterials,* 2014, **35**, 711-719.

20. K. Zhan, C. Kim, K. Sung, H. Ejima and N. Yoshie, *Biomacromolecules,* 2017, **18**, 2959-2966.

21. D. Bajuk-Bogdanović, I. Holclajtner-Antunović, M. Todorović, U. B. Mioć and J. Zakrzewska, *J. Serb. Chem. Soc.,* 2008, **73**, 197-209.

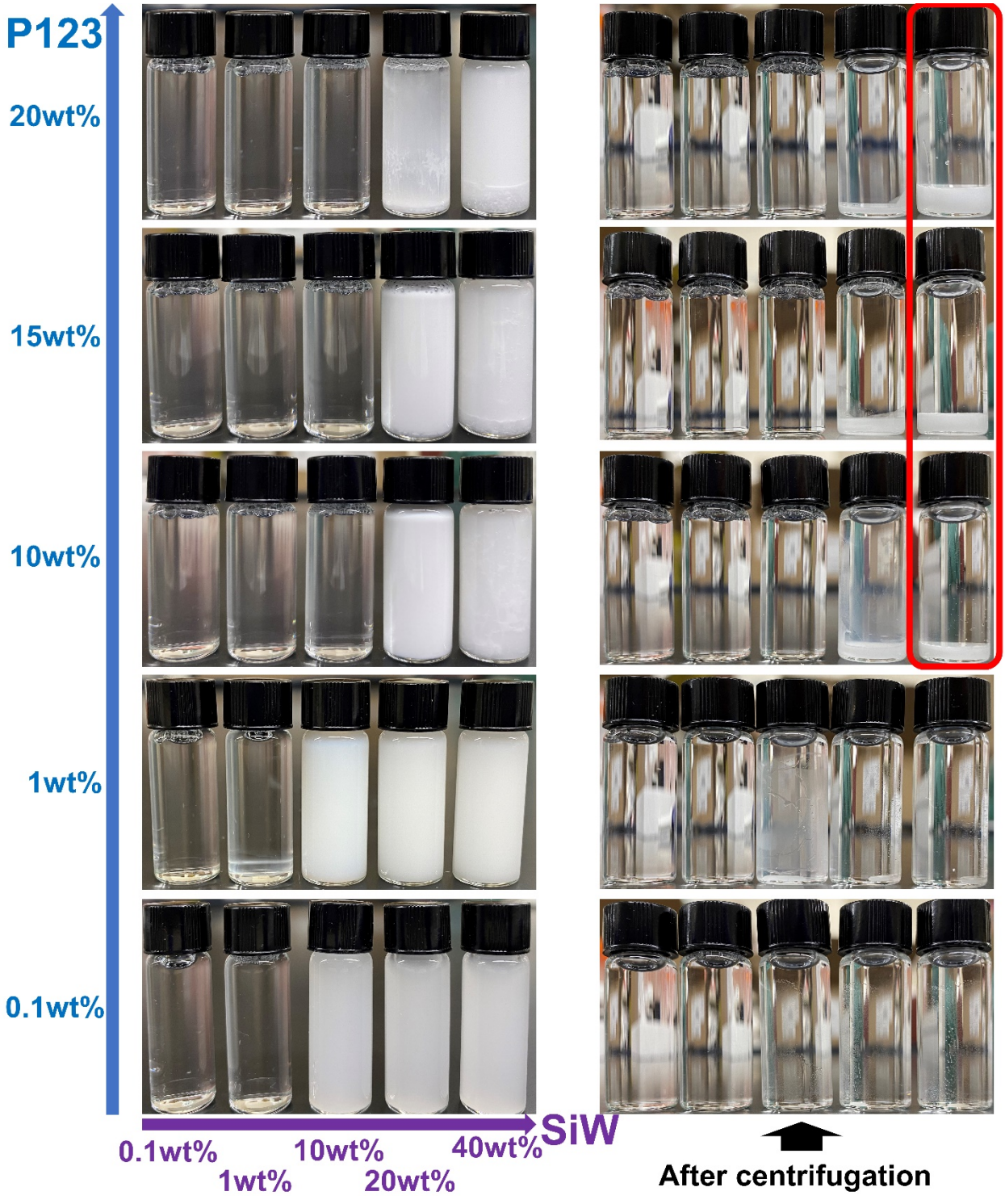

Figure 3.S1. Corresponding pictures of the phase diagram between SiW and P123 with various concentrations. (Left: upon mixing of the two aqueous solutions; Right: after centrifugation)

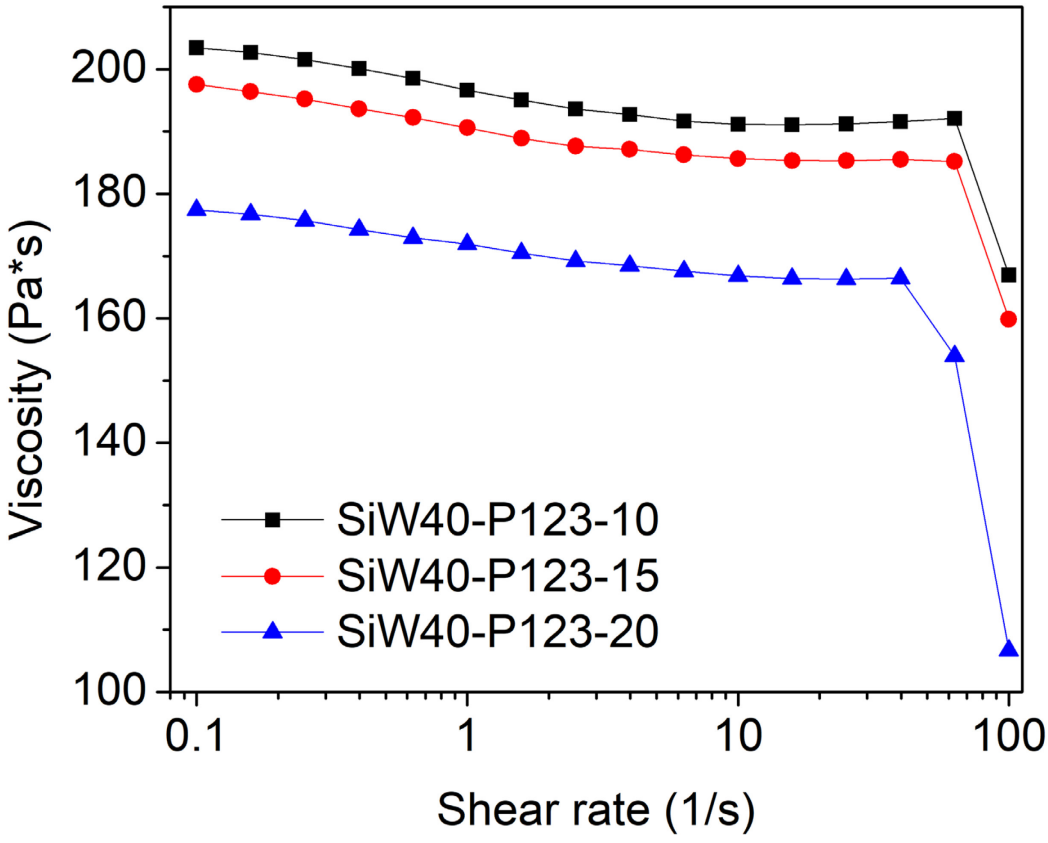

Figure 3.S2. Viscosities of SiW40-P123-10, SiW40-P123-15, SiW40-P123-20 coacervates with shear rate ranging from 0.1 to 100/s.

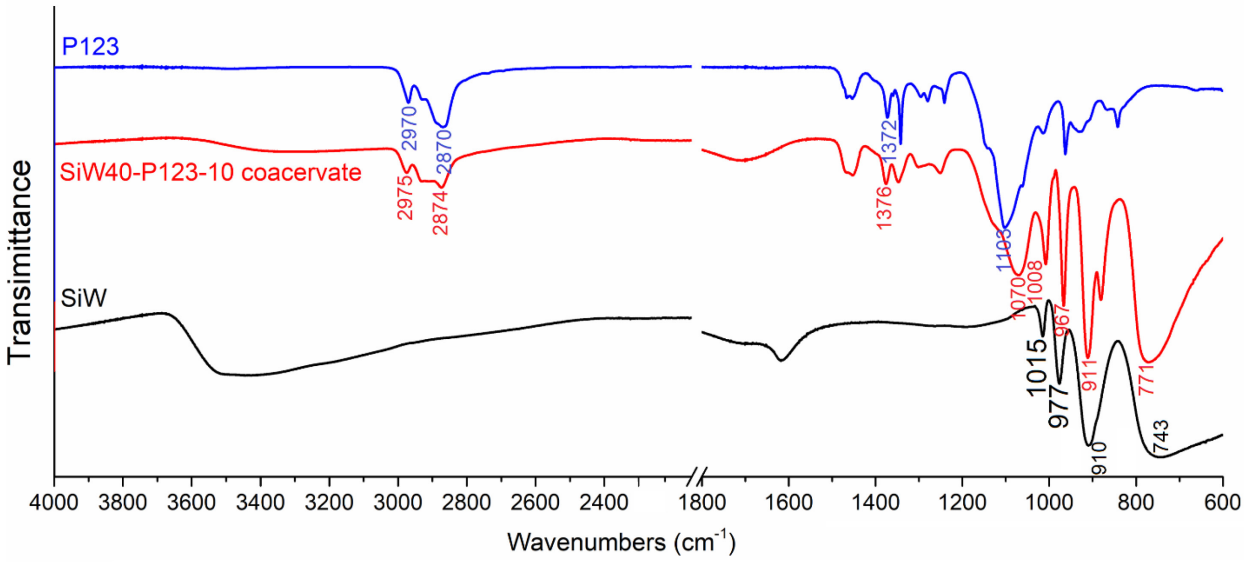

Figure 3.S3. FTIR spectra of P123, SiW and freeze-dried SiW40-P123-10 coacervate.

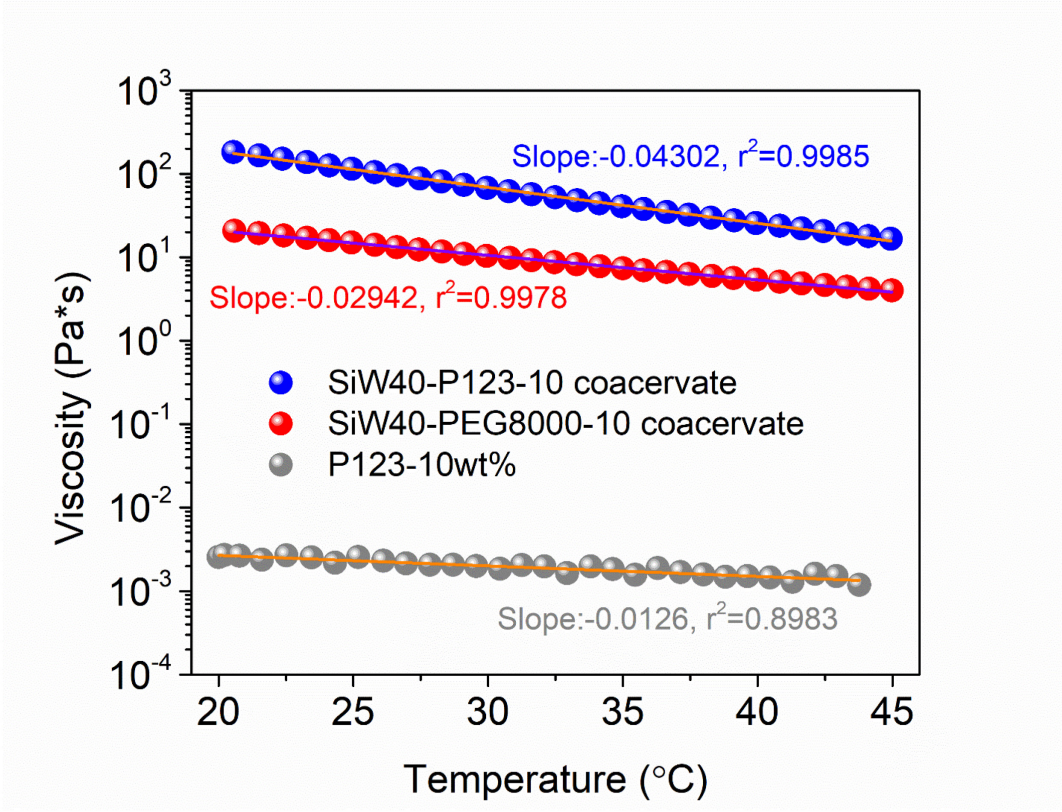

Figure 3.S4. Variations of viscosity versus temperature for SiW40-P123-10 coacervate, SiW40-PEG8000-10 coacervate and 10 wt% P123 aqueous solution.

Figure 3.S5. Pictures for the formation of SiW40-P123-10 coacervate and the corresponding supernatant prepared with SiW solution at pH=1.14 (left) and the mixture of 40 wt% SiW (pH= 1.75) and 10 wt% P123 aqueous solutions (right).

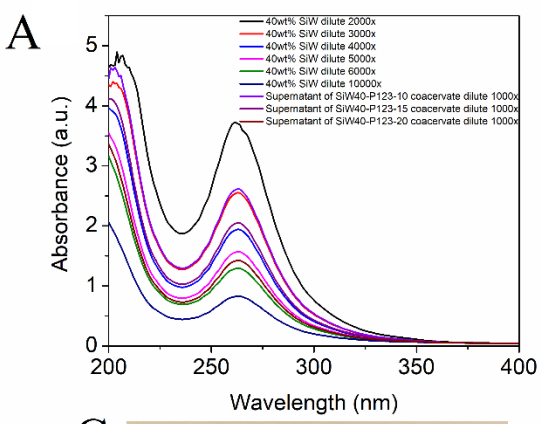

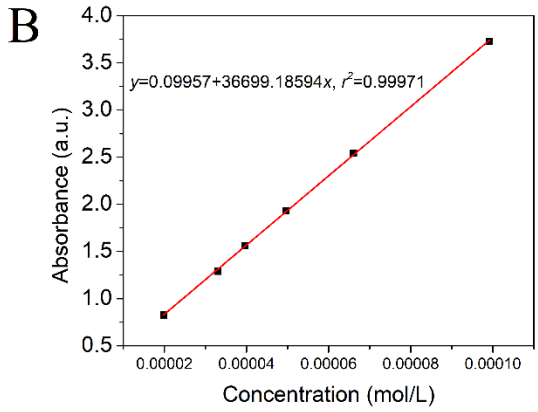

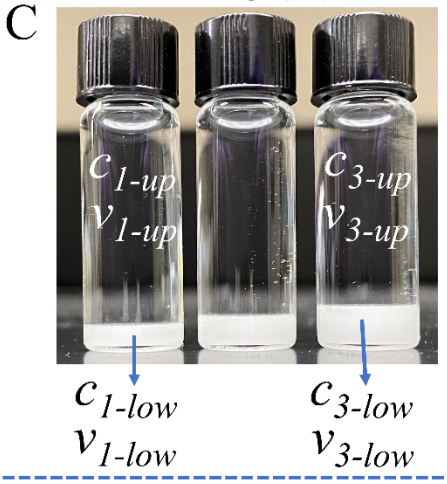

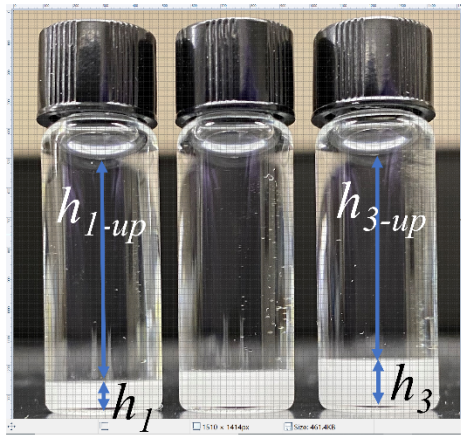

E

Mixing 1ml 40wt% SiW and 1ml 10/15/20wt% P123 , respectively.

m(1ml 40wt% SiW)=(1.423g+1.4299g+1.4268g)/3=1.4265g

*c=c(40wt% SiW)=n/v=m/MV=0.4*1.4265g/(2878.17g/mol*1ml)=0.19825mol/l*

h_1*=83 pixels,* $h_{1\text{-}up}$*=756 pixels,* h_3*=156 pixels,* $h_{3\text{-}up}$*=690 pixels*

$v_{1\text{-}up}+v_{1\text{-}low}$ *=2ml,* $v_{1\text{-}up}$*:* $v_{1\text{-}low}$*=* $h_{1\text{-}up}$ *:*h_1 *=756:83*

$v_{1\text{-}up}$*=1.80215ml,* $v_{1\text{-}low}$*=0.19785ml*

$v_{3\text{-}up}+v_{3\text{-}low}$ *=2ml,* $v_{3\text{-}up}$*:* $v_{3\text{-}low}$*=* $h_{3\text{-}up}$ *:*h_3 *=690:156*

$v_{3\text{-}up}$*=1.63121ml,* $v_{3\text{-}low}$*=0.36879ml*

$v_{3\text{-}low}/v_{1\text{-}low}$*= 0.36879ml/ 0.19785ml=186.4%, increased by 86.4%*

$c_{1\text{-}up}$ *=(y-0.09957)/36699.18594*1000=(2.605-0.09957)/36699.18594*1000=0.06827mol/l*

$c_{3\text{-}up}$ *=(y-0.09957)/36699.18594*1000=(1.419-0.09957)/36699.18594*1000=0.03595mol/l*

$c_{1\text{-}up}\,v_{1\text{-}up}+c_{1\text{-}low}\,v_{1\text{-}low}=c*1ml$, $c_{1\text{-}low}$*=0.38017mol/l*

$c_{3\text{-}up}\,v_{3\text{-}up}+c_{3\text{-}low}\,v_{3\text{-}low}=c*1ml$, $c_{3\text{-}low}$*=0.37856mol/l*

Figure 3.S6. Calculation of volume of SiW-P123 coacervate phases and corresponding supernatants as well as concentration of SiW in SiW-P123 coacervate phases. (A) UV-vis was employed to measure light absorbance of a series of diluted 40wt% SiW aqueous solution and diluted supernatants of SiW40-P123-10/15/20 coacervates. It was demonstrated that SiW has a

characterized absorption peak at 262.6nm.[1] (B) Standard absorbance-concentration relationship was plotted based on results of (A), where concentration of SiW in supernatants of SiW40-P123-10/15/20 coacervates can be calculated according to the fitted linear equation. (C) Representation of concentration of SiW in SiW40-P123-10 ($c_{1\text{-low}}$) and SiW40-P123-20 ($c_{3\text{-low}}$) coacervate phases as well as corresponding supernatants ($c_{1\text{-up}}$ and $c_{3\text{-up}}$). And representation of volumes of SiW40-P123-10 ($v_{1\text{-low}}$) and SiW40-P123-20 ($v_{3\text{-low}}$) coacervate phases as well as volumes of their corresponding supernatants ($v_{1\text{-up}}$ and $v_{3\text{-up}}$). (D) The heights of SiW40-P123-10 (h_1) and SiW40-P123-20 (h_3) coacervate phases and corresponding supernatant phases ($h_{1\text{-up}}$ and $h_{3\text{-up}}$) were measured by counting number of pixels in the vertical direction. (E) The deduction process of calculating volume ratio of SiW40-P123-20 coacervate phase to SiW40-P123-10 coacervate phase as well as concentrations of SiW in their coacervate phases.

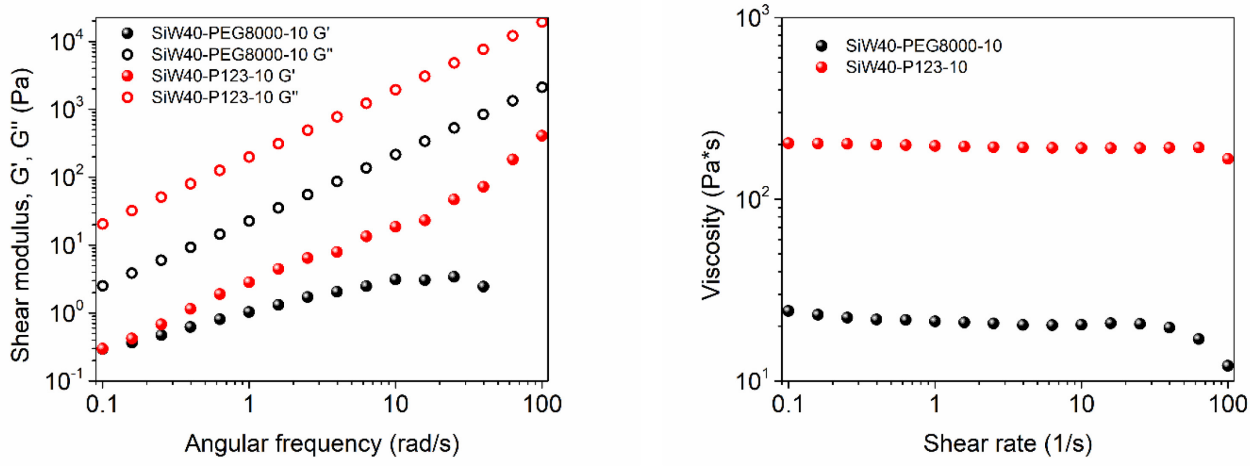

Figure 3.S7. Shear storage modulus, shear loss modulus and viscosity of SiW40-P123-10 coacervate and SiW40-PEG8000-10 coacervate.

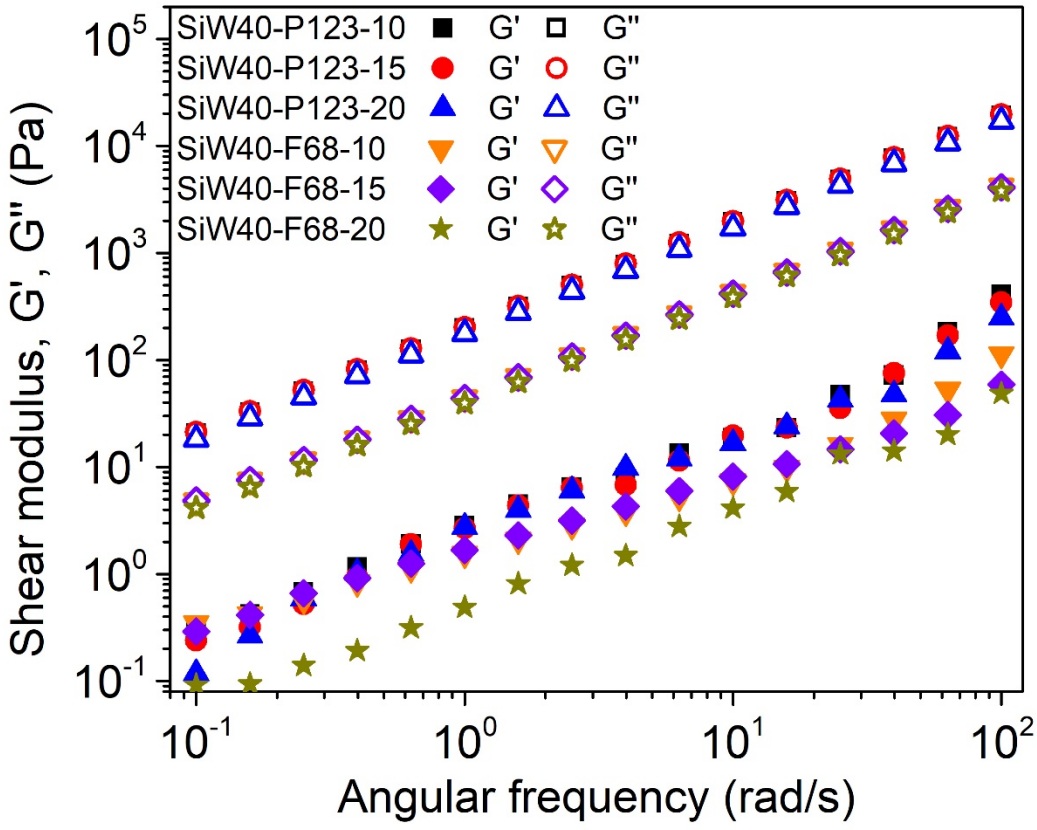

Figure 3.S8. Shear loss modulus G'' and shear storage modulus G' of SiW40-P123-10, SiW40-P123-15, SiW40-P123-20, SiW40-F68-10, SiW40-F68-15, SiW40-F68-20 coacervates.

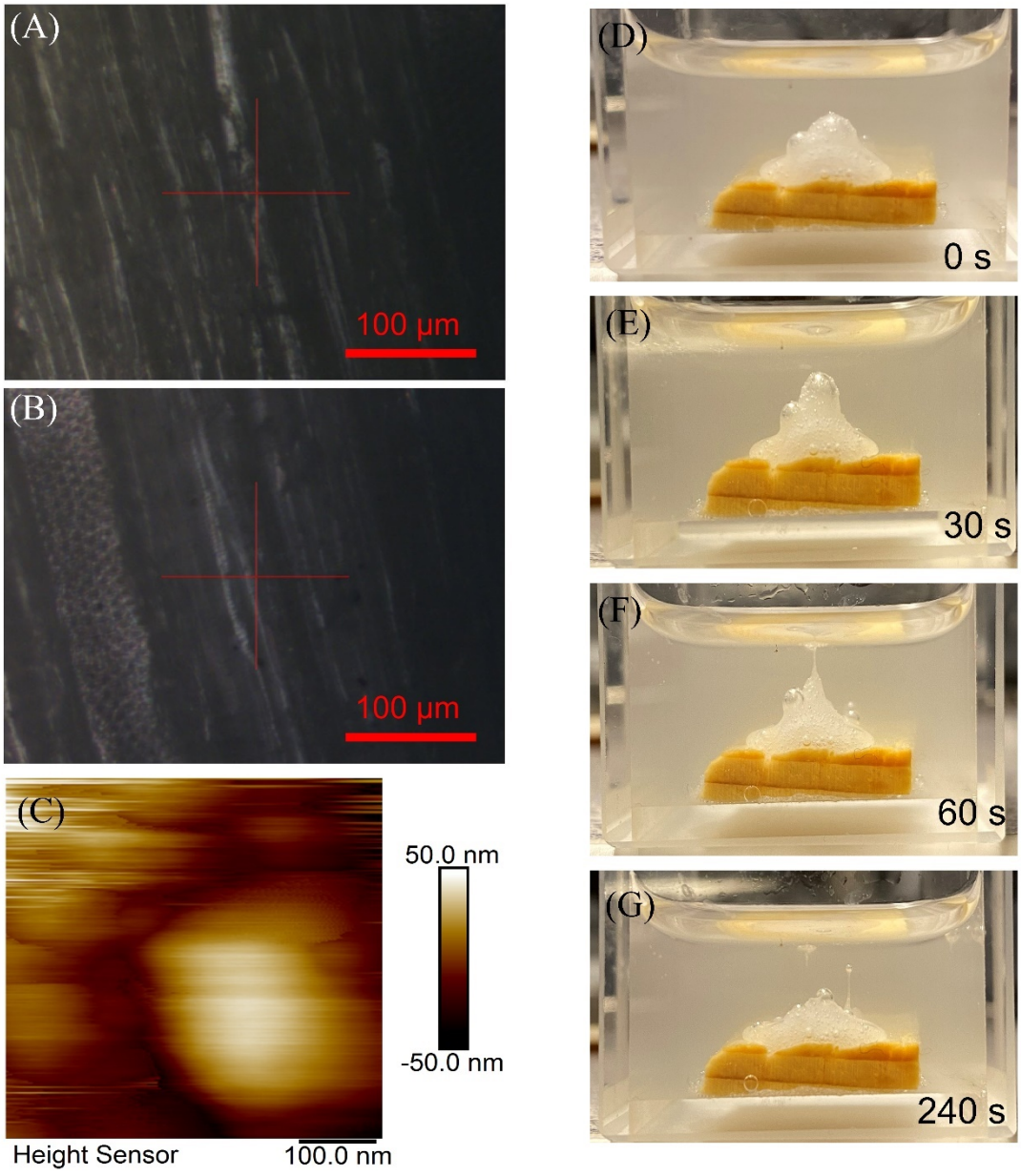

Figure 3.S9. (A-B) Microtubes and micropores on the wood surface observed under an AFM. (C)AFM image of the rough wood surface. (D-G) SiW40-P123-10 coacervate could spread on the wood surface.

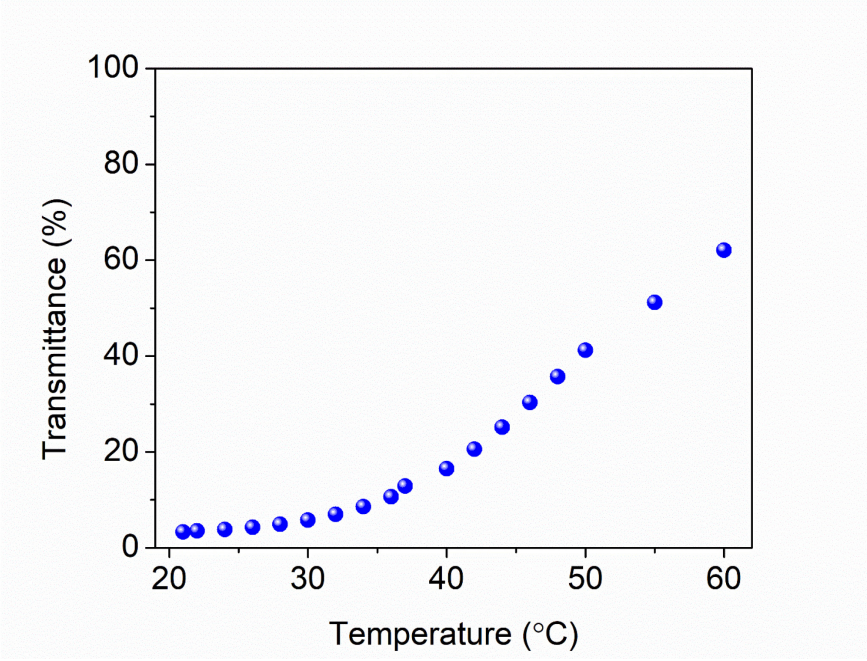

Figure 3.S10. The change of transmittance at 550 nm of the SiW40-P123-10 coacervate with temperature ranging from 21 ℃ to 60 ℃.

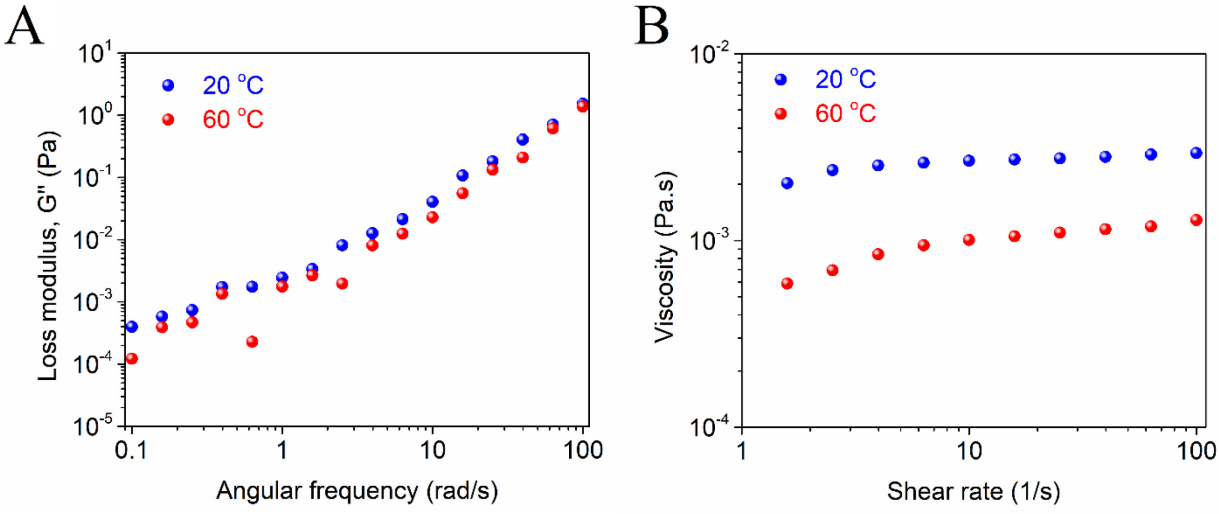

Figure 3.S11. (A) Shear loss modulus and (B) viscosity of P123 aqueous solution at temperatures of 20 ℃ and 60 ℃.

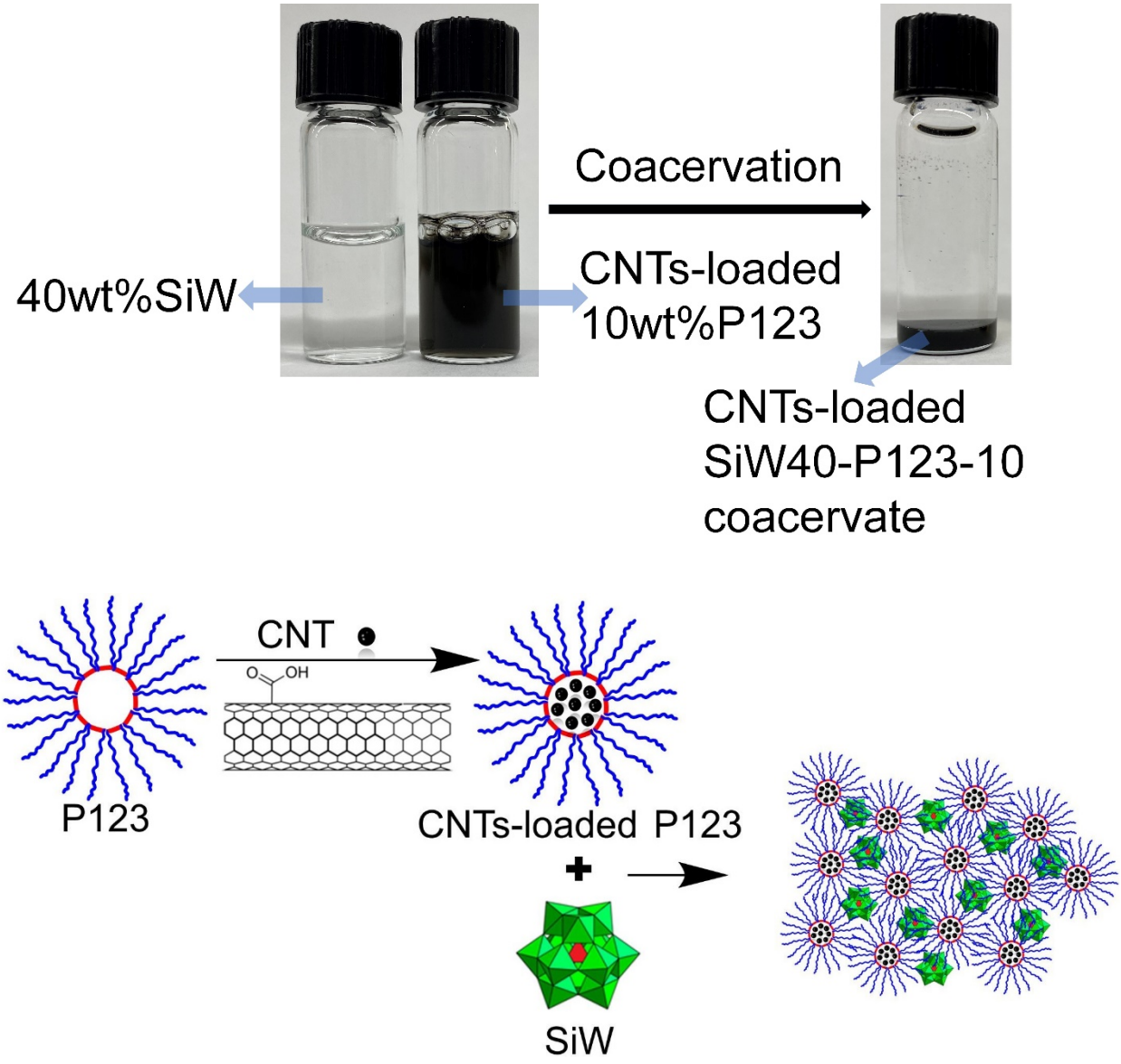

Figure 3.S12. CNTs-loaded SiW40-P123-10 coacervate and corresponding schematic intermolecular interactions.

References

1. G. P. Maier, M. V. Rapp, J. H. Waite, J. N. Israelachvili and A. Butler, *Science,* 2015, **349**, 628-632.
2. A. M. Smith, *Biological Adhesives*, Springer, Berlin, Germany, 2016.
3. J. H. Waite, *Nat. Mater.,* 2008, **7**, 8-9.
4. B. P. Lee, P. B. Messersmith, J. N. Israelachvili and J. H. Waite, *Annu. Rev. Mater. Res.,* 2011, **41**, 99-132.
5. H. Shao and R. J. Stewart, *Adv. Mater.,* 2010, **22**, 729-733.
6. Q. Ye, F. Zhou and W. Liu, *Chem. Soc. Rev.,* 2011**, 40**, 4244-4258.
7. C. Zhang, B. Wu, Y. Zhou, F. Zhou, W. Liu and Z. Wang, *Chem. Soc. Rev.,* 2020**, 49**, 3605-3637.
8. R. J. Stewart, J. C. Weaver, D. E. Morse and J. H. Waite, *J. Exp. Biol.,* 2004, **207**, 4727-4734.
9. S. Kim, J. Huang, Y. Lee, S. Dutta, H. Y. Yoo, Y. M. Jung, Y. Jho, H. Zeng and D. S. Hwang,

   Proc. Natl. Acad. Sci. U.S.A., 2016, **113**, E847-E853.
10. S. Kim, H. Y. Yoo, J. Huang, Y. Lee, S. Park, Y. Park, S. Jin, Y. M. Jung, H. Zeng, D. S. Hwang and Y. Jho, *ACS Nano,* 2017, **11**, 6764-6772.
11. G. C. Yeo, F. W. Keeley and A. S. Weiss, *Adv. Colloid Interface Sci.,* 2011, **167**, 94-103.
12. A. Miserez, T. Schneberk, C. Sun, F. W. Zok and J. H. Waite, *Science,* 2008, **319**, 1816-1819.
13. A. Miserez, Y. Li, J. H. Waite and F. Zok, *Acta Biomater.,* 2007, **3**, 139-149.
14. C. E. Sing and S. L. Perry, *Soft Matter,* 2020, **16**, 2885-2914.
15. D. Priftis and M. Tirrell, *Soft Matter,* 2012, **8**, 9396-9405.

16. R. Chollakup, W. Smitthipong, C. D. Eisenbach and M. Tirrell, *Macromol.,* 2010, **43**, 2518-2528.

17. H. Zhao, C. Sun, R. J. Stewart and J. H. Waite, *J. Biol. Chem.,* 2005, **280**, 42938-42944.

18. K. Kim, M. Shin, M. Koh, J. H. Ryu, M. S. Lee, S. Hong and H. Lee, *Adv. Funct. Mater.,* 2015, **25**, 2402-2410.

19. Q. Peng, J. Chen, Z. Zeng, T. Wang, L. Xiang, X. Peng, J. Liu and H. Zeng, *Small,* 2020, **16**,
2004132.

20. M. Dompe, F. J. Cedano-Serrano, O. Heckert, N. van den Heuvel, J. van der Gucht, Y. Tran, D. Hourdet, C. Creton and M. Kamperman, *Adv. Mater.,* 2019, **31**, 1808179.

21. A. Narayanan, J. R. Menefee, Q. Liu, A. Dhinojwala and A. Joy, *ACS Nano,* 2020, **14**, 8359-8367.

22. Z. Wang, S. Zhang, S. Zhao, H. Kang, Z. Wang, C. Xia, Y. Yu and J. Li, *Chem. Eng. J.,* 2021,
404*,* 127069.

23. X. Li, Z. Du, Z. Song, B. Li, L. Wu, Q. Liu, H. Zhang and W. Li, *Adv. Funct. Mater.,* 2018, **28**, 1800599.

24. G. Yang, Y. M. Zhang, Y. Cai, B. Yang, C. Gu and S. X. Zhang, *Chem. Soc. Rev.,* 2020, **49**, 8687-8720.

25. A. Cannavale, U. Ayr, F. Fiorito and F. Martellotta, *Energies,* 2020, **13**, 1449.

26. W. Wu, M. Wang, J. Ma, Y. Cao and Y. Deng, *Adv. Electron. Mater.,* 2018, **4**, 1800185.

27. J. Zhao, Y. Tian, Z. Wang, S. Cong, D. Zhou, Q. Zhang, M. Yang, W. Zhang, F. Geng and Z. Zhao, *Angew. Chem.,* 2016, **128**, 7277-7281.

28. J. Wang, L. Zhang, L. Yu, Z. Jiao, H. Xie, X. W. Lou and X. W. Sun, *Nat. Commun.,* 2014, **5**, 4921.

29. Y. Tian, W. Zhang, S. Cong, Y. Zheng, F. Geng and Z. Zhao, *Adv. Funct. Mater.,* 2015, **25**, 5833-5839.

30. Y. Tian, S. Cong, W. Su, H. Chen, Q. Li, F. Geng and Z. Zhao, *Nano Lett.,* 2014, **14**, 2150-2156.

31. Y. Zhang, S. W. Ng, X. Lu and Z. Zheng, *Chem. Rev.,* 2020, **120**, 2049-2122.

32. J. Zhang, W. Zhang, Z. Yang, Z. Yu, X. Zhang, T. C. Chang and A. Javey, *Sens. Actuators. B,* 2014, **202**, 708-713.

33. W. Wu, *Nanoscale,* 2017, **9**, 7342-7372.

34. Y. Aleeva and B. Pignataro, *J. Mater. Chem. C,* 2014, **2**, 6436-6453.

35. D. S. Hwang, H. Zeng, A. Srivastava, D. V. Krogstad, M. Tirrell, J. N. Israelachvili and J. H. Waite, *Soft Matter,* 2010, **6**, 3232-3236.

36. S. M. Wang, J. Hwang and E. Kim, *J. Mater. Chem. C,* 2019, **7**, 7828-7850.

37. A. Pitto-Barry and N. P. E. Barry, *Polym. Chem.,* 2014, **5**, 3291-3297.

38. J. Xu, X. Li, J. Li, X. Li, B. Li, Y. Wang, L. Wu and W. Li, *Angew. Chem. Int. Ed.,* 2017, **56**, 8731-8735.

39. Y. Su, J. Wang and H Liu, *Langmuir,* 2002, **18**, 5370-5374.

40. I. V. Kozhevnikov, *Chem. Rev.,* 1998, **98**, 171-198.

41. J. Chen, Q. Peng, T. Thundat and H. Zeng, *Chem. Mater.,* 2019, **31**, 4553-4563.

42. J. Chen, B. Yan, X. Wang, Q. Huang, T. Thundat and H. Zeng, *Polym. Chem.,* 2017, **8**, 3066-3073.

43. R. Ganguly, A. Kunwar, B. Dutta, S. Kumar, K. C. Barick, A. Ballal, V. K. Aswal and P. A. Hassan, *Colloids Surf. B,* 2017, **152**, 176-182.

44. N. Suthiwangcharoen and R. Nagarajan, *RSC Adv.,* 2014, **4**, 10076-10089.

45. J. N. Israelachvili, Intermolecular and Surface Forces, 2nd ed., Academic Press, New York, 1992.

46. Q. Wang and J. B. Schlenoff, *Macromolecules,* 2014, **47**, 3108-3116.

47. J. T. G. Overbeek and M. J. Voorn, *J. Cell. Comp. Physiol.,* 1957, **49**, 7-26.

48. K. P. Ananthapadmanabhan and E. D. Goddard, *Langmuir,* 1987, **3**, 25-31.

49. P. Zhang, O. Gourgas, A. Lainé, M. Murshed, D. Mantovani and M. Cerruti, *Cryst. Growth Des.,* 2020, **20**, 7170-7179.

50. D. S. Hwang, H. Zeng, Q. Lu, J. N. Israelachvili and J. H. Waite, Soft Matter, 2012, **8**, 5640-5648

51. P. Karnal, P. Roberts, S. Gryska, C. King, C. Barrios and J. Frechette, ACS Appl. Mater. Interfaces, 2017, **9**, 42344-42353.

52. S. Baik1, D. W. Kim, Y. Park, T.-J. Lee, S. H. Bhang and C. Pang, Nature, 2017, **546**, 396-400.

53. J. P. Jones, M. Sima, R. G. O'Hara and R. J. Stewart, Adv. Healthcare Mater., 2016, **5**, 795-801.

54. L. Han, B. Yan, L. Zhang, M. Wu, J. Wang, J. Huang, Y. Deng and H. Zeng, Colloids Surf., A, 2018, **539**, 37-45.

55. H. Fan, J. Wang and J. P. Gong, *Adv. Funct. Mater.,* 2020, 2009334.

56. H. Fan, J. Wang, Z. Tao, J. Huang, P. Rao, T. Kurokawa and J. P. Gong, *Nat. Commun.,* 2019, **10**, 5127.

57. K. Yamazoe, Y. Higaki, Y. Inutsuka, J. Miyawaki, Y. T. Cui, A. Takahara and Y. Harada, *Langmuir,* 2017, **33**, 3954-3959.

58. T. Yamase, *Chem. Rev.,* 1998, **98**, 307-325.

59. D. L. Long, R. Tsunashima and L. Cronin, *Angew. Chem. Int. Ed.,* 2010, **49**, 1736-1758.

CHAPTER 4 Coacervate-Based Instant and Repeatable Underwater Adhesive with Anticancer and Antibacterial Applications

4.1 Introduction

Instant, robust and repeatable underwater adhesion is a great challenge for the development of advanced adhesives, as water usually acts as a destroyer to prevent the intimate contact between surfaces of adhesives and substrates by forming hydration layers.[1] Various bioinspired strategies have been developed to improve the underwater adhesion, including fabricating patterned microstructures on elastomers inspired by geckos, modifying the physical/chemical properties of the surfaces by employing the approaches of marine mussels or sandcastle worms,[2, 3] preparing hydrogels that combine macroscale surface structure and nanoscale dynamic bonds by mimicking clingfish,[4] and developing coacervation-driven adhesives inspired by sessile organisms. Among these strategies, adhesive coacervates have acquired great attention due to their facile preparation, easy and accurate delivery, as well as high adhesion strength underwater. Coacervate is a polyelectrolyte-rich liquid phase usually separating from the mixture of oppositely charged polyelectrolyte aqueous solutions, which has attracted much research interest in multifarious fields, including the study of the origin of life because of its high resemblance with precellular systems[5] and membrane-free organelles,[6] the construction of extracellular matrices (e.g., lung, blood vessel, skin),[7] as well as the development of materials with gradient properties (e.g., squid beak).[8] Especially, coacervation unveils the secret of underwater adhesion of sessile organisms and attracts much research interest in underwater adhesives, where the concentrated adhesive proteins in the coacervate phase can easily spread on various substrates, taking advantage of the low interfacial energy.[9-11]

Sandcastle worm can build a protective shield with shells, stones, or sands to survive in turbulent sea environment through secreting adhesives that derive from the coacervation between oppositely charged proteins.[10] Inspired by this phenomenon, adhesive coacervates driven by electrostatic interaction between oppositely charged components were first investigated, where a phosphate-gelatin-divalent cation three-component coacervation system was developed and possessed underwater adhesion up to 765 kPa after curing of 24 h.[12] A positively charged hydrophobic amino acid was also demonstrated to form adhesive coacervates with negatively charged hetero-polyacids, but the underwater shear strength was only about 15 kPa after a contact time of 15 min.[13] Fast curing (25 s) and strong underwater contact adhesion ($\geqslant$2 J m^{-2}) could be simultaneously accomplished between a catechol-tethered weak polyanion and a polycation actuated by solvent exchange from DMSO to water, while complex polymer synthesis was required.[14] Instant underwater adhesion (122.3 ± 14.3 kPa for glass substrate) was also achieved by electrostatic interaction-driven coacervation between polyamidoamine epichlorohydrin and lignosulfonate, but the adhesive property was not repeatable.[15] Recently, short-range strong cation-π interaction between amines groups and tyrosine sidechains was proved to play a critical role in the coacervation of adhesive mussel foot proteins.[16] Although their nanomechanics as wet adhesives were investigated, the production of large-scale adhesives was not reported considering the high cost and complexity of the recombination of mussel foot proteins.[16-18] An underwater adhesive enabled by cation-π interaction and hydrogen-bonding interaction between polyamidoamine epichlorohydrin and tannic acid possessed instant underwater adhesion, but reliable adhesion was only achieved after 24 h curing.[19] Therefore, it remains a great challenge to acquire instant and repeatable underwater adhesives via a facile method, which have promising applications in tissue glue, hemostasis, and wound dressing. In a previous work, we reported a

hemostatic adhesive coacervate driven by hydrogen-bonding interaction between silicotungstic acid and polyethylene glycol, which had repeatable wet adhesion.[20] In aqueous environment, supramolecular architectures purely endowed by hydrogen-bonding interactions usually lack high stability due to the competition of intermolecular hydrogen bonds from polar water molecules. Inspired by the double helix structure of DNA, where hydrogen bonds were protected by the aromatic rings of nucleobases,[21] hydrophobic moieties have been employed to shield hydrogen bond-associated intermolecular interactions. For example, our previous study demonstrated alkylene spacer was harnessed to protect the quadruple hydrogen bonding between self-complementary 2-ureido-4[1H]-pyrimidinone (UPy) groups, where the rupture force and unbinding energy of the self-complementary UPy-UPy dimers were noticeably enhanced with a longer alkylene spacer.[22] Moreover, UPy groups could be directly encapsulated within the hydrophobic cores of sodium dodecyl sulfate (SDS) micelles to create robust and reversible intermolecular interactions, which enabled the fabrication of an extremely stretchable and fast self-healing hydrogel.[23] Besides desired mechanical properties, adhesive coacervates with diverse functionalities such as hemostatic,[20, 24] electrochromic,[25] stimuli-responsive,[26, 27] antibacterial properties,[19, 20] etc. are urgently needed to better satisfy the increasing demands of advanced materials applied in diverse fields.

In this work, we report the fabrication of a series of novel instant and repeatable underwater adhesives originating from coacervation between tannic acid (TA) and poly(ethylene glycol)$_{77}$-*b*-poly(propylene glycol)$_{29}$-*b*-poly(ethylene glycol)$_{77}$ (PEG-PPG-PEG, F68) aqueous solutions, formed by a one-step mixing. The coacervation was mainly driven by the hydrogen bonding between tannic acid and the PEG shells of F68 micelles, where the hydrophobic PPG cores of F68 micelles provided a second crosslinking to reinforce the network. The multiple hydrophobic aromatic rings of tannic acid also facilitated dehydration of the surfaces of the

adhesive and substrates underwater, promoting hydrogen bonding interaction, metal coordination and/or hydrophobic interactions at the interfaces. The synergy of the hydrogen bonding and hydrophobic interactions effectively enhanced the mechanical property and the adhesiveness of the coacervates. Notably, the as-prepared coacervate adhesive could be strengthened by repeatable cycles of attachment-detachment, where the underwater adhesion strength between two stainless steel cylinders was improved from ~120 kPa to ~160 kPa after 1000 cycles. Meanwhile, the coacervates could be easily painted on and bind various substrates underwater with instant and excellent adhesion strength up to 1.1 MPa on porcine skin and 602.1 kPa on poly(methyl methacrylate) (PMMA). Due to the innate anticancer and antibacterial properties of TA, the TA-F68 coacervates exhibit outstanding biological activities, holding great potential for applications in biological fields, such as injectable drug carriers, biocompatible tissue glues and wound dressings.

4.2. Experimental methods

4.2.1 Materials

Tannic acid (TA), Pluronic® F68 (poly(ethylene glycol)$_{77}$-*b*-poly(propylene glycol)$_{29}$-*b*-poly(ethylene glycol)$_{77}$, average M_n ~8,400), Pluronic® P123 (poly(ethylene glycol)$_{19}$-*b*-poly(propylene glycol)$_{69}$-*b*-poly(ethylene glycol)$_{19}$, average M_n ~5,800), poly(ethylene glycol) (BioUltra, for molecular biology, 8000), NaCl, and NaOH were purchased from Sigma-Aldrich and used as received. Poly(methyl methacrylate) (PMMA) round disks with diameter of 18.5 mm, wood and glass round disks with diameter of 25 mm were purchased from Amazon Canada.

4.2.2 Preparation of coacervates

TA aqueous solutions with weight percentages of 0.1%, 1%, 10%, 20%, 30% and 40%, and F68/PEG8000 aqueous solutions with weight percentages of 0.1%, 1%, 10%, 20% and 30% were prepared using deionized water. In a typical preparation process of the coacervate, TA aqueous solution and F68/PEG8000 aqueous solution were directly mixed at the volume ratio of 1:1, followed by vigorously shaking and centrifugation at the speed of 7000 rpm for 30 mins. The coacervate was acquired as the dense bottom phase. Meanwhile, the phase diagrams of coacervation was obtained using TA and F68/PEG8000 aqueous solutions at various concentrations. The coalescence of coacervate droplets was observed under a confocal microscope, and the sample was prepared by dropping 10 μL 40 wt% TA aqueous solution on a glass slide, followed by the addition of 10 μL 10 wt% F68 aqueous solution on the previous drop, which was then covered by a coverslip. To quantitatively monitor the growth of coacervate droplets, dynamic light scattering (DLS) technique was employed to measure the size of coacervate droplets as a function of time.

4.2.3 Rheological properties of coacervates

The rheological properties of the coacervates were studied by a TA Instruments AR-G2 rheometer using a 20 mm (diameter) 2° cone geometry with a gap of 53 μm. Oscillatory angular frequency sweep ranging from 0.1 rad/s to 100 rad/s at a fixed strain of 2% was carried out at 20 ℃ to characterize the shear moduli of the coacervates. The viscosity of the coacervates was characterized with shear rate ranging from 0.1/s to 100/s at 20 ℃. The rheological properties of TA and F68 aqueous solutions were measured using a DIN concentric cylinder with an operating gap of 5917.1 μm, and the parameters/conditions of the tests were consistent with those of the

coacervates. To investigate the effect of pH on the viscosity of the coacervates, the pH of 40 wt% TA aqueous solutions was adjusted with saturated NaOH to the desired value, followed by mixing with 10 wt% F68 to form coacervates. To compare the rheological properties between TA-F68 and TA-P123, the measurements of the corresponding coacervates (40 wt% TA and 10 wt% F68/P123) were conducted at 37 ℃.

4.2.4 Underwater adhesion properties of coacervates

Underwater adhesion properties of the coacervates were characterized on an AGS-X universal tensile testing machine (Shimadzu, Japan) at room temperature. A water container was attached to the compression cylinders to provide an underwater environment. PMMA, wood and glass round disks were glued on the center of the two compression cylinders with super glue, respectively, until totally dried in air. Then the two compression cylinders were mounted onto the tensile testing machine with a 5000 N load cell and immersed underwater. Subsequently, 100 μL coacervate was injected on the lower cylinder and being compressed by the upper cylinder with a force of 30 N for 10 s. The adhesion strength was then obtained by lifting the upper cylinder at a constant speed of 100 mm min^{-1}. For the cyclic tests, the two substrates were first separated with a distance of 3 mm (defined as zero displacement), and then the upper substrate approached the coacervate-delivered (100 μL) lower substrate until the two substrates contacted with each other and were pressed under a force of ~30 N for 10 s with a coacervate layer at the interface. Subsequently, the two substrates were separated back to zero displacement followed by further separation of 5 mm. During separation, the detected largest pulling-off force was regarded as adhesion force and used to calculate the underwater adhesion strength. Both the approaching and separation speeds were 100 mm min^{-1}. The substrates for cyclic adhesion test were porcine skin

and stainless steel surface, respectively, where the porcine skin was bonded onto the compression cylinders with superglue.

4.2.5 Anticancer properties of coacervates

The anticancer properties of the coacervate against A549 human lung epithelial cancer cell line and Huh7 human hepatoma cell line were assessed by MTS assay. A549 cells (200 μL cell suspension with complete growth media) were seeded into two 96-well plates at a density of 2×10^4 and 5×10^4 cells per well, respectively, while Huh7 cells (200 μL cell suspension with complete growth media) were seeded into a 96-well plate at a density of 5×10^4 cells per well. The cell suspensions were then incubated at 37 ℃ for 24 h. 100 mg mL^{-1} stock solution of coacervate dissolved in DMSO was prepared and was diluted to a series of concentrations, including 50, 20, 10, 5, 2, and 0.2 mg mL^{-1}. Subsequently, 1.01 μL of coacervate solutions (100, 50, 20, 10, 5, 2, and 0.2 mg mL^{-1}) were added into cell suspensions with final coacervate concentrations to be 500, 250, 100, 50, 25, 10, 1 μg mL^{-1}, respectively. While 2.02 μL of 100 mg mL^{-1} coacervate solution was added into cell suspensions to achieve an aimed coacervation concentration of 1000 μg mL^{-1}. After incubated at 37 ℃ for another 24 h, the coacervate solutions were removed, and each well was washed with 200 μL of Dulbecco's phosphate-buffered saline (DPBS) to remove residual samples before the addition of MTS solution (20 μL MTS in 200 μL DPBS). After incubation of the plate at 37 °C for 3 h, the optical density at 490 nm (OD_{490nm}) was measured using a microplate reader, and the cell viability was calculated by comparing OD_{490nm} of cells treated with/without coacervate solutions.

4.2.6 Antibacterial properties of coacervates

Gram-positive *S. aureus* (ATCC25923) and Gram-negative *E. coli* (ATCC25922) were employed as the model bacteria. First, the standard profile of bacterial concentration versus light absorbance at 600 nm was plotted based on agar plating and microplate reader. Then bacterial suspensions in Luria-Bertani (LB) broth (10 g tryptone, 5 g yeast extract, 10 g NaCl) were prepared followed by adjustment of bacterial concentration to 10^9 CFU (colony-forming unit) mL^{-1} with the addition of LB broth. After that, a serials of the *E. coli* and *S. aureus* diluted suspensions (each by ten-fold) were prepared and 100 μL of the dilution was added into each well of the corresponding 96-well plates where the experimental group were prepared with the addition of 50 μL coacervate while the control group was left blank. Then the 96-well plates were incubated at 37 ℃ for 24 h. Subsequently, 20 μL bacteria suspension was transferred from each well and then diluted in ten-fold serial for further use. Nutrient agar media was made by adding 25 g LB broth and 15 g agar into 1000 ml deionized water, autoclaving at 121 °C for 30 min. Subsequently, 15 ml of the nutrient mixture was poured into a sterilized glass petri dish at 70 °C to prepare LB solid plate for bacteria incubation and colony counting. After the agar plates were cooled and solidified, 100 μl of the bacteria suspensions as well as their corresponding diluted solutions were applied on the entire surface of an agar plate, respectively. The agar plates were incubated at 37 °C for 24 h for calculation of CFU. Inhibition efficiency was calculated as (1-CFU of experimental group/CFU of control group)*100%.

4.3. Results and Discussion

4.3.1 Fabrication and phase behaviors of the TA-F68 coacervates

The fabrication process of the TA-F68 coacervate was quite facile, where a typical coacervate was prepared by directly mixing 40 wt% TA aqueous solution (deep brown) with 10 wt% F68 aqueous solution (colorless and transparent) at a volume ratio of 1:1 followed by vigorous shaking, yielding a turbid solution (**Figure 4.1A**). Dispersed coacervate droplets with sizes of several to tens of micrometers could be observed under an optical microscope (**Figure 4.1B**), where small coacervate droplets collided with each other and coalesced into big ones. After centrifugation for 30 mins, a coacervate phase completely separated from the corresponding immiscible supernatant was obtained (**Figure 4.1C**). The microstructure of the coacervate was characterized by a cryogenic transmission electron microscopy (cryo-TEM), showing a continuous tubular network and distinguishable coacervate droplets (**Figure 4.1D**), which suggested stable and strong physical interactions between TA and F68 micelles. The as-prepared coacervate was highly viscous and could immediately and firmly bind different inorganic and organic substances (e.g., glass, metal, stone, wood, plastics, chicken gizzard, pork flesh, and pork bone) to human skin underwater (**Figure 4.1E**). Meanwhile, the coacervate could be easily painted on substrates (e.g., glass slide) underwater with desired shapes and resist high-speed water flow, suggesting its excellent underwater adhesive property (**Figure 4.1F**), which was also demonstrated by lifting a 500 g stainless steel weight in a water tank (**Figure 4.1G**). Mass production of the coacervate can be easily achieved due to the facile preparation process, and the low cost of the raw materials suggests its potential for industrial production.

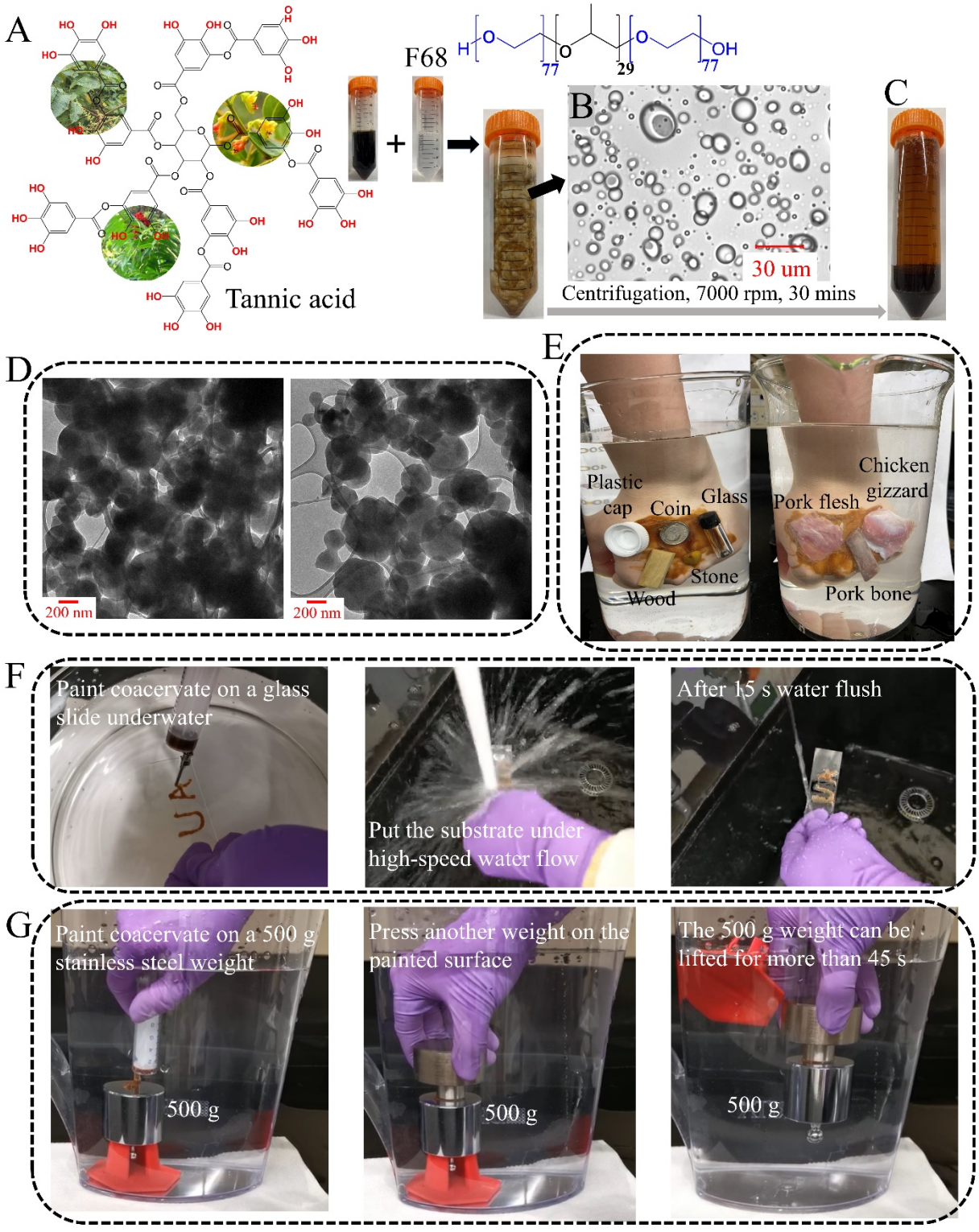

Figure 4.1. Fabrication of TA-F68 coacervate and its underwater adhesive properties. (A) Molecular structures of TA and F68, and a turbid solution was obtained after mixing and vigorous

shaking of the aqueous solutions. (B) Dispersed coacervate droplets ranging from several to tens of micrometers observed under an optical microscope. (C) Complete liquid-liquid phase separation achieved by centrifugation of 7000 rpm for 30 minutes. (D) Cryo-TEM images of the coacervate. (E) The as-prepared coacervate could firmly bind different substances (e.g., glass, metal, stone, wood, plastic cap, chicken gizzard, pork flesh, and pork bone) to a human hand underwater. (F) The as-prepared coacervate could be facilely painted on glass slide underwater with desired shapes and resist high-speed water flow. (G) The coacervate could adhere two stainless-steel surfaces together and lift a 500 g weight underwater.

Phase behavior and coacervation of TA and F68 aqueous solutions were investigated under different solution concentrations and the phase diagram is shown in **Figure 4.2A**, where the corresponding coacervates were named as TAx-F68-y (x and y represent the weight percentage of TA aqueous solution and F68 aqueous solution, respectively). When the concentration of TA ranged from 0.1 wt% to 10 wt% and was mixed with 0.1 wt% or 1 wt% F68 solution at a fixed volume ratio of 1:1, the mixture of the two aqueous solutions immediately turned turbid due to the generation of coacervate droplets. Growth of the coacervate droplets was detected by dynamic light scattering (DLS) and the time-dependent size change of the coacervate droplets is illustrated in **Figure 4.2B**. When TA concentrations was fixed, the coacervate droplets formed with 1 wt% F68 were bigger than those generated with 0.1 wt% F68, owing to the higher amount of dispersed F68 micelles (both 0.1 wt% and 1 wt% were below the concentration of entanglement C_e of F68, **Figure 4.S1**) that facilitated the formation and growth of coacervate droplets. However, at a constant F68 concentration, the size of coacervate droplets decreased when the concentration of TA increased from 0.1 wt% to 1 wt%, which was possibly because that the higher number of TA

molecules resulted in the formation of more coacervate droplet nuclei which had less chance to coalesce.[6] Further increasing the concentration of TA to 10 wt%, the coacervate droplets could coalesce to sizes of micrometers. No coacervation was detected with high concentration of F68 (10 wt%, 20 wt% and 30 wt%) and low concentrations of TA (0.1 wt% and 1 wt%), which might due to the entanglements among F68 polymer chains; while coacervation could be observed at higher TA concentrations. As the concentrations of F68 were above C_e (**Figure 4.S1**), TA molecules in dilute solutions could not effectively interact with the F68 polymer chains to form a stable coacervate network. For all the other experimental concentrations on the phase diagram (**Figure 4.2A**), a macroscale phase separation could be instantly observed once the two solutions were mixed. The water contents of the coacervates prepared with different TA and F68 concentrations were determined to be 13.3-32.5 wt% (**Table 4.S1**), revealing the coacervates were rich in organic components. As illustrated in **Figure 4.2C**, both TA and F68 solutions exhibited low viscosities (<0.06 Pa·s), while the viscosities of corresponding coacervates drastically increased by more than 10000 times (up to 590 Pa·s for TA40-F68-10 coacervate), demonstrating robust intermolecular interactions between TA molecules and F68 micelles. When the concentration of F68 was fixed at 30 wt%, viscosities of the corresponding coacervates were enhanced with the increase of TA concentration, owing to the higher crosslinking density between TA molecules and F68 micelles. However, when the concentration of TA solution was fixed at 40 wt%, the viscosities of corresponding coacervates decreased with a higher concentration of F68 (**Figure 4.2C**), where less TA content was detected in the formed coacervate phase (**Figure 4.S2**). The liquid-like behavior of the coacervates was demonstrated by frequent sweep rheological measurements, with loss modulus G'' always higher than storage modulus G' (**Figure 4.2D**).

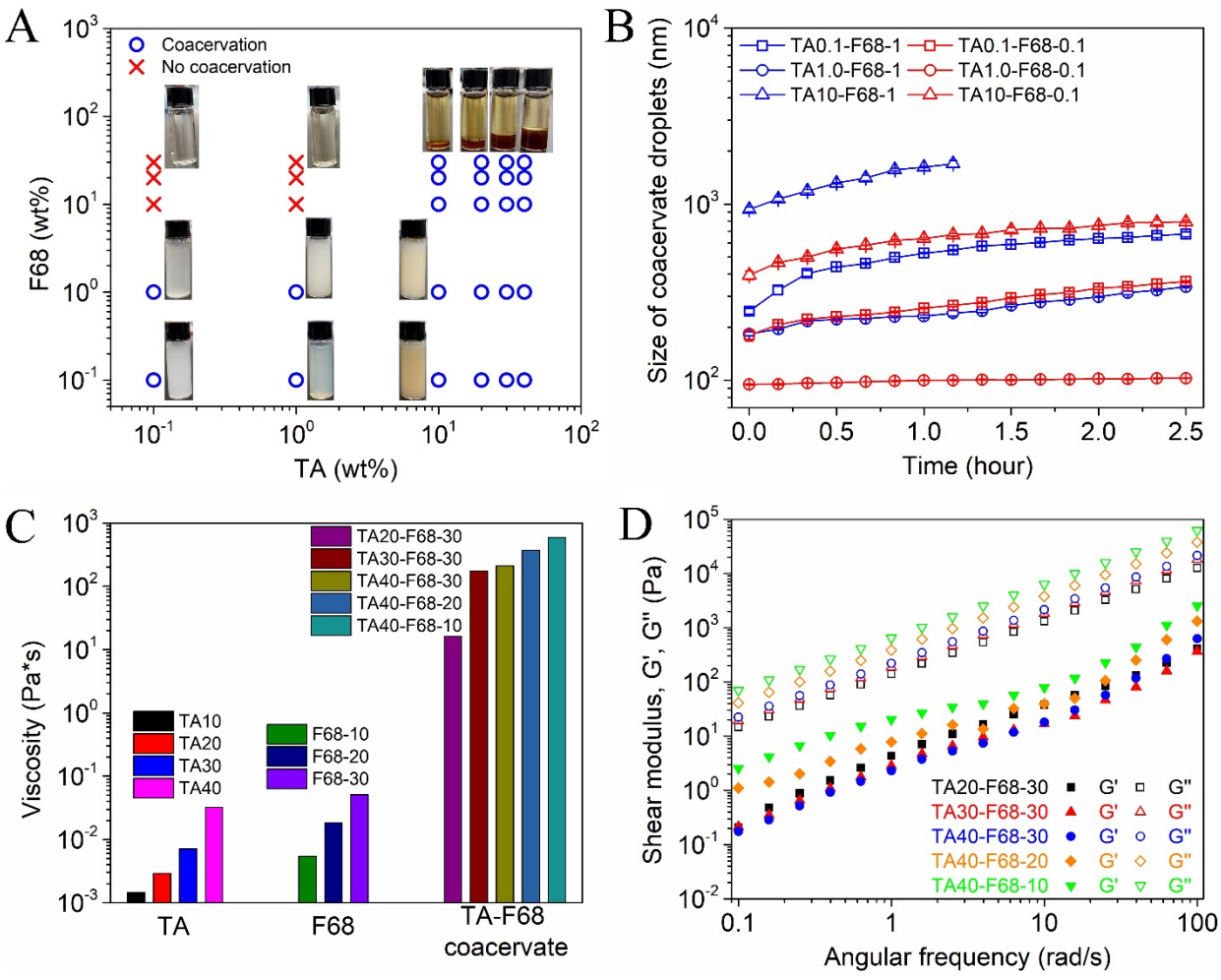

Figure 4.2. Phase behaviors of TA and F68 aqueous solutions as well as rheological properties of the corresponding coacervates. (A) Phase diagram of TA and F68 aqueous solutions of different concentrations mixed at a fixed 1:1 volume ratio. (B) Time-dependent size variation of the coacervate measured by DLS. (C) Viscosities of TA solutions, F68 solutions and the corresponding TA-F68 coacervates. (D) Shear storage modulus G' and shear loss modulus G'' of TA-F68 coacervates.

4.3.2 Molecular interactions of the TA-F68 coacervates

The molecular interactions of TA-F68 coacervates were first investigated via Fourier Transform Infrared (FTIR) spectroscopy. As shown in **Figure 4.3A**, the stretching vibration of hydroxyl groups (-OH) in TA displayed an obvious shift after coacervation with F68, and a slight shift of the C=O stretching was also detected, which was attributed to the formation of intermolecular hydrogen bonding between hydroxyl groups of TA and etheric oxygens of PEG shells of F68 as well as the intramolecular hydrogen bonding within hydroxyl and carbonyl groups of TA.[24, 28] As for F68, C-O-C shifted from 1099.7 to 1073.9 cm^{-1} after coacervation, indicating associated intermolecular interactions of the etheric oxygens.[20] The maintained C-H stretching (2882.6 to 2876.1 cm^{-1}) of CH_3 and CH_2 twist (1279.3 to 1309.7 cm^{-1}) of PPG suggesting the hydrophobic interaction among methyl groups of F68 micelles in the formed coacervate.[29] To further demonstrate the interaction mechanism within the coacervate, dimethyl sulfoxide (DMSO), a well-known hydrogen bond acceptor, was employed to interfere with the hydrogen bonding between TA and F68 through competing with etheric oxygens of F68 PEG shells to interact with hydroxyl groups of TA.[24] As shown in **Figure 4.3B,** the TA40-F68-10 coacervate was completely dissolved in DMSO, suggesting the coacervation between TA and F68 was mainly driven by hydrogen bonding. As the association/dissociation of TA (pKa1 of 4.9 ± 0.5, pKa2 of 7.4 ± 0.6)[30] is highly dependent on the pH of the solution, the effect of pH on coacervation was also studied, where TA solutions (40 wt%, original pH was 2.98) with different pH values (adjusted by NaOH) were mixed with 10 wt% F68 aqueous solutions respectively and the coacervation phenomena were investigated. With the increase of pH, both loss modulus G'' and viscosity of the corresponding coacervate experienced a slight increment followed by a continuous decrease (**Figure 4.3C**). The slight enhancement of the loss modulus and viscosity below pH 4.09 was possibly due to the increased electrostatic interaction between Na^+ and dissociated TA and/or

cation-π interaction between Na^+ and phenolic aromatic rings,[31-32] as the viscosities of 40 wt% TA solution and the corresponding coacervates also increased with gradual addition of NaCl (**Figure 4.3D**). When the pH value was above 4.09, the decrease of viscosity was primarily attributed to the continuous dissociation of TA, leading to the reduction of available hydroxyl groups as proton donors for hydrogen-bonding interaction. As hydrogen-bonding interaction was usually affected by temperature,[33] the viscosity of TA40-F68-10 coacervate was characterized with temperature ranging from 25 ℃ to 45 ℃, displaying a noticeable decline with the elevated temperature owing to thermo-weakened hydrogen-bonding interaction (**Figure 4.S3**). Therefore, the coacervation phenomenon was mainly driven by hydrogen-bonding interaction between hydroxyl groups of TA and etheric oxygens of F68 PEG shells, which was illustrated in **Figure 4.3E**.

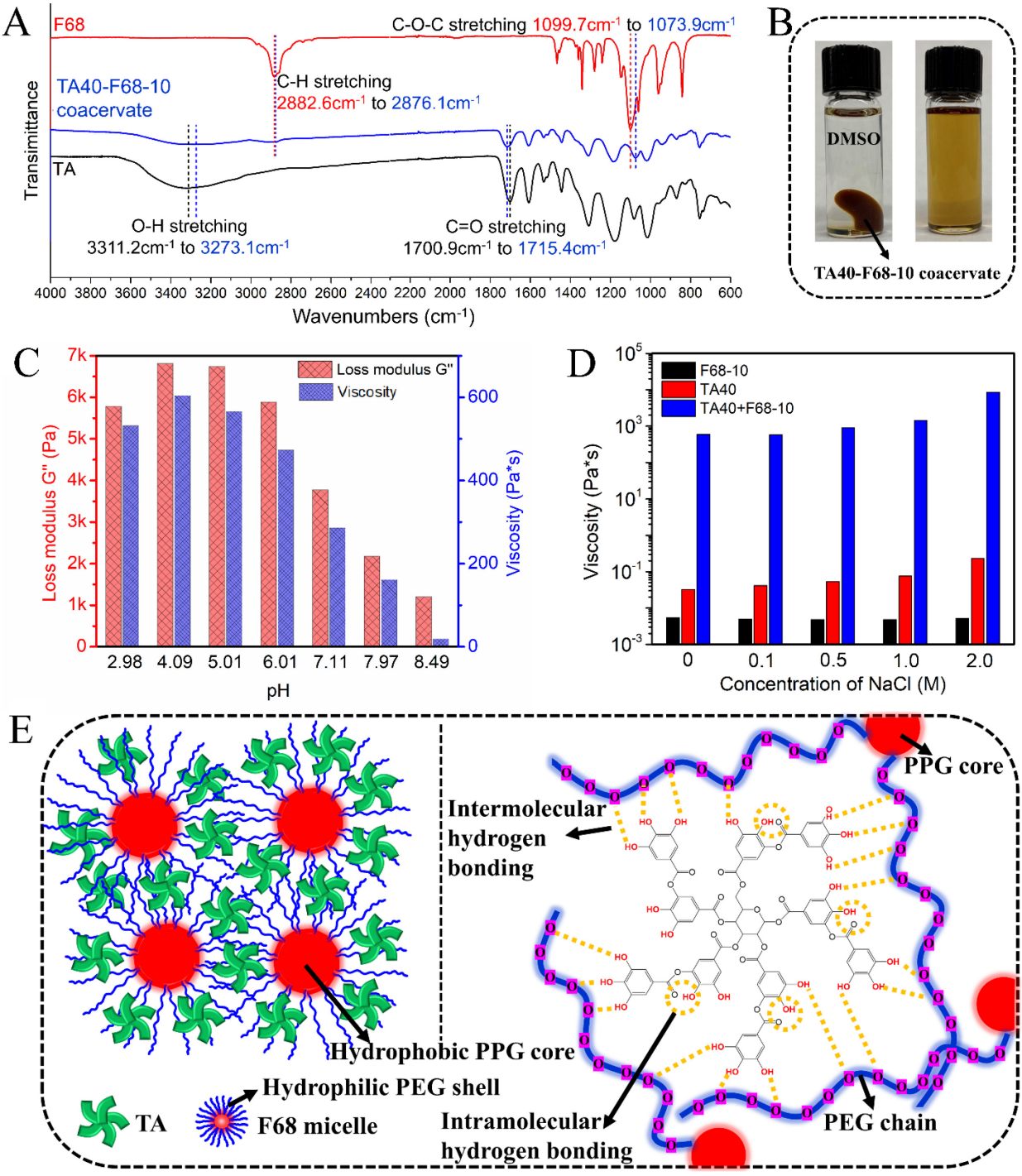

Figure 4.3. Intermolecular interaction between TA and F68. (A) FTIR spectra of TA, F68 and corresponding TA40-F68-10 coacervate. (B) Immersed TA40-F68-10 coacervate with DMSO would totally dissolve TA40-F68-10 coacervate. (C) Loss modulus and viscosity of TA40-F68-10 coacervates where pH of 40 wt% TA was adjusted with saturated NaOH aqueous solution

before coacervation. (D) Effect of NaCl on viscosity of 40 wt% TA aqueous solution, 10 wt% F68 aqueous solution and TA40-F68-10 coacervate. (E) Proposed intermolecular interactions of TA-F68 coacervate.

The role of hydrophobic PPG block of F68 playing in the formation of TA-F68 coacervates was studied, by comparing with TA-PEG coacervates that was generated with PEG8000 (poly(ethylene glycol), 8000 g mol^{-1}) instead of F68. As each PEG8000 chain can provide 181 etheric oxygens, which is higher than 77 etheric oxygens offered by an F68 molecule, it tends to form more hydrogen bonds with TA and yield coacervates over a broader concentration range (**Figure 4.4A** and **Figure 4.2A**). Owing to hydrophobic interaction among PPG blocks, F68 polymer chains would self-assemble into micelles, where PPG blocks served as hydrophobic cores to act as a second crosslinking that further enhanced the strength of intermolecular interactions. This interaction mechanism was demonstrated by the rheological properties of TA-F68 and TA-PEG8000 coacervates. As shown in **Figure 4.4B**, the viscosity and loss modulus of TA-F68 coacervates were almost twice the values of the corresponding TA-PEG8000 coacervates (with the same concentration of TA and F68/PEG8000, respectively). In addition, another PEG-PPG-PEG block polymer P123 was also used to form coacervates, which contained a longer hydrophobic PPG block and shorter hydrophilic PEG chains compared to F68 (**Figure 4.4C**). As displayed in **Figure 4.4C**, the viscosity and shear moduli of TA40-P123-10 coacervates were all higher than those of TA40-F68-10 coacervates, which was mainly attributed to the stronger hydrophobic interactions among the PPG cores of P123 micelles. Therefore, the introduction of hydrophobic PPG block greatly strengthened attractive intermolecular interaction of PEG-based

polymers with TA molecules, via synergistic cooperation of hydrogen-bonding and hydrophobic interactions.

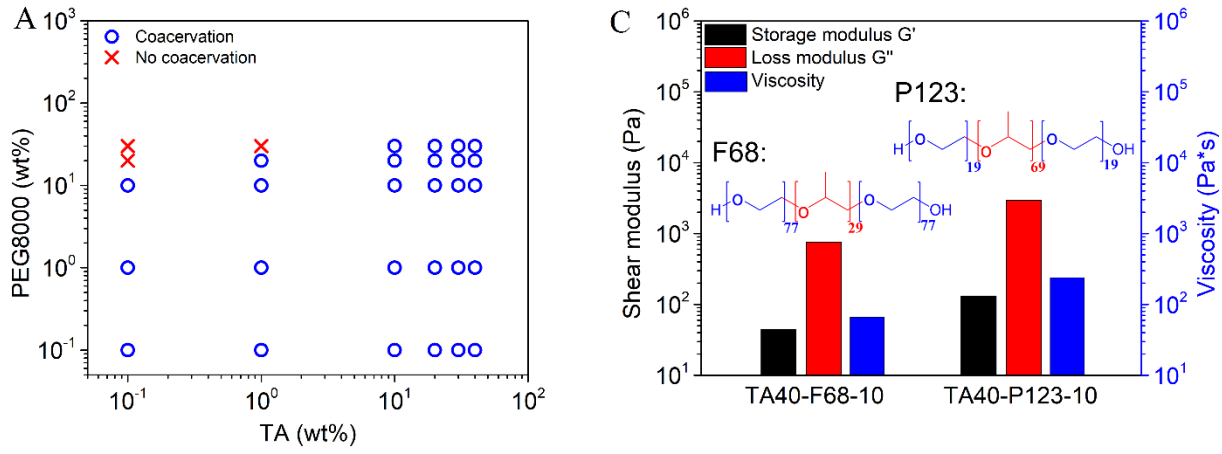

B

Coacervates	Loss modulus (Pa) at 10 rad/s	Viscosity (Pa*s) at 1/s	Coacervates	Loss modulus (Pa) at 10 rad/s	Viscosity (Pa*s) at 1/s
TA20-F68-30	1312.8	57.7	TA20-PEG-30	558.8	33.4
TA30-F68-30	1816.2	180.9	TA30-PEG-30	794.1	79.4
TA40-F68-30	2160.8	213.5	TA40-PEG-30	894.7	88.4
TA40-F68-20	3790.2	380.4	TA40-PEG-20	1415.3	138.9
TA40-F68-10	6328.5	612.1	TA40-PEG-10	2996.9	288.5

Figure 4.4. Phase diagram and rheological properties of TA-F68, TA-PEG8000 and TA-P123 coacervates. (A) Phase diagram of TA and PEG8000 solutions. (B) Loss moduli and viscosities of TA-F68 and TA-PEG8000 coacervates. (C) Shear moduli and viscosities of TA40-F68-10 and TA40-P123-10 coacervates.

4.3.3 Underwater adhesive properties

The underwater adhesive properties of TA-F68 coacervates were quantitatively examined using a tensile tester and the results are shown in **Figure 4.5**. As illustrated in **Figure 4.5A**, cyclic adhesion tests were implemented underwater for both TA40-F68-10 and TA40-PEG-10 coacervates, which were repeated 1000 times using two stainless steel substrates. In the first 100 cycles, the adhesion strengths of both coacervates were similar

around 120 kPa. However, when the tests were repeated more than 100 times, the adhesion strength of TA40-PEG-10 remained stable while that of the TA40-F68-10 coacervate gradually improved up to 160 kPa, which was most likely due to the protection provided by the hydrophobicity of PPG blocks against water and the mechanical training of polymer chains.[34] The detachment of the adherent surfaces was caused by cohesive failure resulted from the relatively weak mechanical property of the coacervates in the test system, where the coacervates still adhered to the separated surfaces (**Figure 4.5B**).[35] Additionally, cyclic adhesion test of TA40-F68-10 coacervate was carried out between two porcine skin surfaces (**Figure 4.5C**). Adhesion strength of the coacervate progressively improved from 516.4 kPa to 1.1 MPa with increasing number of approaching-retracting cycles, which was possibly due to the increased true contact area of the skins (the coacervate could enter the pores of skin) after repeatedly applying the pressure. The instant underwater adhesion of the TA40-F68-10 coacervate on different substrates was quantitatively examined and the results are presented in **Figure. 4.5D**, showing the highest adhesion strength of 602.1 kPa on poly(methyl methacrylate) (PMMA, contact angle of 67.3°), which was contributed by the cooperation of hydrogen-bonding interaction (electronegative oxygen atoms of PMMA served as proton acceptors) and hydrophobic interaction (substantial methyl groups of PMMA repelled water molecules). The adhesion strength of the coacervate on wood surface was determined to be 213.5 kPa. Although the initial water contact angle of wood was 74.8° owing to the abundant hydrophobic polyphenolic lignin, it rapidly decreased to 18.2° within 3 minutes due to the presence of microtubes and micropores on the wood surface. Hence, when the coacervate was sandwiched between two wood surfaces, it tended to be squeezed into microtubes and/or micropores, reducing the effective contact area of the two surfaces and impairing the adhesion strength. The lowest adhesion strength of 131.7 kPa was found

between hydrophilic glass surfaces (water contact angle of 15.1°), where the interfacial adhesion was mainly contributed by hydrogen-bonding interaction. To the best of our knowledge, the instant underwater adhesion strength of the as-prepared coacervate is superior to the previously reported coacervates (<200 kPa for all cases[20, 24, 36] and ~420 kPa for PMMA substrate[19]) and even some adhesive hydrogels (≤180 kPa[35, 37]). On the basis of its excellent adhesion properties and repeatability, the coacervate holds great promise for various applications, especially those in aqueous or wet environments.

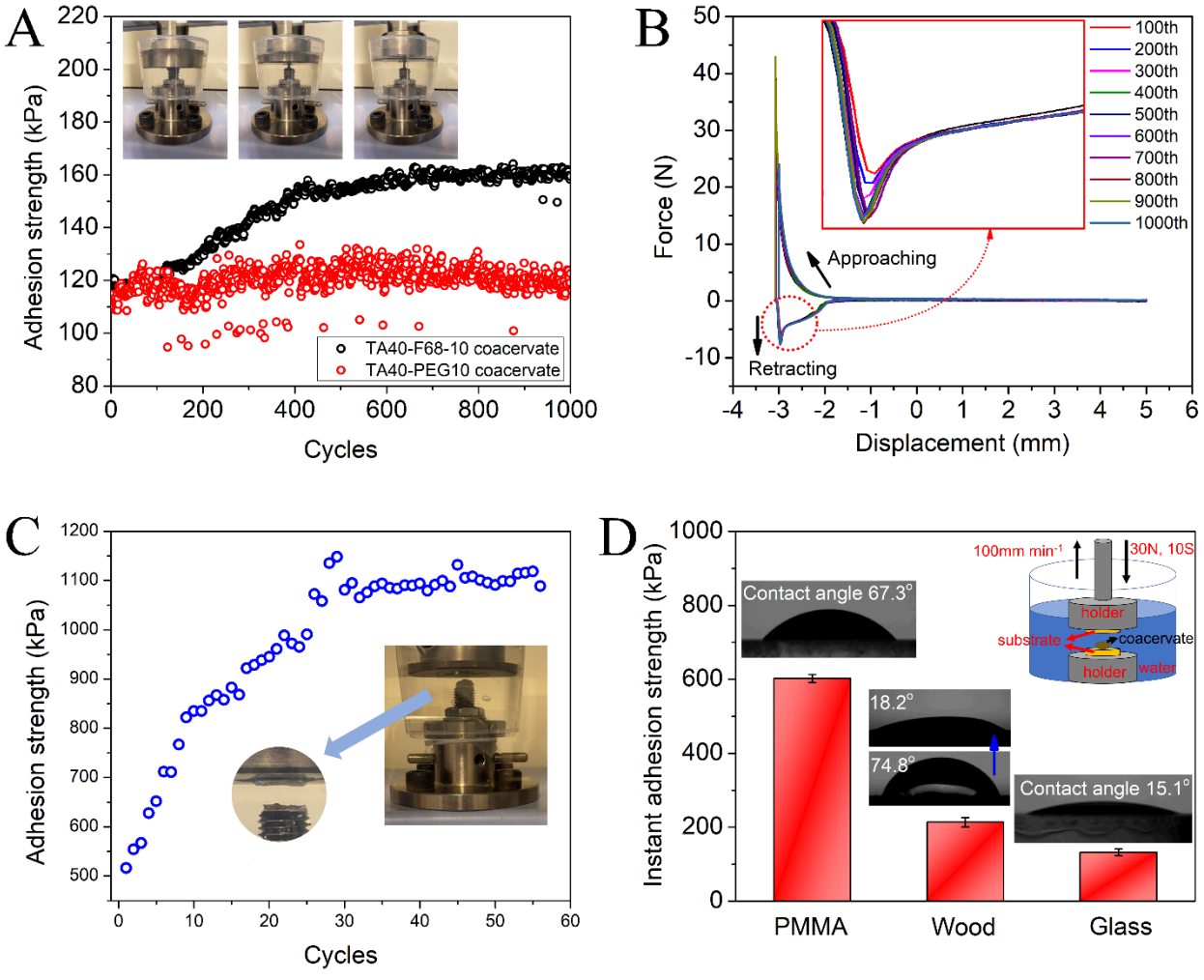

Figure 4.5. Instant and repeatable underwater adhesive properties of the TA40-F68-10 coacervate. (A) Cyclic underwater adhesion test of TA40-F68-10 and TA40-PEG-10 coacervates between

stainless steel surfaces and (B) the corresponding force-displacement profiles. (C) Cyclic underwater adhesion test of TA40-F68-10 coacervate between two porcine skins. (D) Instant underwater adhesion strength of the TA40-F68-10 coacervate on different substrates including PMMA, wood and glass. The inserted images are the contact angles of water on PMMA, wood and glass substrates. The inserted schematic image shows the experimental setup of the underwater adhesion tests.

4.3.4 Anticancer properties

TA has been widely recognized as an anticancer agent of various cancer cells (e.g., breast cancer cells, prostate cancer cells, head and neck cancer cells, liver cancer cells, colon cancer cells, glioma cancer cells) through inducing cell cycle arrest and apoptosis or inhibiting proliferation.[38-41] Herein, the anticancer property of TA40-F68-10 coacervate was characterized using A549 human lung epithelial cancer cell line and Huh7 human hepatoma cell line, which was examined by MTS assay (**Figure 4.6**). As TA40-F68-10 coacervate was insoluble in water, it was first dissolved in DMSO and then added into the plates with seeded cancer cells with a desired volume, cell density, and concentration of coacervate. It was demonstrated that after 24 h incubation, the coacervate exerted its anticancer property on A549 cells (2×10^4 cells per well, **Figure 4.6A**) when concentration up to 1000 μg mL^{-1}, showing cell viability of only 29.4%. Considering the cell size of A549 cells (~60 μm) was larger than that of Huh7 cells (~21.9 μm), 5×10^4 cells per well was used for Huh7 cell line to compare the antibacterial property of the coacervate (**Figure 4.6B**).[42, 43] The activity of Huh7 cells was sensitive to the existence of coacervate, where the cell viability gradually decreased when the concentration of the coacervate ranging from 1 μg mL^{-1} to 100 μg mL^{-1}. When the coacervate concentration further increased to

250 μg mL^{-1}, 500 μg mL^{-1} and 1000 μg mL^{-1}, the viability of Huh7 cells noticeably reduced to 42.3%, 39.9%, and 30.4%, respectively. Considering the cell death caused by competition among cells for nutrients, the anticancer property of the coacervate on A549 cell line was also inspected with 5×10^4 cells per well (**Figure 4.6C**), where a decrease of cell viability of A549 cell line could be noticed when the concentration of coacervate reached 250 μg mL^{-1}. Although the higher cell density could result in lower cell viability of A549 cells with coacervate concentration below 500 ug mL^{-1}, it could raise the cell viability when the concentration of coacervate was 1000 μg mL^{-1} as compared to the 2×10^4 cells per well case in **Figure 4.6A**. Apart from the innate anticancer property of TA, the TA40-F68-10 coacervate was capable of encapsulating hydrophobic anticancer drugs such as curcumin[44] in hydrophobic PPG cores (**Figure 4.S4**) to further enhance the anticancer property. Therefore, the developed TA-F68 coacervate provides a novel paradigm for the fabrication of anticancer agents, where tunable drug-loading efficiency could be achieved by varying the types and concentrations of Pluronic micelles.[45]

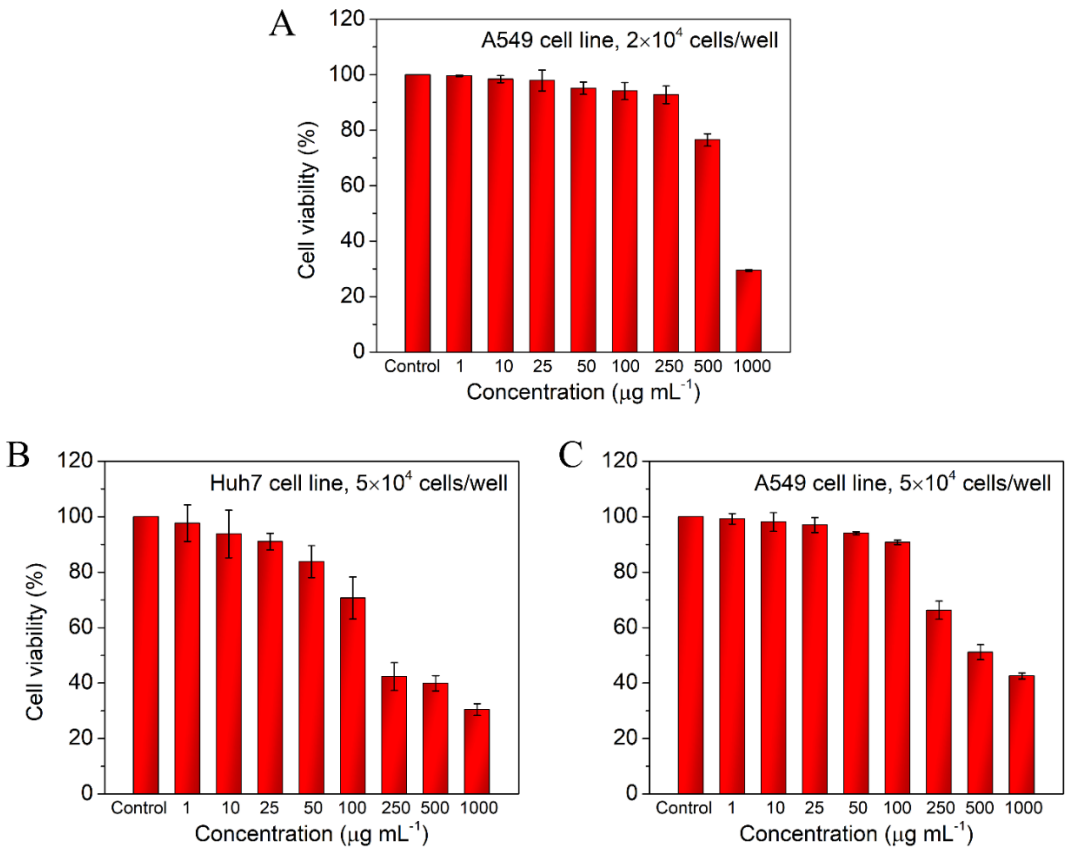

Figure 4.6. Anticancer properties of the TA40-F68-10 coacervate. (A) and (C) Cell viability of (A) A549 cell line with a cell density of 2×10^4 cells per well, (B) Huh7 cell line with a cell density of 5×10^4 cells per well, and (C) Huh7 cell line with a cell density of 5×10^4 cells per well after 24 h incubation with various concentrations of DMSO-dissolved TA40-F68-10 coacervate.

4.3.5 Antibacterial properties

As microorganisms accumulation commonly occurs on implanted materials, it is highly desired to endow implanted materials with antimicrobial properties to minimize the risk of inflammation and infection.[46] The antibacterial performance of TA40-F68-10 coacervate was examined against both Gram-positive *Staphylococcus aureus* (*S. aureus*) and Gram-negative *Escherichia coli* (*E. coli*) bacteria with concentration from 10^3 CFU mL^{-1} to 10^9 CFU mL^{-1} as shown in **Figure 4.7A**. It was demonstrated that the coacervate was able to kill more than 99% of

S. aureus over the measured concentration range, where the inhibition efficiency was still up to 99.69% when the extremely high concentration of 10^9 CFU mL^{-1} was applied. The inhibition efficiency of the coacervate against 10^9 CFU mL^{-1} *E coli* could also reach 99.34%. Meanwhile, the antibacterial property of the coacervates loaded with or without curcumin (**Figure 4.S4**) were examined by comparing the average widths of the inhibition zone against ~2×10^8 CFU mL^{-1} *S. aureus*, where Tegaderm firm and blank drug-sensitive test paper were served as control groups, respectively. As indicated in **Figure 4.7B**, the width of the inhibition zone for curcumin-loaded coacervate and pure coacervate were 1.48 mm and 0.89 mm, respectively, suggesting that the loading of curcumin enhanced the antibacterial performance of the coacervate. The excellent innate antibacterial property of the coacervate is attributed to TA, which has been extensively employed as an effective antibacterial ingredient for diverse hydrogels, complexes, or membranes,[47] holding great potential in biomedical applications such as tissue glues and wound dressings.

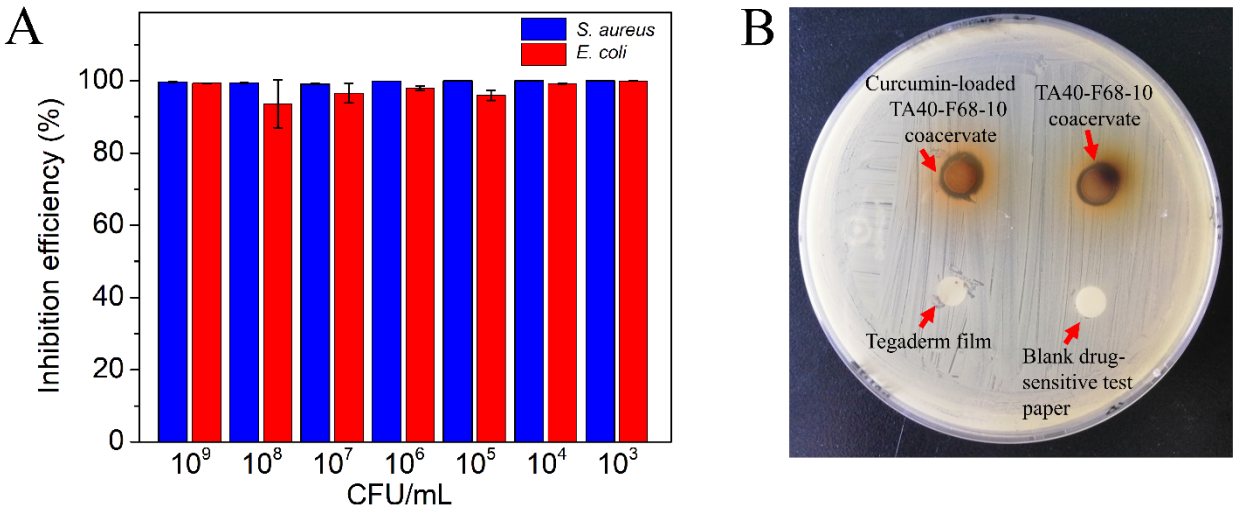

Figure 4.7. Antibacterial properties of TA40-F68-10 coacervate (A) Inhibition efficiencies of *S. aureus* and *E. coli* after 24 h incubation with TA40-F68-10 coacervate. (B) Antibacterial

performances of curcumin-loaded coacervate, pure coacervate, Tegaderm film, and blank drug-sensitive test paper against *S. aureus*.

4.4. Conclusions

In this work, we have developed a novel instant and repeatable underwater adhesive via a facile one-step mixing of TA and F68 aqueous solutions, which also exhibits excellent anticancer and antibacterial properties. The formation of the TA-F68 adhesive coacervates is driven by the synergy of hydrogen-bonding interaction and hydrophobic interaction, where the coacervation process is mainly actuated by the intermolecular hydrogen bonding between hydroxyl groups of TA and etheric oxygens of F68, and the hydrophobic cores of F68 micelles offer an additional crosslinking, significantly enhancing the mechanical properties (e.g., shear moduli, viscosity) of the coacervates. The rheological properties of the as-prepared coacervates can be modulated over several orders of magnitude for practical applications by varying the concentrations of TA and F68 and modulating the pH/salt concentration of the environment. The coacervates can be easily painted on surfaces underwater and instantly resist the high-speed water flow, which shows robust and instant underwater adhesion on various substrates with adhesion strength up to 1.1 MPa on porcine skin and 602.1 kPa on PMMA. Besides, the coacervate exhibits repeatable underwater adhesive property, being capable of withstanding at least 1000 cycles of attachment-detachment. To the best of our knowledge, the repeatable adhesive property of the novel coacervate developed in this work is superior to a lot of previously reported underwater adhesives. The biological activities of TA endow the TA-F68 coacervate with innate anticancer and antibacterial properties, which can be further enhanced by the drug loading capability of F68 micelles, holding great

potential for diverse biomedical applications, such as injectable drug carriers, biocompatible tissue glues and wound dressings.

4.5 Supporting Information

Table 4.S1. Water content of TA-F68 coacervates

Coacervate	$Weight_{bottle}$ (g)	$Weight_{bottle+coacervate}$ (g)	$Weight_{bottle+freeze\text{-}dried\ coacervate}$ (g)	Water content (%)
TA20+F68-30	3.3411	3.9228	3.7335	32.5
TA30+F68-30	3.3426	4.1189	3.9120	26.7
TA40+F68-30	3.3554	4.2812	4.1579	13.3
TA20+F68-20	3.3210	3.8097	3.6679	29.0
TA30+F68-20	3.3563	4.0044	3.8944	17.0
TA40+F68-20	3.3256	4.1066	3.9773	16.6
TA20+F68-10	3.3251	3.7094	3.6300	20.7
TA30+F68-10	3.3449	3.7966	3.6951	22.5
TA40+F68-10	3.3406	3.8001	3.6831	25.5

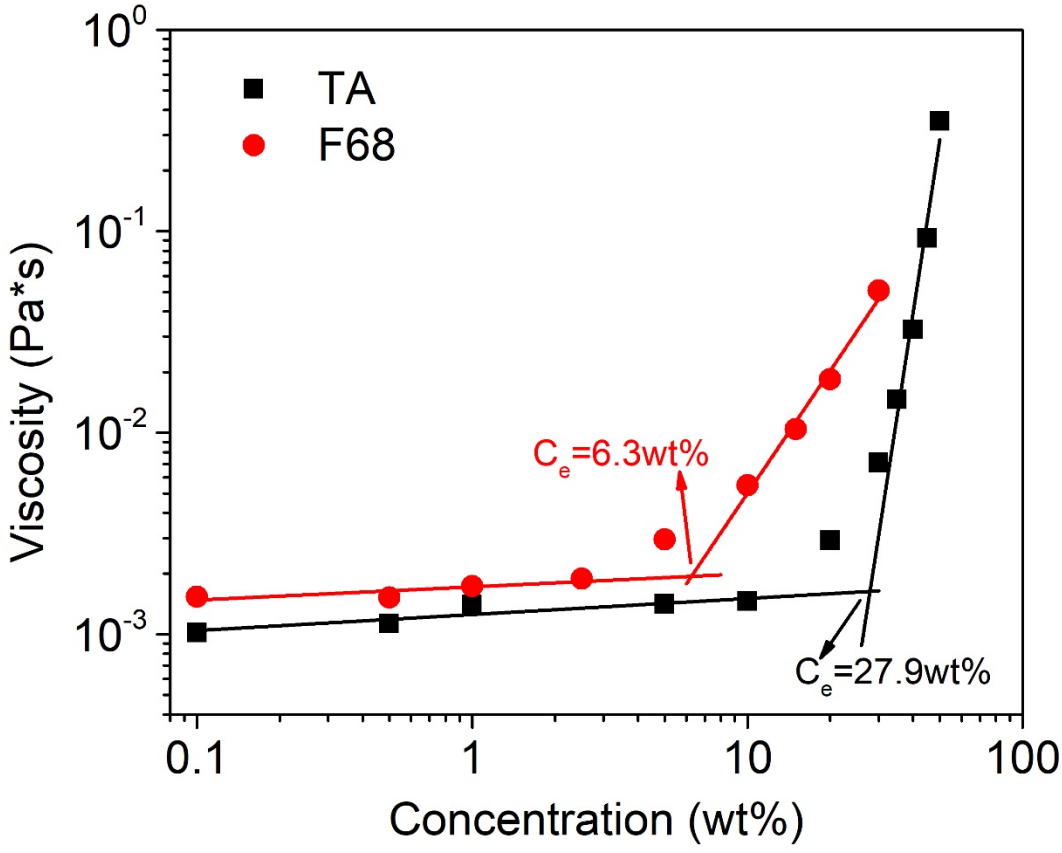

Figure 4.S1. Viscosities of TA and F68 aqueous solutions under different concentrations.

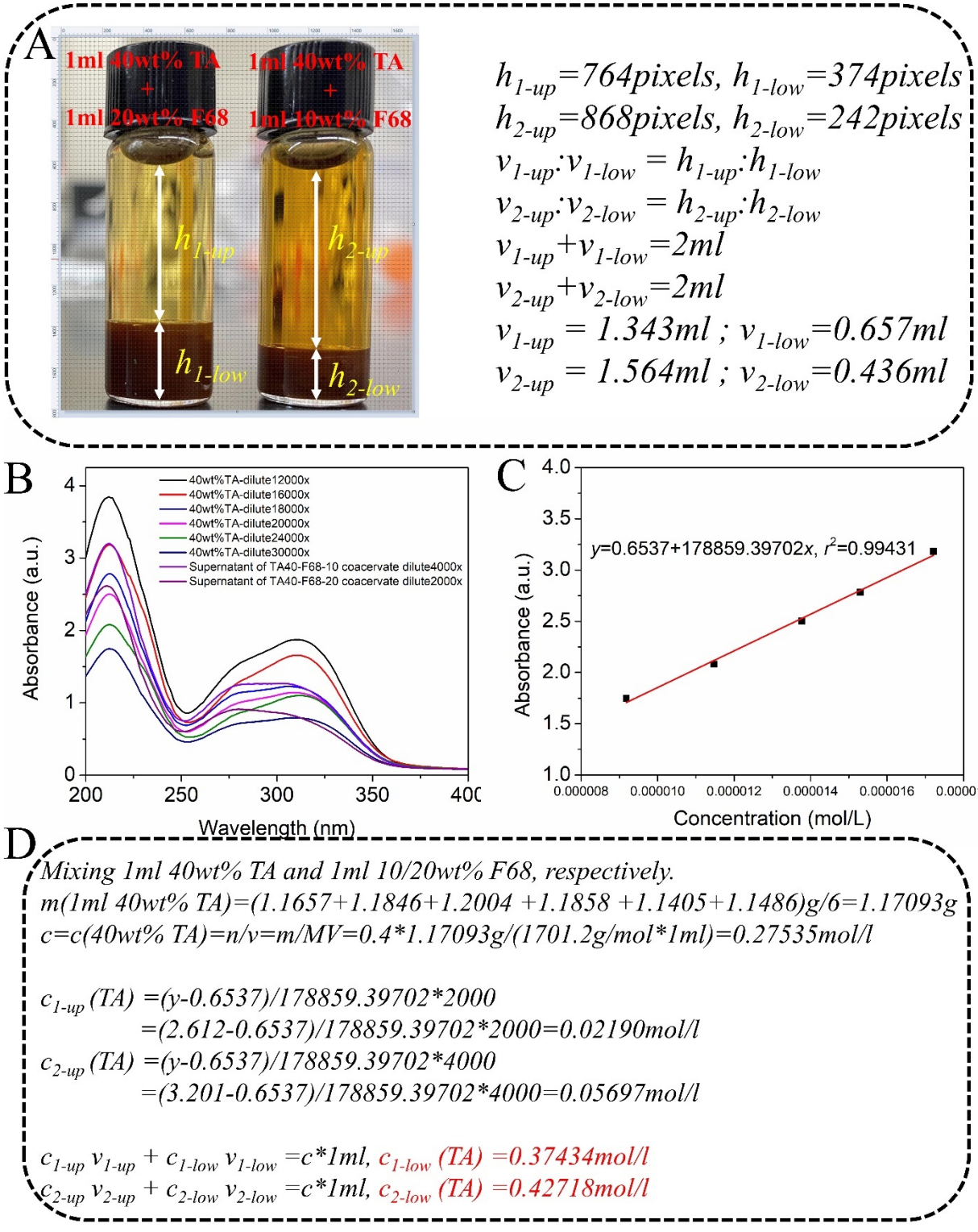

Figure 4.S2. Calculation of volume of TA-F68 coacervate phases and corresponding supernatants as well as concentration of TA in TA-F68 coacervate phases. (A) The heights of TA40-F68-20

(h_1) and TA40-F68-10 (h_2) coacervate phases and corresponding supernatant phases ($h_{1\text{-up}}$ and $h_{3\text{-up}}$) were measured by counting number of pixels in the vertical direction. Volumes of TA40-F68-20 ($v_{1\text{-low}}$) and TA40-F68-10 ($v_{2\text{-low}}$) coacervate phases as well as volumes of their corresponding supernatants ($v_{1\text{-up}}$ and $v_{2\text{-up}}$) were figured out. (B) UV-vis was employed to measure light absorbance of a series of diluted 40wt% TA aqueous solution and diluted supernatants of TA40-F68-10/20 coacervates. It was demonstrated that TA has a characterized absorption peak at 212 nm. (C) Standard absorbance-concentration relationship was plotted based on results of (B), where concentration of TA in supernatants of TA40-F68-10/20 coacervates can be calculated according to the fitted linear equation. (D) Concentration of TA in TA40-F68-20 ($c_{1\text{-low}}$) and TA40-F68-10 ($c_{2\text{-low}}$) coacervate phases as well as corresponding supernatants ($c_{1\text{-up}}$ and $c_{2\text{-up}}$) were deducted and calculated.

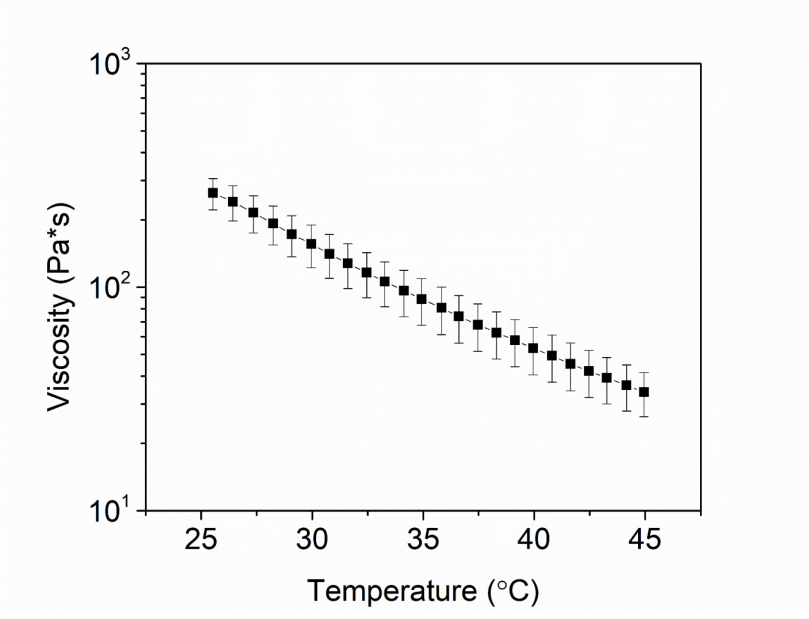

Figure 4.S3. Variation of viscosity of TA40-F68-10 coacervate along with temperature.

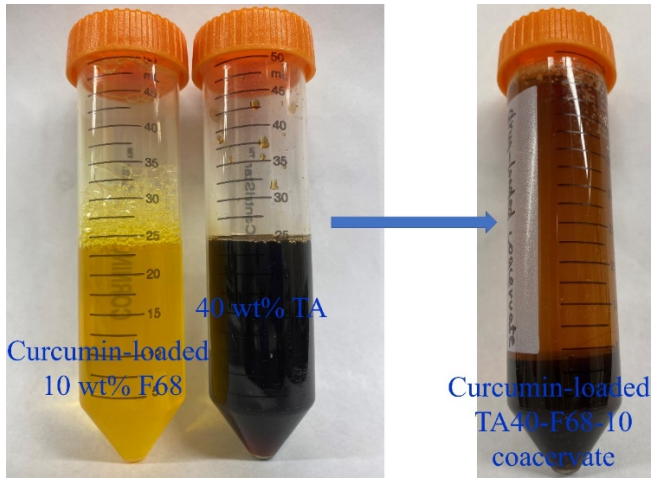

Figure 4.S4. Hydrophobic drug curcumin can be loaded within the hydrophobic cores of F68 micelles (10 wt%) followed by coacervation with 40 wt% TA to form curcumin-loaded TA40-F68-10 coacervate.

References

1. G. P. Maier, M. V. Rapp, J. H. Waite, J. N. Israelachvili, A. Butler, *Science* **2015**, *349*, 628.

2. H. Lee, B. P. Lee, P. B. Messersmith, *Nature* **2007,** *448*, 338.

3. Y. Ma, S. Ma, Y. Wu, X. Pei, S. N. Gorb, Z. Wang, W. Liu, F. Zhou, *Adv. Mater.* **2018,** *30*, 1801595.

4. P. Rao, T. L. Sun, L. Chen, R. Takahashi, G. Shinohara, H. Guo, D. R. King, T. Kurokawa, J. P. Gong, *Adv. Mater.* **2018,** *30*, 1801884.

5. D. Zwicker, R. Seyboldt, C. A. Weber, A. A. Hyman, F. Jülicher, *Nat. Phys.* **2016,** *13*, 408.

6. W. M. Aumiller Jr, C. D. Keating, *Nat. Chem.* **2016,** *8*, 129.

7. G. C. Yeo, F. W. Keeley, A. S. Weiss, *Adv. Colloid Interface Sci.* **2011,** *167*, 94.

8. Y. Tan, S. Hoon, P. A. Guerette, W. Wei, A. Ghadban, C. Hao, A. Miserez, J. H. Waite, *Nat. Chem. Biol.* **2015,** *11*, 488.

9. B. P. Lee, P. B. Messersmith, J. N. Israelachvili, J. H. Waite, *Annu. Rev. Mater. Res.* **2011**, *41*, 99.

10. R. J. Stewart, J. C. Weaver, D. E. Morse, J. H. Waite, *J. Exp. Biol.* **2004**, *207*, 4727.

11. D. S. Hwang, H. Zeng, A. Srivastava, D. V. Krogstad, M. Tirrell, J. N. Israelachvili, J. H. Waite, *Soft Matter* **2010**, *6*, 3232.

12. H. Shao, R. J. Stewart, *Adv. Mater.* **2010**, *22*, 729.

13. X. Li, Z. Du, Z. Song, B. Li, L. Wu, Q. Liu, H. Zhang, W. Li, *Adv. Funct. Mater.* **2018**, *28*, 1800599.

14. Q. Zhao, D. W. Lee, B. K. Ahn, S. Seo, Y. Kaufman, J. N. Israelachvili, J. H. Waite, *Nat. Mater.* **2016,** *15*, 407.

15. C. Wei, X. Zhu, H. Peng, J. Chen, F. Zhang, Q. Zhao, *ACS Sustainable Chem. Eng.* **2019,** *7* , 4508.

16. S. Kim, H. Y. Yoo, J. Huang, Y. Lee, S. Park, Y. Park, S. Jin, Y. M. Jung, H. Zeng, D. S. Hwang, Y. Jho, *ACS Nano* **2017,** *11*, 6764.

17. S. Kim, J. Huang, Y. Lee, S. Dutta, H. Y. Yoo, Y. M. Jung, Y. Jho, H. Zeng, D. S. Hwang, *Proc. Natl. Acad. Sci. U.S.A.* **2016**, *113*, E847.

18. G. P. Maier, M. V. Rapp, J. H. Waite, J. N. Israelachvili, A. Butler, *Science*, **2015**, *349*, 628.

19. Z. Wang, S. Zhang, S. Zhao, H. Kang, Z. Wang, C. Xia, Y. Yu, J. Li, *Chem. Eng. J.* **2021**, *404,* 127069

20. Q. Peng, J. Chen, Z. Zeng, T. Wang, L. Xiang, X. Peng, J. Liu, H. Zeng, *Small* **2020**, *16*, 2004132.

21. J. H. K. Ky Hirschberg, L. Brunsveld, A. Ramzi, J. A. J. M. Vekemans, R. P. Sijbesma, E. W. Meijer, *Nature* **2000**, *407*, 167.

22. J. Chen, M. Wu, L. Gong, J. Zhang, B. Yan, J. Liu, H. Zhang, T. Thundat, H. Zeng, *J. Phys. Chem. C* **2019,** *123*, 4540.

23. I. Jeon, J. Cui, W. R. K. Illeperuma, J. Aizenberg, J. J. Vlassak, *Adv. Mater.* **2016,** *28*, 4678.

24. K. Kim, M. Shin, M. Koh, J. H. Ryu, M. S. Lee, S. Hong, H. Lee, *Adv. Funct. Mater.* **2015**, *25*, 2402.

25. J. Xu, X. Li, J. Li, X. Li, B. Li, Y. Wang, L. Wu, W. Li, *Angew. Chem. Int. Ed.* **2017**, *56*, 8731.

26. P. G. Lawrence, Y. Lapitsky, *Langmuir* **2015,** *31*, 1564.

27. M. Dompe, F. J. Cedano-Serrano, O. Heckert, N. van den Heuvel, J. van der Gucht, Y. Tran,

D. Hourdet, C. Creton, M. Kamperman, *Adv Mater* **2019,** *31*, e1808179.

28. K. H. Khoultchaev, P. Pang, R. J. Kerekes, P. Englezos, *Can. J. Chem. Eng.* **1998,** *76*, 261.

29. Y. Su, J. Wang, H Liu, *Langmuir* **2002**, *18*, 5370.

30. D. Lin, N. Liu, K. Yang, L. Zhu, Y. Xu, B. Xing, *Carbon* **2009,** *47*, 2875.

31. F. Weber, E. Sagstuen, Q. Z. Zhong, T. Zheng, H. Tiainen, *ACS Appl. Mater. Interfaces* **2020,** *12*, 52457.

32. Q. Lu, D. X. Oh, Y. Lee, Y. Jho, D. S. Hwang, Zeng, H. *Angew. Chem. Int. Ed. Engl.* **2013,** *52*, 3944.

33. J. Chen, Q. Peng, T. Thundat, H. Zeng,. *Chem. Mater.* **2019**, *31*, 4553.

34. S. Lin, J. Liu, X. Liu, X. Zhao, *Proc. Natl. Acad. Sci. U.S.A.* **2019,** *116*, 10244.

35. H. Fan, J. Wang, J. P. Gong, *Adv. Funct. Mater.* **2020**, 2009334.

36. D. Lee, H. Hwang, J. S. Kim, J. Park, D. Youn, D. Kim, J. Hahn, M. Seo, H. Lee, *ACS Appl. Mater. Interfaces* **2020,** *12*, 20933.

37. H. Fan, J. Wang, Z. Tao, J. Huang, P. Rao, T. Kurokawa, J. P. Gong, *Nat. Commun.* **2019**, *10*, 5127.

38. W. Baer-Dubowska, H. Szaefer, A. Majchrzak-Celińska, V. Krajka-Kuźniak, *Curr. Pharmacol. Rep.* **2020,** *6*, 28.

39. B. Baby, P. Antony, R. Vijayan, *Crit. Rev. Food Sci. Nutr.* **2018,** *58*, 2491.

40. I. Yildirim, T. Kutlu, *Int. J. Biol. Chem.* **2015,** *9*, 332.

41. S. M. Hadi, S. H. Bhat, A. S. Azmi, S. Hanif, U. Shamim, M. F. Ullah, *Semin. Cancer Biol.* **2007,** *17*, 370.

42. K. Liu, C. Cheng, C. Chang, J. Chao, *Nanotechnology* **2007,** *18,* 325102.

43. E. Berger, N. Vega, M. Weiss-Gayet, A. Geloen, *Biomed. Res. Int.* **2015,** *2015*, 821761.

44. A. Sahu, N. Kasoju, P. Goswami, U. Bora, *J. Biomater. Appl.* **2011,** *25*, 619.

45. A. Pitto-Barry, N. P. E. Barry, *Polym. Chem.* **2014,** *5*, 3291.

46. M. C. Giano, Z. Ibrahim, S. H. Medina, K. A. Sarhane, J. M. Christensen, Y. Yamada, G. Brandacher, J. P. Schneider, *Nat. Commun.* **2014,** *5*, 4095.

47. B. Kaczmarek, *Materials* **2020,** *13*, 3224.

CHAPTER 5 Conclusions and Future Work

5.1 Major Conclusions and Contributions

In this thesis work, three coacervation systems driven by hydrogen-bonding interaction have been reported, which are applied for the development of novel instant wet/underwater adhesives with multifunctionalities. The major conclusions and original contributions are presented as below.

(1) Wet adhesive coacervates with hemostatic and antibacterial properties have been prepared from facile one-step mixing of SiW and PEG, where the driving force for coacervation is most likely originated from the hydrogen bonding between oxygens of SiW and etheric oxygens of PEG bridged by hydrated protons. The as-prepared coacervate is easily paintable underwater and show strong wet adhesion to diverse substrates. This work demonstrates that coacervation can occur in salt-free environments via non-electrostatic interactions, providing a new platform for engineering multifunctional coacervate materials as tissue glues, wound dressings, and membrane-free cell systems.

(2) Instant paintable underwater adhesives with tunable optical and electrochromic properties in a salt-free system have been developed. The coacervation can be readily achieved via one-step mixing of SiW and P123 aqueous solutions driven by hydrogen-bonding where the hydrophobic cores of P123 micelles provided a second crosslinking to reinforce the network. The as-prepared coacervate possesses instant and excellent underwater adhesion and can be facilely painted underwater on diverse substrates, showing resistance to water flush as well as repeatable stretching and bending of the substrates, superior to a lot of previously reported coacervates. The adhesive also exhibits outstanding stability in high-salt aqueous solutions up to 3 M for at least 1200 h. The introduction of P123 endows the adhesives with thermo-responsive optical property,

while the innate reduction-related color switch of SiW offered the electrochromic property. Our findings present a new approach for the development of salt-free and multifunctional coacervation material systems, holding great promise in bioengineering applications and for the fabrication of novel flexible electronics, such as smart aqueous batteries and low-power electrochromic windows.

(3) Instant and repeatable underwater adhesives with anticancer and antibacterial properties have been fabricated via a facile one-step mixing of TA and F68 aqueous solutions. The coacervation process is mainly actuated by the intermolecular hydrogen bonding between hydroxyl groups of TA and etheric oxygens of F68, and the hydrophobic cores of F68 micelles offer an additional crosslinking, significantly enhancing the mechanical properties of the coacervates. The rheological properties of as-prepared coacervates can be modulated by varying concentrations of TA and F68 aqueous solutions and/or adding salt like NaCl. Meanwhile, the coacervates can be paintable underwater and be able to instantly resist flushing of running water, as well as show robust and instant underwater adhesion on various substrates with adhesion strength up to 1.1 MPa on porcine skin and 602.1 kPa on PMMA. Besides, the coacervate exhibits repeatable underwater adhesive property, being capable of enduring at least 1000 cycles of attachment-detachment, which is the most repeatable underwater adhesive to the best of our knowledge. Such wet adhesion performance of the developed TA-F68 coacervate is superior to that of a lot of previously reported coacervate materials, even some hydrogels. Moreover, the TA-F68 coacervate possesses innate anticancer and antibacterial properties owing to the biological activities of TA while F68 confers the coacervate with drug loading capability to further enhance biological activities, holds great potential in biomedical applications, such as injectable drug carriers, biocompatible tissue glues and wound dressings.

5.2 Future Work

In this study, hydrogen-bonding interaction has been exploited as the driving force for coacervation towards the preparation of wet/underwater adhesives, paving the way to advanced applications in diverse fields such as bioengineering and electronics. Although the instant and repeatable underwater adhesives with multifunctionalities have been successively developed, there are still unaddressed challenges regarding practical applications. Some suggestions for future research are presented.

(1) The developed SiW-PEG underwater adhesives with potential application as paintable cathodes of aqueous batteries possess relatively fast color-switching in the procedure of discharging while its charging process is low-efficient. To accomplish sensitive color-switching and high-efficient charging-discharging process, SiW as a typical representative of Keggin-structured polyoxometalates can be substituted by other materials with higher reduction potentials. Besides, to better control the thickness and roughness of the electrochromic adhesive coating, in-situ formation of coacervate on conductive substrates can be achieved by deposition of one component of the complex coacervation system on the substrates.

(2) Although additional crosslinks such as hydrophobic cores of micelles have been introduced into coacervates to reinforce the networks, they are still not sufficiently strong to resist cohesion failure upon large tensile forces. Therefore, strain-stiffening/hardening coacervates that can maintain their integrity under external mechanical stresses and properly perform their physiological functions are demanding especially when these systems are subjected to large deformations close to the maximum strain.

(3) Despite that coacervation has been considered to play a significant role in the formation of elastic skin, lung, and blood vessels, the studies of applying coacervates to the development of

artificial tissues such as implantable skins are still in the initial stage. Strengthening coacervate-based biomaterials will provide a promising approach to the fabrication of artificial tissues.

Bibliography

1. Sing, C. E.; Perry, S. L. Recent progress in the science of complex coacervation. *Soft Matter* **2020,** *16*, 2885-2914.

2. Shin, Y.; Brangwynne, C. P. Liquid phase condensation in cell physiology and disease. *Science* **2017,** *357*, eaaf4382.

3. Holehouse, A. S., Pappu, R. V. Protein polymers: Encoding phase transitions. *Nat. Mater.* **2015,** *14*, 1083-1084.

4. Hyman, A. A.; Weber, C. A.; Julicher, F. Liquid-liquid phase separation in biology. *Annu. Rev. Cell Dev. Biol.* **2014,** *30*, 39-58.

5. Keating, C. D. Aqueous phase separation as a possible route to compartmentalization of biological molecules. *Acc. Chem. Res.* **2012,** *45*, 2114-2124.

6. de Jong, H. G. B. Die Koazervation und ihre Bedeutung für die Biologie. *Protoplasm* **1932,** *15*, 110-173.

7. Koga, S.; Williams, D. S.; Perriman, A. W.; Mann, S. Peptide-nucleotide microdroplets as a step towards a membrane-free protocell model. *Nat. Chem.* **2011,** *3*, 720-724.

8. Schuster, B. S.; Reed, E. H.; Parthasarathy, R.; Jahnke, C. N.; Caldwell, R. M.; Bermudez, J. G.; Ramage, H.; Good, M. C.; Hammer, D. A. Controllable protein phase separation and modular recruitment to form responsive membraneless organelles. *Nat. Commun.* **2018,** *9*, 2985.

9. Okihana, H.; Ponnamperuma, C. A protective function of the coacervates against UV light on the primitive Earth. *Nature* **1982,** *299*, 347–349.

10. Yeo, G. C.; Keeley, F. W.; Weiss, A. S. Coacervation of tropoelastin. *Adv. Colloid Interface Sci.* **2011,** *167*, 94-103.

11. Tan, Y.; Hoon, S.; Guerette, P. A.; Wei, W.; Ghadban, A.; Hao, C.; Miserez, A.; Waite, J. H. Infiltration of chitin by protein coacervates defines the squid beak mechanical gradient. *Nat. Chem. Biol.* **2015,** *11*, 488-495.

12. Miserez, A.; Schneberk, T.; Sun, C.; Zok, F. W.; Waite, J. H. The transition from stiff to compliant materials in squid beaks. *Science* **2008,** *319*, 1816-1819.

13. Ambadipudi, S.; Biernat, J.; Riedel, D.; Mandelkow, E.; Zweckstetter, M. Liquid-liquid phase separation of the microtubule-binding repeats of the Alzheimer-related protein Tau. *Nat. Commun.* **2017,** *8*, 275.

14. Stewart, R. J.; Weaver, J. C.; Morse, D. E.; Waite, J. H. The tube cement of Phragmatopoma californica: a solid foam. *J. Exp. Biol.* **2004,** *207*, 4727-4734.

15. Zhao, H.; Sun, C.; Stewart, R. J.; Waite, J. H. Cement proteins of the tube-building polychaete Phragmatopoma californica. *J Biol Chem* **2005,** *280*, 42938-42944.

16. Stewart, R. J.; Wang, C. S.; Shao, H. Complex coacervates as a foundation for synthetic underwater adhesives. *Adv. Colloid Interface Sci.* **2011,** *167*, 85-93.

17. Hofman, A. H.; van Hees, I. A.; Yang, J.; Kamperman, M. Bioinspired underwater adhesives by using the supramolecular toolbox. *Adv. Mater.* **2018,** *30*, 1704640.

18. Muhoza, B.; Xia, S.; Wang, X.; Zhang, X.; Li, Y.; Zhang, S. Microencapsulation of essential oils by complex coacervation method: preparation, thermal stability, release properties and applications. *Crit. Rev. Food Sci. Nutr.* **2020**, 1-20.

19. Llamas, S.; Guzman, E.; Ortega, F.; Baghdadli, N.; Cazeneuve, C.; Rubio, R. G.; Luengo, G. S. Adsorption of polyelectrolytes and polyelectrolytes-surfactant mixtures at surfaces: a physico-chemical approach to a cosmetic challenge. *Adv. Colloid Interface Sci.* **2015,** *222*, 461-487.

20. Xu, Y.; Mazzawi, M.; Chen, K.; Sun, L.; Dubin, P. L. Protein purification by polyelectrolyte coacervation: influence of protein charge anisotropy on selectivity. *Biomacromolecules* **2011,** *12*, 1512-1522.

21. Sinclair, S. M.; Bhattacharyya, J.; McDaniel, J. R.; Gooden, D. M.; Gopalaswamy, R.; Chilkoti, A.; Setton, L. A. A genetically engineered thermally responsive sustained release curcumin depot to treat neuroinflammation. *J. Controlled Release* **2013,** *171*, 38-47.

22. McDaniel, J. R.; Callahan, D. J.; Chilkoti, A. Drug delivery to solid tumors by elastin-like polypeptides. *Adv. Drug Deliv. Rev.* **2010,** *62*, 1456-1467.

23. Chenglong, W.; Shuhan, X.; Jiayi, Y.; Wencai, G.; Guoxiong, X.; Hongjing, D. Dextran-based coacervate nanodroplets as potential gene carriers for efficient cancer therapy. *Carbohydr. Polym.* **2020,** *231*, 115687.

24. Zhang, Z.; Liu, Q.; Sun, Z.; Phillips, B. K.; Wang, Z.; Al-Hashimi, M.; Fang, L.; Olson, M. A. Poly-lipoic ester-based coacervates for the efficient removal of organic pollutants from water and increased point-of-use versatility. *Chem. Mater.* **2019,** *31*, 4405-4417.

25. Chilivery, R.; Begum, G.; Chaitanya, V.; Rana, R. K. Tunable surface wrinkling by a bio-inspired polyamine anion coacervation process that mediates the assembly of polyoxometalate nanoclusters. *Angew. Chem. Int. Ed.* **2020,** *59*, 8160-8165.

26. Liu, J.; Tian, L.; Qiao, Y.; Zhou, S.; Patil, A.; Wang, K.; Li, M.; Mann, S. Hydrogel-immobilized coacervate droplets as modular micro-reactor assemblies. *Angew. Chem. Int. Ed.* **2020,** *59*, 6853-6859.

27. Lv, K.; Perriman, A. W.; Mann, S. Photocatalytic multiphase micro-droplet reactors based on complex coacervation. *Chem. Commun.* **2015,** *51*, 8600-8602.

28. Jehle, F.; Macias-Sanchez, E.; Fratzl, P.; Bertinetti, L.; Harrington, M. J. Hierarchically-structured metalloprotein composite coatings biofabricated from co-existing condensed liquid phases. *Nat. Commun.* **2020,** *11*, 862.

29. Jones, J. P.; Sima, M.; O'Hara, R. G.; Stewart, R. J. Water-borne endovascular embolics inspired by the undersea adhesive of marine sandcastle worms. *Adv. Healthcare Mater.* **2016,** *5*, 795-801.

30. Tjaden Modderman, R. S.; Holleman, L. W. J. Coacervation. *Nature* **1932,** *129*, 654.

31. Dubin, P.; Perry, S.; Xu, Y. Foreword. *Adv Colloid Interface Sci* **2017,** *239*, 1.

32. Dubin, P. L.; Kayitmazer, A. B.; Huang, Q. Polyelectrolyte-macroion coacervation. Foreword. *Adv Colloid Interface Sci* **2011,** *167*, 1.

33. Veis, A. A review of the early development of the thermodynamics of the complex coacervation phase separation. *Adv. Colloid Interface Sci.* **2011,** *167*, 2-11.

34. Kayitmazer, A. B. Thermodynamics of complex coacervation. *Adv. Colloid Interface Sci.* **2017,** *239*, 169-177.

35. Sing, C. E. Development of the modern theory of polymeric complex coacervation. *Adv. Colloid Interface Sci.* **2017,** *239*, 2-16.

36. Xiao, J.; Li, Y.; Huang, Q. Application of Monte Carlo simulation in addressing key issues of complex coacervation formed by polyelectrolytes and oppositely charged colloids. *Adv. Colloid Interface Sci.* **2017,** *239*, 31-45.

37. Jho, Y.; Yoo, H. Y.; Lin, Y.; Han, S.; Hwang, D. S. Molecular and structural basis of low interfacial energy of complex coacervates in water. *Adv. Colloid Interface Sci.* **2017,** *239*, 61-73.

38. Liu, Y.; Winter, H. H.; Perry, S. L. Linear viscoelasticity of complex coacervates. *Adv. Colloid Interface Sci.* **2017,** *239*, 46-60.

39. Uversky, V. N. Protein intrinsic disorder-based liquid-liquid phase transitions in biological systems: Complex coacervates and membrane-less organelles. *Adv Colloid Interface Sci* **2017,** *239*, 97-114.

40. Muiznieks, L. D.; Keeley, F. W. Biomechanical Design of Elastic Protein Biomaterials: A Balance of Protein Structure and Conformational Disorder. *ACS Biomater. Sci. Eng.* **2016,** *3*, 661-679.

41. Wise, S. G.; Yeo, G. C.; Hiob, M. A.; Rnjak-Kovacina, J.; Kaplan, D. L.; Ng, M. K.; Weiss, A. S. Tropoelastin: a versatile, bioactive assembly module. *Acta Biomater.* **2014,** *10*, 1532-1541.

42. Mithieux, S. M.; Wise, S. G.; Weiss, A. S. Tropoelastin-a multifaceted naturally smart material. *Adv. Drug Deliv. Rev.* **2013,** *65*, 421-428.

43. Stewart, R. J.; Wang, C. S.; Song, I. T.; Jones, J. P. The role of coacervation and phase transitions in the sandcastle worm adhesive system. *Adv. Colloid Interface Sci.* **2017,** *239*, 88-96.

44. Park, S.; Kim, S.; Jho, Y.; Hwang, D. S. Cation-pi interactions and their contribution to mussel underwater adhesion studied using a surface forces apparatus: A Mini-Review. *Langmuir* **2019,** *35*, 16002-16012.

45. Schmitt, C.; Turgeon, S. L. Protein/polysaccharide complexes and coacervates in food systems. *Adv. Colloid Interface Sci.* **2011,** *167*, 63-70.

46. Blocher, W. C.; Perry, S. L. Complex coacervate-based materials for biomedicine. *Wiley Interdiscip. Rev. Nanomed. Nanobiotechnol.* **2017,** *9*, 1442.

47. Devi, N.; Sarmah, M.; Khatun, B.; Maji, T. K. Encapsulation of active ingredients in polysaccharide-protein complex coacervates. *Adv. Colloid Interface Sci.* **2017,** *239*, 136-145.

48. Kizilay, E.; Kayitmazer, A. B.; Dubin, P. L. Complexation and coacervation of polyelectrolytes with oppositely charged colloids. *Adv. Colloid Interface Sci.* **2011,** *167*, 24-37.

49. Cini, N.; Ball, V. Polyphosphates as inorganic polyelectrolytes interacting with oppositely charged ions, polymers and deposited on surfaces: fundamentals and applications. *Adv. Colloid Interface Sci.* **2014,** *209*, 84-97.

50. Berret, J. F. Controlling electrostatic co-assembly using ion-containing copolymers: from surfactants to nanoparticles. *Adv. Colloid Interface Sci.* **2011,** *167*, 38-48.

51. Wang, M.; Wang, Y. Development of surfactant coacervation in aqueous solution. *Soft Matter* **2014,** *10*, 7909-7919.

52. Guzman, E.; Llamas, S.; Maestro, A.; Fernandez-Pena, L.; Akanno, A.; Miller, R.; Ortega, F.; Rubio, R. G. Polymer-surfactant systems in bulk and at fluid interfaces. *Adv. Colloid Interface Sci.* **2016,** *233*, 38-64.

53. Miyake, M. Recent progress of the characterization of oppositely charged polymer/surfactant complex in dilution deposition system. *Adv. Colloid Interface Sci.* **2017,** *239*, 146-157.

54. Zhao, W.; Wang, Y. Coacervation with surfactants: From single-chain surfactants to gemini surfactants. *Adv. Colloid Interface Sci.* **2017,** *239*, 199-212.

55. Voets, I. K.; de Keizer, A.; Cohen Stuart, M. A. Complex coacervate core micelles. *Adv. Colloid Interface Sci.* **2009,** *147-148*, 300-318.

56. Myakonkaya, O.; Eastoe, J. Low energy methods of phase separation in colloidal dispersions and microemulsions. *Adv. Colloid Interface Sci.* **2009,** *149*, 39-46.

57. Tiwary, A. K.; Zheng, Y. Protein phase separation in mitosis. *Curr. Opin. Cell Biol.* **2019,** *60*, 92-98.

58. Banani, S. F.; Lee, H. O.; Hyman, A. A.; Rosen, M. K. Biomolecular condensates: organizers of cellular biochemistry. *Nat. Rev. Mol. Cell Biol.* **2017,** *18*, 285-298.

59. Zhou, L.; Shi, H.; Li, Z.; He, C. Recent advances in complex coacervation design from macromolecular assemblies and emerging applications. *Macromol. Rapid Commun.* **2020,** *41*, 2000149.

60. Raghavan, S. R.; Edlund, H.; Kaler, E. W. Cloud-point phenomena in wormlike micellar systems containing cationic surfactant and salt. *Langmuir* **2002,** *18*, 1056–1064.

61. Purkait, M. K.; Vijay, S. S.; DasGupta, S.; De, S. Separation of congo red by surfactant mediated cloud point extraction. *Dyes Pigm.* **2004,** *63*, 151-159.

62. Purkait, M. K.; Banerjee, S.; Mewara, S.; DasGupta, S.; De, S. Cloud point extraction of toxic eosin dye using Triton X-100 as nonionic surfactant. *Water Res.* **2005,** *39*, 3885-3890.

63. Betre, H.; Ong, S. R.; Guilak, F.; Chilkoti, A.; Fermor, B.; Setton, L. A. Chondrocytic differentiation of human adipose-derived adult stem cells in elastin-like polypeptide. *Biomaterials* **2006,** *27*, 91-99.

64. Maeda, T.; Takenouchi, M.; Yamamoto, K.; Aoyagi, T. Analysis of the formation mechanism for thermoresponsive-type coacervate with functional copolymers consisting of N-Isopropylacrylamide and 2-Hydroxyisopropylacrylamide. *Biomacromolecules* **2006,** *7*, 2230-2236.

65. Cirulis, J. T.; Bellingham, C. M.; Davis, E. C.; Hubmacher, D.; Reinhardt, D. P.; Mecham, R. P.; Keeley, F. W. Fibrillins, fibulins, and matrix-associated glycoprotein modulate the kinetics and morphology of in vitro self-assembly of a recombinant elastin-like polypeptide. *Biochemistry* **2008,** *47*, 12601–12613.

66. Cirulis, J. T.; Keeley, F. W. Kinetics and morphology of self-assembly of an elastin-like polypeptide based on the alternating domain arrangement of human tropoelastin. *Biochemistry* **2010,** *49*, 5726-5733.

67. Wasilewski, T. Coacervates as a modern delivery system of hand dishwashing liquids. *J. Surfactants Deterg.* **2010,** *13*, 513-520.

68. Wasilewski, T.; Bujak, T. Effect of the type of nonionic surfactant on the manufacture and properties of hand dishwashing liquids in the coacervate form. *Ind. Eng. Chem. Res.* **2014,** *53*, 13356-13361.

69. Seweryn, A.; Wasilewski, T.; Bujak, T. Effect of salt on the manufacturing and properties of hand dishwashing liquids in the coacervate form. *Ind. Eng. Chem. Res.* **2016,** *55*, 1134-1141.

70. Ferreira, L. A.; Teixeira, J. A. Salt effect on the aqueous two-phase system PEG 8000-sodium sulfate. *J. Chem. Eng. Data* **2011,** *56*, 133-137.

71. Yang, G.; Wong, M. K.; Lin, L. E.; Yip, C. M. Nucleation and growth of elastin-like peptide fibril multilayers: an in situ atomic force microscopy study. *Nanotechnology* **2011,** *22*, 494018.

72. He, D.; Miao, M.; Sitarz, E. E.; Muiznieks, L. D.; Reichheld, S.; Stahl, R. J.; Keeley, F. W.; Parkinson, J. Polymorphisms in the human tropoelastin gene modify in vitro self-assembly and mechanical properties of elastin-like polypeptides. *PLoS One* **2012,** *7*, e46130.

73. Ilevbare, G. A.; Taylor, L. S. Liquid-liquid phase separation in highly supersaturated aqueous solutions of poorly water-soluble drugs: Implications for solubility enhancing formulations. *Cryst. Growth Des.* **2013,** *13*, 1497-1509.

74. Miao, M.; Reichheld, S. E.; Muiznieks, L. D.; Huang, Y.; Keeley, F. W. Elastin binding protein and FKBP65 modulate in vitro self-assembly of human tropoelastin. *Biochemistry* **2013,** *52*, 7731-7741.

75. Sokolova, E.; Spruijt, E.; Hansen, M. M.; Dubuc, E.; Groen, J.; Chokkalingam, V.; Piruska, A.; Heus, H. A.; Huck, W. T. Enhanced transcription rates in membrane-free protocells formed by coacervation of cell lysate. *Proc. Natl. Acad. Sci. U.S.A.* **2013,** *110*, 11692-11697.

76. Muiznieks, L. D.; Cirulis, J. T.; van der Horst, A.; Reinhardt, D. P.; Wuite, G. J.; Pomes, R.; Keeley, F. W. Modulated growth, stability and interactions of liquid-like coacervate assemblies of elastin. *Matrix Biol.* **2014,** *36*, 39-50.

77. Wei, W.; Tan, Y.; Martinez Rodriguez, N. R.; Yu, J.; Israelachvili, J. N.; Waite, J. H. A mussel-derived one component adhesive coacervate. *Acta Biomater.* **2014,** *10*, 1663-1670.

78. Ahn, B. K.; Das, S.; Linstadt, R.; Kaufman, Y.; Martinez-Rodriguez, N. R.; Mirshafian, R.; Kesselman, E.; Talmon, Y.; Lipshutz, B. H.; Israelachvili, J. N.; Waite, J. H. High-performance mussel-inspired adhesives of reduced complexity. *Nat. Commun.* **2015,** *6*, 8663.

79. Dandurand, J.; Samouillan, V.; Lacabanne, C.; Pepe, A.; Bochicchio, B. Water structure and elastin-like peptide aggregation. *J. Therm. Anal. Calorim.* **2015,** *120*, 419-426.

80. Elbaum-Garfinkle, S.; Kim, Y.; Szczepaniak, K.; Chen, C. C.; Eckmann, C. R.; Myong, S.; Brangwynne, C. P. The disordered P granule protein LAF-1 drives phase separation into droplets with tunable viscosity and dynamics. *Proc. Natl. Acad. Sci. U.S.A.* **2015,** *112*, 7189-7194.

81. Jiang, H.; Wang, S.; Huang, Y.; He, X.; Cui, H.; Zhu, X.; Zheng, Y. Phase transition of spindle-associated protein regulate spindle apparatus assembly. *Cell* **2015,** *163*, 108-122.

82. Nott, T. J.; Petsalaki, E.; Farber, P.; Jervis, D.; Fussner, E.; Plochowietz, A.; Craggs, T. D.; Bazett-Jones, D. P.; Pawson, T.; Forman-Kay, J. D.; Baldwin, A. J. Phase transition of a disordered nuage protein generates environmentally responsive membraneless organelles. *Mol. Cell* **2015,** *57*, 936-947.

83. Navon, Y.; Zhou, M.; Matson, J. B.; Bitton, R. Dendritic Elastin-like Peptides: The effect of branching on thermoresponsiveness. *Biomacromolecules* **2016,** *17*, 262-270.

84. Suyama, K.; Taniguchi, S.; Tatsubo, D.; Maeda, I.; Nose, T. Dimerization effects on coacervation property of an elastin-derived synthetic peptide $(FPGVG)_5$. *J. Pept. Sci.* **2016,** *22*, 236-243.

85. Cai, H.; Gabryelczyk, B.; Manimekalai, M. S. S.; Gruber, G.; Salentinig, S.; Miserez, A. Self-coacervation of modular squid beak proteins-a comparative study. *Soft Matter* **2017,** *13*, 7740-7752.

86. Annabi, N.; Zhang, Y.; Assmann, A.; Sani, E. S.; Cheng, G.; Lassaletta, A. D.; Vegh, A.; Dehghani, B.; Ruiz-Esparza, G. U.; Wang, X.; Gangadharan, S.; Weiss, A. S.; Khademhosseini, A. Engineering a highly elastic human protein-based sealant for surgical applications. *Sci. Transl. Med.* **2017,** *9*, eaai7466.

87. Reichheld, S. E.; Muiznieks, L. D.; Keeley, F. W.; Sharpe, S. Direct observation of structure and dynamics during phase separation of an elastomeric protein. *Proc. Natl. Acad. Sci. U.S.A.* **2017,** *114*, E4408-E4415.

88. Simon, J. R.; Carroll, N. J.; Rubinstein, M.; Chilkoti, A.; Lopez, G. P. Programming molecular self-assembly of intrinsically disordered proteins containing sequences of low complexity. *Nat. Chem.* **2017,** *9*, 509-515.

89. Franzmann, T. M.; Jahnel, M.; Pozniakovsky, A.; Mahamid, J.; Holehouse, A. S.; Nuske, E.; Richter, D.; Baumeister, W.; Grill, S. W.; Pappu, R. V.; Hyman, A. A.; Alberti, S. Phase separation of a yeast prion protein promotes cellular fitness. *Science* **2018,** *359*, eaao5654.

90. Mohammadi, P.; Aranko, A. S.; Lemetti, L.; Cenev, Z.; Zhou, Q.; Virtanen, S.; Landowski, C. P.; Penttila, M.; Fischer, W. J.; Wagermaier, W.; Linder, M. B. Phase transitions as intermediate steps in the formation of molecularly engineered protein fibers. *Commun. Biol.* **2018,** *1*, 86.

91.Tatsubo, D.; Suyama, K.; Miyazaki, M.; Maeda, I.; Nose, T. Stepwise mechanism of temperature-dependent coacervation of the elastin-like peptide analogue dimer, (C(WPGVG)3)2. *Biochemistry* **2018,** *57*, 1582-1590.

92. Gabryelczyk, B.; Cai, H.; Shi, X.; Sun, Y.; Swinkels, P. J. M.; Salentinig, S.; Pervushin, K.; Miserez, A. Hydrogen bond guidance and aromatic stacking drive liquid-liquid phase separation of intrinsically disordered histidine-rich peptides. *Nat. Commun.* **2019,** *10*, 5465.

93. Gourgas, O.; Cole, G. B.; Muiznieks, L. D.; Sharpe, S.; Cerruti, M. Effect of the ionic concentration of simulated body fluid on the minerals formed on cross-linked elastin-like polypeptide membranes. *Langmuir* **2019,** *35*, 15364-15375.

94. Gourgas, O.; Muiznieks, L. D.; Bello, D. G.; Nanci, A.; Sharpe, S.; Cerruti, M. Cross-linked elastin-like polypeptide membranes as a model for medial arterial calcification. *Biomacromolecules* **2019,** *20*, 2625-2636.

95. Ianiro, A.; Wu, H.; van Rijt, M. M. J.; Vena, M. P.; Keizer, A. D. A.; Esteves, A. C. C.; Tuinier, R.; Friedrich, H.; Sommerdijk, N.; Patterson, J. P. Liquid-liquid phase separation during amphiphilic self-assembly. *Nat. Chem.* **2019,** *11*, 320-328.

96. Rizvi, A.; Patel, U.; Ianiro, A.; Hurst, P. J.; Merham, J. G.; Patterson, J. P. Nonionic block copolymer coacervates. *Macromolecules* **2020,** *53*, 6078-6086.

97. Chen, N.; Zhao, Z.; Wang, Y.; Dimova, R. Resolving the mechanisms of soy glycinin self-coacervation and hollow-condensate formation. *ACS Macro Lett.* **2020,** *9*, 1844-1852.

98. Liu, B.; Fan, Y.; Li, H.; Zhao, W.; Luo, S.; Wang, H.; Guan, B.; Li, Q.; Yue, J.; Dong, Z.; Wang, Y.; Jiang, L. Control the entire journey of pesticide application on superhydrophobic plant surface by dynamic covalent trimeric surfactant coacervation. *Adv. Funct. Mater.* **2020,** *31*, 2006606.

99. Madinya, J. J.; Chang, L.-W.; Perry, S. L.; Sing, C. E. Sequence-dependent self-coacervation in high charge-density polyampholytes. *Mol. Syst. Des. Eng.* **2020,** *5*, 632-644.

100. Mohammadi, P.; Jonkergouw, C.; Beaune, G.; Engelhardt, P.; Kamada, A.; Timonen, J. V. I.; Knowles, T. P. J.; Penttila, M.; Linder, M. B. Controllable coacervation of recombinantly produced spider silk protein using kosmotropic salts. *J. Colloid Interface Sci.* **2020,** *560*, 149-160.

101. Reed, E. H.; Schuster, B. S.; Good, M. C.; Hammer, D. A. SPLIT: stable protein coacervation using a light induced transition. *ACS Synth. Biol.* **2020,** *9*, 500-507.

102. Zhang, P.; Gourgas, O.; Lainé, A.; Murshed, M.; Mantovani, D.; Cerruti, M. Coacervation conditions and cross-linking determines availability of carbonyl groups on elastin and its calcification. *Cryst. Growth Des.* **2020,** *20*, 7170-7179.

103. Pei, Y.; Zheng, Y.; Li, Z.; Liu, J.; Zheng, X.; Tang, K.; Kaplan, D. L. Ethanol-induced coacervation in aqueous gelatin solution for constructing nanospheres and networks: Morphology, dynamics and thermal sensitivity. *J. Colloid Interface Sci.* **2021,** *582*, 610-618.

104. Rowland, A. T.; Cacace, D. N.; Pulati, N.; Gulley, M. L.; Keating, C. D. Bioinspired mineralizing microenvironments generated by liquid-liquid phase coexistence. *Chem. Mater.* **2019,** *31*, 10243-10255.

105. Kim, S.; Huang, J.; Lee, Y.; Dutta, S.; Yoo, H. Y.; Jung, Y. M.; Jho, Y.; Zeng, H.; Hwang, D. S. Complexation and coacervation of like-charged polyelectrolytes inspired by mussels. *Proc. Natl. Acad. Sci. U.S.A.* **2016,** *113*, E847-E853.

106. Hwang, D. S.; Zeng, H.; Srivastava, A.; Krogstad, D. V.; Tirrell, M.; Israelachvili, J. N.; Waite, J. H. Viscosity and interfacial properties in a mussel-inspired adhesive coacervate. *Soft Matter* **2010,** *6*, 3232-3236.

107. Zheng, J.; Tang, C. H.; Sun, W. Heteroprotein complex coacervation: Focus on experimental strategies to investigate structure formation as a function of intrinsic and external physicochemical parameters for food applications. *Adv. Colloid Interface Sci.* **2020,** *284*, 102268.

108. Ducker, W. A.; Senden, T. J.; Pashley, R. M. Measurement of forces in liquids using a force microscope. *Langmuir* **1992,** *8*, 1831-1836.

109. Ducker, W. A.; Senden, T. J.; Pashley, R. M. Direct measurement of colloidal forces using an atomic force microscope. *Nature* **1991,** 353, 239–241.

110. Butt, H. J.; Cappella, B.; Kappl, M. Force measurements with the atomic force microscope: Technique, interpretation and applications. *Surf. Sci. Rep.* **2005,** *59*, 1-152.

111. Lu, Q.; Oh, D. X.; Lee, Y.; Jho, Y.; Hwang, D. S.; Zeng, H. Nanomechanics of cation-pi interactions in aqueous solution. *Angew. Chem. Int. Ed.* **2013,** *52*, 3944-3948.

112. Sprakel, J.; Besseling, N. A.; Leermakers, F. A.; Cohen Stuart, M. A. Equilibrium capillary forces with atomic force microscopy. *Phys. Rev. Lett.* **2007,** *99*, 104504.

113. Spruijt, E.; Sprakel, J.; Cohen Stuart, M. A.; van der Gucht, J. Interfacial tension between a complex coacervate phase and its coexisting aqueous phase. *Soft Matter* **2010,** *6*, 172-178.

114. Lim, S.; Moon, D.; Kim, H. J.; Seo, J. H.; Kang, I. S.; Cha, H. J. Interfacial tension of complex coacervated mussel adhesive protein according to the Hofmeister series. *Langmuir* **2014,** *30*, 1108-1115.

115. Priftis, D.; Farina, R.; Tirrell, M. Interfacial energy of polypeptide complex coacervates measured via capillary adhesion. *Langmuir* **2012,** *28*, 8721-8729.

116. Kim, S.; Faghihnejad, A.; Lee, Y.; Jho, Y.; Zeng, H.; Hwang, D. S. Cation-pi interaction in DOPA-deficient mussel adhesive protein mfp-1. *J. Mater. Chem. B* **2015,** *3*, 738-743.

117. Kim, S.; Yoo, H. Y.; Huang, J.; Lee, Y.; Park, S.; Park, Y.; Jin, S.; Jung, Y. M.; Zeng, H. Hwang, D. S.; Jho, Y. Salt triggers the simple coacervation of an underwater adhesive when cations meet aromatic pi electrons in seawater. *ACS Nano* **2017,** *11*, 6764-6772.

118. Israelachvili, J. N. Intermolecular and surface forces. **2011**.

119. Desiraju, G. R. Chemistry beyond the molecule. *Nature* **2001,** *412*, 397–400.

120. Yang, L.; Tan, X.; Wang, Z.; Zhang, X. Supramolecular polymers: Historical development, preparation, characterization, and functions. *Chem. Rev.* **2015,** *115*, 7196-239.

121. Lee, B. P.; Messersmith, P. B.; Israelachvili, J. N.; Waite, J. H. Mussel-inspired adhesives and coatings. *Annu. Rev. Mater. Res.* **2011,** *41*, 99-132.

122. Waite, J. H.; Andersen, N. H.; Jewhurst, S.; Sun, C. Mussel adhesion: Finding the tricks worth mimicking. *J. Adhes.* **2005,** *81*, 297-317.

123. Hinterdorfer, P.; Dufrene, Y. F. Detection and localization of single molecular recognition events using atomic force microscopy. *Nat. Methods* **2006,** *3*, 347-355.

124. Peng, Q.; Chen, J.; Zeng, Z.; Wang, T.; Xiang, L.; Peng, X.; Liu, J.; Zeng, H. Adhesive coacervates driven by hydrogen-bonding interaction. *Small* **2020,** 16, 2004132.

125. Priftis, D.; Megley, K.; Laugel, N.; Tirrell, M. Complex coacervation of poly(ethylene-imine)/polypeptide aqueous solutions: thermodynamic and rheological characterization. *J. Colloid. Interface. Sci.* **2013,** *398*, 39-50.

126. Momeni, A.; Filiaggi, M. J. Rheology of polyphosphate coacervates. *J. Rheol.* **2016,** *60*, 25-34.

127. Liberatore, M. W.; Wyatt, N. B.; Henry, M.; Dubin, P. L.; Foun, E. Shear-induced phase separation in polyelectrolyte/mixed micelle coacervates. *Langmuir* **2009,** *25*, 13376-13383.

128. Xu, M.; Lewis, J. A. Phase behavior and rheological properties of polyamine-rich complexes for direct-write assembly. *Langmuir* **2007,** *23*, 12752–12759.

129. Wang, Q.; Schlenoff, J. B. The polyelectrolyte complex/coacervate continuum. *Macromolecules* **2014,** *47*, 3108-3116.

130. Spruijt, E.; Cohen Stuart, M. A.; van der Gucht, J. Linear viscoelasticity of polyelectrolyte complex coacervates. *Macromolecules* **2013,** *46*, 1633-1641.

131. Jing, B.; Xu, D.; Wang, X.; Zhu, Y. Multiresponsive, critical gel behaviors of polyzwitterion-polyoxometalate coacervate complexes. *Macromolecules* **2018,** *51*, 9405-9411.

132. Priftis, D.; Laugel, N.; Tirrell, M. Thermodynamic characterization of polypeptide complex coacervation. *Langmuir* **2012,** *28*, 15947-15957.

133. Kim, K.; Shin, M.; Koh, M.-Y.; Ryu, J. H.; Lee, M. S.; Hong, S.; Lee, H. TAPE: A medical adhesive inspired by a ubiquitous compound in plants. *Adv. Funct. Mater.* **2015,** *25*, 2402-2410.

134. Xu, J.; Li, X.; Li, J.; Li, X.; Li, B.; Wang, Y.; Wu, L.; Li, W. Wet and functional adhesives from one-step aqueous self-assembly of natural amino acids and polyoxometalates. *Angew. Chem. Int. Ed.* **2017,** *56*, 8731-8735.

135. Inostroza-Brito, K. E.; Collin, E.; Siton-Mendelson, O.; Smith, K. H.; Monge-Marcet, A.; Ferreira, D. S.; Rodriguez, R. P.; Alonso, M.; Rodriguez-Cabello, J. C.; Reis, R. L.; Sagues, F.; Botto, L.; Bitton, R.; Azevedo, H. S.; Mata, A. Co-assembly, spatiotemporal control and morphogenesis of a hybrid protein-peptide system. *Nat. Chem.* **2015,** *7*, 897-904.

136. Biedermann, F.; Schneider, H. J. Experimental binding energies in supramolecular complexes. *Chem. Rev.* **2016,** *116*, 5216-5300.

137. Ozsvar, J.; Mithieux, S. M.; Wang, R.; Weiss, A. S. Elastin-based biomaterials and mesenchymal stem cells. *Biomater. Sci.* **2015,** *3*, 800-809.

138. Narayanan, A.; Menefee, J. R.; Liu, Q.; Dhinojwala, A.; Joy, A. Lower critical solution temperature-driven self-coacervation of nonionic polyester underwater adhesives. *ACS Nano* **2020,** *14*, 8359-8367.

139. Fan, Y.; Wang, Y. Self-assembly and functions of star-shaped oligomeric surfactants. *Langmuir* **2018,** *34*, 11220-11241.

140. Danino, D.; Talmon, Y.; Levy, H.; Beinert, G.; Zana, R. Branched threadlike micelles in an aqueous solution of a trimeric surfactant. *Science* **1995,** *269*, 1420-1421.

141. Chollakup, R.; Smitthipong, W.; Eisenbach, C. D.; Tirrell, M. Phase behavior and coacervation of aqueous poly(acrylic acid)-poly(allylamine) solutions. *Macromolecules* **2010,** *43*, 2518-2528.

142. Cochereau, R.; Nicolai, T.; Chassenieux, C.; Silva, J. V. C. Mechanism of the spontaneous formation of plant protein microcapsules in aqueous solution. *Colloids Surf., A* **2019,** *562*, 213-219.

143. Zhao, H.; Zhou, X.; Wang, J.; Ma, X.; Guo, M.; Liu, D. Heat-induced hollow microcapsule formation using fava bean legumin. *Food Hydrocolloids* **2021,** *112*, 106207.

144. Yuan, D.; Yang, X.; Tang, C.; Zheng, Z.; Wei, M.; Ahmad, I.; Yin, S. Physicochemical and functional properties of acidic and basic polypeptides of soy glycinin. *Food Res. Int.* **2009,** *42*, 700-706.

145. Fan, H.; Wang, J.; Tao, Z.; Huang, J.; Rao, P.; Kurokawa, T.; Gong, J. P. Adjacent cationic-aromatic sequences yield strong electrostatic adhesion of hydrogels in seawater. *Nat. Commun.* **2019,** *10*, 5127.

146. Fasting, C.; Schalley, C. A.; Weber, M.; Seitz, O.; Hecht, S.; Koksch, B.; Dernedde, J.; Graf, C.; Knapp, E. W.; Haag, R. Multivalency as a chemical organization and action principle. *Angew. Chem. Int. Ed.* **2012,** *51*, 10472-98.

147. Badjic, J. D.; Nelson, A.; Cantrill, S. J.; Turnbull, W. B.; Stoddart, J. F. Multivalency and cooperativity in supramolecular chemistry. *Acc. Chem. Res.* **2005,** *38*, 723-732.

148. Li, P.; Banjade, S.; Cheng, H. C.; Kim, S.; Chen, B.; Guo, L.; Llaguno, M.; Hollingsworth, J. V.; King, D. S.; Banani, S. F.; Russo, P. S.; Jiang, Q. X.; Nixon, B. T.; Rosen, M. K. Phase transitions in the assembly of multivalent signalling proteins. *Nature* **2012,** *483*, 336-340.

149. Xiang, S.; Kato, M.; Wu, L. C.; Lin, Y.; Ding, M.; Zhang, Y.; Yu, Y.; McKnight, S. L. The LC Domain of hnRNPA2 adopts similar conformations in hydrogel polymers, liquid-like droplets, and nuclei. *Cell* **2015,** *163*, 829-839.

150. Zhang, J.; Jia, G.; Wanbin, Z.; Minghao, J.; Wei, Y.; Hao, J.; Liu, X.; Gan, Z.; Sun, A. Nanoencapsulation of zeaxanthin extracted from Lycium barbarum L. by complex coacervation with gelatin and CMC. *Food Hydrocolloids* **2021,** *112*, 106280.

151. Ferreira, S.; Nicoletti, V. R. Microencapsulation of ginger oil by complex coacervation using atomization: Effects of polymer ratio and wall material concentration. *J. Food Eng.* **2021,** *291*, 110214.

152. Vecchies, F.; Sacco, P.; Marsich, E.; Cinelli, G.; Lopez, F.; Donati, I. Binary solutions of hyaluronan and lactose-modified chitosan: The influence of experimental variables in assembling complex coacervates. *Polymers* **2020,** *12*, 897.

153. Tang, Y.; Scher, H. B.; Jeoh, T. Industrially scalable complex coacervation process to microencapsulate food ingredients. *Innovative Food Sci. Emerg. Technol.* **2020,** *59*, 102257.

154. Santos, M. B.; de Carvalho, C. W. P.; Garcia-Rojas, E. E. Microencapsulation of vitamin D3 by complex coacervation using carboxymethyl tara gum (Caesalpinia spinosa) and gelatin A. *Food Chem.* **2021**, *343*, 128529.

155. Kanha, N.; Surawang, S.; Pitchakarn, P.; Laokuldilok, T. Microencapsulation of copigmented anthocyanins using double emulsion followed by complex coacervation: Preparation, characterization and stability. *LWT Food Sci. Technol.* **2020,** *133*, 110154.

156. Hernández-Nava, R.; López-Malo, A.; Palou, E.; Ramírez-Corona, N.; Jiménez-Munguía, M. T. Encapsulation of oregano essential oil (Origanum vulgare) by complex coacervation between gelatin and chia mucilage and its properties after spray drying. *Food Hydrocolloids* **2020,** *109*, 106077.

157. Hernandez-Fernandez, M. A.; Garcia-Pinilla, S.; Ocampo-Salinas, O. I.; Gutierrez-Lopez, G. F.; Hernandez-Sanchez, H.; Cornejo-Mazon, M.; Perea-Flores, M. J.; Davila-Ortiz, G. Microencapsulation of vanilla oleoresin (V. planifolia Andrews) by complex coacervation and spray drying: Physicochemical and microstructural characterization. *Foods* **2020,** *9*, 1375.

158. Heckert Bastos, L. P.; Vicente, J.; Corrêa dos Santos, C. H.; Geraldo de Carvalho, M.; Garcia-Rojas, E. E. Encapsulation of black pepper (Piper nigrum L.) essential oil with gelatin and sodium alginate by complex coacervation. *Food Hydrocolloids* **2020,** *102*, 105605.

159. Gharanjig, H.; Gharanjig, K.; Hosseinnezhad, M.; Jafari, S. M. Development and optimization of complex coacervates based on zedo gum, cress seed gum and gelatin. *Int. J. Biol. Macromol.* **2020,** *148*, 31-40.

160. Furlani, F.; Donati, I.; Marsich, E.; Sacco, P. Characterization of chitosan/hyaluronan complex coacervates assembled by varying polymers weight ratio and chitosan physical-chemical composition. *Colloids Interfaces* **2020,** *4*, 12.

161. Ferreira, S.; Nicoletti, V. R. Complex coacervation assisted by a two-fluid nozzle for microencapsulation of ginger oil: Effect of atomization parameters. *Food Res. Int.* **2020,** *138* (Pt B), 109828.

162. Emamverdian, P.; Moghaddas Kia, E.; Ghanbarzadeh, B.; Ghasempour, Z. Characterization and optimization of complex coacervation between soluble fraction of Persian gum and gelatin. *Colloids Surf., A* **2020,** *607*, 125436.

163. Dai, H. H.; Li, X. D.; Wei, A. C.; Wang, X. D.; Wang, D. Y. Characterization and oxidative stability of cold-pressed sesame oil microcapsules prepared by complex coacervation. *J. Oleo Sci.* **2020,** *69*, 685-692.

164. Vecchione, D.; Grimaldi, A. M.; Forte, E.; Bevilacqua, P.; Netti, P. A.; Torino, E. Hybrid core-shell (HyCoS) nanoparticles produced by complex coacervation for multimodal applications. *Sci Rep* **2017,** *7*, 45121.

165. Cao, Y.; Fang, Y.; Nishinari, K.; Phillips, G. O. Effects of conformational ordering on protein/polyelectrolyte electrostatic complexation: ionic binding and chain stiffening. *Sci. Rep.* **2016,** *6*, 23739.

166. Kayitmazer, A. B.; Koksal, A. F.; Kilic Iyilik, E. Complex coacervation of hyaluronic acid and chitosan: effects of pH, ionic strength, charge density, chain length and the charge ratio. *Soft Matter* **2015,** *11*, 8605-8612.

167. Boral, S.; Bohidar, H. B. Effect of ionic strength on surface-selective patch binding-induced phase separation and coacervation in similarly charged gelatin-agar molecular systems. *J. Phys. Chem. B* **2010,** *114*, 12027–12035.

168. Song, J. K.; Kang, H. C.; Kim, K. S.; Chin, I.-J. Microcapsules by complex coacervation for electronic ink. *Molecular Crystals and Liquid Crystals* **2007,** *464*, 263-269.

169. Nakagawa, K.; Iwamoto, S.; Nakajima, M.; Shono, A.; Satoh, K. Microchannel emulsification using gelatin and surfactant-free coacervate microencapsulation. *J. Colloid Interface Sci.* **2004,** *278*, 198-205.

170. Vargas, S. A.; Delgado-Macuil, R. J.; Ruiz-Espinosa, H.; Rojas-Lopez, M.; Amador-Espejo, G. G. High-intensity ultrasound pretreatment influence on whey protein isolate and its use on complex coacervation with kappa carrageenan: Evaluation of selected functional properties. *Ultrason. Sonochem.* **2021,** *70*, 105340.

171. Gheonea, I.; Aprodu, I.; Cîrciumaru, A.; Râpeanu, G.; Bahrim, G. E.; Stănciuc, N. Microencapsulation of lycopene from tomatoes peels by complex coacervation and freeze-drying:

Evidences on phytochemical profile, stability and food applications. *J. Food Eng.* **2021,** *288*, 110166.

172. Zhang, Z.-K.; Xiao, J.-X.; Huang, G.-Q. Pickering emulsions stabilized by ovalbumin-sodium alginate coacervates. *Colloids Surf., A* **2020,** *595*, 124712.

173. Yücetepe, A.; Yavuz-Düzgün, M.; Şensu, E.; Bildik, F.; Demircan, E.; Özçelik, B. The impact of pH and biopolymer ratio on the complex coacervation of Spirulina platensis protein concentrate with chitosan. *Journal of Food Science and Technology* **2020**. https://doi.org/10.1007/s13197-020-04636-7

174. Yavuz-Düzgün, M.; Zeeb, B.; Dreher, J.; Özçelik, B.; Weiss, J. The impact of esterification degree and source of pectins on complex coacervation as a tool to mask the bitterness of potato protein isolates. *Food Biophysics* **2020,** *15*, 376-385.

175. Yang, S.; Li, X.; Hua, Y.; Chen, Y.; Kong, X.; Zhang, C. Selective complex coacervation of pea whey proteins with chitosan to purify main 2S albumins. *J. Agric. Food Chem.* **2020,** *68*, 1698-1706.

176. Yan, J. N.; Nie, B.; Jiang, X. Y.; Han, J. R.; Du, Y. N.; Wu, H. T. Complex coacervation of scallop (Patinopecten yessoensis) male gonad hydrolysates and kappa-carrageenan: Effect of NaCl and KCl. *Food Res. Int.* **2020,** *137*, 109659.

177. Tavares, L.; Souza, H. K. S.; Gonçalves, M. P.; Rocha, C. M. R. Physicochemical and microstructural properties of composite edible film obtained by complex coacervation between chitosan and whey protein isolate. *Food Hydrocolloids* **2021,** *113*, 106471.

178. Tavares, L.; Noreña, C. P. Z. Encapsulation of ginger essential oil using complex coacervation method: Coacervate formation, rheological property, and physicochemical characterization. *Food Bioprocess Technol.* **2020,** *13*, 1405-1420.

179. Sarkar, R.; Dutta, A.; Patra, A.; Saha, S. Bio-inspired biopolymeric coacervation for entrapment and targeted release of anthocyanin. *Cellulose* **2021,** *28*, 377–388.

180. Ocak, B. Gum arabic and collagen hydrolysate extracted from hide fleshing wastes as novel wall materials for microencapsulation of Origanum onites L. essential oil through complex coacervation. *Environ. Sci. Pollut. Res. Int.* **2020,** *27*, 42727-42737.

181. Naderi, B.; Keramat, J.; Nasirpour, A.; Aminifar, M. Complex coacervation between oak protein isolate and gum Arabic: optimization & functional characterization. *Int. J. Food Prop.* **2020,** *23*, 1854-1873.

182. Lin, Y.; Fichou, Y.; Zeng, Z.; Hu, N. Y.; Han, S. Electrostatically driven complex coacervation and amyloid aggregation of Tau are independent processes with overlapping conditions. *ACS Chem. Neurosci.* **2020,** *11*, 615-627.

183. Lan, Y.; Ohm, J.-B.; Chen, B.; Rao, J. Microencapsulation of hemp seed oil by pea protein isolate−sugar beet pectin complex coacervation: Influence of coacervation pH and wall/core ratio. *Food Hydrocolloids* **2020,** *113*, 106423.

184. Lan, Y.; Ohm, J. B.; Chen, B.; Rao, J. Phase behavior and complex coacervation of concentrated pea protein isolate-beet pectin solution. *Food Chem.* **2020,** *307*, 125536.

185. Ghadermazi, R.; Khosrowshahi Asl, A.; Tamjidi, F. Complexation and coacervation of whey protein isolate with quince seed mucilage. *J. Dispersion Sci. Technol.* **2020**, 1822862.

186. Costa, A. M. M.; Moretti, L. K.; Simões, G.; Silva, K. A.; Calado, V.; Tonon, R. V.; Torres, A. G. Microencapsulation of pomegranate (Punica granatum L.) seed oil by complex coacervation: Development of a potential functional ingredient for food application. *LWT Food Sci. Technol.* **2020,** *131*, 109519.

187. Huang, K. Y.; Yoo, H. Y.; Jho, Y.; Han, S.; Hwang, D. S. Bicontinuous fluid structure with low cohesive energy: Molecular basis for exceptionally low interfacial tension of complex coacervate fluids. *ACS Nano* **2016,** *10*, 5051-5062.

188. Niu, F.; Dong, Y.; Shen, F.; Wang, J.; Liu, Y.; Su, Y.; Xu, R.; Wang, J.; Yang, Y. Phase separation behavior and structural analysis of ovalbumin–gum arabic complex coacervation. *Food Hydrocolloids* **2015,** *43*, 1-7.

189. Ortony, J. H.; Hwang, D. S.; Franck, J. M.; Waite, J. H.; Han, S. Asymmetric collapse in biomimetic complex coacervates revealed by local polymer and water dynamics. *Biomacromolecules* **2013,** *14*, 1395-1402.

190. Hwang, D. S.; Waite, J. H.; Tirrell, M. Promotion of osteoblast proliferation on complex coacervation-based hyaluronic acid-recombinant mussel adhesive protein coatings on titanium. *Biomaterials* **2010,** *31*, 1080-1084.

191. Xia, Q.; Akanbi, T. O.; Wang, B.; Li, R.; Liu, S.; Barrow, C. J. Investigation of enhanced oxidation stability of microencapsulated enzymatically produced tuna oil concentrates using complex coacervation. *Food Funct.* **2020,** *11*, 10748-10757.

192. Wang, X.; Shi, C.; Mo, J.; Xu, Y.; Wei, W.; Zhao, J. An inorganic biopolymer polyphosphate controls positively charged protein phase transitions. *Angew. Chem. Int. Ed.* **2020,** *59*, 2679-2683.

193. Tiwari, P.; Bharti, I.; Bohidar, H. B.; Quadir, S.; Joshi, M. C.; Arfin, N. Complex coacervation and overcharging during interaction between hydrophobic zein and hydrophilic laponite in aqueous ethanol solution. *ACS Omega* **2020,** *5*, 33064–33074.

194. Ferreira, M.; Jing, B.; Lorenzana, A.; Zhu, Y. Effect of polyampholyte net charge on complex coacervation between polyampholytes and inorganic polyoxometalate giant anions. *Soft Matter* **2020,** *16*, 10280-10289.

195. Kim, H.; Jeon, B. J.; Kim, S.; Jho, Y.; Hwang, D. S. Upper critical solution temperature (UCST) behavior of coacervate of cationic protamine and multivalent anions. *Polymers* **2019,** *11*, 691.

196. Lee, Y.; Deelman, T. E.; Chen, K.; Lin, D. S. Y.; Tavakkoli, A.; Karp, J. M. Therapeutic luminal coating of the intestine. *Nat. Mater.* **2018,** *17*, 834-842.

197. Baroudi, I.; Simonnet-Jégat, C.; Roch-Marchal, C.; Leclerc-Laronze, N.; Livage, C.; Martineau, C.; Gervais, C.; Cadot, E.; Carn, F.; Fayolle, B.; Steunou, N. Supramolecular assembly of gelatin and inorganic polyanions: Fine-tuning the mechanical properties of nanocomposites by varying their composition and microstructure. *Chem.Mater.* **2015,** *27*, 1452-1464.

198. Pawar, N.; Bohidar, H. B. Anisotropic domain growth and complex coacervation in nanoclay-polyelectrolyte solutions. *Adv. Colloid Interface Sci.* **2011,** *167*, 12-23.

199. Park, S.; Barnes, R.; Lin, Y.; Jeon, B.-j.; Najafi, S.; Delaney, K. T.; Fredrickson, G. H.; Shea, J.-E.; Hwang, D. S.; Han, S. Dehydration entropy drives liquid-liquid phase separation by molecular crowding. *Commun. Chem.* **2020,** *3*, 83.

200. Mabesoone, M. F. J.; Gopez, J. D.; Paulus, I. E.; Klinger, D. Tunable biohybrid hydrogels from coacervation of hyaluronic acid and PEO-based block copolymers. *Journal of Polymer Science* **2020,** *58*, 1276-1287.

201. Love, C.; Steinkuhler, J.; Gonzales, D. T.; Yandrapalli, N.; Robinson, T.; Dimova, R.; Tang, T. D. Reversible pH-responsive coacervate formation in lipid vesicles activates dormant enzymatic reactions. *Angew. Chem. Int. Ed.* **2020,** *59*, 5950-5957.

202. Hwang, M. P.; Fecek, R. J.; Qin, T.; Storkus, W. J.; Wang, Y. Single injection of IL-12 coacervate as an effective therapy against B16-F10 melanoma in mice. *J. Controlled Release* **2020,** *318*, 270-278.

203. Huang, X.; Tian, L.; Wang, Z.; Zhang, J.; Chan, Y. S.; Cheng, S. H.; Yao, X. Bioinspired robust all-aqueous droplet via diffusion-controlled interfacial coacervation. *Adv. Funct. Mater.* **2020,** *30*, 2004166.

204. Dos Santos de Macedo, B.; de Almeida, T.; da Costa Cruz, R.; Netto, A. D. P.; da Silva, L.; Berret, J. F.; Vitorazi, L. Effect of pH on the complex coacervation and on the formation of layers of sodium alginate and PDADMAC. *Langmuir* **2020,** *36*, 2510-2523.

205. Drobot, B.; Iglesias-Artola, J. M.; Le Vay, K.; Mayr, V.; Kar, M.; Kreysing, M.; Mutschler, H.; Tang, T. D. Compartmentalised RNA catalysis in membrane-free coacervate protocells. *Nat. Commun.* **2018,** *9*, 3643.

206. Yin, Y.; Niu, L.; Zhu, X.; Zhao, M.; Zhang, Z.; Mann, S.; Liang, D. Non-equilibrium behaviour in coacervate-based protocells under electric-field-induced excitation. *Nat. Commun.* **2016,** *7*, 10658.

207. Cousin, F.; Gummel, J.; Combet, S.; Boue, F. The model Lysozyme-PSSNa system for electrostatic complexation: Similarities and differences with complex coacervation. *Adv. Colloid Interface Sci.* **2011,** *167*, 71-84.

208. Choi, S. W.; Lee, S. H.; Mok, H.; Park, T. G. Multifunctional siRNA delivery system: polyelectrolyte complex micelles of six-arm PEG conjugate of siRNA and cell penetrating peptide with crosslinked fusogenic peptide. *Biotechnol. Prog.* **2010,** *26*, 57-63.

209. Mi, X.; Blocher McTigue, W. C.; Joshi, P. U.; Bunker, M. K.; Heldt, C. L.; Perry, S. L. Thermostabilization of viruses via complex coacervation. *Biomater. Sci.* **2020,** *8*, 7082-7092.

210. Lu, T.; Spruijt, E. Multiphase complex coacervate droplets. *J. Am. Chem. Soc.* **2020,** *142*, 2905-2914.

211. Dompe, M.; Cedano-Serrano, F. J.; Vahdati, M.; Hourdet, D.; van der Gucht, J.; Kamperman, M.; Kodger, T. E. Hybrid complex coacervate. *Polymers* **2020,** *12*, 320.

212. Blocher McTigue, W. C.; Voke, E.; Chang, L. W.; Perry, S. L. The benefit of poor mixing: kinetics of coacervation. *Phys. Chem. Chem. Phys.* **2020,** *22*, 20643-20657.

213. Aramaki, K.; Shiozaki, Y.; Kosono, S.; Ikeda, N. Coacervation in cationic polyelectrolyte solutions with anionic amino acid surfactants. *J. Oleo Sci.* **2020,** *69*, 1411-1416.

214. Dompe, M.; Cedano-Serrano, F. J.; Vahdati, M.; Sidoli, U.; Heckert, O.; Synytska, A.; Hourdet, D.; Creton, C.; van der Gucht, J.; Kodger, T.; Kamperman, M. Tuning the interactions in multiresponsive complex coacervate-based underwater adhesives. *Int. J. Mol. Sci.* **2019,** *21*, 100.

215. Meng, X.; Perry, S. L.; Schiffman, J. D. Complex coacervation: Chemically stable fibers electrospun from aqueous polyelectrolyte solutions. *ACS Macro Lett.* **2017,** *6*, 505-511.

216. Liu, X.; Chapel, J. P.; Schatz, C. Structure, thermodynamic and kinetic signatures of a synthetic polyelectrolyte coacervating system. *Adv. Colloid Interface Sci.* **2017,** *239*, 178-186.

217. Chang, L. W.; Lytle, T. K.; Radhakrishna, M.; Madinya, J. J.; Velez, J.; Sing, C. E.; Perry, S. L. Sequence and entropy-based control of complex coacervates. *Nat. Commun.* **2017,** *8*, 1273.

218. Sun, Y.; Peng, C.; Wang, X.; Wang, R.; Chen, Y.; Zhang, D.; Ferreira, J. Phase behavior of polyelectrolyte complexes and rheological behavior of alumina suspensions for direct ink writing. *J. Am. Ceram. Soc.* **2016,** *99*, 1902-1910.

219. Fu, J.; Schlenoff, J. B. Driving forces for oppositely charged polyion association in aqueous solutions: Enthalpic, entropic, but not electrostatic. *J. Am. Chem. Soc.* **2016,** *138*, 980-990.

220. Semenov, S. N.; Wong, A. S.; van der Made, R. M.; Postma, S. G.; Groen, J.; van Roekel, H. W.; de Greef, T. F.; Huck, W. T. Rational design of functional and tunable oscillating enzymatic networks. *Nat. Chem.* **2015,** *7*, 160-165.

221. Perry, S.; Li, Y.; Priftis, D.; Leon, L.; Tirrell, M. The effect of salt on the complex coacervation of vinyl polyelectrolytes. *Polymers* **2014,** *6*, 1756-1772.

222. Black, K. A.; Priftis, D.; Perry, S. L.; Yip, J.; Byun, W. Y.; Tirrell, M. Protein encapsulation via polypeptide complex coacervation. *ACS Macro Lett.* **2014,** *3*, 1088-1091.

223. Tan, Y.; Yildiz, U. H.; Wei, W.; Waite, J. H.; Miserez, A. Layer-by-layer polyelectrolyte deposition: a mechanism for forming biocomposite materials. *Biomacromolecules* **2013,** *14*, 1715-1726.

224. Krogstad, D. V.; Lynd, N. A.; Choi, S.-H.; Spruell, J. M.; Hawker, C. J.; Kramer, E. J.; Tirrell, M. V. Effects of polymer and salt concentration on the structure and properties of triblock copolymer coacervate hydrogels. *Macromolecules* **2013,** *46*, 1512-1518.

225. Chollakup, R.; Beck, J. B.; Dirnberger, K.; Tirrell, M.; Eisenbach, C. D. Polyelectrolyte molecular weight and salt effects on the phase behavior and coacervation of aqueous solutions of poly(acrylic acid) sodium salt and poly(allylamine) hydrochloride. *Macromolecules* **2013,** *46*, 2376-2390.

226. Gratson, G. M.; Lewis, J. A. Phase behavior and rheological properties of polyelectrolyte inks for direct-write assembly. *Langmuir* **2005,** *21*, 457–464.

227. van der Burgh, S.; de Keizer, A.; Stuart, M. A. C. Complex coacervation core micelles. colloidal stability and aggregation mechanism. *Langmuir* **2004,** *20*, 1073-1084.

228. Gobbo, P.; Tian, L.; Pavan Kumar, B.; Turvey, S.; Cattelan, M.; Patil, A. J.; Carraro, M.; Bonchio, M.; Mann, S. Catalytic processing in ruthenium-based polyoxometalate coacervate protocells. *Nat. Commun.* **2020,** *11*, 41.

229. Facciotti, C.; Saggiomo, V.; Bunschoten, A.; Hove, J. B.; Rood, M. T. M.; Leeuwen, F. W. B.; Velders, A. H. Assembly, disassembly and reassembly of complex coacervate core micelles with redox-responsive supramolecular cross-linkers. *ChemSystemsChem* **2020,** *2*, e1900032.

230. Facciotti, C.; Saggiomo, V.; Bunschoten, A.; Fokkink, R.; Hove, J. B. T.; Wang, J.; Velders, A. H. Cyclodextrin-based complex coacervate core micelles with tuneable supramolecular host-guest, metal-to-ligand and charge interactions. *Soft Matter* **2018,** *14*, 9542-9549.

231. Qiao, Y.; Li, M.; Booth, R.; Mann, S. Predatory behaviour in synthetic protocell communities. *Nat. Chem.* **2017,** *9*, 110-119.

232. Tian, L.; Martin, N.; Bassindale, P. G.; Patil, A. J.; Li, M.; Barnes, A.; Drinkwater, B. W.; Mann, S. Spontaneous assembly of chemically encoded two-dimensional coacervate droplet arrays by acoustic wave patterning. *Nat. Commun.* **2016,** *7*, 13068.

233. Dora Tang, T. Y.; Che Hak, C.; Thompson, A. J.; Kuimova, M. K.; Williams, D. S.; Perriman, A. W.; Mann, S. Fatty acid membrane assembly on coacervate microdroplets as a step towards a hybrid protocell model. *Nat. Chem.* **2014,** *6*, 527-533.

234. Jiang, L. X.; Huang, J. B.; Bahramian, A.; Li, P. X.; Thomas, R. K.; Penfold, J. Surface behavior, aggregation and phase separation of aqueous mixtures of dodecyl trimethylammonium bromide and sodium oligoarene sulfonates: the transition to polyelectrolyte/surfactant behavior. *Langmuir* **2012,** *28*, 327-338.

235. Kizilay, E.; Maccarrone, S.; Foun, E.; Dinsmore, A. D.; Dubin, P. L. Cluster formation in polyelectrolyte-micelle complex coacervation. *J. Phys. Chem. B* **2011,** *115*, 7256-7263.

236. Kogej, K. Association and structure formation in oppositely charged polyelectrolyte-surfactant mixtures. *Adv. Colloid Interface Sci.* **2010,** *158*, 68-83.

237. Deng, M.; Cao, M.; Wang, Y. Coacervation of cationic gemini surfactant with weakly charged anionic polyacrylamide *J. Phys. Chem. B* **2009,** *113*, 9436-9440.

238. Bhattacharyya, A.; Argillier, J. Microencapsulation by complex coacervation : Effect of cationic surfactants. *J. Surface Sci. Technol.* **2005,** *21*, 161-168.

239. Anema, S. G.; de Kruif, C. G. Complex coacervates of lactotransferrin and beta-lactoglobulin. *J. Colloid Interface Sci.* **2014,** *430*, 214-220.

240. Yan, Y.; Kizilay, E.; Seeman, D.; Flanagan, S.; Dubin, P. L.; Bovetto, L.; Donato, L.; Schmitt, C. Heteroprotein complex coacervation: bovine beta-lactoglobulin and lactoferrin. *Langmuir* **2013,** *29*, 15614-15623.

241. de Kruif, C. G.; Pedersen, J.; Huppertz, T.; Anema, S. G. Coacervates of lactotransferrin and beta- or kappa-casein: structure determined using SAXS. *Langmuir* **2013,** *29*, 10483-10490.

242. Anema, S. G.; de Kruif, C. G. Coacervates of lysozyme and beta-casein. *J. Colloid Interface Sci.* **2013,** *398*, 255-261.

243. Anema, S. G.; de Kruif, C. G. Co-acervates of lactoferrin and caseins. *Soft Matter* **2012,** *8*, 4471-4478.

244. Spoelstra, W. K.; van der Sluis, E. O.; Dogterom, M.; Reese, L. Nonspherical coacervate shapes in an enzyme-driven active system. *Langmuir* **2020,** *36*, 1956–1964.

245. Aumiller Jr, W. M.; Keating, C. D. Phosphorylation-mediated RNA/peptide complex coacervation as a model for intracellular liquid organelles. *Nat. Chem.* **2016,** *8*, 129-137.

246. Liu, X.; Xie, X.; Du, Z.; Li, B.; Wu, L.; Li, W. Aqueous self-assembly of arginine and K8SiW11O39: fine-tuning the formation of a coacervate intended for sprayable anticorrosive coatings. *Soft Matter* **2019,** *15*, 9178-9186.

247. Muller, W. E. G.; Tolba, E.; Wang, S.; Neufurth, M.; Lieberwirth, I.; Ackermann, M.; Schroder, H. C.; Wang, X. Nanoparticle-directed and ionically forced polyphosphate coacervation: a versatile and reversible core-shell system for drug delivery. *Sci. Rep.* **2020,** *10*, 17147.

248. Prather, L. J.; Weerasekare, G. M.; Sima, M.; Quinn, C.; Stewart, R. J. Aqueous liquid-liquid phase separation of natural and synthetic polyguanidiniums. *Polymers* **2019,** *11*, 649.

249. Hoang, J.; Park, C. S.; Lee, H. J.; Marquez, M. D.; Zenasni, O.; Gunaratne, P. H.; Lee, T. R. Quaternary ammonium-terminated films formed from mixed bidentate adsorbates provide a high-capacity platform for oligonucleotide delivery. *ACS Appl. Mater. Interfaces* **2018,** *10*, 40890-40900.

250. Lee, S.; Lin, W.; Kuo, C.; Karakachian, M.; Lin, Y.; Yu, B.; Shyue, J. Photooxidation of amine-terminated self-assembled monolayers on gold. *J. Phys. Chem. C* **2010,** *114*, 10512-10519.

251. Lim, S.; Choi, Y. S.; Kang, D. G.; Song, Y. H.; Cha, H. J. The adhesive properties of coacervated recombinant hybrid mussel adhesive proteins. *Biomaterials* **2010,** *31*, 3715-3722.

252. Shao, H.; Stewart, R. J. Biomimetic underwater adhesives with environmentally triggered setting mechanisms. *Adv. Mater.* **2010,** *22*, 729-733.

253. Priftis, D.; Tirrell, M. Phase behaviour and complex coacervation of aqueous polypeptide solutions. *Soft Matter* **2012,** *8*, 9396-9405.

254. Pathak, J.; Priyadarshini, E.; Rawat, K.; Bohidar, H. B. Complex coacervation in charge complementary biopolymers: Electrostatic versus surface patch binding. *Adv. Colloid Interface Sci.* **2017,** *250*, 40-53.

255. Chen, J.; Wu, M.; Gong, L.; Zhang, J.; Yan, B.; Liu, J.; Zhang, H.; Thundat, T.; Zeng, H. Mechanistic understanding and nanomechanics of multiple hydrogen-bonding interactions in aqueous environment. *J. Phys. Chem. C* **2019,** *123*, 4540-4548.

256. Lee, D.; Hwang, H.; Kim, J. S.; Park, J.; Youn, D.; Kim, D.; Hahn, J.; Seo, M.; Lee, H. VATA: A poly(vinyl alcohol)- and tannic acid-based nontoxic underwater adhesive. *ACS Appl. Mater. Interfaces* **2020,** *12*, 20933-20941.

257. Jang, Y.; Hsieh, M. C.; Dautel, D.; Guo, S.; Grover, M. A.; Champion, J. A. Understanding the coacervate-to-vesicle transition of globular fusion proteins to engineer protein vesicle size and membrane heterogeneity. *Biomacromolecules* **2019,** *20*, 3494-3503.

258. Kaushik, P.; Pandey, P. K.; Aswal, V. K.; Bohidar, H. B. Ubiquity of complex coacervation of DNA and proteins in aqueous solution. *Soft Matter* **2020,** *16*, 9525-9533.

259. Xu, J.; Li, X.; Li, C.; Chen, J.; Xiao, Y. Hexafluoroisopropanol-induced salt-free catanionic surfactant coacervate extraction method for determination of fluoroquinolones in milk samples. *Food Chem.* **2018,** *242*, 122-130.

260. Last, M. G. F.; Deshpande, S.; Dekker, C. pH-Controlled coacervate-membrane interactions within liposomes. *ACS Nano* **2020,** *14*, 4487-4498.

261. Chen, G.; Dong, S.; Chen, Y.; Gao, Y.; Zhang, Z.; Li, S.; Chen, Y. Complex coacervation of zein-chitosan via atmospheric cold plasma treatment: Improvement of encapsulation efficiency and dispersion stability. *Food Hydrocolloids* **2020,** *107*, 105943.

262. Perry, S. L.; Leon, L.; Hoffmann, K. Q.; Kade, M. J.; Priftis, D.; Black, K. A.; Wong, D.; Klein, R. A.; Pierce, C. F.; Margossian, K. O.; Whitmer, J. K.; Qin, J.; de Pablo, J. J.; Tirrell, M. Chirality-selected phase behaviour in ionic polypeptide complexes. *Nat. Commun.* **2015,** *6*, 6052.

263. Wang, M.; Fan, Y.; Han, Y.; Nie, Z.; Wang, Y. Coacervation of cationic gemini surfactant with N-benzoylglutamic acid in aqueous solution. *Langmuir* **2013,** *29*, 14839-47.

264. Deng, J.; Walther, A. Programmable ATP-fueled DNA coacervates by transient liquid-liquid phase separation. *Chem* **2020,** *6*, 3329-3343.

265. Mitrea, D. M.; Cika, J. A.; Guy, C. S.; Ban, D.; Banerjee, P. R.; Stanley, C. B.; Nourse, A.; Deniz, A. A.; Kriwacki, R. W. Nucleophosmin integrates within the nucleolus via multi-modal interactions with proteins displaying R-rich linear motifs and rRNA. *Elife* **2016,** *5*, e13571.

266. Fromm, S. A.; Kamenz, J.; Noldeke, E. R.; Neu, A.; Zocher, G.; Sprangers, R. In vitro reconstitution of a cellular phase-transition process that involves the mRNA decapping machinery. *Angew. Chem. Int. Ed.* **2014,** *53*, 7354-7359.

267. Saez-Atienzar, S.; Masliah, E. Cellular senescence and Alzheimer disease: the egg and the chicken scenario. *Nat. Rev. Neurosci.* **2020,** *21*, 433-444.

268. Fan, H.; Wang, J.; Gong, J. P. Barnacle cement proteins-inspired tough hydrogels with robust, long-lasting, and repeatable underwater adhesion. *Adv. Funct. Mater.* **2020,** *2009334*.

269. Poudyal, R. R.; Pir Cakmak, F.; Keating, C. D.; Bevilacqua, P. C. Physical principles and extant biology reveal roles for RNA-containing membraneless compartments in origins of life chemistry. *Biochemistry* **2018,** *57*, 2509-2519.

270. Basul, S.; Bhattacharya, G. Some aspects of the phenomenon of coacervation. *Science* **1952,** *115*, 544-545.

271. Bohidar, H. B. Coacervates: A novel state of soft matter-An overview. *J. Surface Sci. Technol.* **2008,** *24*, 105-124.

272. Thomson, J. A.; Schurtenberger, P.; Thurston, G. M.; Benedek, G. B. Binary liquid phase separation and critical phenomena in a protein water solution. *Proc. Natl. Acad. Sci. USA* **1987,** *84*, 7079-7083.

273. Dompe, M.; Cedano-Serrano, F. J.; Heckert, O.; van den Heuvel, N.; van der Gucht, J.; Tran, Y.; Hourdet, D.; Creton, C.; Kamperman, M. Thermoresponsive complex coacervate-based underwater adhesive. *Adv. Mater.* **2019,** *3*, 1808179.

274. Lawrence, P. G.; Lapitsky, Y. Ionically cross-linked poly(allylamine) as a stimulus-responsive underwater adhesive: ionic strength and pH effects. *Langmuir* **2015,** *31*, 1564-1574.

275. Shao, H.; Weerasekare, G. M.; Stewart, R. J. Controlled curing of adhesive complex coacervates with reversible periodate carbohydrate complexes. *J. Biomed. Mater. Res. A* **2011,** *97*, 46-51.

276. Monahan, J.; Wilker, J. J. Cross-linking the protein precursor of marine mussel adhesives Bulk measurements and reagents for curing. *Langmuir* **2004,** *20*, 3724–3729.

277. Chen, J.; Peng, Q.; Thundat, T.; Zeng, H., Stretchable, injectable, and self-healing conductive hydrogel enabled by multiple hydrogen bonding toward wearable electronics. *Chem. Mater.* **2019,** *31*, 4553-4563.

278. Williams, G. A.; Ishige, R.; Cromwell, O. R.; Chung, J.; Takahara, A.; Guan, Z. Mechanically robust and self-healable superlattice nanocomposites by self-assembly of single-component "sticky" polymer-grafted nanoparticles. *Adv. Mater.* **2015,** *27*, 3934-3941.

279. Ahn, B. K.; Lee, D. W.; Israelachvili, J. N.; Waite, J. H. Surface-initiated self-healing of polymers in aqueous media. *Nat. Mater.* **2014,** *13*, 867-872.

280. Perrau, M. B.; Iliopoulos, I.; Audebert, R. Phase separation of polyelectrolyte/nonionic polymer systems in aqueous solution: effects of salt and charge density. *Polymer* **1989,** *30*, 2112-2117.

281. Yang, S.; Ma, S.; Wang, C.; Xu, J.; Zhu, M. Polymer complexation by hydrogen bonding at the interface. *Aust. J. Chem.* **2014,** *67*, 11-21.

282. Li, L.; Yan, B.; Yang, J.; Chen, L.; Zeng, H. Novel mussel-inspired injectable self-healing hydrogel with anti-biofouling property. *Adv. Mater.* **2015,** *27*, 1294-1299.

283. Zumbuehl, A.;, Ferreira, L.; Kuhn, D.; Astashkina, A.; Long, L.; Yeo, Y.; Iaconis, T.; Ghannoum, M.; Fink, G. R.; Langer R.; Kohane, D. S. Antifungal hydrogels. *Proc. Natl. Acad. Sci. U.S.A.* **2007,** *104*, 12294-12998.

284. Hancock, R. E.; Sahl, H. G. Antimicrobial and host-defense peptides as new anti-infective therapeutic strategies. *Nat. Biotechnol.* **2006,** *24*, 1551-1557.

285. Baek, K.; Liang, J.; Lim, W. T.; Zhao, H.; Kim, D. H.; Kong, H. In situ assembly of antifouling/bacterial silver nanoparticle-hydrogel composites with controlled particle release and matrix softening. *ACS Appl. Mater. Interfaces* **2015,** *7*, 15359-15367.

286. Li, L.; Yan, B.; Yang, J.; Huang, W.; Chen, L.; Zeng, H. Injectable self-healing hydrogel with antimicrobial and antifouling properties. *ACS Appl. Mater. Interfaces* **2017,** *9*, 9221-9225.

287. Anselmo, A. C.; Mitragotri, S. A review of clinical translation of inorganic nanoparticles. *AAPS J.* **2015,** *17*, 1041-1054.

288. Bijelic, A.; Aureliano, M.; Rompel, A. Polyoxometalates as potential next-generation metallodrugs in the combat against cancer. *Angew. Chem.* **2019,** *58*, 2980-2999.

289. Song, Y. F.; Tsunashima, R. Recent advances on polyoxometalate-based molecular and composite materials. *Chem. Soc. Rev.* **2012,** *41*, 7384-7402.

290. Jing, B.; Qiu, J.; Zhu, Y. Organic-inorganic macroion coacervate complexation. *Soft Matter* **2017,** *13*, 4881-4889.

291. Kozhevnikov, I. V. Catalysis by heteropoly acids and multicomponent polyoxometalates in liquid-phase reactions. *Chem. Rev.* **1998,** *98*, 171-198.

292. Kozhevnikov, I.V. Advances in catalysis by heteropolyacids. *Russ. Chem. Rev.* **1987,** *56*, 811-825.

293. Desbrieres, J. Viscosity of semiflexible chitosan solutions: Influence of concentration, temperature, and role of intermolecular interactions. *Biomacromolecules* **2002,** *3*, 342-349.

294. Cho, J.; Heuzey, M.-C.; Bégin, A.; Carreau, P. J. Viscoelastic properties of chitosan solutions: Effect of concentration and ionic strength. *J. Food Eng.* **2006,** *74*, 500-515.

295. Jing, B.; Wang, X.; Wang, H.; Qiu, J.; Shi, Y.; Gao, H.; Zhu, Y. Shape and mechanical control of poly(ethylene oxide) based polymersome with polyoxometalates via hydrogen bond. *J. Phys. Chem. B* **2017,** *121*, 1723-1730.

296. Lin, X.; Wang, Y.; Wu, L. Hexagonal mesostructure and its disassembly into nanofibers of a diblock molecule/polyoxometalate hybrid. *Langmuir* **2009,** *25*, 6081-6087.

297. Kozhevnikov, I. V.; Sinnema, A.; Bekkum, H. Proton sites in Keggin heteropoly acids from ^{17}O NMR. *Catal. Lett.* **1995,** *34*, 213-221.

298. Xue, N.; Qiu, X.-P.; Aseyev, V.; Winnik, F. M. Nonequilibrium liquid-liquid phase separation of poly(N-isopropylacrylamide) in water/methanol mixtures. *Macromolecules* **2017,** *50*, 4446-4453.

299. Hwang, D. S.; Zeng, H.; Lu, Q.; Israelachvili, J.; Waite, J. H. Adhesion mechanism in a DOPA-deficient foot protein from green mussels. *Soft Matter* **2012,** *8*, 5640-5648.

300. Karnal, P.; Roberts, P.; Gryska, S.; King, C.; Barrios, C.; Frechette, J. Importance of substrate functionality on the adhesion and debonding of a pressure-sensitive adhesive under water. *ACS Appl. Mater. Interfaces* **2017,** *9*, 42344-42353.

301. Chen, J.; Liu, J.; Thundat, T.; Zeng, H. Polypyrrole-doped conductive supramolecular elastomer with stretchability, rapid self-healing, and adhesive property for flexible electronic sensors. *ACS Appl. Mater. Interfaces* **2019,** *11*, 18720-18729.

302. Kim, H.; Mizumachi, H. Miscibility and shear creep resistance of acrylic pressure-sensitive adhesives: Acrylic copolymer and tackifier resin systems. *J. Appl. Polym. Sci.* **1995,** *58*, 1891-1899.

303. Fujita, M.; Takemura, A.; Ono, H.; Kajiyama, M.; Hayashi, S.; Mizumachi, H. Effects of miscibility and viscoelasticity on shear creep resistance of natural-rubber-based pressure-sensitive adhesives. *J. Appl. Polym. Sci.* **2000,** *75*, 1535-1545.

304. Murakami, Y.; Yokoyama, M.; Nishida, H.; Tomizawa, Y.; Kurosawa, H. A simple hemostasis model for the quantitative evaluation of hydrogel-based local hemostatic biomaterials on tissue surface. *Colloids Surf., B* **2008,** *65*, 186-189.

305. Giano, M. C.; Ibrahim, Z.; Medina, S. H.; Sarhane, K. A.; Christensen, J. M.; Yamada, Y.; Brandacher, G.; Schneider, J. P. Injectable bioadhesive hydrogels with innate antibacterial properties. *Nat. Commun.* **2014,** *5*, 4095.

306. Katz, S.; Izhar, M.; Mirelman, D. Bacterial adherence to surgical sutures. A possible factor in suture induced infection. *Ann. Surg.* **1981,** *194*, 35-41.

307. George, D. L,; Arnow, P. M.; Fox, A. S.; Baker, A. L.; Thistlethwaite, J. R.; Emond, J. C.; Whitington, P. F.; Broelsch, C. E. Bacterial infection as a complication of liver transplantation: Epidemiology and risk factors. *Rev. Infect. Dis.* **1991,** *13*, 387–396.

308. Wade, J. J.; Rolando, N.; Hayllar, K.; Philpott-Howard, J.; Casewell, M.W.; Williams, R. Bacterial and fungal infections after liver transplantation: an analysis of 284 patients-hepatology. *Hepatology* **1995,** *21*, 1328-1336.

309. Bijelic, A.; Aureliano, M.; Rompel, A. The antibacterial activity of polyoxometalates: structures, antibiotic effects and future perspectives. *Chem. Commun.* **2018,** *54*, 1153-1169.

310. Danner, E. W.; Kan, Y.; Hammer, M. U.; Israelachvili, J. N.; Waite, J. H. Adaptive synergy between catechol and lysine promotes wet adhesion by surface salt displacement. *Science* **2015,** *349*, 628-632.

311. Smith A. M. *Biological Adhesives*, Springer, Berlin, Germany, **2016**.

312. Waite, J. h., Mussel power. *Nature Materials* **2008,** *7*, 8-9.

313. Ye, Q.; Zhou, F.; Liu, W. Bioinspired catecholic chemistry for surface modification. *Chem. Soc. Rev.* **2011,** *40*, 4244-4258.

314. Zhang, C.; Wu, B.; Zhou, Y.; Zhou, F.; Liu, W.; Wang, Z. Mussel-inspired hydrogels: from design principles to promising applications. *Chem. Soc. Rev.* **2020,** *49*, 3605-3637.

315. Miserez, A.; Li, Y.; Waite, J. H.; Zok, F. Jumbo squid beaks: inspiration for design of robust organic composites. *Acta Biomater.* **2007,** *3*, 139-149.

316. Wang, Z.; Zhang, S.; Zhao, S.; Kang, H.; Wang, Z.; Xia, C.; Yu, Y.; Li, J. Facile biomimetic self-coacervation of tannic acid and polycation: Tough and wide pH range of underwater adhesives. *Chem. Eng. J.* **2021,** *404*, 127069.

317. Li, X.; Du, Z.; Song, Z.; Li, B.; Wu, L.; Liu, Q.; Zhang, H.; Li, W. Bringing hetero-polyacid-based underwater adhesive as printable cathode coating for self-powered electrochromic aqueous batteries. *Adv. Funct. Mater.* **2018,** *28*, 1800599.

318. Yang, G.; Zhang, Y. M.; Cai, Y.; Yang, B.; Gu, C.; Zhang, S. X. Advances in nanomaterials for electrochromic devices. *Chem. Soc. Rev.* **2020,** *49*, 8687-8720.

319. Cannavale, A.; Ayr, U.; Fiorito, F.; Martellotta, F. Smart electrochromic windows to enhance building energy efficiency and visual vomfort. *Energies* **2020,** *13*, 1449.

320. Wu, W.; Wang, M.; Ma, J.; Cao, Y.; Deng, Y. Electrochromic metal oxides: Recent progress and prospect. *Adv. Electron. Mater.* **2018,** *4*, 1800185.

321. Zhao, J.; Tian, Y.; Wang, Z.; Cong, S.; Zhou, D.; Zhang, Q.; Yang, M.; Zhang, W.; Geng, F.; Zhao, Z. Trace H_2O_2-assisted high-capacity tungsten oxide electrochromic batteries with ultrafast charging in seconds. *Angew. Chem.* **2016,** *128*, 7277-7281.

322. Wang, J.; Zhang, L.; Yu, L.; Jiao, Z.; Xie, H.; Lou, X. W.; Sun, X. W. A bi-functional device for self-powered electrochromic window and self-rechargeable transparent battery applications. *Nat. Commun.* **2014,** *5*, 4921.

323. Tian, Y.; Zhang, W.; Cong, S.; Zheng, Y.; Geng, F.; Zhao, Z. Unconventional aluminum ion intercalation/deintercalation for fast switching and highly stable electrochromism. *Adv. Funct. Mater.* **2015,** *25*, 5833-5839.

324. Tian, Y.; Cong, S.; Su, W.; Chen, H.; Li, Q.; Geng, F.; Zhao, Z. Synergy of $W_{18}O_{49}$ and polyaniline for smart supercapacitor electrode integrated with energy level indicating functionality. *Nano Lett.* **2014,** *14*, 2150-2156.

325. Zhang, Y.; Ng, S. W.; Lu, X.; Zheng, Z. Solution-processed transparent electrodes for emerging thin-film solar cells. *Chem. Rev.* **2020,** *120*, 2049-2122.

326. Zhang, J.; Zhang, W.; Yang, Z.; Yu, Z.; Zhang, X.; Chang, T. C.; Javey, A. Vertically aligned tungsten oxide nanorod film with enhanced performance in photoluminescence humidity sensing. *Sens. Actuators, B* **2014,** *202*, 708-713.

327. Wu, W. Inorganic nanomaterials for printed electronics: a review. *Nanoscale* **2017,** *9*, 7342-7372.

328. Aleeva Y.; Pignataroa B. Recent advances in upscalable wet methods and ink formulation for printed electronics. *J. Mater. Chem. C* **2013,** *2*, 6436-6453.

329. Wang, S; Hwang, J.; Kim, E. Polyoxometalates as promising materials for electrochromic devices. *J. Mater. Chem. C* **2019,** *7*, 7828-7850.

330. Pitto-Barry, A.; Barry, N. P. E. Pluronic® block-copolymers in medicine: from chemical and biological versatility to rationalisation and clinical advances. *Polym. Chem.* **2014,** *5*, 3291-3297.

331. Su, Y.; Wang, J.; Liu, H. FTIR spectroscopic study on effects of temperature and polymer composition on the structural properties of PEO-PPO-PEO block copolymer micelles. *Langmuir* **2002,** *18*, 5370-5374.

332. Chen, J.; Yan, B.; Wang, X.; Huang, Q.; Thundat, T.; Zeng, H. Core cross-linked double hydrophilic block copolymer micelles based on multiple hydrogen-bonding interactions. *Polym. Chem.* **2017,** *8*, 3066-3073.

333. Ganguly, R.; Kunwar, A.; Dutta, B.; Kumar, S.; Barick, K. C.; Ballal, A.; Aswal, V. K.; Hassan, P. A. Heat-induced solubilization of curcumin in kinetically stable pluronic P123 micelles and vesicles: An exploit of slow dynamics of the micellar restructuring processes in the aqueous pluronic system. *Colloids Surf., B* **2017,** *152*, 176-182.

334. Suthiwangcharoen, N. and Nagarajan R. Controlled design and construction of multifunctional nanoparticles by molecular self-assembly. *RSC Adv*., **2014**, *4*, 10076-10089.

335. Overbeek, J. T. J. and Voorn, M. J. Phase separation in polyelectrolyte solutions. Theory of complex coacervation. *J. Cell. Comp. Physiol.* **1957,** *49*, 7-26.

336. Ananthapadmanabhan, K. P.; Goddard, E. D. Aqueous biphase formation in polyethylene oxide-inorganic salt systems. *Langmuir* **1987**, *3,* 25-31.

337. Baik, S.; Kim, D. W.; Park, Y.; Lee, T. J.; Ho Bhang, S.; Pang, C. A wet-tolerant adhesive patch inspired by protuberances in suction cups of octopi. *Nature* **2017**, *546*, 396-400.

338. Han, L.; Yan, B.; Zhang, L.; Wu, M.; Wang, J.; Huang, J.; Deng, Y.; Zeng, H. Tuning protein adsorption on charged polyelectrolyte brushes via salinity adjustment. *Colloids Surf., A* **2018**, *539*, 37-45.

339. Yamazoe, K.; Higaki, Y.; Inutsuka, Y.; Miyawaki, J.; Cui, Y. T.; Takahara, A.; Harada, Y. Enhancement of the hydrogen-bonding network of water confined in a polyelectrolyte brush. *Langmuir* **2017,** *33*, 3954-3959.

340. Yamase, T. Photo- and electrochromism of polyoxometalates and related Materials. *Chem. Rev.* **1998,** *98*, 307−325.

341. Long, D.-L.; Tsunashima, R.; Cronin, L. Polyoxometalates: Building blocks for functional nanoscale systems. *Angew. Chem. Int. Ed.* **2010,** *49*, 1736-1758.

342. Lee, H.; Lee, B. P.; Messersmith, P. B. A reversible wet/dry adhesive inspired by mussels and geckos. *Nature* **2007,** *448*, 338-341.

343. Ma, Y.; Ma, S.; Wu, Y.; Pei, X.; Gorb, S. N.; Wang, Z.; Liu, W.; Zhou, F. Remote control over underwater dynamic attachment/detachment and locomotion. *Adv. Mater.* **2018,** *30*, 1801595.

344. Rao, P.; Sun, T. L.; Chen, L.; Takahashi, R.; Shinohara, G.; Guo, H.; King, D. R.; Kurokawa, T.; Gong, J. P. Tough hydrogels with fast, strong, and reversible underwater adhesion based on a multiscale design. *Adv. Mater.* **2018,** *30*, 1801884.

345. Zwicker, D.; Seyboldt, R.; Weber, C. A.; Hyman, A. A.; Jülicher, F. Growth and division of active droplets provides a model for protocells. *Nat. Phys.* **2016,** *13*, 408-413.

346. Zhao, Q.; Lee, D. W.; Ahn, B. K.; Seo, S.; Kaufman, Y.; Israelachvili, J. N.; Waite, J. H. Underwater contact adhesion and microarchitecture in polyelectrolyte complexes actuated by solvent exchange. *Nat. Mater.* **2016,** *15*, 407-412.

347. Wei, C.; Zhu, X.; Peng, H.; Chen, J.; Zhang, F.; Zhao, Q. Facile preparation of lignin-based underwater adhesives with improved performances. *ACS Sustainable Chem. Eng.* **2019,** *7*, 4508-4514.

348. Maier, G. P.; Rapp, M. V.; Waite, J. H.; Israelachvili, J. N.; Butler, A. Adaptive synergy between catechol and lysine promotes wet adhesion by surface salt displacement. *Science* **2015**, *349*, 628-632.

349. Hirschberg, J. H. K. K.; Brunsveld, L.; Ramzi, A.; Vekemans. J. A. J. M.; Sijbesma, R. P.; Meijer, E. W. Helical self-assembled polymers from cooperative stacking of hydrogen-bonded pairs. *Nature* **2000,** *407*, 167-170.

350. Jeon, I.; Cui, J.; Illeperuma, W. R.; Aizenberg, J.; Vlassak, J. J. Extremely stretchable and fast self-healing hydrogels. *Adv. Mater.* **2016,** *28*, 4678-4683.

351. Khoultchaev, Kh.Kh.; Pang, P.; Kerekes, R.J.; Englezos, P. Enhancement of the retention performance of the poly(ethylene oxide)-tannic acid system by poly(diallyldimethyl ammonium chloride). *Can. J. Chem. Eng.* **1998,** *76*, 261-266.

352. Lin, D.; Liu, N.; Yang, K.; Zhu, L.; Xu, Y.; Xing, B. The effect of ionic strength and pH on the stability of tannic acid-facilitated carbon nanotube suspensions. *Carbon* **2009,** *47*, 2875-2882.

353. Weber, F.; Sagstuen, E.; Zhong, Q. Z.; Zheng, T.; Tiainen, H. Tannic acid radicals in the presence of alkali metal salts and their impact on the formation of silicate-phenolic networks. *ACS Appl. Mater. Interfaces* **2020,** *12*, 52457-52466.

354. Lin, S.; Liu, J.; Liu, X.; Zhao, X. Muscle-like fatigue-resistant hydrogels by mechanical training. *Proc. Natl. Acad. Sci. U.S.A.* **2019,** *116*, 10244-10249.

355. Baer-Dubowska, W.; Szaefer, H.; Majchrzak-Celińska, A.; Krajka-Kuźniak, V. Tannic acid: Specific form of tannins in cancer chemoprevention and therapy-old and new Applications. *Curr. Pharmacol. Rep.* **2020,** *6*, 28-37.

356. Baby, B.; Antony, P.; Vijayan, R. Antioxidant and anticancer properties of berries. *Crit. Rev. Food Sci. Nutr.* **2018,** *58*, 2491-2507.

357. Yildirim, I.; Kutlu, T. Anticancer agents: Saponin and tannin. *Int. J. Biol. Chem.* **2015,** *9*, 332-340.

358. Hadi, S. M.; Bhat, S. H.; Azmi, A. S.; Hanif, S.; Shamim, U.; Ullah, M. F. Oxidative breakage of cellular DNA by plant polyphenols: a putative mechanism for anticancer properties. *Semin. Cancer Biol.* **2007,** *17*, 370-376.

359. Liu, K.-K.; Cheng, C.-L.; Chang, C.-C.; Chao, J.-I. Biocompatible and detectable carboxylated nanodiamond on human cell. *Nanotechnology* **2007,** *18*, 325102.

360. Berger, E.; Vega, N.; Weiss-Gayet, M.; Geloen, A. Gene network analysis of glucose linked signaling pathways and their role in human hepatocellular carcinoma cell growth and survival in HuH7 and HepG2 cell lines. *Biomed. Res. Int.* **2015,** *2015*, 821761.

361. Sahu, A.; Kasoju, N.; Goswami, P.; Bora, U. Encapsulation of curcumin in Pluronic block copolymer micelles for drug delivery applications. *J. Biomater. Appl.* **2011,** *25*, 619-639.

362. Kaczmarek, B. Tannic acid with antiviral and antibacterial activity as a promising component of biomaterials-A minireview. *Materials* **2020,** *13,* 3224.